Hydrocarbon Pool Mechanisms in zeolite catalysts studied by Kerr-gated Raman Spectroscopy

Emma Jane Campbell

Department of Chemistry

University College London

Supervisor: Professor Andrew M. Beale

Thesis submitted for the degree of Doctor of Philosophy 2021

Declaration

I, Emma Jane Campbell, confirm that the work presented in this thesis is my own except where specified in the text and acknowledgements.

05/07/2021

Abstract

Hydrocarbon pools (HCP) are thought to be an integral part of some zeolite-catalysed hydrocarbon conversion mechanisms. The composition of a HCP can vary due to reaction conditions and to zeolite properties, i.e., topology and acidity. The HCP composition and behaviour control the activity and selectivity of the reaction, and therefore a full understanding of the speciation in these reactions is necessary for future reaction developments to improve efficiency. In this thesis, Kerr-gated Raman Spectroscopy is applied under operando conditions using a visible wavelength laser (400 nm) to identify HCP intermediates during catalytic conversion of methanol, and biomass derived model-compounds. In this work the application of the Kerr-gate is vital for removing the inherent emission signals from zeolite samples which typically dominate Raman spectra.

In Chapter 3, this technique is used to unravel the Methanol-to-Olefins (MTO) reaction. The first part of this chapter identifies the role of polyenes during the initial stages of catalyst deactivation in small pore zeolites, while the second part interrogates how calcium affects the HCP and therefore the reaction mechanism.

Chapter 4 focuses on furan conversion, as a model compound for biomass to study Catalytic Fast Pyrolysis (CFP). This reaction is followed by Raman and UV-Vis spectroscopy during temperature ramping, allowing the changes that lead to aromatics and olefins production on four zeolites (ZSM-5, beta, Zeolite Y and ferrierite) to be followed and understood. Only in ZSM-5 is benzofuran observed to form on the zeolite, an intermediate linked with higher aromatic formation. Chapter 5 continues the study of converting model compounds of biomass using ZSM-5 only, but changing the chemical feed to acetic acid, acetaldehyde, and hydrogenated furan.

Finally, in Chapter 6, the results from a UV-Raman study of the MTO and CFP reactions are shown, demonstrating the usefulness of probing samples with different incident wavelengths to capitalize on resonance enhancement.

Acknowledgements

A huge thank you goes to my supervisors. Prof. Andrew Beale thank you for giving me the chance to take on this project in the first place, I'm very grateful to have had this opportunity and to you that you always had an open door for discussing problems. I owe a vast thank you to Dr Ines Lezcano-Gonzalez for her support throughout this project, from our intense conversations in organic chemistry to great ideas in experimental planning, it has been wonderful to work with you. Thanks to Dr Igor Sazanovich for his genius and calm demeanour during beamtime difficulties, and for excellent physics explanations geared to chemists. Thanks to Dr Mike Watson at Johnson Matthey for fruitful discussions – particularly in CFP – and for offering support in this research project.

I have to thank my friends at the CatHub. Firstly, Andrea, Rachel, and Alex; it was a pleasure to share the PhD journey with you guys and I'm so glad to have met and worked with you. Thanks to Monik for your positive attitude and kindness, always willing to help everyone around you, and importantly for keeping me near sanity through lockdown! Toni, thanks for the long walks and coffees on Sunday afternoons, I look forward to many more. To friends that I was lucky enough to share an office with; Pip, Evan, Donnie and (towards the end) Wilm, as well as everyone else in the CatHub students office, thanks for creating a great atmosphere for working even during stressful times. Thank you to everyone who helped on Kerr-gate beamtimes, notably Stefan, who assisted in the majority of my experiments, bringing plenty of curiosity and energy. And a special thanks to June; thank you for picking me up and urging me forwards when I needed it, I'll always be grateful for the real and open chats.

I give my highest appreciation to my family for their love and support throughout my entire life, without it I know I wouldn't have come so far. Thank you for encouraging me through the tough parts of the last few years, and I'm always so glad to celebrate with you in the high points.

Statement of impact

The work in this thesis explored the capability of the Kerr-gated spectrometer of the Ultra facility at the Central Laser Facility (CLF) to interrogate catalytic reactions, with sponsorship from the CLF and Johnson Matthey. The reactions explored – Methanol-to-Hydrocarbons (MTH) and catalytic fast pyrolysis (CFP) – are highly relevant in the development of chemical processes that lead to platform chemicals from renewable resources, moving away from crude oil as a feedstock, as well as potentially being carbon neutral.

The project was exploratory in terms of understanding the detection capabilities of the Kerr-gate, and a lot has been learned which has opened further opportunities for using this time-resolved method to interrogate catalytic systems, to tackle other unanswered questions in the field. Through studying the catalytic systems via *operando* Kerr-gated Raman Spectroscopy, molecular intermediates have been identified during reaction, which has led to an improved understanding of the active and deactivating species. This information is key in the design and development of new catalysts for the MTH and CFP processes.

Contents

1 Introduction 1

1.1 Motivation 1

1.2 Zeolites as catalysts 2

1.3 Acid-base properties of zeolites 4

1.4 Catalytic mechanisms in zeolites 5

1.5 Methanol to Hydrocarbons 6

1.6 Catalytic Fast Pyrolysis 11

1.7 *Operando* spectroscopy 15

1.8 References 16

2 Methodology and materials 20

2.1 Methodology 20

2.1.1 Raman Spectroscopy 20

2.1.2 Diffuse Reflectance UV-Vis Spectroscopy 29

2.1.3 Mass Spectrometry 32

2.1.4 Powder X-Ray Diffraction 33

2.1.5 Nitrogen physisorption 35

2.1.6 NH_3-Temperature Programmed Desorption 37

2.1.7 SEM-EDX 39

2.1.8 X-ray Fluorescence 40

2.1.9 Thermogravimetric analysis of spent catalyst samples 41

2.2 Materials 42

2.2.1 Synthesis of H-ZSM-5 42

2.2.2 Chabazite Materials 42

2.2.3 Impregnation of calcium into H-ZSM-5 and H-SSZ-13 by incipient wetness 42

2.2.4 Materials from Zeolyst International 43

2.3 Materials Characterisation 44

2.3.1 H-ZSM-5 (Si/Al = 40) and Ca-ZSM-5 44

2.3.2 H-SSZ-13 and Ca-SSZ-13 53

2.3.3 H-SAPO-34 62

2.3.4 ZSM-5 (Si/Al = 15) 68

2.3.5 Ferrierite, Beta and Zeolite Y from Zeolyst Int. 73

2.4 References 78
3 Methanol to Hydrocarbons 80
3.1 Introduction 80
3.2 Prior work 82
3.3 Methanol -to-Olefins H-SSZ-13 87
3.3.1 Isothermal reaction at 280 °C 88
3.3.2 Isothermal reaction at 350 °C 93
3.3.3 Discussion 96
3.4 Methanol-to-Olefins on H-SAPO-34 98
3.4.1 Discussion 108
3.5 Methanol-to-Olefins Ca/H-ZSM-5 110
3.5.1 Diffuse Reflectance UV-Vis Spectroscopy 115
3.5.2 Discussion 117
3.6 Methanol-to-Olefins Ca/H-SSZ-13 117
3.6.1 Diffuse Reflectance UV-Vis experiment 124
3.6.2 Thermogravimetric analysis of coke 126
3.6.3 Discussion 127
3.7 Conclusions 128
3.8 References 129
4 Furan conversion: a comparison of topology 133
4.1 Introduction 133
4.2 Room temperature adsorption 136
4.3 H-ZSM-5 Temperature programmed reaction 142
4.4 Ferrierite Temperature Programmed Reaction 149
4.5 H-Y Temperature programmed reaction 154
4.6 H-Beta Temperature Programmed Reaction 159
4.7 Thermo-gravimetric Analysis of coked zeolites 163
4.8 Comparison and discussion 165
4.9 Conclusions 169
4.10 References 170
5 Conversion of oxygenated hydrocarbons on H-ZSM-5: Acetaldehyde, acetic acid, furan and 2,3-dihydrofuran 174
5.1 Introduction 174
5.2 Room temperature adsorption 176

5.2.1 Acetaldehyde 176
5.2.2 Acetic Acid 179
5.2.3 Furan 181
5.2.4 2,3-dihydrofuran 182
5.3 Temperature programmed reactions 184
5.3.1 Acetaldehyde 184
5.3.2 Acetic Acid 189
5.3.3 Furan 195
5.3.4 2,3-dihydrofuran 199
5.4 Quenched spectra 202
5.5 Discussion and comparison 203
5.6 Conclusions 205
5.7 References 205
6 UV Raman Spectroscopy 208
6.1 Introduction 208
6.2 Methanol-to-Olefins 211
6.2.1 H-SAPO-34 211
6.2.2 MTH SSZ-13 215
6.2.3 Discussion on the application of UV-Raman to MTO 218
6.3 Conversion of furan, acetaldehyde, acetic acid and 2,3-dihydrofuran 219
6.3.1 Furan 219
6.3.2 Acetaldehyde 223
6.3.3 Acetic acid 225
6.3.4 2,3-dihydrofuran 228
6.4 Conclusions 230
6.5 References 231
7 Conclusions and future work 234
7.1 Conclusions 234
7.2 Future work 236
Appendix 238
Isothermal reaction of H-SSZ-13 catalyst in MTO at 450 °C 238

1 Introduction

1.1 Motivation

As the human population grows, there is ever increasing demand for food, water, and energy, while oil reserves are dwindling around the world, currently predicted to meet 49.5 years' of demand.[1] While production of energy from renewable sources continues to grow, an overall increase in world consumption means that year-on-year, greater quantities of crude oil are needed to meet the demands. According to the BP Statistical Review of World Energy 2020, in 2019, oil still accounted for 33 % of the energy consumption for the world, and coal for another 27 %.[1]

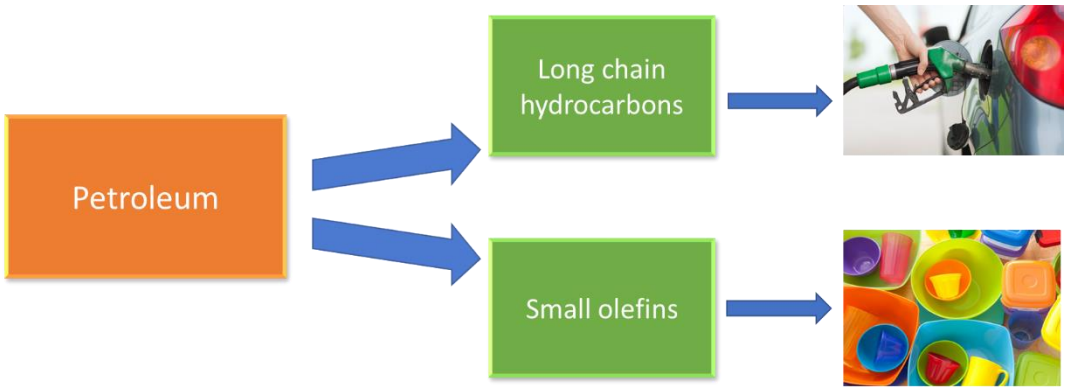

Figure 1 Crude oil is cracked to give longer chain hydrocarbons which are used as transportation fuels, and small olefins which are used for plastics and as an important chemical in synthetic chemistry.

Apart from a high demand for energy, over the past decades the environmental impact of industrialisation has been realised, and global agreements to slow climate change have been made to reduce carbon emissions, pushing for a focus on sourcing fuels that as well as being renewable, have minimal environmental impact. Starting at the World Climate Conference in 1978, to the most recent agreements (the Paris Agreement of 2015, and the Glasgow Climate Pact 2021) long-term goals are set for countries to develop strategies to decrease greenhouse gas emissions in an aim to prevent the global temperature from raising more than 2 °C above pre-industrial temperatures.[2] For example,

Germany outlined that by 2050 all of their energy should come from renewable resources, and any hydrocarbons should be produced from biomass obtained from waste products,[3] and the US initially outlined the use of carbon capture technologies to make use of gaseous CO_2 to provide “negative emissions”.[4] However, efficiencies of chemical pathways need to be improved if the production of hydrocarbons from renewable sources is to compete with the low cost of processing fossil fuels.

Fossil fuels such as natural gas and light fractions of crude oil are also sources of small olefins, as highlighted in Figure 1, which are commodity chemicals for producing plastics and as starting materials for feedstocks required in the pharmaceutical industry. Ethene is typically produced through steam cracking of naphtha or light hydrocarbons while propene is produced as a product of the fluid catalytic cracking (FCC) of naphtha.[5] In the past decade a surge in shale gas production has led to an abundance of methane as well as cheaper ethane (and propane), prompting a shift towards steam cracking of ethane to produce ethene. Cheap methane has also opened avenues for transforming C1 hydrocarbons into high value chemicals, such as methane to methanol (*via* syngas), or Fischer-Tropsch synthesis of hydrocarbons.[6,7] Although shale gas provides an alternative source than crude oil offering routes to such essential chemicals as ethene and propene, it is still extremely problematic in regards to environmental pollution and is another finite raw material.[5]

It is well recognised that there needs to be a shift to sources of hydrocarbons that are less finite, that also emit less pollution or greenhouse gases into the atmosphere for both transportation fuels and chemical feedstocks. The development of new materials as catalysts for such processes will be important to make the conversion of renewable hydrocarbons (such as biomass, bio-methanol or bio-ethanol) competitive with the current infrastructure for converting fossil fuels.

1.2 Zeolites as catalysts

One such family of catalytic materials are zeolites. The microporous structures and compositions of zeolites give them important properties such as their high

surface area, adsorption capacity, ion-exchange capacity, and acid/base properties. Zeolites are minerals composed of silica and alumina arranged in crystalline structures containing pore networks of channels, cavities and windows of molecular dimensions varying from 3 to 12 Å.[8] The primarily building blocks of zeolites are $TO_{4/2}$ tetrahedron, where T is conventionally Si or Al, although they may also include other heteroatoms e.g., B, Ti, P or Zn, which changes the chemical properties of the material. T atoms are linked together through bridging oxygen atoms. Primary tetrahedra link up periodically to form secondary building units, which are joined into the three-dimensional, macromolecular structures.[9]

Zeolites can be classified as small, medium, large, or extra-large pore, depending on the number of T atoms included in the largest pore window which gives access to the channel system, windows being made up of 8, 10, 12 or 14 membered rings, respectively.[10] Depending on the channel arrangements, zeolites can be one, two or three dimensional, which – along with channel widths – affects the ease with which molecules exterior to the zeolite can diffuse into and through its channel systems.[10,11] These properties give rise to applications as molecular sieves, where large molecules are excluded from the internal structure based on their size, or as “reaction cavities”, where reactant molecules become encapsulated such that they react in closer proximity and without perturbation from the external environment.[11] These properties along with their high thermal and hydrothermal stability and ion-exchange capacity allow them to be used for many industrial applications as selective catalysts, adsorbents and molecular sieves.[7,12]

Zeolites were first employed industrially as catalysts for isomerization reactions. Whilst zeolites were proven to also function as cracking catalysts, they deactivated too quickly through carbon laydown. Once a method for dealuminating zeolites in 1962 was discovered, they were employed for the FCC of petroleum distillates.[13,14] Solid acid catalysts had previously been used for the application, but in their amorphous forms of silica and alumina. The introduction of zeolite Y to FCC enhanced gasoline production enormously, and still today this process is used for refining large-molecule petroleum feedstocks, with a huge economic impact.[13,14] Zeolite Y has large three-dimensional pores with large spherical cages at channel intersections. The products of cracking over this

catalyst are mainly large hydrocarbons and thus the process yields high gasoline fractions. In 1973, ZSM-5 was synthesised, a more product selective zeolite with smaller rings (than zeolite Y) at channel openings, made with a higher silica content which contributes to improved thermal stability.[15] ZSM-5 can be used as a FCC catalyst with higher selectivity towards olefin production such as propene.[16] Through understanding how topologies impact product distribution, and choosing a catalyst based on this information, high selectivity to desired products can be achieved. Either diffusion can be restricted, known as product shape selectivity, or certain intermediates can be hindered to prevent unwanted side reactions – known as transition state shape selectivity.[14] As well as selecting the ideal topology for a reaction, the acidity of a zeolite should be considered and where possible, tuned to improve selectivity and catalyst lifetime.

1.3 Acid-base properties of zeolites

In traditional zeolites of silica and alumina, the Si atoms are substituted with tetrahedral Al^{3+} ions within the lattice and these tetrahedrally coordinated Al^{3+} induce a negative charge on the structure, which is counter balanced by an extra-framework cation.[14] Cations can be organic in nature if the zeolite is synthesised using an organic template, or, inorganic metal ions from an inorganic template or synthesis reagents. This is demonstrated in Figure 2 in which the negative charge of the framework as induced by the aluminium anion is neutralised by a sodium cation. Cations can be readily exchanged to tune the nature of zeolites to their application.[8,14,17]

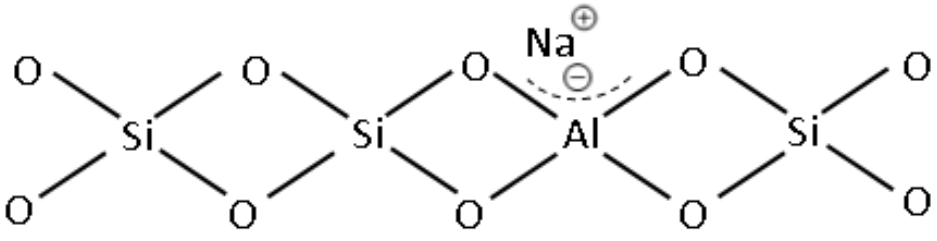

Figure 2 Illustration of a structure of a zeolite containing four silica tetrahedra and one alumina tetrahedra whose negative charge is counter-balanced by a sodium cation.

Zeolites are said to be solid acids. When the species counter-balancing the negative charge is a proton, the surface is Brønsted acidic. These Brønsted sites

are referred to as bridging hydroxyl groups, and the zeolite is catalytically active for chemical processes which utilise their acidity.[14] To yield a Brønsted acidic zeolite, the as-synthesised zeolite with inorganic metal cations must be ion-exchanged by contact with a solution of ammonium salt, leaving NH_4^+ ions to compensate the negative framework charge, followed by thermal decomposition to leave a proton. If the charge compensating species is organic, thermal decomposition alone is enough to leave the surface acidic.[10] Lewis acidity is also present in zeolites, its origin can be due to extra-framework aluminium brought about by chemical or thermal treatment or other extra-framework cations can also contribute to Lewis acidity.[18,19]

The Brønsted acidity of zeolites can be altered by changing the ratio of Si/T^{3+}, by altering the composition of the synthesis gel, or by post-synthesis treatments with acids, bases or steam to remove T^{3+} from the framework.[14] Generally, a higher Si/T^{3+} ratio results in fewer Brønsted acid sites that are typically stronger acid sites than in materials with low Si/T^{3+} ratio, as the T^{3+} atoms become more dispersed and the negative charge on the framework becomes more localised.[10] Post-synthetic treatments can be used to dealuminate the framework and create extra-framework aluminium sites which are Lewis acidic, or the acid sites can be tuned by the introduction of metal ions to the surface of zeolites, to introduce Lewis acid sites. This results in multivalent cations balancing the negative framework charge of multiple aluminium sites to replace protons.[20] Alkali metal ions are often used to decrease acidity where necessary. Selectivity of the Methanol-to-Hydrocarbons reaction (MTH) has been increased towards light olefins by the addition of calcium to ZSM-5, removing much of the Brønsted acidity for example,[21,22] while Zn^{2+} ions on ZSM-5 result in sites that promote dehydrogenation and cyclization of propane.[20,23]

1.4 Catalytic mechanisms in zeolites

In zeolite catalysed reactions, the zeolite may play a direct role, where the proton or metal cation compensating the framework charge is the active site forming products which then diffuse out of the structure. In these reactions the zeolite topology determines which products can form within, and which can leave the framework. The MTH reaction is less typical, working through an indirect

mechanism. It is well-established that the reaction selectivity depends upon the identity of a pool of hydrocarbons that builds up in the zeolite pores, the methanol reacts with this pool causing it to split off the products. In this case, changing the zeolite topology indirectly plays a role in the product distribution, because the size and shape of the pores define the identity of the hydrocarbon pool (HCP).[24,25] Some groups have reported HCP-type behaviour in other zeolite catalysed mechanisms, including catalytic fast pyrolysis,[26,27] which is a process for upgrading biomass to higher value products, although the identification of this type of hydrocarbon pool has been little studied.

1.5 Methanol to Hydrocarbons

A reaction to form gasoline from methanol was first commercialised in 1977 by Mobil in New Zealand.[28] Its discovery came at a time when oil prices rose, and it was of economic importance to explore alternative methods of obtaining the products traditionally gained from petroleum oil.[29] The reaction allows transformation of methanol (derived *via* syngas from carbon from coal, natural gas or biomass) into light olefins and gasoline. Zeolites are employed as catalysts for the reaction, with different zeolite topologies allowing the products of the reaction to be tailored, giving the commercialised Methanol-to-Olefins (MTO) or Methanol-to-Gasoline (MTG) reactions.[24,30]

The widely accepted mechanism of methanol to hydrocarbons is based on a hydrocarbon pool (HCP). This mechanism is complicated and has been extensively reported on in literature over the past 40 years. The autocatalytic nature of the reaction was first evidenced in 1978 shortly after reaction discovery through kinetic studies.[31] The hydrocarbon pool mechanism was proposed by Kolboe and evidenced in their investigation of the MTH reaction over SAPO-34 in 1994, through isotopic labelling experiments in which ^{13}C-methanol and ^{12}C-ethanol were reacted.[32] The isotopic distribution of the products showed clearly that ethene is formed directly from ethanol and neither ethanol nor ethene is involved in the formation of higher products. However the reaction of methanol proceeds from an adsorbed hydrocarbon which adds reactant (methanol) and undergoes cracking to split-off products; their proposed scheme is reproduced in Figure 3.[32]

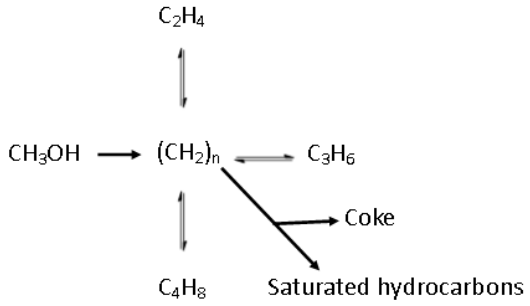

Figure 3 Hydrocarbon pool mechanism proposed by Dahl and Kolboe. Figure reproduced from ref 32.

Later, methylbenzenes were shown to be key intermediates in the reaction by analysis of the species trapped inside the pores of SAPO-34 by dissolution followed by gas chromatography-mass spectrometry.[33] The main products of the reaction were ethene and propene, being the only molecules small enough to diffuse out of the small pores of the catalyst. The larger reactive intermediates remained trapped within the large *cha* cages. Arstad and Kolboe found that during the reaction there was a heavy presence of penta- and hexamethylbenzenes, and when the methanol was ceased and the catalyst was flushed with carrier gas, the quantity of higher methylated benzenes decreases as the quantity of di-, tri- and tetramethylbenzenes increased, suggesting that the more methylated benzenes split-off small olefins leaving lower methylated benzenes.[34] Haw and Song *et al.* also proved that methylbenzenes are the reactive species involved in the MTH reaction within the catalyst pores through ^{13}C-NMR experiments.[35–37]

The reaction of methanol to form hydrocarbons over zeolites is autocatalytic; in the presence of small amounts of product, the rate of conversion is increased, and continues to increase until reaching steady state. Thus, an induction period is observed where methanol conversion increases with time during the early reaction stages as the HCP is built up,[31] in this period the main product is dimethyl ether, formed through the dehydration of methanol, which is catalysed by Brønsted acid sites. During the autocatalytic stage of the reaction, once the HCP is established, two cyclic mechanisms are proposed to take place simultaneously in the catalyst pores: the pairing and side chain mechanisms.[38]

Aromatics are methylated and when a carbon atom within a ring is methylated twice it is *gem*-methylated.[39] In the pairing mechanism, *gem*-methylated species undergo ring contraction, to form a 5-membered ring and a side chain which can be eliminated as an olefin and the ring expands back to being 6-membered.[39] These 5-membered rings have been confirmed also by UV-Vis spectroscopy to form from the contraction of highly methylated benzenium ions, to release ethene, and then expand again to a lower methylated benzenium ion.[40] In the side chain mechanism, *gem*-methylation is followed by deprotonation to yield an exocyclic double bond which can then be methylated and olefins eliminated.[38,39] This is illustrated in Figure 4, a reaction scheme reproduced from that of Lesthaeghe *et al.* showing the pairing and side chain mechanisms which are widely accepted in the methanol to olefins reaction.[38]

Topology dictates which mechanism dominates in the reaction, as some intermediates are sterically hindered and therefore become less significant in the

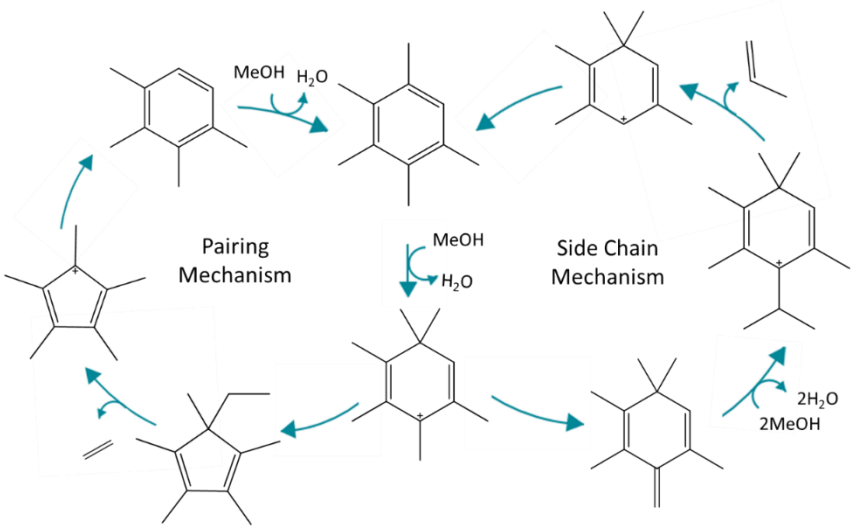

Figure 4 Illustration of the side chain and pairing mechanisms in the MTH reaction. In this reaction scheme, pentamethylbenzene is *gem*-methylated and undergoes ring contraction or deprotonation depending on whether the pairing mechanism or side chain mechanism is preferred. Recreated from ref 38.

reaction, others may experience stabilisation effects by the zeolite. In zeolites where pore dimensions are more restricted, lower-methylated benzenium ions are more stable.[39] Lower-methylated benzenes dominate in the smaller pores of ZSM-5 with MFI topology where the HCP will consist of smaller methylated

aromatics. Here, ethene is preferred as the main product. Higher-methylated benzenium ions most easily exist in larger zeolite pores. Higher methylated benzenes dominate in zeolites with larger intersections such as in the CHA and BEA topology, preferring propene as the main product.[38,39]

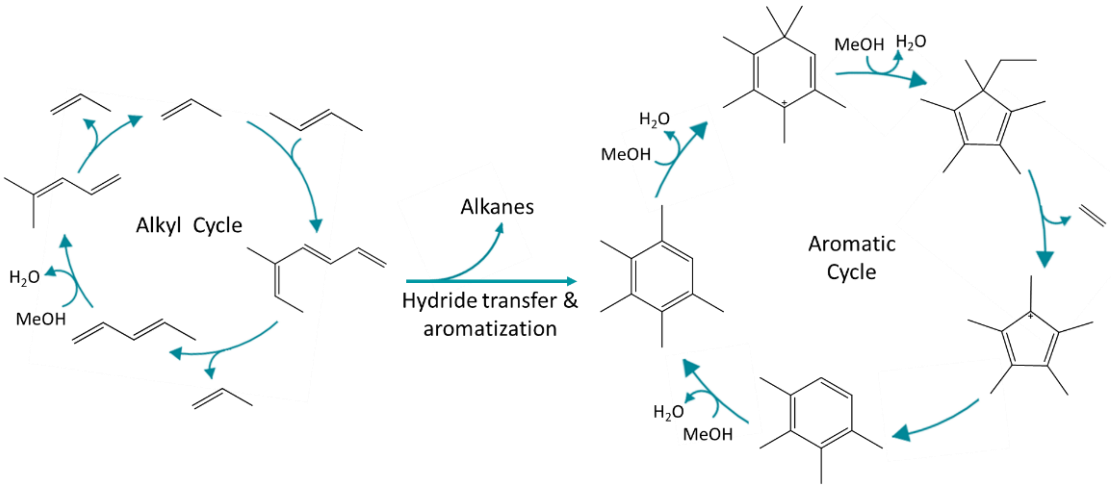

Figure 5 Dual cycle mechanism as proposed by Bjorgen *et al.* consisting of an alkene cycle in which alkenes undergo methylation and cracking and may be aromatised to follow an aromatic cycle. Reproduced from Bjorgen and Olsbye.[43,44]

Investigations of ZSM-5 using $^{13}C/^{12}C$ switching experiments have shown that higher methylated benzenes are not reactive species in this catalytic cycle in ZSM-5. They showed that ethene is formed from lower methylated benzenes in agreement with the pairing mechanism, but propene and higher alkenes are formed by methylation of alkenes and cracking. This was named the dual cycle mechanism and consists of an aromatic cycle which may function through side chain and pairing mechanisms, and an alkene cycle.[41] This is illustrated in Figure 5 which is reproduced from a review written by Olsbye *et al.* who's group first proved this dual cycle mechanism to be the case in ZSM-5.[25] The mechanism is in agreement with early studies by Dessau and LaPierre, who theorised that ethene is produced from the methylation of larger carbenium ions and cracking.[42] It is generally accepted that pairing and side chain methylation exists in larger pore zeolites where lesser spatial limitations allow higher methylated benzenes to react, such as H-Beta, a large pore zeolite and in the large cavities of SAPO-34 which has CHA topology.

The dual cycle mechanism as illustrated in Figure 5 consists of two inter-linked cycles, one composed of alkyl chains which are methylated and cracked, and which can undergo hydride transfer and cyclization reactions to form aromatic species which undergo methylation and ring contraction to produce small olefins.[43,44] These cycles are most likely to occur in the medium pore zeolites such as H-ZSM-5, where highly methylated benzenes are more spatially restricted and are inactive.[45] In addition to the effect of topologies, acid sites play an important role in the reaction selectivity as they can stabilise cationic species. Stronger acid sites are needed to stabilise methyl benzene cations, particularly the lower methylated benzenium ions which are less stable than the higher methylated.[46]

Given that the aromatic production continues during the reaction, these cycles are thought to work simultaneously, with larger alkenes forming aromatics.[45] An example of such a reaction is given in Figure 6, where an alkene is protonated, the resulting carbocation can then abstract a hydride from the neighbouring neutral species to give one now saturated C-C bond i.e., a paraffin, and leaving a more conjugated alkene structure that is positively charged and might cyclise before the zeolite recovers its proton. The overall result is one more conjugated species and one paraffin.

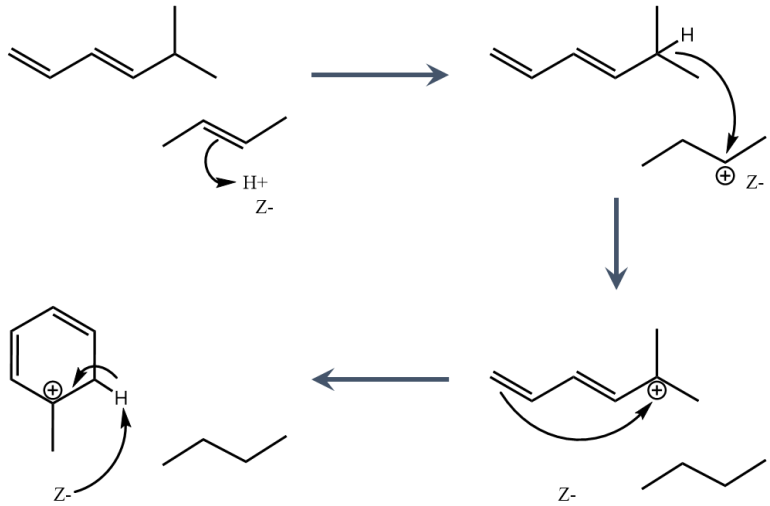

Figure 6 Example of the protonation of an alkene by the zeolite acid site which allows the cation to abstract a hydride ion from a neutral species to form a paraffin, while cyclization of the now extended alkene species occurs. The overall result is an aromatic species and a paraffin.

It is possible that through this understanding of the reaction mechanism, the yield of the desired product can be increased. For example, by tailoring a catalyst to prevent the formation of aromatics, it is possible to control selectivity so that propene is the main product.[45] An example is the impregnation of H-ZSM-5 with Ca^{2+} which eliminates Brønsted acid sites and creates new Lewis acidic centres, heavily changing the type of HCP species formed. Brønsted sites are necessary for the formation of aromatic hydrocarbons in the mechanism, and without them ethene selectivity is hindered, but propene selectivity is favoured.

During the MTH reaction, the catalyst deactivates due to carbonaceous species depositing on the zeolite surface, blocking acid sites or channels. The deactivation of a zeolite can depend on its acidity and topology.[47,48] Desorption of products is also an important aspect in catalysis. Very high acidities may result in strongly adsorbed species, causing product inhibition and eventually depositing on the surface as coke.[25] A high density of acid sites creates a more difficult the diffusion pathway and more favourable condensation reactions as coke is deposited.[25] Zeolites topologies also play a role in catalyst deactivation. Studies have shown that zeolites with CHA topology deactivate much faster than those with MFI topology. This is attributed to the large *cha* cages which allow polyaromatic species to form which become trapped, while MFI topology has more restricted internal voids of channels and channel intersections that mostly limit aromatics formation to monoaromatics.[25,49]

1.6 Catalytic Fast Pyrolysis

To produce renewable hydrocarbons for fuels and other petrochemical products, the conversion of biomass is an extremely attractive route that can be considered carbon neutral – since CO_2 is absorbed in the first place for photosynthesis.[50–52] Biomass conversion shows good potential to directly replace fossil fuels and reduce net emissions of greenhouse gases, producing petroleum-like products which can be compatible with the current infrastructure for transport fuels. Lignocellulosic biomass – dry plant matter consisting of cellulose, hemicellulose and lignin – is often studied as a feedstock for biofuels because of its ease of availability and cheap cost.[53,54] Exemplar structures of such species are illustrated in Figure 7.

Pyrolysis is the thermal decomposition of biomass at temperatures between 400 and 650 °C in the absence of oxygen, resulting in volatile species which will condense into bio-oil as a viscous fluid, and bio-char as a solid species.[55] Fast pyrolysis involves using high heating rates (500 – 1000 °C s^{-1}) and rapid cooling or, quenching, to condense products and prevent their further conversion. Fast pyrolysis shows a high yield of liquid fuel products, retaining most of the energy from the biomass feedstock. However, the bio-oil is a miscible mixture of polar organic compounds with some water,[56] the liquid contains complex mixtures of oxygenated aliphatic and aromatic compounds, which are undesirable as transportation fuels as they are less stable, have lower heating values, are immiscible with hydrocarbons and can cause bio-oils to have a range of properties depending on composition.[53,56,57] These problems make it necessary to upgrade bio-oil before it can be used as fuel. It is necessary to narrow the range of compounds present, and remove undesirable oxygenates. Catalytic fast pyrolysis (CFP) can produce a higher quality bio-oil by the removal of oxygenated species before the products of pyrolysis are quenched. This can be performed *in situ* where the catalyst is mixed directly with the feedstock in the pyrolysis reactor, or *ex situ* where the catalyst is mixed only with the vapours. The production of liquid fuels directly in one step from solid biomass would be the ideal.[54]

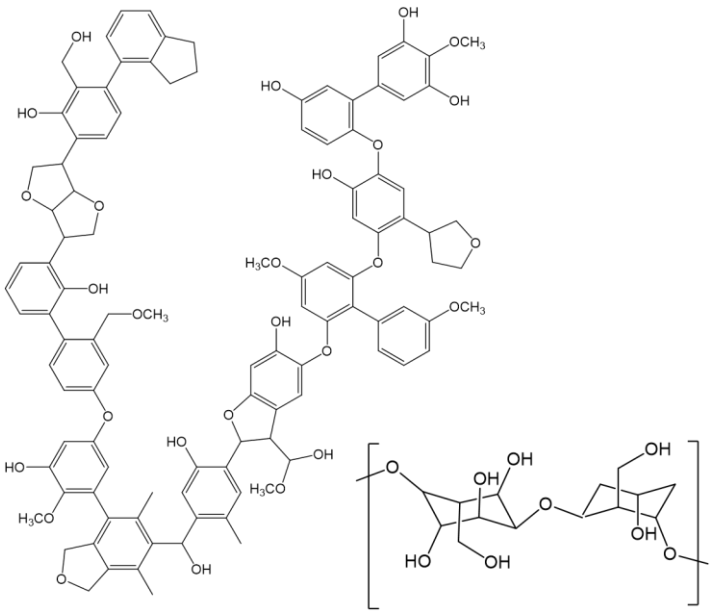

Figure 7 Exemplar organic structures that make up woody biomass materials: lignin and cellulose.

Catalysts for the reaction can typically be zeolites,[58] although supported metals or metal oxides have also been applied as catalysts. For example, MgO contains basic sites which are effective in reducing carboxylic acid groups in bio-oil, and has shown comparable performance in removing oxygen from bio-oils to H-ZSM-5.[59] Pt-Al_2O_3 has converted furan (co-fed with H_2) through decarbonylation to C_7, butanal was observed as a minor product as a result of ring opening mechanism.[60] For the purposes of this thesis the following sections will focus on zeolite catalysed CFP.

When biomass is pyrolyzed, three main steps are followed:

1) thermal decomposition of the biomass into volatile organic species,
2) their dehydration, bond cleavage and rearrangement reactions to some dehydrated species such as aldehydes, carboxylic acids, furan, furfural and methylated furan
3) these dehydrated species react with catalyst active sites to be decarboxylated, decarbonylated and dehydrated to form aromatics, CO, CO_2 and H_2O.[54,61]

Given the complexity of the mechanism, some studies choose model compounds as representative biomass feeds to simplify the reaction, knowing, as explained above, that the product distributions will be similar. Model compounds include glucose, furfural, furan, aldehydes, olefins, phenol, aromatics.[27,62–67]

The use of different feedstocks has been shown to produce similar product distributions.[54] Carlson *et al.* compared the conversion of glucose, xylitol, cellulose and cellobiose over H-ZSM-5 with a Si/Al ratio of 60, they found that all feeds gave similar product distributions of aromatics, CO, CO_2 and coke, and the aromatic distributions were very similar, suggesting common reaction intermediates in ZSM-5.[54] In a separate study from the same group, glucose, sorbitol, glycerol, tetrahydrofuran, methanol and hydrogenated bio-oil fractions were converted in a fixed-bed reactor using H-ZSM-5, and the authors showed that the effective hydrogen-to-carbon ratio (H/C_{eff}) value of the feedstock was a major factor in the yield of aromatics and olefins produced, as well as in the deactivation rate.[68]

Bio-oils and biomass typically have a relatively low H/C_{eff} compared to crude oil; a ratio often used as a measure of fuel quality, that can also help to explain the hydrogen deficiency of biomass.[27,69] H/C_{eff} is given by the ratio of H/C after removal of all oxygen by dehydration, i.e.:

$$\left(\frac{\mathrm{H}}{\mathrm{C}}\right)_{\mathrm{eff}} = \frac{n\mathrm{H} - 2n\mathrm{O}}{\mathrm{C}} \qquad (1)$$

For comparison, petroleum has a H/C_{eff} of 1 – 2, methanol of 2, and that of biomass derived feedstocks typically lies between 0 and 0.67, making biomass a hydrogen deficient feedstock. Several research groups have shown during biomass conversion over zeolite catalysts that the catalyst lifetime is a function of H/C_{eff} where higher ratios give greater product yield.[68,70,71] The hydrogen deficiency of the species in these reactions are related to the high coking rate, leading to the need for frequent catalyst regeneration, and for this reason, a hydro-processing step can be implemented to increase H/C_{eff}.[68,70] During CFP, the removal of CO and CO_2 from the vapours leads to low yields of hydrocarbons, but the removal of oxygen by water leaves a further hydrogen deficient so catalyst coking means that there is a need to frequently regenerate the catalyst.[26]

Many believe that in zeolite catalysts, CFP operates via a hydrocarbon pool mechanism like MTH, where the reactants enter the pores to build up into a pool of hydrocarbons that react continuously with new feed. Research has consistently shown that the reaction features a similar induction period to MTH, where conversion increases after some time-on-stream, suggesting that a certain level of hydrocarbons on the surface are needed to push the deoxygenation reactions to form aromatics and olefins, in an autocatalytic nature.[26,50,72] Carlson *et al.* conducted a study converting ^{13}C and ^{12}C glucose over ZSM-5 and confirmed that the aromatics formed contained a randomly mixed ^{13}C and ^{12}C, while the oxygenated species detected contained either all ^{12}C or all ^{13}C indicating that they did not enter the hydrocarbon pool before leaving the reactor.[61] The results also indicate that naphthalene was composed partially of a segment of randomly distributed $^{12}C/^{13}C$ and partially of a monoisotopic segment – they therefore suggested that naphthalene forms from reaction of benzene (random C distribution) directly with an oxygenated fragment.[61]

In terms of the role that zeolites hold in CFP, Carlson *et al.* compared CFP of glucose over H-ZSM-5, with Silicalite-1 as a material with analogous topology but without Brønsted acid sites, and silica-alumina catalyst containing Brønsted acid sites but in an amorphous structure, and beta zeolite and zeolite Y with larger pores. Both Silicalite-1 and silica-alumina produced primarily coke (40 and 85 % respectively), and beta zeolite and zeolite Y also produced large amounts of coke (70 and 50 %) all with low aromatic yields. ZSM-5 in contrast showed 30 % selectivity to coke but also the highest aromatic selectivity at 30 %. Apart from ZSM-5, all other catalysts gave aromatic selectivity of 8 % or less. In fact, publications from Bakhshi *et al*.,[73] Jae *et al*.,[74] and Mihalcik *et al.*,[75] also identified ZSM-5 as the zeolite that gives the highest yield to aromatic hydrocarbons.

Operando studies would be helpful for a thorough understanding of the hydrocarbon species involved in catalytic fast pyrolysis. If future studies could improve our understanding of these intermediates, it may be possible to design a catalyst which can stabilise those intermediates which yield the desired products.

1.7 *Operando* spectroscopy

Several groups have worked to apply spectroscopic techniques to catalysts while the catalysts are working under operating conditions with catalyst activity being recorded, known as *operando*. To study MTH, UV-Vis,[76–78] DRIFTS,[76] NMR,[37,79] and UV-Raman[80] have all been applied to study zeolites under *operando* conditions with insightful results to the mechanism. By studying during reaction, any intermediates that are thermally unstable and will not be isolated through thermal quenching can be detected during the reaction. We can interrogate the catalyst surface and link with reaction products in the reactor outlet to determine structure-activity relationships while any species which may be changed upon cooling may be detected under operating conditions.

Raman spectroscopy is a vibrational spectroscopic technique that can be applied under a large range of temperatures and pressures to study solid, liquid and gas phases, making it useful for the study of catalytic reactions.[81] Raman also has the benefit of being able to study the reaction through sample darkening and with

a good time resolution for *operando* studies (measurements typically recorded in s or min). Three main problems tend to inhibit the use of Raman to study catalytic reactions: low signal to noise ratio, beam-induced sample damage by the high laser power, and fluorescence. In this project, wavelengths of light near the visible region will be used to achieve higher signal to noise ratio through resonance enhancement, while the 400 nm wavelength used to irradiate the catalyst will induce less damage than a UV wavelength laser. A Kerr-gated Raman spectrometer is employed to cut fluorescence from the detector. The process of Raman scattering, and the function of the Kerr-gated spectrometer are described in the subsequent section.

1.8 References

1. Statistical Review of World Energy 2020, BP, https://www.bp.com/content/dam/bp/business-sites/en/global/corporate/pdfs/energy-economics/statistical-review/bp-stats-review-2020-full-report.pdf, 2020.
2. Background on the UNFCCC: The international response to climate change, United Nations Framework Convention on Climate Change, http://unfccc.int/essential_background/items/6031.php, 2014.
3. Climate Action Plan 2050 Principles and goals of the German government climate policy, Federal Ministry for the Environment, Nature Conservation, Building and Nuclear Safety, https://unfccc.int/sites/default/files/resource/Klimaschutzplan_2050_eng_bf.pdf, 2016.
4. United States Mid Century Strategy for Deep Decarbonization, The White House Washington, http://unfccc.int/files/focus/longterm_strategies/application/pdf/mid_century_strategy_report-final_red.pdf, 2016.
5. I. Amghizar, L. A. Vandewalle, K. M. Van Geem and G. B. Marin, Engineering, 2017, 3, 171–178.
6. G. B. Combes, J. B. Claridge, J. R. Gallagher and M. J. Rosseinsky, Fischer-tropsch catalyst comprising cobalt, magnesium and precious metal, WO2013054091 A1, 2011.
7. B. Yilmaz and U. Müller, Topics in Catalysis, 2009, 52, 888–895.
8. S. Kulprathipanja, Ed., Wiley: Zeolites in Industrial Separation and Catalysis, John Wiley and Sons, 2010.
9. IZA Structure Commission, Database of Zeolite Structures, http://www.iza-structure.org, (accessed 13 June 2017).
10. M. Stöcker, Zeolite Characterization and Catalysis, Springer Netherlands, 2009.
11. A. Corma and H. Garcia, European Journal of Inorganic Chemistry, 2004, 2004, 1143–1164.
12. K. Gleichmann, B. Unger and A. Brandt, in Zeolites Useful Minerals, ed. C. Belviso, InTech, 2016.

13. G. Ertl, H. Knözinger, F. Schüth and J. Weitkamp, Handbook of Heterogeneous Catalysis, VCH, Weinheim, 2008, vol. 1.
14. J. Weitkamp, Solid State Ionics, 2000, 131, 175–188.
15. T. F. Degnan, G. K. Chitnis and P. H. Schipper, Microporous and Mesoporous Materials, 2000, 35, 245–252.
16. E. T. C. Vogt and B. M. Weckhuysen, Chemical Society Reviews, 2015, 44, 7342–7370.
17. S. Bhatia, Zeolite Catalysts: Principles and Applications, CRC Press, 1989.
18. P. A. Jacobs and H. K. Beyer, Journal of Physical. Chemistry., 1979, 83, 1174–1177.
19. A. Auroux, M. Muscas, D. J. Coster and J. J. Fripiat, Catalysis Letters, 1994, 28, 179–186.
20. J. A. Biscardi, G. D. Meitzner and E. Iglesia, Journal of Catalysis, 1998, 179, 192–202.
21. I. Yarulina, S. Bailleul, A. Pustovarenko, J. R. Martinez, K. D. Wispelaere, J. Hajek, B. M. Weckhuysen, K. Houben, M. Baldus, V. Van Speybroeck, F. Kapteijn and J. Gascon, ChemCatChem, 2016, 8, 3057–3063.
22. S. Zhang, B. Zhang, Z. Gao and Y. Han, Reaction Kinetics, Mechanisms and Catalysis, 2010, 99, 447–453.
23. Y. J. Du, W. D. Hu, C. M. Wang, J. Zhou, G. Yang, Y. D. Wang and W. M. Yang, Catalysis Science & Technology, 2021, 11, 2031–2046.
24. P. Tian, Y. Wei, M. Ye and Z. Liu, ACS Catalysis, 2015, 5, 1922–1938.
25. U. Olsbye, S. Svelle, M. Bjørgen, P. Beato, T. V. W. Janssens, F. Joensen, S. Bordiga and K. P. Lillerud, Angewandte Chemie International Edition., 2012, 51, 5810–5831.
26. C. Mukarakate, J. D. McBrayer, T. J. Evans, S. Budhi, D. J. Robichaud, K. Iisa, J. ten Dam, M. J. Watson, R. M. Baldwin and M. R. Nimlos, Green Chemistry, 2015, 17, 4217–4227.
27. Y. T. Cheng and G. W. Huber, ACS Catalysis, 2011, 1, 611–628.
28. C. D. Chang and A. J. Silvestri, Journal of Catalysis, 1977, 47, 249–259.
29. F. J. Keil, Microporous and Mesoporous Materials, 1999, 29, 49–66.
30. Gasoline synthesis (TIGAS), Haldor Topsoe, https://www.topsoe.com/subprocess/gasoline-synthesis-tigas, (accessed 5 June 2017).
31. N. Y. Chen and W. J. Reagan, Journal of Catalysis, 1979, 59, 123–129.
32. I. M. Dahl and S. Kolboe, Journal of Catalysis, 1994, 149, 458–464.
33. B. Arstad and S. Kolboe, Catalysis Letters, 2001, 71, 209–212.
34. B. Arstad and S. Kolboe, Journal of the American Chemical Society, 2001, 123, 8137–8138.
35. W. Song, H. Fu and J. F. Haw, Journal of the American Chemical Society, 2001, 123, 4749–4754.
36. T. Xu, D. H. Barich, P. W. Goguen, W. Song, Z. Wang, J. B. Nicholas and J. F. Haw, Journal of the American Chemical Society, 1998, 120, 4025–4026.
37. J. F. Haw, J. B. Nicholas, W. Song, F. Deng, Z. Wang, T. Xu and C. S. Heneghan, Journal of the American Chemical Society, 2000, 122, 4763–4775.

38. D. Lesthaeghe, A. Horré, M. Waroquier, G. B. Marin and V. Van Speybroeck, Chemistry a European Journal, 2009, 15, 10803–10808.
39. D. Lesthaeghe, B. De Sterck, V. Van Speybroeck, G. B. Marin and M. Waroquier, Angewandte Chemie, 2007, 119, 1333–1336.
40. E. D. Hernandez and F. C. Jentoft, ACS Catalysis, 2020, 10, 5764–5782.
41. S. Svelle, F. Joensen, J. Nerlov, U. Olsbye, K.-P. Lillerud, S. Kolboe and M. Bjørgen, Journal of the American Chemical Society, 2006, 128, 14770–14771.
42. R. M. Dessau and R. B. LaPierre, Journal of Catalysis, 1982, 78, 136–141.
43. M. Bjørgen, S. Svelle, F. Joensen, J. Nerlov, S. Kolboe, F. Bonino, L. Palumbo, S. Bordiga and U. Olsbye, Journal of Catalysis, 2007, 249, 195–207.
44. J. S. Martínez-Espín, K. De Wispelaere, T. V. W. Janssens, S. Svelle, K. P. Lillerud, P. Beato, V. Van Speybroeck and U. Olsbye, ACS Catalysis, 2017, 7, 5773–5780.
45. M. Bjørgen, K.-P. Lillerud, U. Olsbye and S. Svelle, Studies in Surface Science and Catalysis, 2007, 167, 463–468.
46. C. M. Wang, Y. D. Wang, Y. J. Du, G. Yang and Z. K. Xie, Catalysis Science & Technology, 2015, 5, 4354–4364.
47. U. Olsbye, M. Bjørgen, S. Svelle, K.-P. Lillerud and S. Kolboe, Catalysis Today, 2005, 106, 108–111.
48. I. M. Dahl, H. Mostad, D. Akporiaye and R. Wendelbo, Microporous and Mesoporous Materials, 1999, 29, 185–190.
49. M. Bjørgen, U. Olsbye and S. Kolboe, Journal of Catalysis, 2003, 215, 30–44.
50. J. Liang, G. Shan and Y. Sun, Renewable and Sustainable Energy Reviews, 2021, 139, 110707.
51. A. Zheng, L. Jiang, Z. Zhao, Z. Huang, K. Zhao, G. Wei and H. Li, Wiley Interdisciplinary Reviews: Energy and Environment, 2017, 6, 234.
52. T. Dickerson and J. Soria, Energies, 2013, 6, 514–538.
53. S. Yaman, Energy Conversion and Management, 2004, 45, 651–671.
54. T. R. Carlson, G. A. Tompsett, W. C. Conner and G. W. Huber, Topics in Catalysis, 2009, 52, 241.
55. M. Balat, M. Balat, E. Kırtay and H. Balat, Energy Conversion and Management, 2009, 50, 3147–3157.
56. A. V. Bridgwater, D. Meier and D. Radlein, Organic Geochemistry, 1999, 30, 1479–1493.
57. C. Liu, H. Wang, A. M. Karim, J. Sun and Y. Wang, Chemical Society Reviews, 2014, 43, 7594–7623.
58. J. R. Carpenter, D. C. Dayton, M. S. Pavani, M. Von Holle, Catalyst compositions and use thereof in catalytic biomass pyrolysis, AU2017279755B2, 2019.
59. Applied Catalysis B: Environmental, 2016, 196, 155–173.
60. R. C. Runnebaum, T. Nimmanwudipong, J. Doan, D. E. Block and B. C. Gates, Catalysis Letters, 2012, 142, 664–666.
61. T. R. Carlson, J. Jae and G. W. Huber, ChemCatChem, 2009, 1, 107–110.

62. C. Liu, T. J. Evans, L. Cheng, M. R. Nimlos, C. Mukarakate, D. J. Robichaud, R. S. Assary and L. A. Curtiss, Journal of Physical Chemistry C, 2015, 119, 24025–24035.
63. S. Du, D. P. Gamliel, M. V. Giotto, J. A. Valla and G. M. Bollas, Applied Catalysis A: General, 2016, 513, 67–81.
64. C. J. Gilbert, J. S. Espindola, W. C. Conner, J. O. Trierweiler and G. W. Huber, ChemCatChem, 2014, 6, 2497–2500.
65. J. D. Adjaye and N. N. Bakhshi, Biomass and Bioenergy, 1995, 8, 131–149.
66. A. Gumidyala, T. Sooknoi and S. Crossley, Journal of Catalysis, 2016, 340, 76–84.
67. U. V. Mentzel and M. S. Holm, Applied Catalysis A: General, 2011, 396, 59–67.
68. H. Zhang, Y. T. Cheng, T. P. Vispute, R. Xiao and G. W. Huber, Energy & Environmental Science, 2011, 4, 2297–2307.
69. A. V. Bridgwater, Fast Pyrolysis of Biomass: A Handbook, CPL Press, Thatcham, England, 2002.
70. T. P. Vispute, H. Zhang, A. Sanna, R. Xiao and G. W. Huber, Science, 2010, 330, 1222–1227.
71. U. V. Mentzel and M. S. Holm, Applied Catalysis A: General, 2011, 396, 59–67.
72. C. Mukarakate, M. J. Watson, J. ten Dam, X. Baucherel, S. Budhi, M. M. Yung, H. Ben, K. Iisa, R. M. Baldwin and M. R. Nimlos, Green Chemistry, 2014, 16, 4891–4905.
73. N. N. Bakhshi and J. D. Adjaye, Biomass and Bioenergy, 1994, 7, 201–211.
74. J. Jae, G. A. Tompsett, A. J. Foster, K. D. Hammond, S. M. Auerbach, R. F. Lobo and G. W. Huber, Journal of Catalysis, 2011, 279, 257–268.
75. D. J. Mihalcik, C. A. Mullen and A. A. Boateng, Journal of Analytical and Applied Pyrolysis, 2011, 92, 224–232.
76. Q. Qian, C. Vogt, M. Mokhtar, A. M. Asiri, S. A. Al-Thabaiti, S. N. Basahel, J. Ruiz-Martínez and B. M. Weckhuysen, ChemCatChem, 2014, 6, 3396–3408.
77. Y. T. Chua, P. C. Stair, J. B. Nicholas, W. Song and J. F. Haw, Journal of the American Chemistry Society, 2003, 125, 866–867.
78. E. Borodina, F. Meirer, I. Lezcano-González, M. Mokhtar, A. M. Asiri, S. A. Al-Thabaiti, S. N. Basahel, J. Ruiz-Martinez and B. M. Weckhuysen, ACS Catalysis, 2015, 5, 992–1003.
79. M. Hunger, M. Seiler and A. Buchholz, Catalysis Letters, 2001, 74, 61–68.
80. P. Beato, E. Schachtl, K. Barbera, F. Bonino and S. Bordiga, Catalysis Today, 2013, 205, 128–133.
81. E. Smith and G. Dent, Modern Raman Spectroscopy: a practical approach, John Wiley & Sons Ltd., Chichester, England, 2004.

2 Methodology and materials

2.1 Methodology

2.1.1 Raman Spectroscopy

Raman spectroscopy is a vibrational spectroscopic technique in which a sample is irradiated with a narrow-band light, and part of the light is scattered from the molecule at a different energy than the incident light. This difference in energy between the collected light and incident light contains vibrational information of the sample. Raman spectra show a set of narrow lines at energies differing from the incident wavelength by the vibrational energy of the sample. A Raman spectrum gives a molecular fingerprint, the values are expressed as Raman shift, given by the difference between the wavenumber of the incident energy and the absolute wavenumber of the scattered energy.[1]

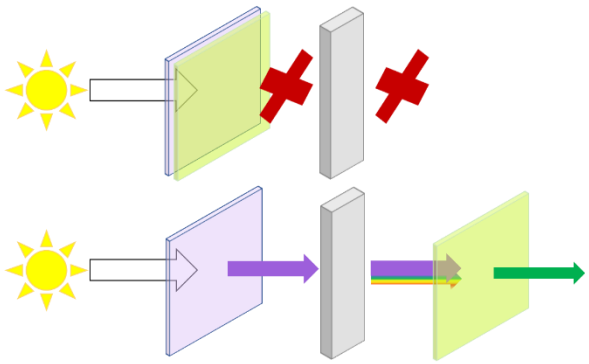

Figure 8 An illustration of the experiment by Raman and Krishnan to observe the inelastic scattering of visible light. With the application of the blue-violet filter only blue-violet light is transmitted, when the green-yellow filter is placed between the sample and the observer, the violet light which dominates (elastically scattered light) is filtered out leaving the green light observable (some of the inelastically scattered light).

The Raman effect was first observed by eye by Raman and Krishnan, who in 1927, observed the effect using a beam of sunlight focused by a telescope objective and a second lens to create a more powerful, focused light on to studied liquids.[2] They were able to observe the Raman effect by using two complementary filters in the light path – one transmitting blue-violet light and the

other green-yellow light which together block all white light of the sunlight. By using the blue-violet filter to allow blue-violet light to excite the sample, they saw blue scattered light, but by placing the green-yellow filter placed between the sample and the observer – thus blocking out the blue light – they observed green light being scattered by the sample. This proved that the incoming blue light was partly scattered at a lower energy.[2] The experiment is illustrated in Figure 8. During following experiments, with the use of a quartz spectrograph and a more powerful mercury light source, they were able to quantify wavelength changes in the scattered light to report the first Raman spectra of benzene, toluene, ether, methanol and water.[3]

Raman scattering is an inherently weak process, when a sample is irradiated with light, most is scattered elastically without a change in energy, but a small amount of light – one in 10^6 photons – will be scattered with a different energy.[1–3] Using lasers to excite the sample enhances the sensitivity of Raman scattering by allowing higher power densities of monochromatic light to reach the sample.[4]

The classical explanation of the Raman effect is based on light scattering by oscillating electric dipoles within molecules, which are induced by the electric field of the laser or incident radiation. The light interacting with the molecule causes the electron clouds around the nuclei to become distorted, such that an unstable virtual state is formed between the molecule and the light in that moment. The light is released again as the molecule relaxes. In moving to the virtual state, if the nuclei of the molecule moved in response to the distorted electron cloud, then energy has been transferred between the molecule and the photon, and the released energy is at a higher or lower energy than the incidence light, the light has been scattered inelastically. This inelastic scattering phenomenon is known as Raman scattering.[1,5] The change in energy corresponds to a characteristic vibrational frequency of the scattering molecule, and therefore each line observed in a Raman spectrum corresponds to a characteristic molecular vibration.[1,3,5]

The energy shifts are defined as Stokes or anti-Stokes shifts depending on whether they are higher or lower in frequency, respectively, than the frequency of the incident energy. This is described in Figure 9 which illustrates the quantum mechanical approach to explaining Raman scattering. In Figure 9, electrons are

excited from the vibrational energy levels of the static molecule to fit the virtual state formed between the light and molecule, then the light is released (a) at equal energy to the incident energy giving rise to elastic scattering, or Rayleigh scattering, (b) at a lower energy than the incident energy to give Stokes scattering, or (c) at a higher energy than the incident energy to give anti-Stokes scattering. This explanation demonstrates how the electrons move between energy levels to give absorbed or emitted photons that are quantized, giving the discrete lines observed in Raman spectroscopy.[1]

During the process, no new electronic states are formed and in Raman scattering, additional energy does not promote electrons to an excited state of the static molecule because the fast process does not allow the nuclei to relax into the distorted geometry. Furthermore, the difference between the scattered energy and the incident energy corresponds to energetic vibrations in the static molecule – not of the virtual state.[1]

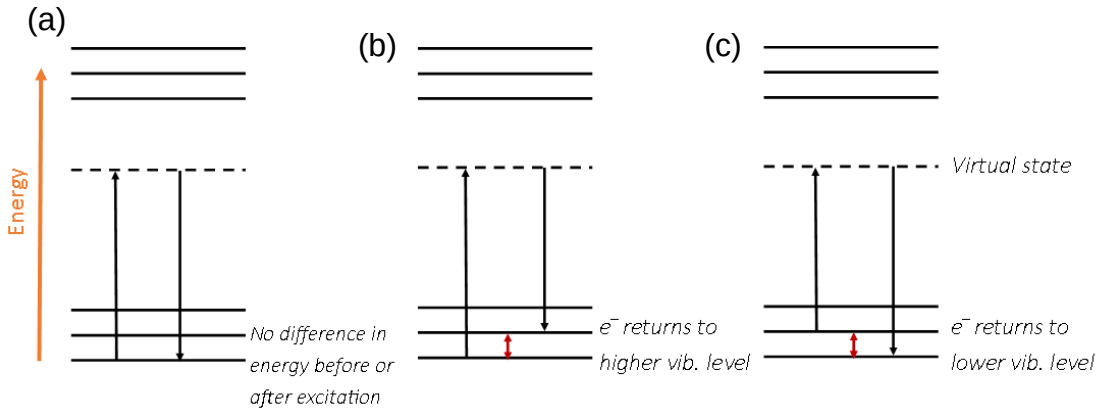

Figure 9 Illustration to the quantum mechanical approach to explaining (a) elastic or Rayleigh scattering, and inelastic or Raman scattering via (b) Stokes (centre) or (c) anti-Stokes (right) shift.

The distortion of an electron cloud depends on the ability of the electrons in the molecule to become polarized, this is known as the polarizability, and is denoted by α. For a molecule or bond to be Raman active, a change in polarizability of the molecule is needed – this is the selection rule for Raman spectroscopy.[1,6] Polarizability can describe how easily the electron clouds around a molecule can be distorted in response to an electric field, i.e. how much the molecular dipole can change.[7] Often symmetrical vibrations in molecules without a dipole moment cause the greatest change in polarizability to give the greatest Raman scattering.

This contrasts with the infrared (IR) spectroscopy selection rule that the molecule must have a change in dipole moment, hence asymmetric molecules give more intense absorptions in IR.[1,5] Symmetrical stretching modes give stronger Raman bands because they lend themselves well to changing polarizability, while in contrast, anti-symmetrical vibrations alter the dipole moment which leads to strong infrared absorptions.[6] If the electrons of a chemical system are delocalised, such as in π-conjugated systems, this also enhances polarizability, and therefore, the π-orbitals involved in a C=C stretch vibration will give rise to greater Raman scattering than the σ-orbitals in a C-C stretch.[7]

The light waves passing by a molecule interact and distort the electron clouds, which in turn move the nuclei and energy is moved between the light and the molecule. The oscillating dipole of the light is much larger than typical molecules (in the order of 0.5 nm versus 200 – 1000 nm for the wavelengths of UV, visible and infrared radiation) and as it passes the molecule polarizes the electrons.

The intensity of Raman scattering is given by Equation (2):

$$I = k\, L\, \alpha^2 \omega^4 \qquad (2)$$

Where *k* is a constant including factors such as the speed of light, *L* is the laser power, *α* is the polarizability of the electrons of a molecule, and *ω* is the frequency of the incident laser. According to the equation, the Raman intensity has a fourth power dependence on the frequency of incidence light and a direct correlation with the laser power. It seems then logical to opt for higher laser powers and low wavelength (UV) lasers for measurements. However, these conditions are far more likely to lead to problems such as sample photodegradation and localised heating and should therefore be carefully considered.[1]

Resonance enhancement

Even using high-powered lasers and optical amplifiers, Raman scattering can be a relatively weak process, and can therefore still lead to a low signal intensity that is often disguised by the spectral noise. One method to improve the signal is to use resonance enhancement; the use of an excitation wavelength that

corresponds to the energy of an electronic transition of the species, where Raman intensity is then gained and the signal can be increased by 10^3 – 10^8.[1,8] It is also possible to selectively enhance a species based on its absorbance spectrum, by selecting a wavelength of excitation close to an absorbance band, selected chromophores can be resonance enhanced.[9,10]

When the molecule enters its excited state, the chromophore of the molecule undergoes geometrical changes, such as bond-lengthening. The changes result in a large increase in polarizability for the chromophore, and therefore the molecular vibrations involved with this part of the molecule result in significantly stronger Raman intensity.[9] This is known as Resonance Raman Spectroscopy (RRS). RRS has been described as a vibronic spectroscopy – involving electronic and vibrational events. Under non-resonance Raman scattering, the excitation has no interaction with the higher electronic state, polarizabilities of the ground state molecule are considered. During RRS, the band positions still occur at the ground state positions, but the intensity of bands now include information about the structure of the electronic state in resonance.[1,5]

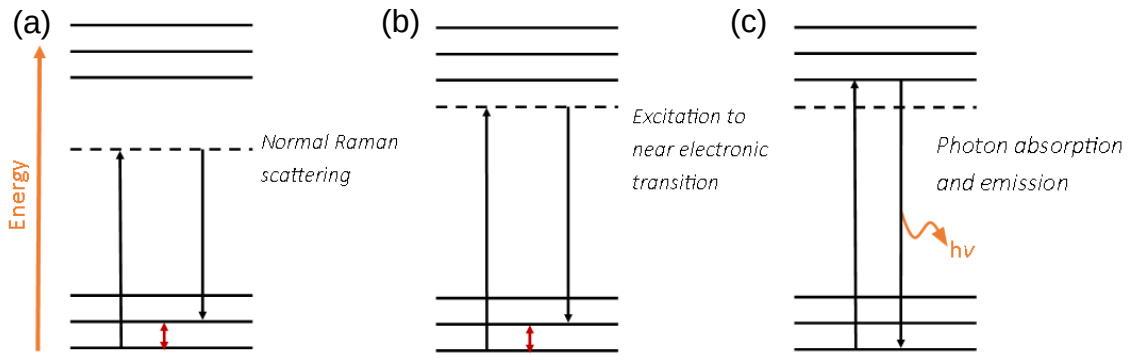

Figure 10 Illustration of the quantum mechanical approach to show the difference between (a) non-resonance enhanced Raman scattering, (b) resonance enhanced Raman scattering, and (c) absorption of a photon followed by emission.

A key difference between the processes in RRS and electronic absorption spectroscopy is that in absorption, the transition is followed by the molecule relaxing into the equilibrium geometry of the excited state. The process involved in scattering, as previously mentioned, is fast with energy released almost immediately and before the nuclei can relax into the geometry of the virtual

excited state.[1] Absorption as well as scattering will occur by use of a laser wavelength to give resonance Raman, where this absorbed energy might leave result in fluorescence, as illustrated in Figure 10c. The ratio of scattering to absorption events depends on the properties of the molecule and are complicated and difficult to predict. It leads to many species being unsuitable to interrogation by RRS when measured through traditional methods.[1]

Fluorescence in spectra

Raman spectroscopy can often be hindered by a strong background signal that may saturate the detector to prevent the detection of Raman scattering. The main source of the background is often fluorescence from the sample. Fluorescence can occur through the presence of impurities, either metal ions or carbonaceous, organic impurities, which act as fluorophores, absorbing photons of the excitation beam and emitting light.[11] Sometimes these impurities can be removed, for example by extra calcination to remove organic species and by taking care to avoid contamination with other metal ions. In the study of zeolites, fluorescence is often assumed to occur because of the presence of these impurities, but there is still some debate about the source of the background. Fluorescence can arise from defect sites.[11] Experiments using MgO have shown that the presence of oxygen vacancies are directly linked with Raman background, and absorption spectroscopy revealed that the defect sites caused by the oxygen vacancies created new absorption bands of lower energy than usually found in MgO. Since zeolites have very high surface areas and many edges, they are likely to contain many defect sites and as such this may sometimes be a source of the fluorescence.[8]

Methods to avoid fluorescence or large background that drowns out Raman signals include time gating methods, the use of UV excitation wavelength (although this can result in sample damage through photochemical changes), the use of IR excitation wavelengths (although this can result in very low signal intensities as Raman scattering is proportional to ω^4 of the light frequency).[1,5,8] In this thesis, time gating methods are utilised, using an optical Kerr-gate to optimise the Raman signal and minimise fluorescence signal detection.

Kerr-gated Raman spectroscopy

Pulsed Raman methodologies make use of the differing fluorescence and Raman lifetimes. Raman scattering is a virtually instant process following the laser pulse, and fluorescence lifetime is in the order of 10^{-6} to 10^{-9} seconds. Optical Kerr-gating is a method which uses short picosecond (ps) laser pulses and a Kerr-gate to temporally reject fluorescence.

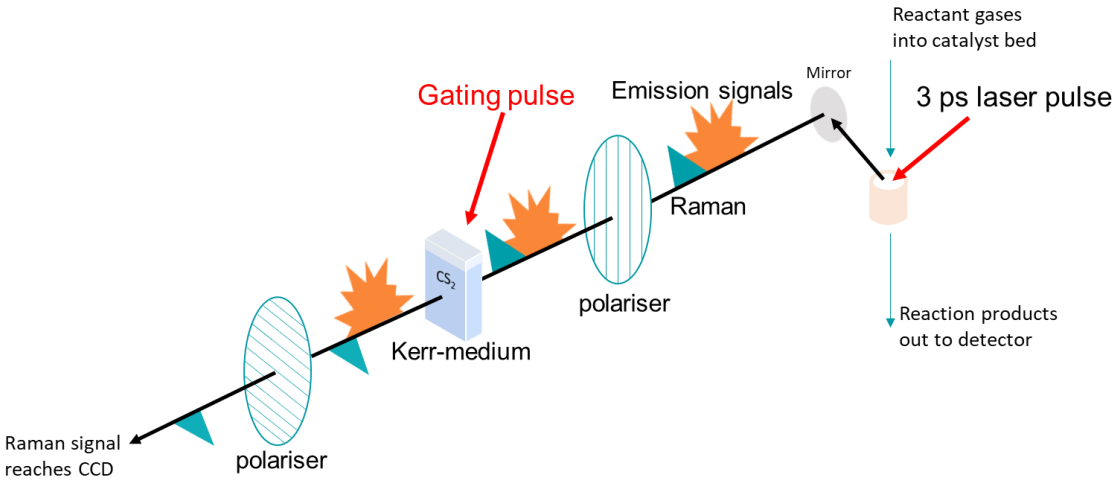

Figure 11 Illustration of the Kerr-gate blocking fluorescence from the detector. Reproduced from ref. 12.

An illustration of the Kerr-gate blocking fluorescence from the detector is shown in Figure 11 and a photograph of the setup in Figure 12. The Kerr-gate is comprised of two cross-polarisers at 90° to one another and a Kerr-medium.[12] As the sample is irradiated, Raman signal is produced, as is fluorescence. All light passes through the first polariser. A gating pulse (second laser beam) is timed for the Raman signal to meet the Kerr-medium so that it is activated for the duration of time that the Raman signal is propagated. The fluorescence which typically takes nanoseconds misses the activation of the Kerr-medium. To activate the Kerr-medium, the laser pulse is rotated to 45° with respect to the polarization of the first polariser. The electric field of the powerful, 800 nm gating pulse partially aligns and polarises the molecules of the Kerr-medium and creates a birefringence in the Kerr medium. This laser-induced birefringence (which only lasts for a few ps) rotates the original polarisation of the signal light passing

through the Kerr-medium. The light now rotated at 90° with respect to the first polariser then passes through the second polariser of the Kerr gate. As the fluorescence arrives at the Kerr-medium later than the Raman signal, it misses the laser pulse, the polarisation of this light is not rotated and it does not pass through the second polariser.[12]

Figure 12 Photograph of the optical elements in the Kerr-gate. From back to front as the light travels through the system: a cross polariser, focusing lens, Kerr-medium (quartz cuvette of CS_2), focusing lens, cross-polariser.

This technique is based on the Kerr-effect, the principle that an isotropic, transparent material becomes birefringent when an electric field is applied.[13] Common Kerr-media include CS_2, benzene and nitrobenzene. For this application, it is important that a Kerr-medium has a high throughput, induces little

noise due to the gating pulse, does not disturb the energy of Raman bands and has high bandwidth for the full spectral range to be trasnmitted.[12]

Kerr-gated Raman spectroscopy requires two pulsed laser probes. At the ULTRA facility of the Central Laser Facility, the Ti-Sapphire laser emitting 800 nm fundamental wavelength at a 10 kHz repetition rate is used, its pulse width is tuned to 3 ps. To activate the Kerr-gate, part of the fundamental 800 nm beam (the gating beam) is focused by a lens to a spot of 1 mm diameter on the Kerr cell. The polarization of the gating beam is at 45 ° between the polarizations of the two polarizers in the Kerr-gate system.

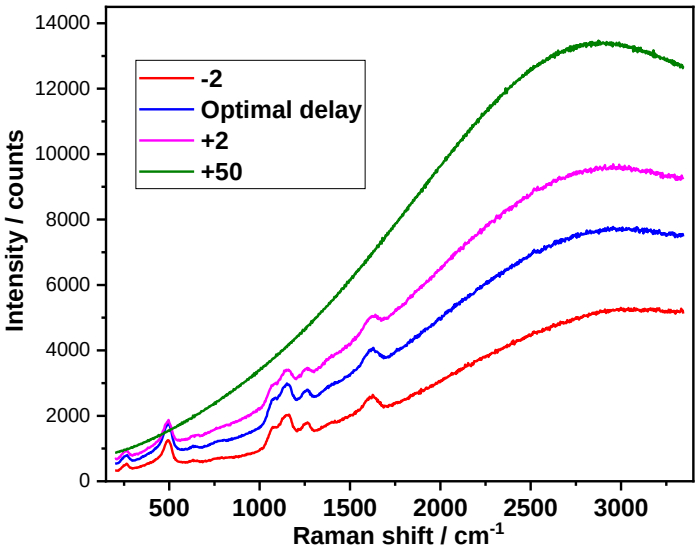

Figure 13 Raw data collected by the Kerr-gate after signal optimization for the maximum Raman intensity reaching the detector. The arrival of the Raman signal at the activated Kerr-gate is optimised to give the optimal delay, and measurements are recorded at approximately 2 ps later and earlier (denoted -2 and +2) to ensure that the optimal delay is recorded for Raman intensity. +50 delay shows only emission signal.

350 mW of the 800 nm fundamental beam is split to generate 120 mW of the second harmonic at 400 nm to be used as a Raman probe, which is set to a horizontal polarization at the sample. The beam is focused by a lens to a spot size of 100 µm on the sample, initiating its Raman scattering. The Raman signal must arrive at the Kerr-cell at the exact time as the gating pulse, this is controlled by sending the 400 nm probe beam via a delay line – a motorized linear stage containing a hollow retroreflector. The delay line allows the arrival time of the

excitation pulse at the sample to be adjusted and optimized to give the highest Raman intensity. Throughout the experiment, several time delays are recorded around the optimal time to ensure that during experiment the best Raman signal is recorded. The optimal time may change due to a change in the sample properties (for example absorbance of the sample might affect the depth of penetration of the beam into the sample which in turn changes the duration of time until the signal reaches the Kerr-cell) then the maximum Raman intensity is still detected. An example is shown in Figure 13 which shows the spectra acquired of calcined H-SAPO-34 prior to a Methanol-to-Hydrocarbons experiment. The optimal signal is shown in blue, but one measurement is taken equivalent to the arrival of signals at the Kerr-cell approximately 2 ps earlier and later, and 50 ps later. At 50 ps no Raman signals are recorded, only the broad emission signal.

The signal which passes through the Kerr-gate is dispersed and detected by a Czerny-Turner spectrograph (Shamrock 303i, Andor) equipped with a CCD camera (iDus DU-420A-BU2, Andor) which is calibrated by recording the Raman spectrum of toluene. The grating used in the system is 1200 lines/mm. The CCD contains a silicone sensor of 1024 x 256 pixels.

The Linkam Cell is fitted to a stage which rapidly moves 2 – 3 mm along its X and Y axes so that the sample is moved in the beam to avoid focusing on one spot that might induce severe photodegradation or thermal heating of the sample.

2.1.2 Diffuse Reflectance UV-Vis Spectroscopy

Ultraviolet-Visible Spectroscopy (UV-Vis) is a technique that allows the detection of electronic transitions between bonding, non-bonding, and antibonding orbitals in organic chromophores. It is useful for the characterisation of adsorbed species on zeolites if they contain a chromophore, giving information about the level of conjugation, and the charge state such as whether the molecule has been protonated by the zeolite acid sites.[14,15] $\pi \rightarrow \pi^*$ transitions typically dominate spectra of organic molecules, but in molecules containing heteroatoms such as O or N, the lone pair of electrons introduces the non-bonding orbital of the molecular orbitals, giving rise to $n \rightarrow \pi^*$ transitions at lower energy.[16] $n \rightarrow \pi^*$

transitions are weaker than π→π*, having weaker extinction coefficients by ~10^{2}.[15]

Diffuse reflectance method and Kubelka-Munk theory

The diffuse reflectance (DR) method can be used to analyse the spectra of solid samples which have a matt or dull surface – such as powders. The light collected by reflection from the powder is weaker when absorption occurs than when it does not occur, and so a diffuse reflected spectrum is measured that is comparative in terms of wavelength with a transmission UV-Vis spectrum. Light shone on the solid surface can be reflected specularly or diffusely, diffusely reflected light is independent of the incidence angle and is predominant on a matte surface. Figure 14a shows an illustration of a powder consisting of randomly oriented particles which diffusely scatter light in all directions, while some specular light from the flat surface is emitted at an angle equal to the angle of incidence. In Figure 14b, the DR-UV-Vis probe is shown collecting backscattered light at the same angle as the light was emitted, resulting in a collection of the diffusely reflected light.

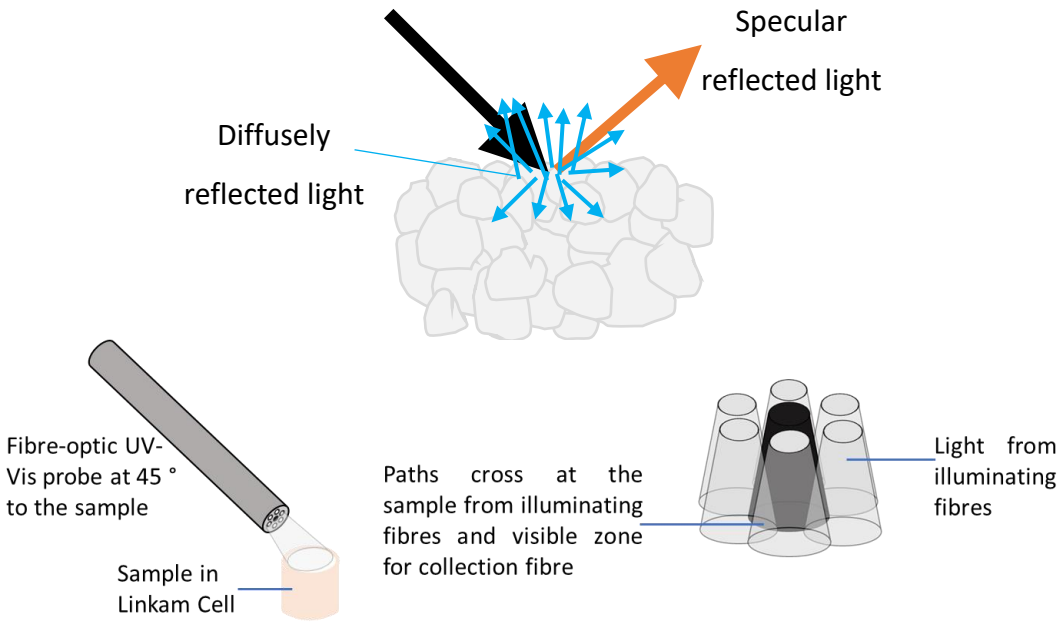

Figure 14 (a) Illustration of diffuse and specular reflected light from a powder containing randomly oriented particles and (b) illustration of the fibre-optic probe illuminating the sample in these measurements, including the 6 illumination fibres surrounding the collection fibre.

The light can also be refracted or diffracted i.e., scattered internally or externally to the body of powder, and by how much varies with absorption by the sample. In spectral regions where absorption is strong, only diffusely reflected light from a short path length is emitted resulting, while in regions of weak absorption light which is not absorbed in long paths is lost to the depth of the sample. For comparison with a transmission spectrum, this results in a spectrum with comparable wavelengths absorbed but artificially stronger weak absorptions and weaker strong absorptions. Collected light therefore requires description to separate the scattered light from the light absorbed by the sample, and the Kubelka-Munk theorem (KM) offers a simple method to do this to approximately correct for the relative intensity differences. The equation for KM is given in Equation (3):

$$f(R_\infty) = \frac{(1 - R_\infty)^2}{2R_\infty} \qquad (3)$$

Where R_∞ is the reflectance of the sample with respect to a perfectly reflecting reflectance standard. In this case a flattened $BaSO_4$ powder was used. Kubelka-Munk theory assumes no specular reflection component, and an infinitely thick, densely packed powder sample of particles. Figure 15 shows an example of a DR-UV-Vis spectrum with intensity given as collected in % Reflectance and after its transformation by KM to Absorbance. KM absorbance is comparative to absorption values in transmission UV-Vis Spectroscopy.

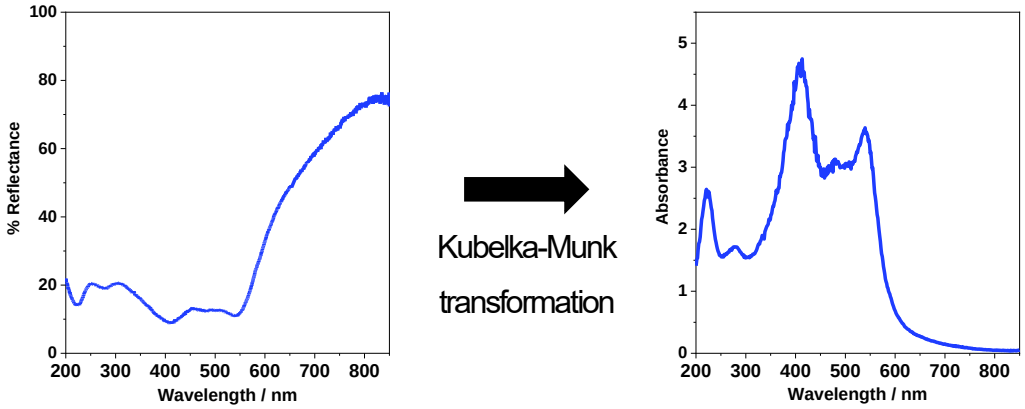

Figure 15 Example of the original UV-Vis spectrum collected in reflectance mode and the result of its transformation via the Kubelka-Munk theory to Absorbance. This spectrum was collected after furan adsorption on H-ZSM-5 followed by 60 minutes of flushing to remove excess.

For UV-Vis experiments the same catalyst treatment and conditions as used for the Kerr-gated Raman measurements were applied also using the same CCR1000 stage. The UV-Vis setup comprises a Flame-S-XR1-ES Ocean Optics spectrometer with a 100 µm slit, DH-2000-S-SUV-TTL light source and QR400-7-SR-BX reflection probe (fibre optic probe). The probe was held to the quartz window such that the excitation light hit the sample at a 45° angle, collecting back the diffusely reflected light at that same angle. Figure 14c shows the 6 illumination fibres at the end of the reflection probe and the single collection probe. The Kubelka-Munk equation was applied to convert reflectance measurements to absorbance values in all cases.

2.1.3 Mass Spectrometry

A mass spectrometer (MS) is used to measure the mass to charge ratio (*m/z*) of gas phase ions. Within the MS, an ion chamber, which requires an ultra-high vacuum, consists of a filament which generates electrons upon application of an electric current, a quadrupole which separates ions based on their mass-to-charge ratio (*m/z*) and an ion detector. Gaseous or vapourised molecules are drawn into the ion chamber where they are hit with electrons from the filament, causing electrons in the molecules to be hit out of their orbit and creating positively charged ions. The positively charged ions are then accelerated towards the quadrupole – four cylindrical metal rods positioned in a square configuration where each pair of opposite rods is connected.[17,18]

In the quadrupole, each pair of rods are charged by a direct voltage (DC) and a radio-frequency voltage (RF), these voltages are used to apply oscillating electrical fields across the four rods that stabilize or de-stabilize the path of positive ions passing through. The attraction of a positive ion to the rod depends on the mass and charge of the ion and the field strength and frequency of the oscillations. A positive ion with a small mass is heavily affected and drawn to the negative poles while large positive ions pass through. Only ions with high *m/z* can pass between the positive rods while only ions with low *m/z* can pass between negative rods, therefore only ions with specific mass to charge ratio meet both criteria, when the correct DC voltages are chosen. The DC range is chosen to scan from small to large values.[17,18]

The ions that can pass through reach a Faraday detector which measures the ion current and is proportional to the concentrations of ions of that *m/z* value. A secondary electron multiplier (SEM) can be used to amplify the signals – cylindrical pieces of metal sheets with a coating that creates a low level of electron work function. Secondary electrons are generated when ions or electrons strike the layer – and multiple metal sheets in series are connected which therefore generates many electrons per ion, and the signal is amplified by up to 10^7.[17] The function of the quadrupole and SEM are illustrated in Figure 16.

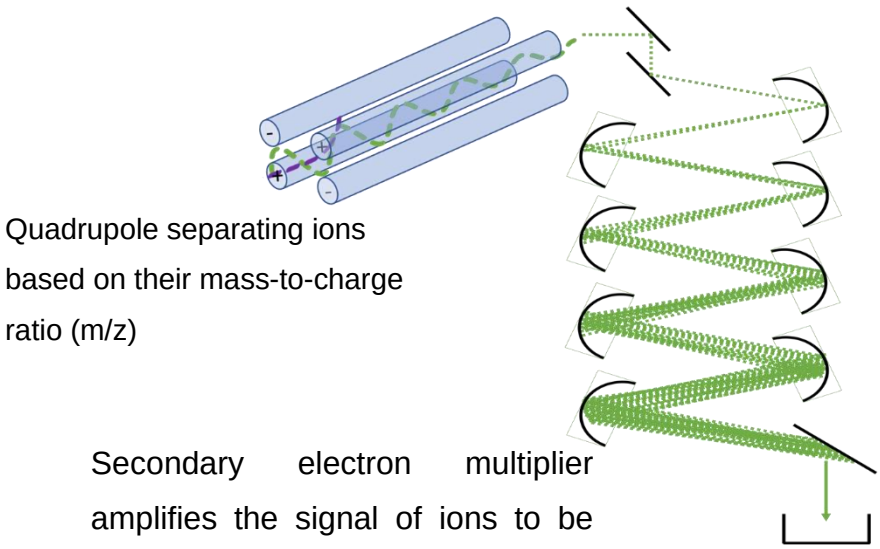

Figure 16 Illustration of the function of the quadrupole and the secondary electron multiplier of the mass spectrometer used as a gas analyser in this PhD thesis.

A Pfeiffer Omnistar GSD 320 Mass Spectrometer was used as an on-line gas analyser in these experiments, fitted with a tungsten filament and using a secondary electron multiplier to allow shorter scans for each *m/z* sampled, 1 s sampling time was used.

2.1.4 Powder X-Ray Diffraction

X-Ray Diffraction examines the long-range order of crystalline materials and can be used as a fast and effective tool to determine whether the correct material phase has been synthesised. The comparable distance of wavelengths of X-rays with interatomic distances make them ideal for the study of repeated planes in a

crystal lattice. When the monochromatic X-rays interact with atoms they are diffracted, and in a crystalline solid, the X-rays will interact with the first layer of atoms while other pass through and are diffracted by sequential layers.[19,20] This is illustrated in Figure 17. The scattering from different layers, or different lattice planes, allows constructive interference to take place causing a higher intensity of scattered X-rays in one direction. Constructive interference can only occur if the difference in path length between the diffracted waves (as indicated by the green dotted lines in Figure 17) is an integer of the X-ray wavelength. These conditions can be summarised by the Bragg equation in (4) where *n* is an integer, *λ* is the wavelength of incident light, *d* is the interplanar distance and *θ* is the incident angle of the incoming X-ray on the crystal:

$$n\lambda = 2dsin(\theta) \quad (4)$$

When these conditions are met, the constructive interference of results in very high intensities reaching the detector, and a plot of intensity against incident angle gives a characteristic fingerprint of the crystal structure.[19,20]

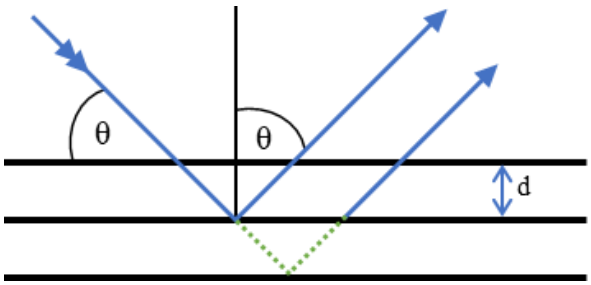

Figure 17 Illustration of the diffraction of X-rays from two parallel planes of a solid. The value of d gives the distance between lattice planes, *θ* gives the incidence angle of the X-rays on the lattice plane. The green dotted line gives the difference in path length of the beam striking the second lattice plane from striking the first plane.

The PXRD patterns in this thesis were collected on a Rikagu SmartLab with a 9 kW Cu source. Measurements were recorded over the range of 2θ from 5 to 55°. In this diffractometer, the X-ray source remains fixed while the detector moves about the sample, known as Bragg-Brentano geometry, to collect the intensity of diffracted X-rays through the set range of angles. The powder sample is placed on a goniometer and pressed to a flat surface for measurement, and

during measurement the sample spins at 1° min^{-1} to avoid any preferred orientation of the powder.

2.1.5 Nitrogen physisorption

Nitrogen physisorption can be used as an indirect means of measuring the surface area and pore characteristics of porous samples. During the measurement, two cells are used, one containing the sample and a second which remains empty as a reference. After vacuum evacuation of the sample, known volumes of nitrogen are dosed at 77 K, a temperature which is maintained by a Dewar of liquid nitrogen below the sample. During the measurements, the relative pressure (P/P_0) in the cell is increased to set values, and the volume of nitrogen allowed in the cell is recorded (V_{ads}). P/P_0 is given by the absolute pressure with respect to the saturation pressure of the adsorbate. The resulting isotherm is a plot of P/P_0 against (V_{ads}). Nitrogen first adsorbs to the outer surface of the sample, as well as on the surface of any mesopores (2 – 50 nm) or macropores (> 50 nm) and filling micropores (pores of < 2 nm). Micropores will be filled at very low relative pressures, therefore for zeolite studies it is common to measure V_{ads} at many values at very low P/P_0.[19,21,22]

An example isotherm for a zeolite is shown in Figure 18. The region of the isotherm at very low pressures is indicated by the red box where the isotherm appears vertical demonstrates the filling of micropores in the sample. As P/P_0 increases the walls of meso and macropores and the external surface area become filled, until a monolayer coverage is achieved, indicated by the region at the knee of the isotherm in the green box. Multilayer coverage occurs as P/P_0 further increases, until towards saturation pressure ($P/P_0 > 0.8$), where a steep increase in V_{ads} indicates the filling of meso or macropores.[21,22]

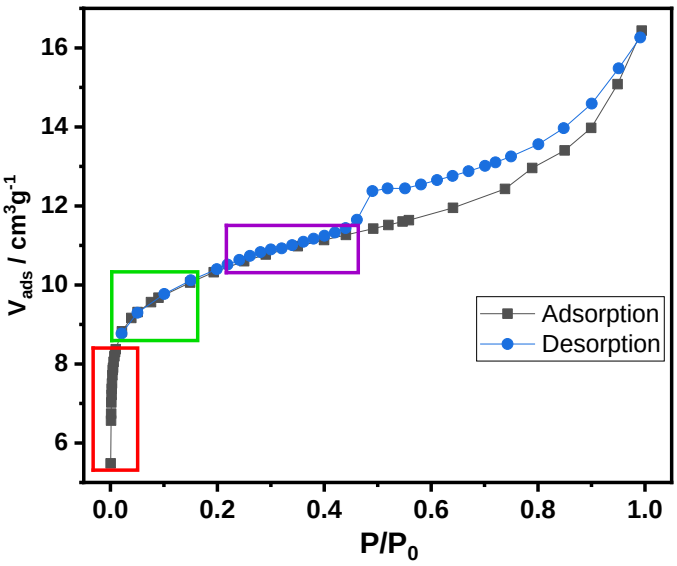

Figure 18 Example plot of Nitrogen adsorption isotherm, recorded for a sample of Zeolite Y from Zeolyst Inc. on a Quadrasorb BET Surface Analyzer. The region in the red box is used for to indicate micropore filling, the green box can be used to analyse the surface are by BET method, the purple box can be used to analyse the micropore volume by the v-t plot method.

To measure surface area the most popular method is the Brunauer-Emmett-Teller method (BET), which uses the low relative pressure region of the isotherm. Using the estimated V_{ads} adsorbate (N_2) required to form a monolayer of coverage over the sample surface, the surface area of the solid can be calculated by conversion into the weight of the monolayer (W_m), and accounting for the cross-sectional area of the adsorbate ($A_{c\text{-}s}$), molar mass of the adsorbate (M) and Avogadro's number (N) according to the equation:

$$S_t = \frac{W_m N\, A_{c-s}}{M} \qquad (5)$$

W_m needs to be calculated by solving the BET equation:

$$\frac{1}{W\left(\left(\frac{P_0}{P}\right)-1\right)} = \frac{1}{W_m C} + \frac{C-1}{W_m C}\left(\frac{P}{P_0}\right) \qquad (6)$$

A linear plot of 1 / $W(P_0/P)$-1 against P/P_0 gives a straight line, where the y-intercept and gradient are used to calculate the value for W_m, and for C, the BET constant for the sample which is related to the energy of adsorption of the first layer.[22]

In microporous materials it is possible to analyse the isotherm to estimate the micropore volume, one method for doing so is the t-plot method. V_{ads} is plotted against the statistical thickness of an adsorbed layer on a similar material that is non-porous at a corresponding pressure (t). The t-plot method requires the selection of 5 points from the adsorption isotherm in the range where multilayer adsorption occurs, at the end of the BET range to plot (indicated by the region in the purple box in Figure 18). Where micropores are present, the y-intercept will be positive, and gives a V_{ads} value which is converted to a liquid volume and is equal to the volume of micropores in the solid sample.[22]

N_2 adsorption was carried out on a Quadrasorb BET after degassing each sample under vacuum at 350 °C for 20 h to remove any adsorbed species. Surface areas were analysed using the BET plot using 5 points between 0.001 and 0.011 relative pressures. Micropore volume was analysed using the V-t method from t-plot by selecting 6 points between 0.3 and 0.5 relative pressures.

2.1.6 NH_3-Temperature Programmed Desorption

Understanding the number and strength of acid sites on a catalyst surface is important for rationalising catalytic behaviour, and the temperature programmed desorption of ammonia is a common technique to analyse the acid properties of solid catalysts. The basis of the technique is that according to equation (7) the probe base, NH_3, reacts with the Brønsted acidic proton of ZH, to give a NH_4^+ species that is the conjugate acid of NH_3.[23]

$$ZH + NH_3 \leftrightarrow Z^- + NH_3^+ \qquad (7)$$

The experiment should consist of the following 4 steps:

1. Catalyst evacuation at high temperature i.e., dehydration and adsorbate removal

2. Adsorption of ammonia on the sample at 373 K
3. Evacuation of weakly adsorbed ammonia for a set amount of time
4. Increase in sample temperature by 10 K min^{-1} until all ammonia which was adsorbed has desorbed.

During desorption step, the gas effluent is monitored by either a thermal conductivity detector (TCD) or by mass spectrometry, and the removal of ammonia correlated with the temperature of desorption (T_D). T_D is strongly influenced by the mass/volume of sample used and the flow rate of the carrier gas, since these parameters change the equilibrium between the adsorbed ammonia and gas-phase ammonia.[24] The density of acid sites can influence the readsorption of ammonia, thereby affecting T_D. Many studies have tried to directly estimate the heat of ammonia adsorption from T_D using combined experimental and theoretical approaches, including infrared spectroscopy and through altering experimental parameters. In this thesis, for simplicity, T_D is reported to give an approximation of acid site strengths, to compare between zeolites measured in the same method.[23,24]

In analysing the acid sites by this way in zeolites, one should be conscious that ammonia can also be adsorbed to the surface that is non-acidic, and due to the small size of the molecule, ammonium ions formed on the surface can allow the chemisorption of a further ammonia molecule. It is also not possible to differentiate Lewis from Brønsted acid sites by this method.[19,23]

NH_3-TPD profiles were recorded on a ChemBET from Quantachrome instruments equipped with a TCD. In each experiment, 0.050 g of sample was supported by quartz wool in a U-bend quartz tube. Samples were pre-treated in a mixture of 20 % oxygen in helium, heated at 10° min^{-1} to 550 °C for 1 h, and then cooled to 100 °C whilst flowing pure helium. A mixture of 5 % ammonia in helium were passed over the sample at a rate of 20 ml min^{-1} for 30 min, and then weakly adsorbed ammonia was removed by flushing with 30 ml min pure helium for 2 h whilst holding at 100 °C. The temperature was then increased by 10 °C min^{-1} to 700 °C and gas effluent monitored in this period for ammonia removal.

2.1.7 SEM-EDX

To image particles, smaller wavelengths are required than visible light. Electron microscopy uses accelerated electrons at high energies (typically 2 – 40 keV). The electron beam might be transmitted through a thin sample or can interact with the surface such that electrons emerge from the sample – and these are the signals used in Scanning Emission Microscopy (SEM). SEM allows magnifications up to 10^6.[25]

A tungsten filament is heated to produce electrons by thermal emission, which pass through a series of optics to focus the electron beam to a small probe, which is scanned across a selected area in a raster. The dimensions of the penetration of the electrons into the surface depends on the energy of the electron beam, on the atomic masses of the elements of the spectrum and the angle at which the electron beam hits the sample. Secondary, backscattered and Auger electrons, and X-rays may be produced from the sample after irradiation. Secondary electrons, as the lowest energy electrons, are produced when they are knocked out of their orbit by incident electrons, and provide the highest spatial resolution being nearer to the shallow sample surface. Backscattered electrons are produced as the incident electron beam can approach the atomic nucleus and are scattered through a large angle, they have higher energies and are slightly deeper than secondary electrons, giving a poorer resolved image.[25] The electron probe approaching a vertical surface, a large fraction of secondary electrons can escape to be collected and the surface will appear bright, while a small fraction are detected from a horizontal surface appearing less bright, this reveals morphological information about the sample.[20] Auger electrons are emitted from close to the sample surface, and can give valuable chemical information – but their low numbers and the high precision required to record them leave these measurements to dedicated instruments.

When higher electron energies are used, the incident electrons can knock out inner-shell electrons from atoms in the sample and an outer-shell electron moves into the inner orbit, producing an X-ray characteristic of the element. These X-ray signals can be used to analyse the chemical composition of the sample, although to a lower resolution of around 1 µm. The X-rays are collected by an energy

dispersive spectrometer, and the technique is known as Energy Dispersive X-ray Spectroscopy (EDX or EDS), and is commonly attached to an SEM.[25]

SEM-EDX was used in this thesis to help in characterising calcium impregnated zeolites. Images were recorded on a JEOL JSM-6610LV Scanning Electron Microscope, paired with a X-Max Energy Dispersive Detector from Oxford Instruments.

2.1.8 X-ray Fluorescence

In XRF, the sample is illuminated by X-rays, causing the excitation of electrons from the core shells which are released. In a similar way to EDX as previously described, the relaxation of electrons to fill the resulting holes occurs quickly and leads to fluorescence, or secondary X-rays being released, which are characteristic of the energy levels of the elements in the sample. The intensity of fluorescent X-rays detected is used to quantify the elements in a sample.[20,26] Figure 19 illustrates the mechanism of XRF. The secondary x-rays are described as Kα or Kβ emission depending on the shell from which the electron has transitioned into the core.[20,26]

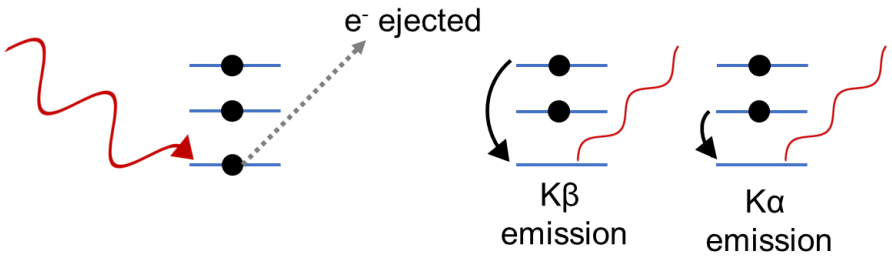

Figure 19 Illustration of the mechanism involved in x-ray fluorescence. X-ray ejects a core electron of an atom, as electrons from higher energy levels relax into the hole created the release x-rays characteristic of the element.

In this thesis, X-ray Fluorescence (XRF) has been used as a means of elemental analysis, to determine the chemical compositions of synthesised and modified zeolites. XRF measurements were collected on an Epsilon3 XL from PANalytical, which uses an energy dispersive detector (EDXRF), detecting a broad range of elements simultaneously (as opposed to wavelength dispersive detection where

the elements are selectively measured).[26,27] Around 100 mg of samples was used as powders for the measurements.

2.1.9 Thermogravimetric analysis of spent catalyst samples

Thermogravimetric analysis (TGA) is a relatively simple experimental technique which records the weight change of a sample during treatment. For these experiments, zeolite samples containing carbonaceous deposits are placed in a small, platinum pan inside a furnace, and are then exposed to an air stream while the temperature is linearly increased from room temperature to 900 °C. The result is a plot of weight loss against temperature, which reveals the temperature at which the carbonaceous deposits are combusted/oxidised and therefore gives some indication of their characteristics. The method can otherwise be known as Temperature Programmed Oxidation (TPO) although this often monitors the outlet gases for CO_x production as opposed (or as well as) the sample weight.

TGA was performed on a Q50 Thermogravimetric Analyzer from TA instruments. Around 10 mg of the used catalyst was loaded into a platinum pan, which was loaded into the furnace of the instrument. The sample was heated at a rate of 5 °C min^{-1} to 900 °C under a flow of 60 ml min^{-1} air. The mass of the sample is weighed and recorded throughout the temperature ramp to detect changes.

2.2 Materials

2.2.1 Synthesis of H-ZSM-5

ZSM-5 was synthesised using nominal Si/Al ratios of 15 and 40 by hydrothermal synthesis. Sodium aluminate (0.0910 g or 0.0686 g, Sigma Aldrich) was added to deionised water (4.8 g) and the solution stirred until dissolved. Tetraethylorthosilicate (5.847 g, >99.8 % Sigma Aldrich) was added dropwise to the solution followed by tetrapropylammonium hydroxide (2.8935 g, 40 % solution in water) which was previously diluted by additional deionised water (2.8 g). The gel was stirred for 45 min, before it was transferred to a PTFE lined autoclave. The synthesis was carried out at 180 °C for 22 h. After the crystallisation, the autoclave was quenched. The solid was filtered, washed with 5 dm^3 of deionised water until neutral pH and dried overnight at 70 °C. The zeolite was calcined in static air to remove the organic template at 550 °C for 8 h, then ion-exchanged with a 1 M solution of NH_4NO_3 at 80 °C for 10 h and washed with 3 dm^3 of deionised water. This was repeated a further two times to yield NH_4-ZSM-5. The ammonium ions were decomposed through calcination at 550 °C for 4 h to obtain the H-form zeolite.

2.2.2 Chabazitic Materials

H-SSZ-13 was prepared in-house by another member of the group by hydrothermal synthesis under static conditions in F^- media, with a nominal Si/Al ratio of 15, according to a method published by Moliner *et al.*[28]

H-SAPO-34 with (Al + P)/Si ratio 18 was purchased from ACS Materials.

2.2.3 Impregnation of calcium into H-ZSM-5 and H-SSZ-13 by incipient wetness

The micropore volume of the zeolite was determined using N_2 adsorption so that the zeolite could be treated by incipient wetness impregnation using a solution of $Ca(NO_3)_2$. H-ZSM-5 or H-SSZ-13 were degassed over 24 h in a round bottomed flask connected to a vacuum pump in a heating mantle at 160 °C. $Ca(NO_3)_2$ was

dissolved in deionised water. The flask was removed from heat and the vacuum receiver closed to prevent air from entering the flask once the vacuum was disconnected. Enough $Ca(NO_3)_2$ solution was injected into the flask to correspond to 90% of the micropore volume and the molarity of the Ca solution made to correspond to 6 wt. % calcium on the zeolite. The powder was agitated for 30 min using a stirrer bar inside the flask and a magnetic plate to create a homogeneous mix. The stoppers were removed from the flask and the flask placed into an oven set to 70 °C overnight. The powders were then calcined at 550 °C for 4 h to remove nitrate ions.

For the preparation of Ca-ZSM-5:
0.4 g of H-ZSM-5 synthesised with Si/Al = 40 was impregnated with 0.066 cm^{-3} of a 9.7 mol dm^{-3} solution of $Ca(NO_2)_3$ in deionised water, corresponding to 6 wt. % Ca on the zeolite.

For the preparation of Ca-SSZ-13:
0.27 g of H-SSZ-13 with Si/Al = 15 was impregnated with 0.052 cm^{-3} of a 7.7 mol dm^{-3} solution of $Ca(NO_3)_2$ in deionised water to correspond to 6 wt. % Ca.

2.2.4 Materials from Zeolyst International

Ferrierite, Beta, Zeolite Y and ZSM-5 were purchased from Zeolyst international in their ammonium forms, product details including their Si/Al ratios are given below in Table 1. Ferrierite, Beta and ZSM-5 purchased in ammonium form, were calcined by muffle furnace at 550 °C for 4 hours to yield their proton forms prior to reaction.

Zeolite purchased	Si/Al ratio	Nominal cation	Product code
Zeolite Y	15	Hydrogen	CBV 720
Ferrierite	10	Ammonium	CP 914C
Beta	12.5	Ammonium	CP 814E
ZSM-5	15	Ammonium	CBV 3024E

Table 1 Zeolites purchased from Zeolyst Int. and used in Chapter 4 of this thesis

2.3 Materials Characterisation

2.3.1 H-ZSM-5 (Si/Al = 40) and Ca-ZSM-5

H-ZSM-5 was impregnated with 6 wt. % Ca with the aim of reducing Brønsted acidity. Characterisation data is presented in this section comparing the zeolite properties before and after impregnation.

Powder X-ray Diffraction

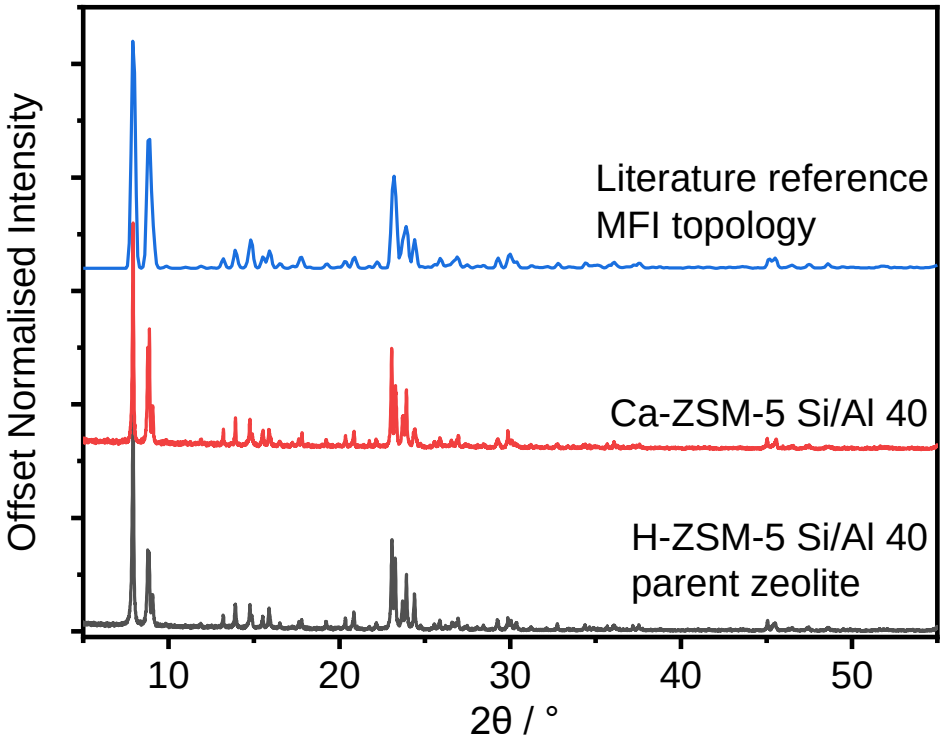

Figure 20 PXRD patterns of H-ZSM-5 synthesised with Si/Al 40, after calcination to remove template and ion exchange and calcination, and H-ZSM-5 after impregnation with calcium nitrate followed by calcination, and reference diffraction pattern for MFI topology.[29] All patterns are normalised to the reflection at 7.9 °.

The diffraction patterns confirm the retention of zeolite crystallinity after impregnation – no further peaks are created which is more easily verified when the patterns are overlaid as in Figure 21, and no peak broadening is observed. Some changes in relative intensity of the peaks are found – in particular, the lesser intensity of the reflection at 2θ = 7.9 and 8.8 ° are related to pore filing

which would indicate incorporation of calcium into the pore network of the zeolite.[19] In Figure 21, the patterns are overlaid to compare intensities, normalised to the reflection at 23.0 ° for comparison. The reflection at 7.9 ° loses 10 % of its intensity, however that at 8.8 ° is 24 % higher.

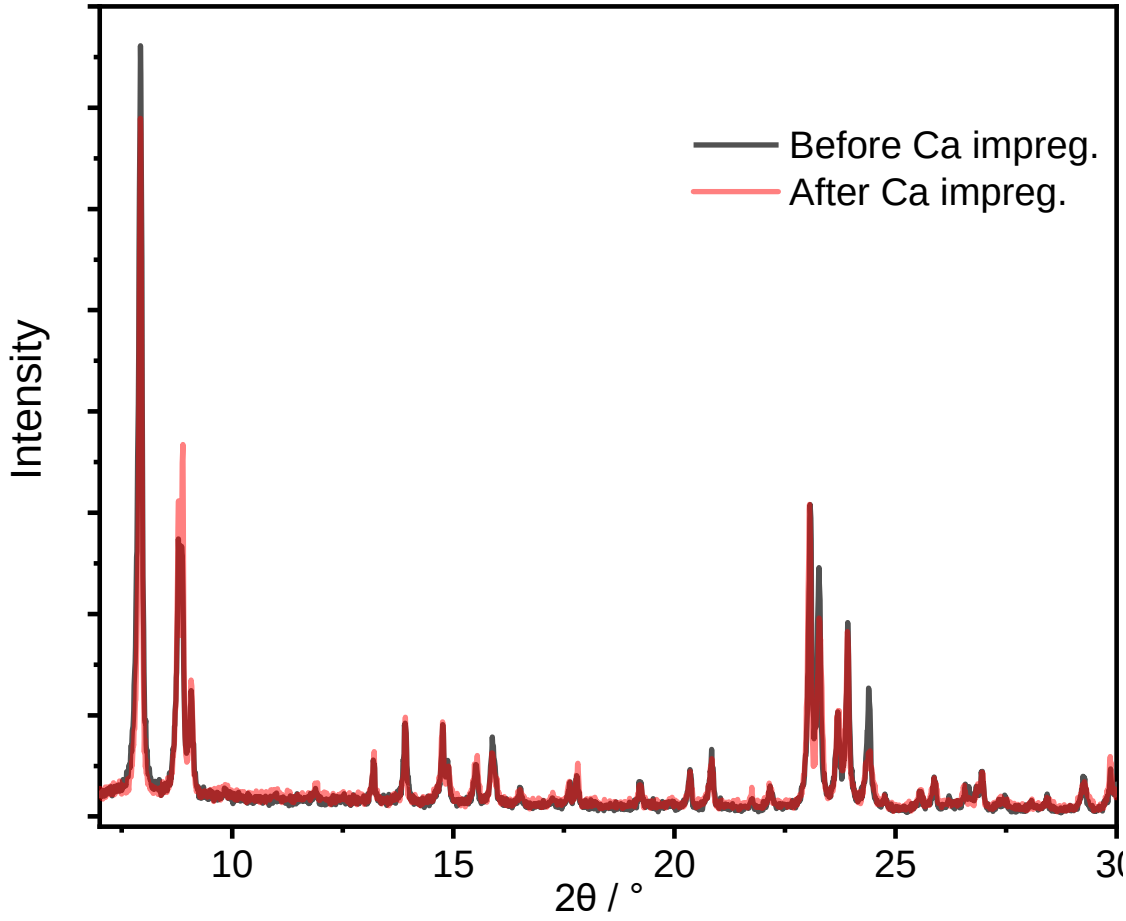

Figure 21 Overlaid PXRD patterns of H-ZSM-5 with Si/Al 40 before and after calcium impregnation, normalised to the peak at 2θ 23 °

Kerr-gated Raman Spectroscopy

The Raman spectrum of Ca/H-ZSM-5 acquired with the Kerr-gated spectrometer is shown in Figure 22. The most intense band at 380 cm^{-1} is attributed to T-O-T and O-T-O bending modes in 5-membered rings.[30,31] In literature, a band at 838 cm^{-1} is assigned to Si-O- stretches which are said to be sensitive to the presence of cations,[30] this peak may be shifted to 813 cm^{-1} in the presence of Ca^{2+} but there is no direct literature evidence to directly support this. Bands

around 1050 and 1200 cm^{-1} are typical of tetrahedral silica polymorphs, due to asymmetric Si-O stretching.

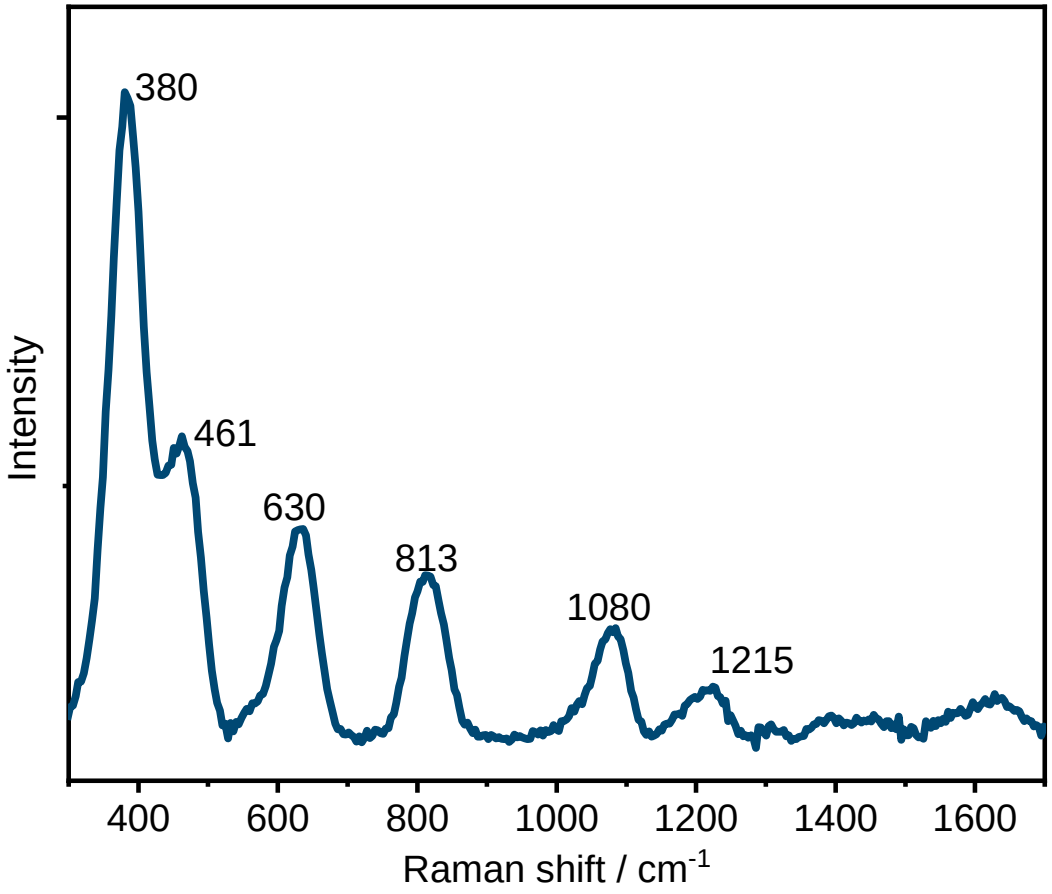

Figure 22 Kerr-gated Raman spectrum acquired of Ca/H-ZSM-5 zeolite. 400 nm probe, 10 mW power, 20 second acquisition, 1200 lines/mm.

$CaCO_3$ shows a strong Raman band at 1080 cm^{-1}.[32,33] Schmid clarified that CaO does not have a first order Raman spectrum, similarly to MgO and NaCl, and it would not be possible to identify CaO here.[33] On exposure to air, CaO would readily react with water and CO_2 in the atmosphere, forming $Ca(OH)_2$ which adsorbs CO_2 to form $CaCO_3$.[34]

Nitrogen physisorption

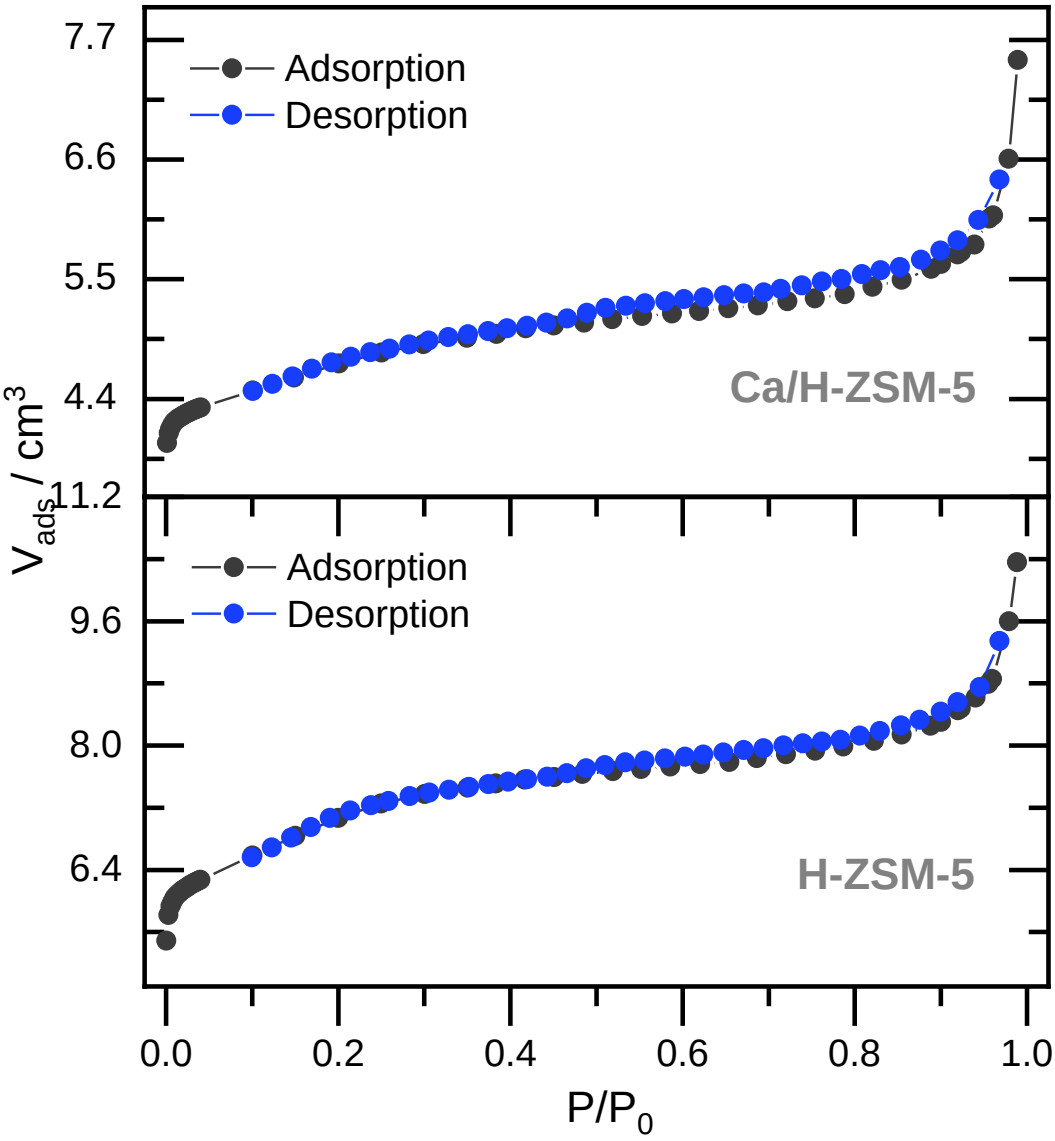

Figure 23 Nitrogen physisorption isotherms collected at 77 K of H-ZSM-5 Si/Al 40 before and after calcium impregnation.

Figure 23 shows the nitrogen physisorption isotherms for H-ZSM-5 synthesised with a Si/Al ratio of 40, before and after impregnation with Ca. In Table 2, a summary is given of the textural properties of the materials. The surface area was calculated from the Multipoint BET method, and micropore analysis by the t-plot method. Analysis of the isotherms before and after impregnation of calcium indicates a loss of micropore volume and area by 32 and 28 %, and overall decrease in surface area by 27 %.

	Multipoint BET Surface Area / $m^2\ g^{-1}$	Micropore volume / cc g^{-1}	Micropore area / $m^2\ g^{-1}$	External surface area / $m^2\ g^{-1}$
H-ZSM-5	487	0.18	420	66
Ca/H-ZSM-5	355	0.12	302	53
Difference	-27 %	-32 %	-28 %	-20 %

Table 2 A summary of textural properties of H-ZSM-5 and Ca-ZSM-5 determined from N_2 physisorption data as calculated from the Multipoint BET and t-plot methods.

NH_3-Temperature Programmed Desorption

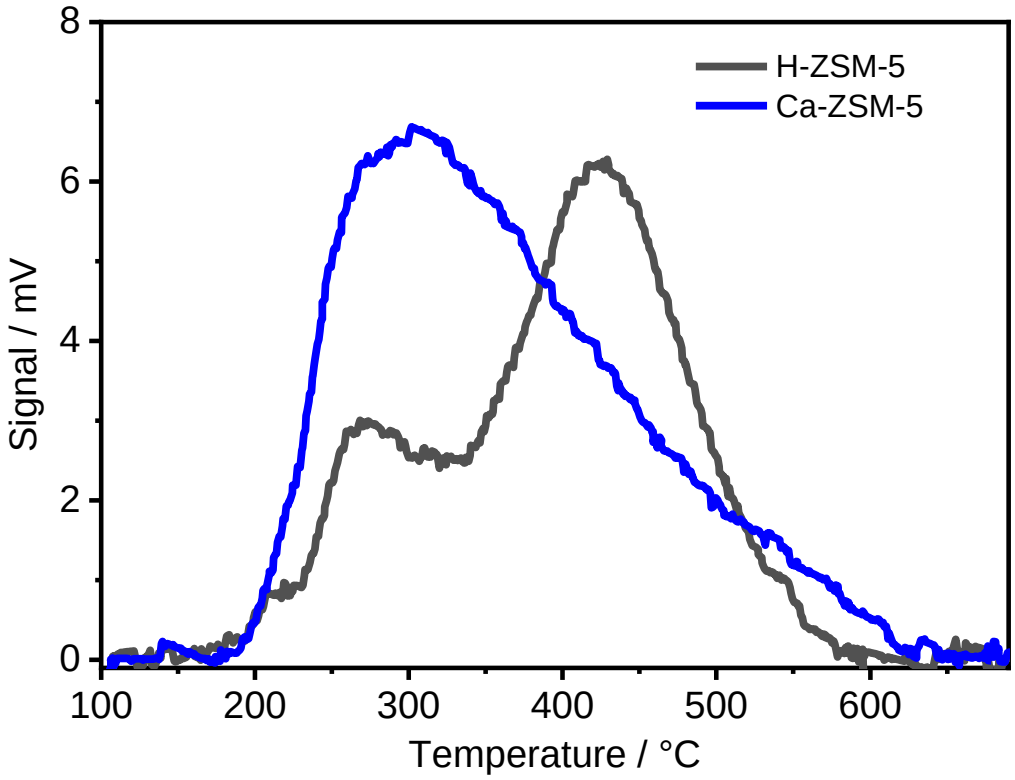

Figure 24 NH_3-TPD profiles of H-ZSM-5 with Si/Al 40 before and after Ca impregnation after adsorption of ammonia for 30 min. at 100 °C, flushing for 2 h and a temperature ramp at 10 °C min^{-1} from 100 to 700 °C.

The results of the temperature-programmed desorption of ammonia (NH_3-TPD) of the parent and impregnated ZSM-5 are shown in Figure 24 and demonstrate a clear change in the acidic properties of the material after impregnation. In the parent zeolite, two peaks indicate weak and strong acid sites, at 275 and 425 °C, respectively. The NH_3-TPD profile of the calcium impregnated zeolite consists of

one very broad peak with a maximum at 300 °C and a broad tail at high temperatures. The prove the presence of more weak acid sites after calcium impregnation than observed in H-ZSM-5 and fewer strong acid sites which desorb ammonia at higher temperature – although some strong acid sites must still be present. This data confirms the loss of the strong Brønsted acid sites of H-ZSM-5 and creation of weaker acid sites by calcium impregnation which are CaO/Ca^{2+} species with Lewis acidic character on Ca-ZSM-5. The result is in line with the work of Yarulina *et al.* who prepared calcium impregnated ZSM-5 by the same method and showed that Lewis acid sites were generated and Brønsted acid sited depleted.[35]

Scanning Emission Microscopy-Energy Dispersive X-rays

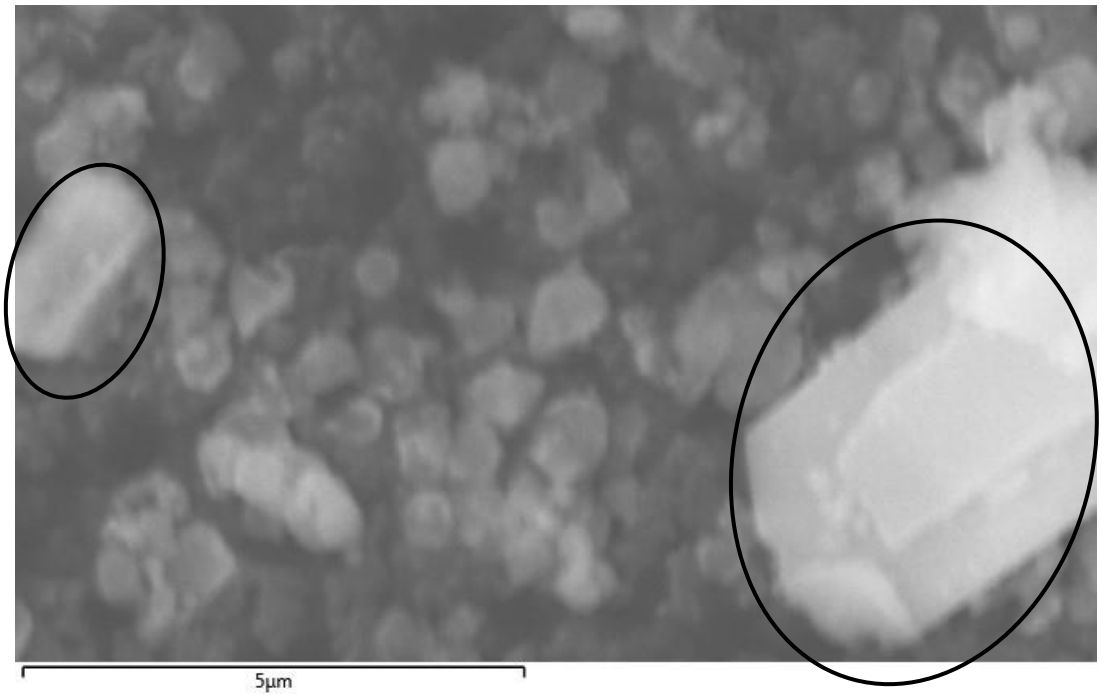

Figure 25 SEM images of Ca/H-ZSM-5 (Si/Al 40) to show particle size and morphology. The circled regions indicate some large particles in the sample.

SEM was used to characterise the particle size and morphology of the Ca/H-ZSM-5 (Si/Al 40) sample, and EDX to assess the calcium dispersion throughout the sample. The images shown in Figure 25 and Figure 26a, for the most part show rounded particles of regular shapes and size of 600 – 700 nm. Figure 25 does also show some much larger particles (which are circled in black for clarity)

which are oblong at 2 x 1 µm and approximately 3 x 5 µm. Such inhomogeneity might be expected from the static synthesis conditions used in the zeolite synthesis method.

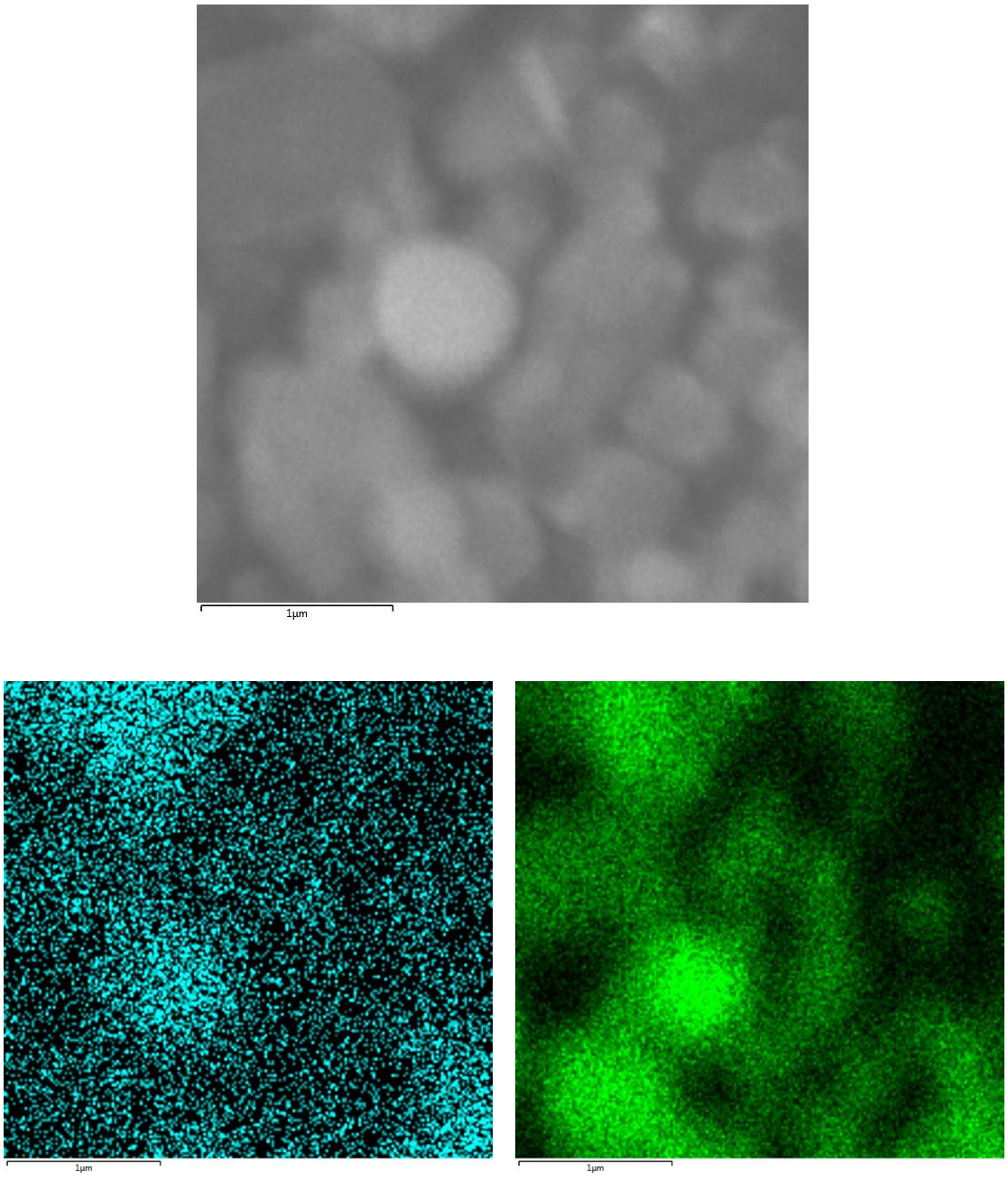

Figure 26 SEM-EDX images of Ca impregnated H-ZSM-5 (Si/Al 40). SEM image collected (top) and EDX data acquired in the same position on Ca (bottom left in cyan) and Si (bottom right) to show Ca incorporation into the zeolite.

Figure 26b and Figure 26c include EDX maps of calcium and silicon, and demonstrate well how the calcium is dispersed within the zeolite sample, with the brightest regions for calcium in cyan in Figure 26b are in the brighter regions for silicon in Figure 26c. Due to the small particle size and brightness shown by the lighter elements in these samples, it was not possible to determine the exact location of the calcium within individual particles but they appear well distributed throughout the silicon distribution.

X-Ray Fluorescence

Table 3 presents the wt. % of elements detected in the sample as oxides, and the relative proportions of those wt. % as elements. The most abundant elements detected were Al and Si, and Ca in the impregnated sample as expected, with some Fe, Cu and Zn detected at low levels (ppm) which are likely contaminants either from the synthesis starting materials (e.g., $NaAlO_2$) or adsorbed from the laboratory during synthesis and post-synthetic treatment. By weight the calcium impregnated sample contained 5.3 % calcium, although the intention was to impregnate with 6 wt. % the lower value might be due to the hygroscopic nature of the $Ca(NO_3)_2.4H_2O$ which can lead to inaccurate weighting.

	H-ZSM-5 (Si/Al 40)		Ca/H-ZSM-5	
Oxide	wt. % measured as oxide	wt. % as element	wt. % measured as oxide	wt. % as element
SiO_2	97.3	45.5	90.0	42.1
Al_2O_3	2.7	1.4	2.6	1.3
CaO	0.01	0.01	7.4	5.3
Fe_2O_3	0.007	0.005	0.08	0.06
CuO	0.0002	0.0001	0.01	0.01
ZnO	0.005	0.004	0.009	0.007

Table 3 wt. % of elements detected by XRF in H-ZSM-5, presented as the metal oxides detected and converted to Wt. % of element.

Table 4 gives the elemental ratios determined from the XRF analysis. The Si/Al ratios of the samples are shown in Table 4 is lower than the nominal ratio used in the synthesis gel, which was 40, meaning that the zeolite synthesised has a higher aluminium content than intended. However, the calcium content is still high enough to be equivalent to 2.6 calcium ions per aluminium site.

Sample	Si/Al	Ca/Al
H-ZSM-5	31	-
Ca/H-ZSM-5	30	2.6

Table 4 Ratios of elements in the parent and calcium impregnated ZSM-5 samples calculated from the relative proportions of elements.

2.3.2 H-SSZ-13 and Ca-SSZ-13

H-SSZ-13 synthesised with Si/Al ratio 15 was impregnated with 6 % wt. Ca in the same way as previously described. Characterisation data is presented in this section to understand the calcium speciation and location.

Powder X-Ray Diffraction

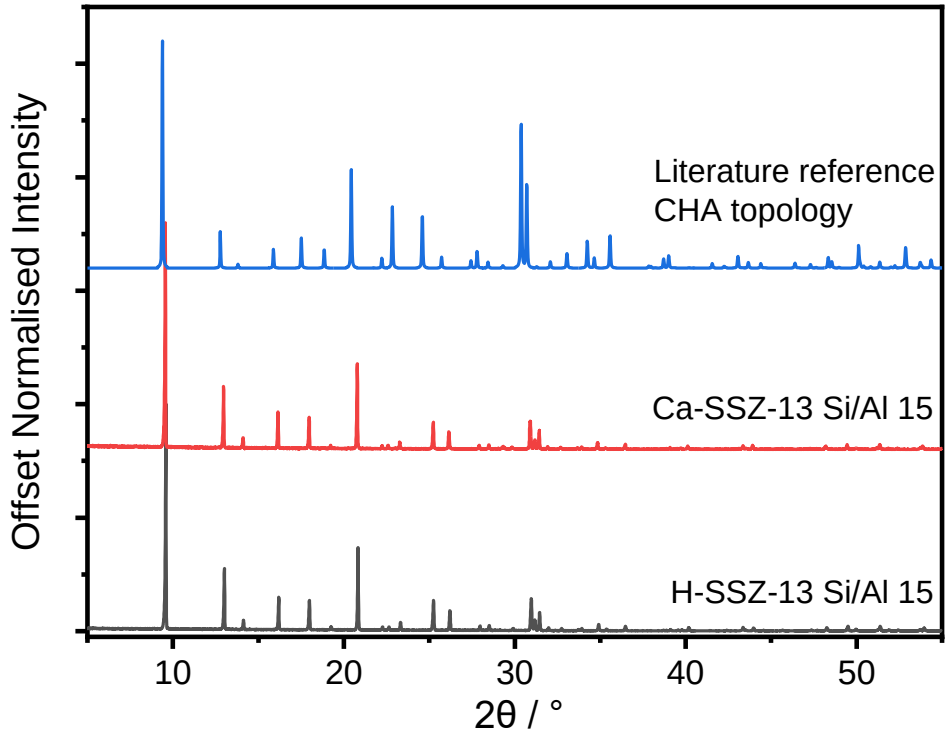

Figure 27 PXRD patterns of H-SSZ-13 with Si/Al 15 as the parent zeolite, and H-SSZ-13 after impregnation with calcium nitrate followed by calcination, and reference pattern for CHA topology.[29]

Figure 27 shows the diffraction patterns of H-SSZ-13 before and after impregnation with calcium, as well as a reference pattern from literature for comparison.[29] All peaks for the CHA topology are present and no extra are found in the PXRD pattern of the parent H-SSZ-13. Figure 28 shows the parent and impregnated SSZ-13 overlaid, with the patterns normalise to the most intense peak at 9.6°. The peaks due to the chabazite topology remain unchanged after

calcium impregnation. A small, new peak after impregnation of calcium at 2θ=29.4° indicates the formation of some $Ca(CO_3)_2$ species.[36]

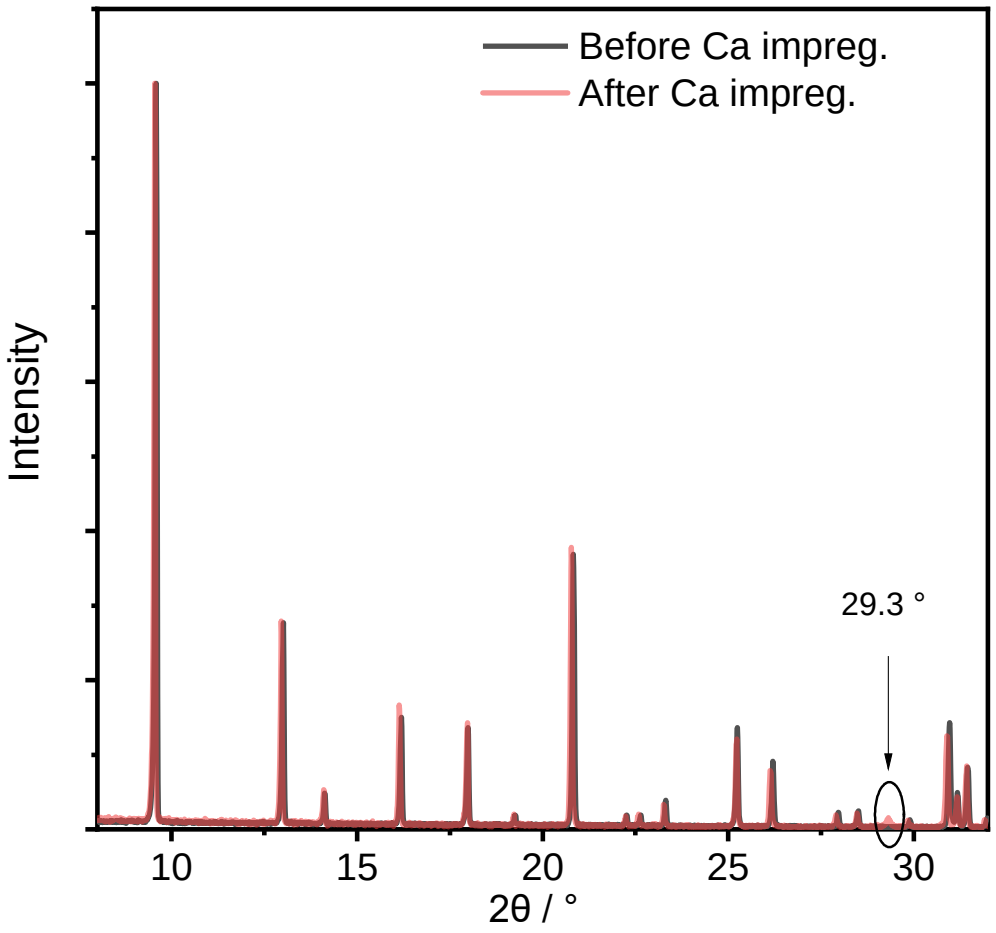

Figure 28 Overlaid diffraction patterns of parent H-SSZ-13 and Ca^{2+} impregnated H-SSZ-13, normalised to the most intense peak at 9.6°.

Kerr-gated Raman Spectroscopy

In Figure 29, Raman spectra are shown of H-SSZ-13 and Ca-SSZ-13. Zeolite vibrations are labelled in grey which are common in both spectra, and the vibration unique to the Ca-SSZ-13 sample, at 1060 cm^{-1} is labelled above its spectrum in black. The zeolite vibrations are assigned to the Si-O bending vibration of the zeolite framework at 479 cm^{-1}, with smaller peaks at 334 cm^{-1} characteristic of pore openings, 805 cm^{-1} due to the T-O-T symmetric stretch and at 1200 cm^{-1} due to the T-O-T asymmetric stretch.[37,38] The new band formed upon calcium impregnation is one at 1060 cm^{-1}. The strong Raman band of

$CaCO_3$ in this region is most likely responsible,[32,33] which also helps to explain the detection of $CaCO_3$ by Raman and earlier by PXRD.

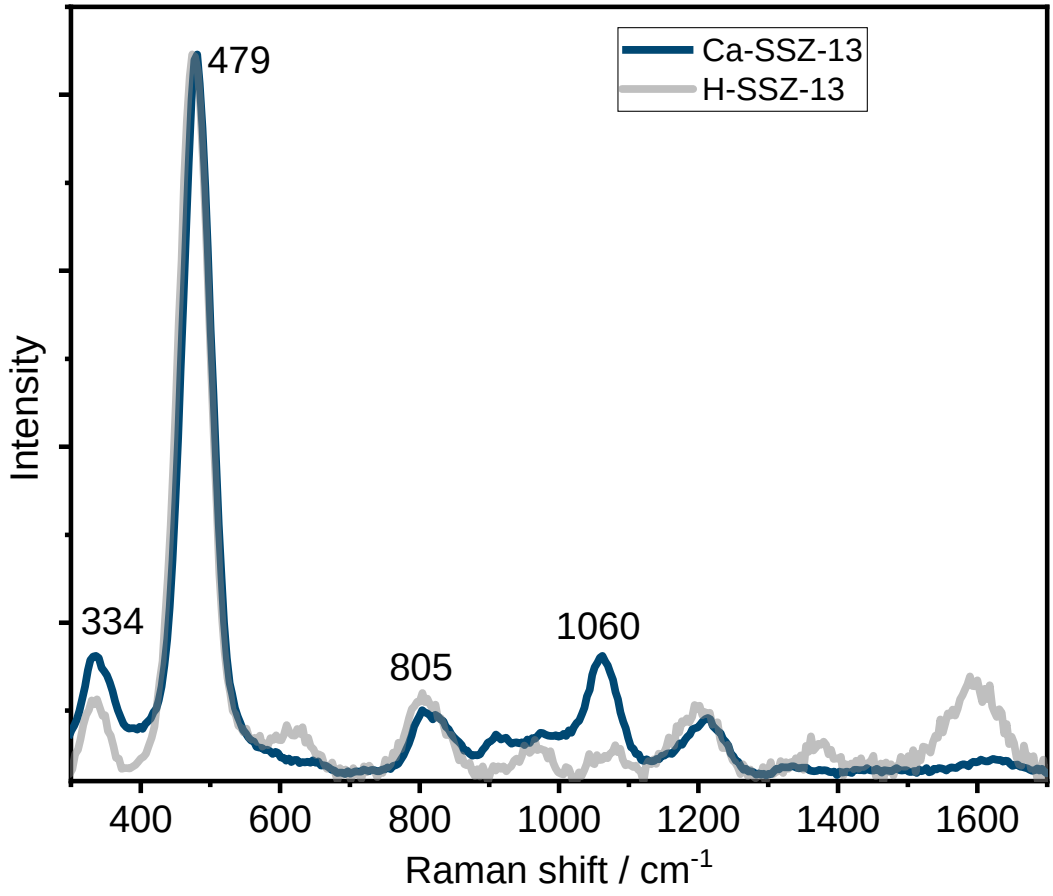

Figure 29 Kerr-gated Raman spectrum acquired of Ca-SSZ-13 in blue, the spectrum of the parent H-SSZ-13 is shown by the grey dotted line underneath. 400 nm probe, 10 mW power, 20 second acquisition, 1200 lines/mm.

Surface area and micropore analysis

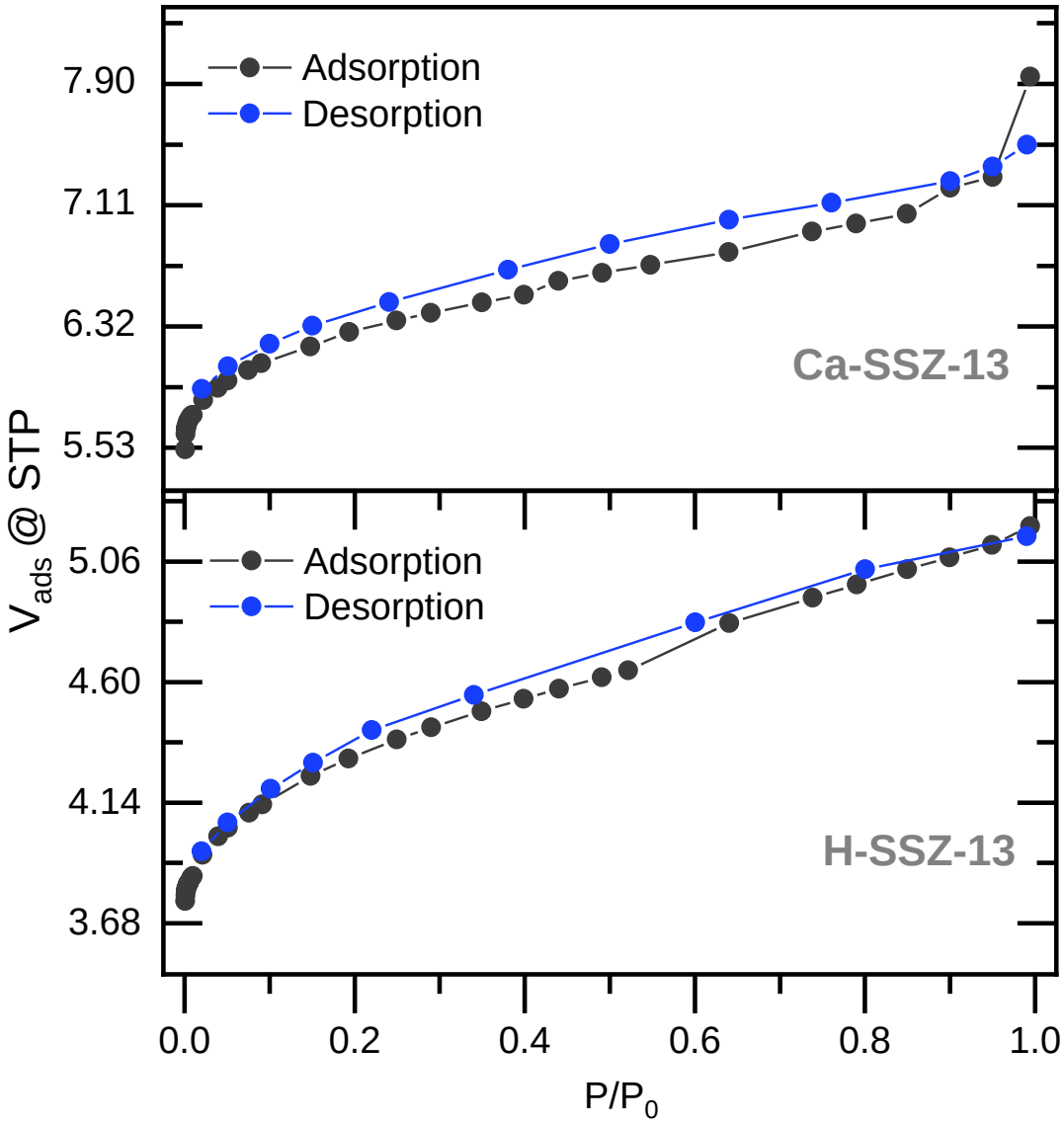

Figure 30 Nitrogen physisorption isotherms collected at 77 K of H-SSZ-13 and Ca impregnated H-SSZ-13.

Figure 30 displays the Nitrogen physisorption isotherms of H-SSZ-13 and Ca-SSZ-13 and the materials' textural properties extracted from the data are summarised in Table 5. The addition of calcium to the zeolite results in significant reductions in surface area and micropore volume. The micropore volume is decreased by 34 %, and the external surface area is also significantly decreased by 40 %, suggesting that some of the calcium species are external to the pore

structure. Calcium carbonate has a low surface area, with calcium carbonate nanoparticles having surface area around 30 – 60 $m^2 g^{-1}$.[39,40]

	Multipoint BET Surface Area / $m^2 g^{-1}$	Micropore volume / cc g^{-1}	Micropore area / $m^2 g^{-1}$	External surface area / $m^2 g^{-1}$
H-SSZ-13	669	0.23	582	86
Ca/H-SSZ-13	444	0.15	392	52
Difference	-34 %	-34 %	-33 %	-40 %

Table 5 A summary of the textural properties of H-SSZ-13 and Ca-SSZ-13 as calculated from the Multipoint BET and t-plot methods.

NH_3-Temperature Programmed Desorption

NH_3-TPD profiles for the parent H-SSZ-13 and impregnated Ca/H-SSZ-13 are shown in Figure 31. The NH_3 desorption trace in H-SSZ-13 contains a low intensity peak at 257 °C and a stronger desorption peak at 491 °C, which indicates that most of the acid sites are strong in this material, requiring high temperatures to desorb NH_3. After impregnation of Ca, the most intense peak is at low temperature at 257 °C with a second, less intense peak at 460 °C. This means that by the addition of calcium, more weak acid sites have been created, and the number of strong acid sites has been reduced. The strong acid sites have not been completely diminished, although the quantity of calcium impregnated should in theory be enough to remove all Brønsted acidity, the PXRD shows some formation of clusters (in the form of $CaCO_3$, reflection at $2\theta=29.4°$) so it is unlikely that the calcium is dispersed well enough to remove all Brønsted acid sites. The higher signal at low temperature is likely a result of the formation of more Lewis acid sites, where ammonia adsorbs at the Ca^{2+} sites.[35]

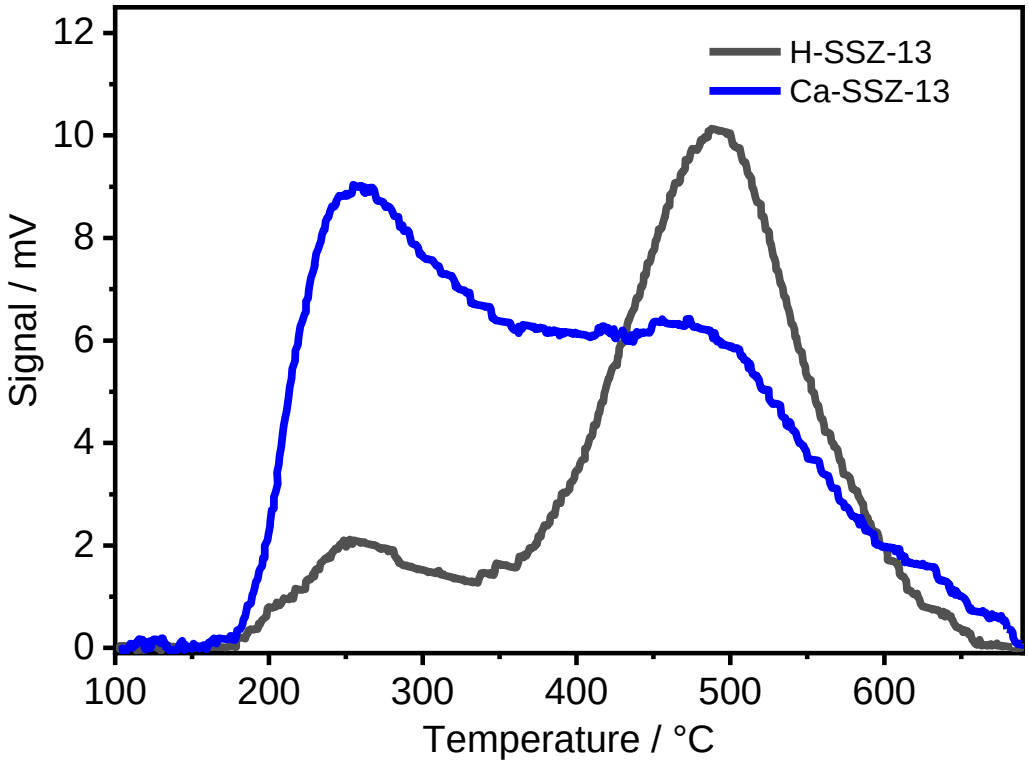

Figure 31 Temperature programmed desorption of ammonia profiles of H-SSZ-13 and Ca/H-SSZ-13 after adsorption of ammonia for 30 min. at 100 °C, flushing for 2 h and a temperature ramp at 10 °C min^{-1} from 100 to 700 °C.

Scanning Emission Microscopy-Energy Dispersive X-rays

The image in Figure 32(a) show particles that are roughly cube shaped, and approximately 7-8 µm in height and width. EDX maps of three Ca-SSZ-13 crystals are shown in Figure 32 highlighting the regions where X-rays characteristic of calcium and silicon are detected. While Si and Al appear to be distributed across the particles, the Ca signals appear brighter around the edges of the crystals and therefore calcium is not as well distributed as in Ca-ZSM-5.

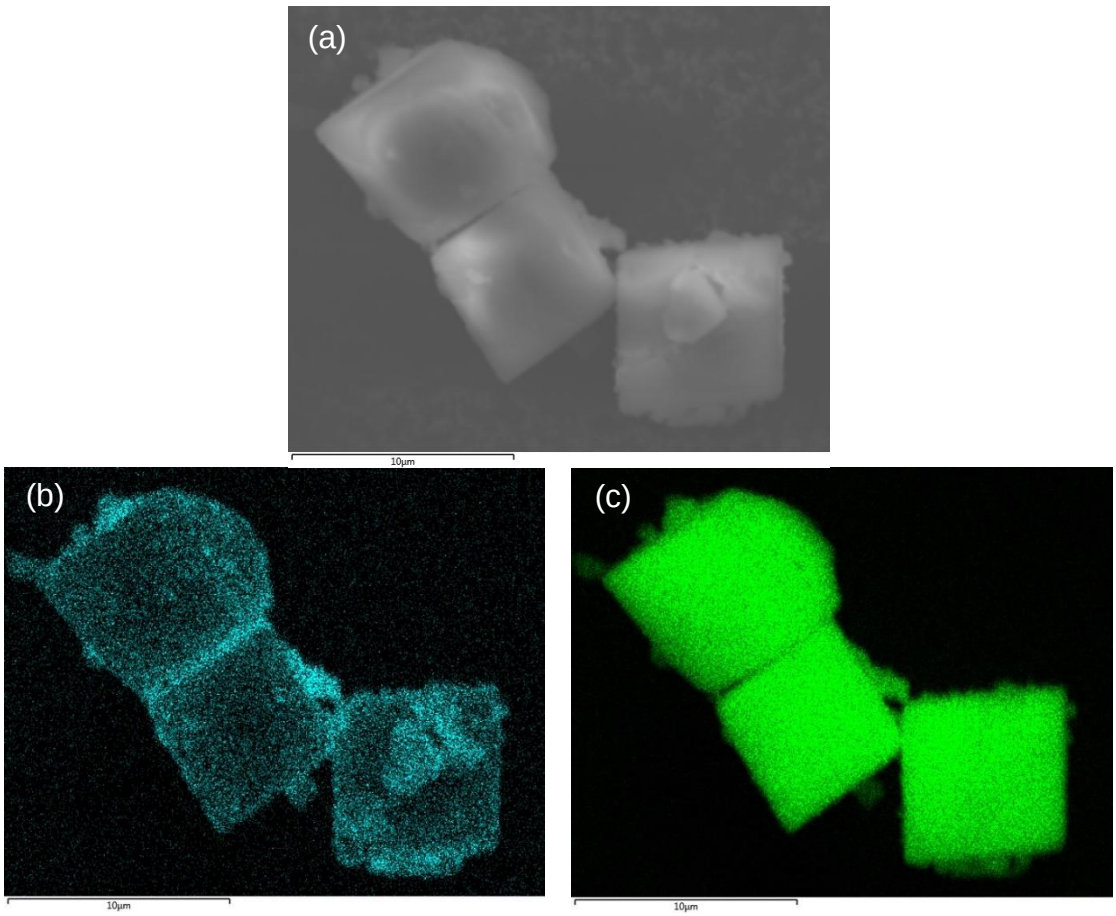

Figure 32 (a) SEM image of three Ca-SSZ-13 particles and EDX data acquired in the same position on (b) Ca and (c) Si to show Ca incorporation into the zeolite.

The mapped region was also analysed by a line-scan, which plots the counts of elements detected over the region labelled Line Data 1 in Figure 33 (a). The plotted results of the line-scan are shown in Figure 33 (b), and again show the higher presence of calcium on the edges of the crystals, which indicates a high concentration on the outsides of the particles.

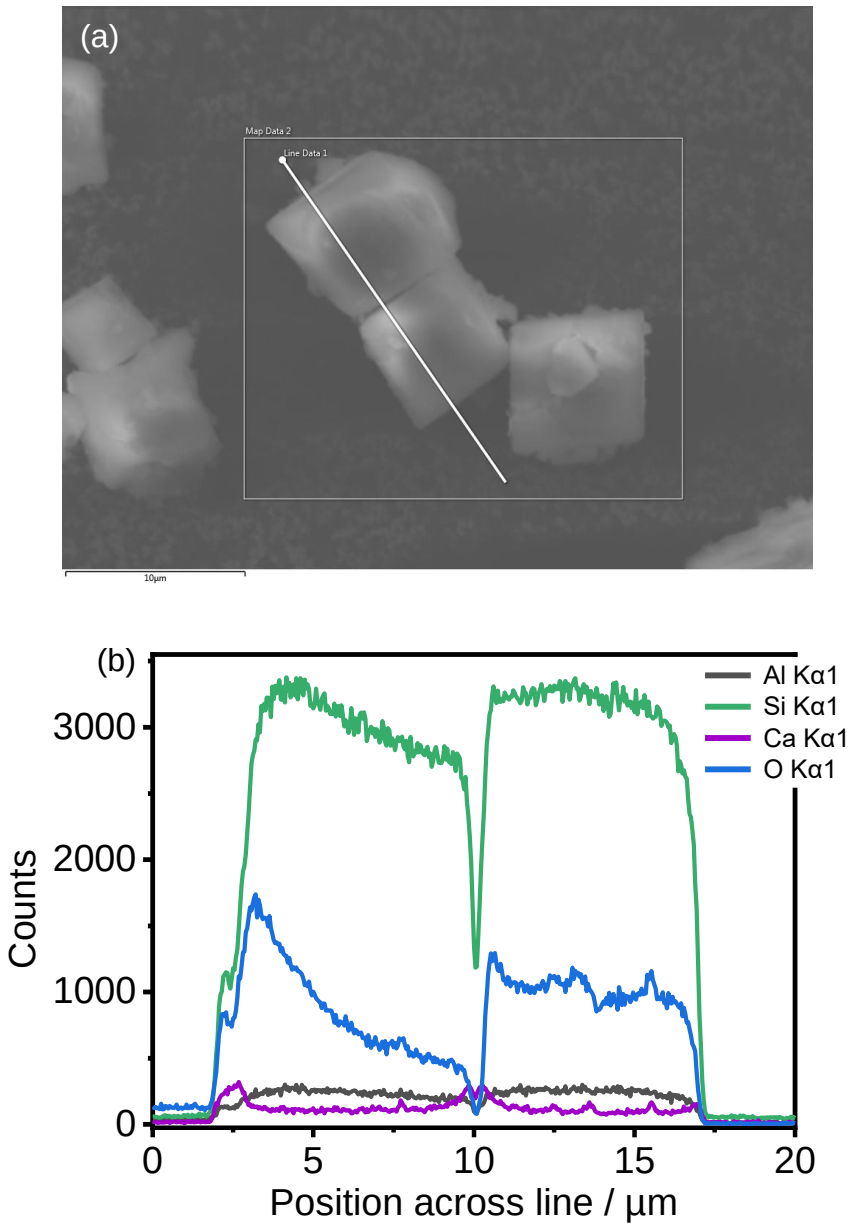

Figure 33 (a) SEM image indicating the region where a map and line map was followed for elemental analysis and (b) the plotted results of counts detected for each element with distance along the line.

In Figure 34, SEM-EDX images are shown of one particle, and again show an even distribution of Al and Si, and preferential sitting for Ca at the crystal edges. This might be due to the smaller pore-openings (at 3.7 x 3.7 Å compared with ZSM-5/MFI topology at 5.3 x 5.6 Å) which makes it more difficult for calcium to be deposited into the pore structure, although calcium is not solely found along the edges, and the loss of much of the strong acidity of the zeolite observed by NH_3-TPD and decreased micropore volume observed through nitrogen physisorption does confirm that some calcium has entered the pores. The

significantly larger particle size will also make it more difficult to realise calcium dispersion inside the particles (diffusion limitations).

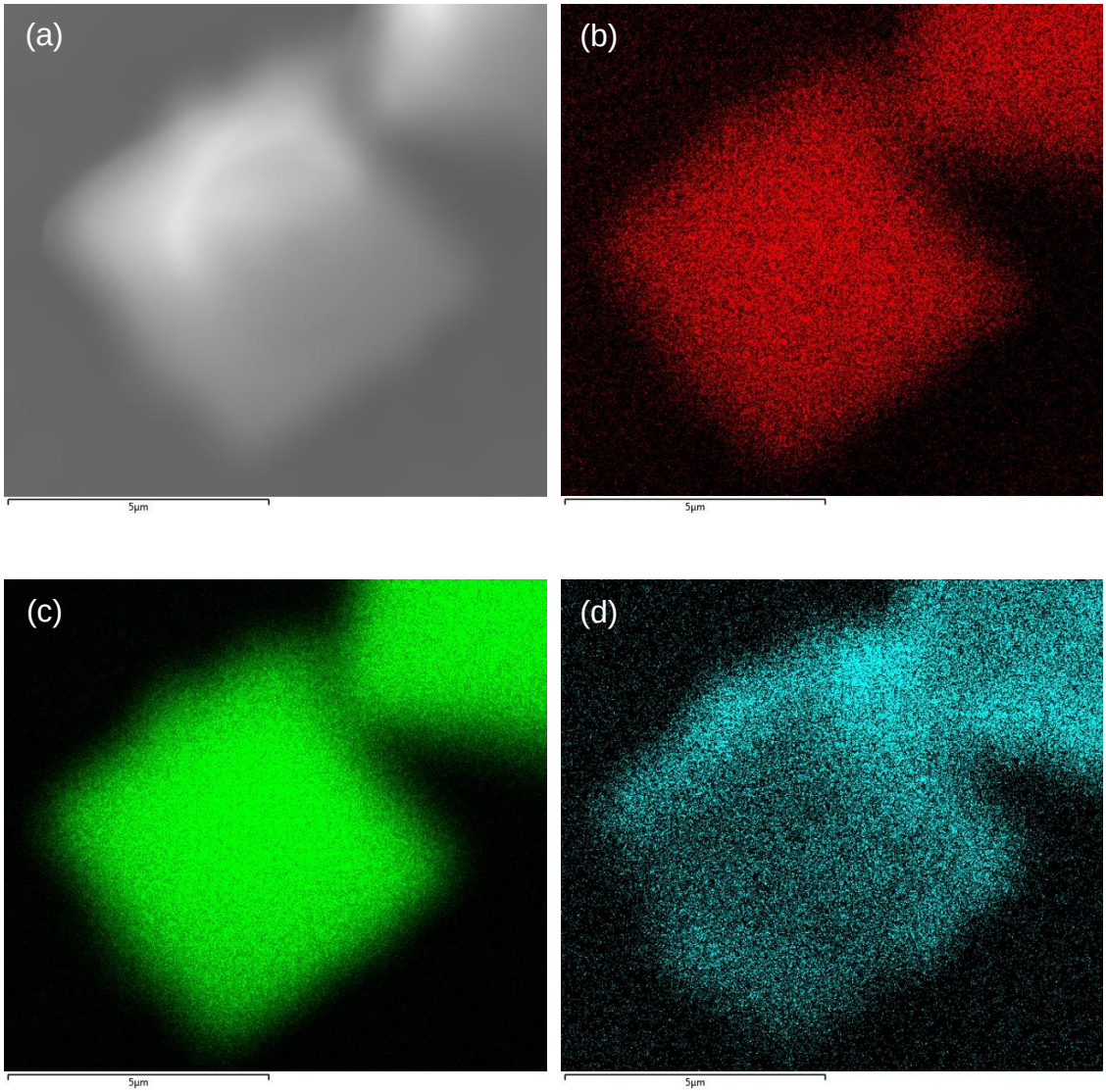

Figure 34 SEM-EDX images of a Ca-SSZ-13 particle (a) SEM image and EDX maps of (b) Al distribution (c) Si distribution (d) Ca distribution.

X-Ray Fluorescence

XRF was used as an alternative method to determine elemental compositions of the bulk samples. The recorded weight % of the elements as oxides and the equivalent weight % of the elements are shown in Table 6, while Table 7 gives the molar ratios of Si/Al and Ca/Al. Si/Al ratio of the zeolite according to XRF was 14.

	H-SSZ-13		Ca-SSZ-13	
Oxide	wt. % as oxide	wt. % as element	wt. % as oxide	wt. % as element
SiO_2	94.3	44.1	87.7	41.0
Al_2O_3	5.7	3.0	5.5	2.9
CaO	0.001	0.07	6.8	4.9
Fe_2O_3	0.001	0.07	0.001	0.04
CuO	0.002	0.10	0.002	0.10
ZnO	0.001	0.06	0.001	0.06

Table 6 wt. % of elements detected by XRF in H-SSZ-13 and Ca-SSZ-13, presented as the metal oxides detected and converted to Wt. % of element.

The ratio of calcium to aluminium (and therefore calcium to Brønsted acid sites in H-SSZ-13) is 1.1. Theoretically, if sufficiently dispersed, one Ca^{2+} could compensate for the negative charge of the placement of two Al atoms in the framework, and a 1:1 ratio should be enough to remove all Brønsted acidity. The results of Yarulina *et al.* show that 2 Ca^{2+} are needed per acid site to remove all Brønsted acidity,[35] which is less than our ratio.

Sample	Si/Al	Ca/Al
H-SSZ-13	14	-
Ca/H-SSZ-13	14	1.1

Table 7 Ratios of elements in the parent and calcium impregnated ZSM-5 samples calculated from the relative proportions of elements.

2.3.3 H-SAPO-34

This material was used to study the conversion of methanol in Chapters 3 and 6. It is a helpful material as a means of comparison with H-SSZ-13 as a catalyst having an analogous structure but different acidic properties. Silicoaluminophosphate (SAPO) materials consist of lattices of P^{5+} and Al^{3+} connected by bridging oxygen atoms whereby substitution by Si^{4+} species induce

a negative charge in the framework that can be compensated by a proton to yield Brønsted acid sites.[41,42]

Powder X-Ray Diffraction

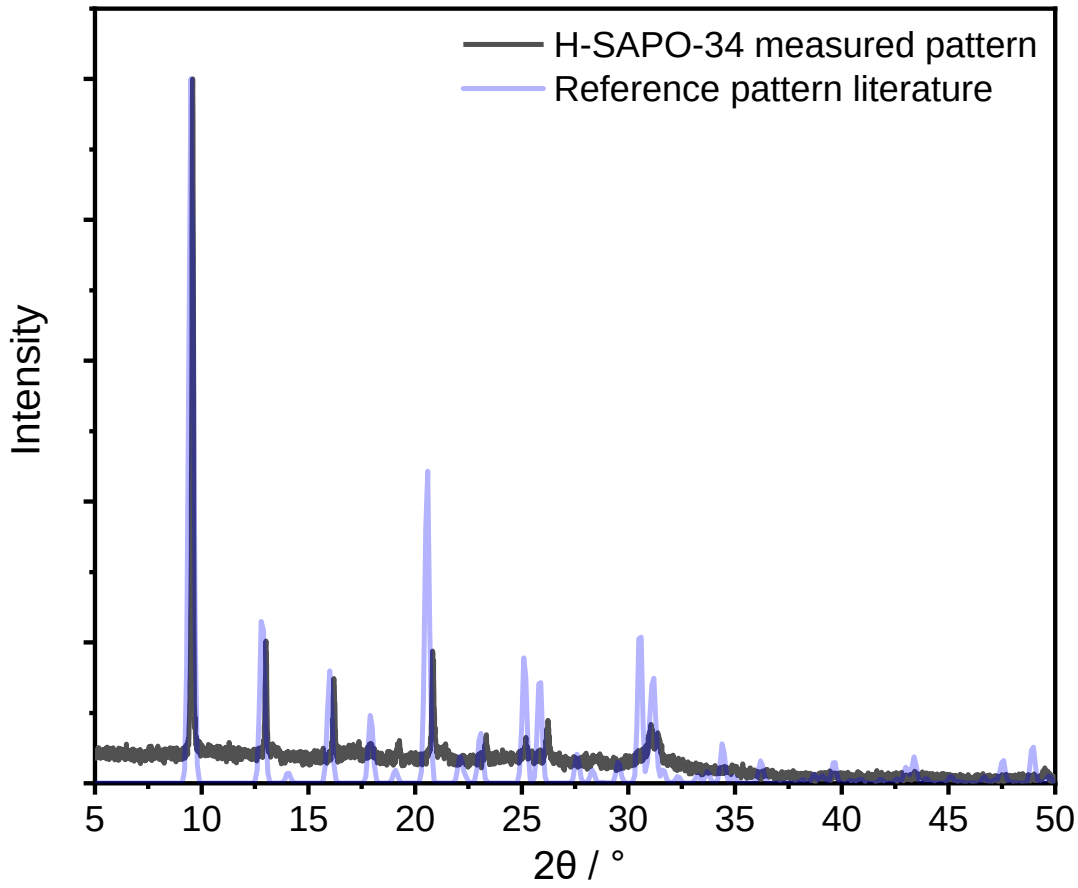

Figure 35 PXRD pattern of H-SAPO-34 purchased from ACS Materials compared with a powder pattern from ref [43].

The PXRD pattern shown in Figure 35 confirms the chabazite crystal structure of our H-SAPO-34 material purchased from ACS Materials.[43]

Kerr-gated Raman Spectroscopy

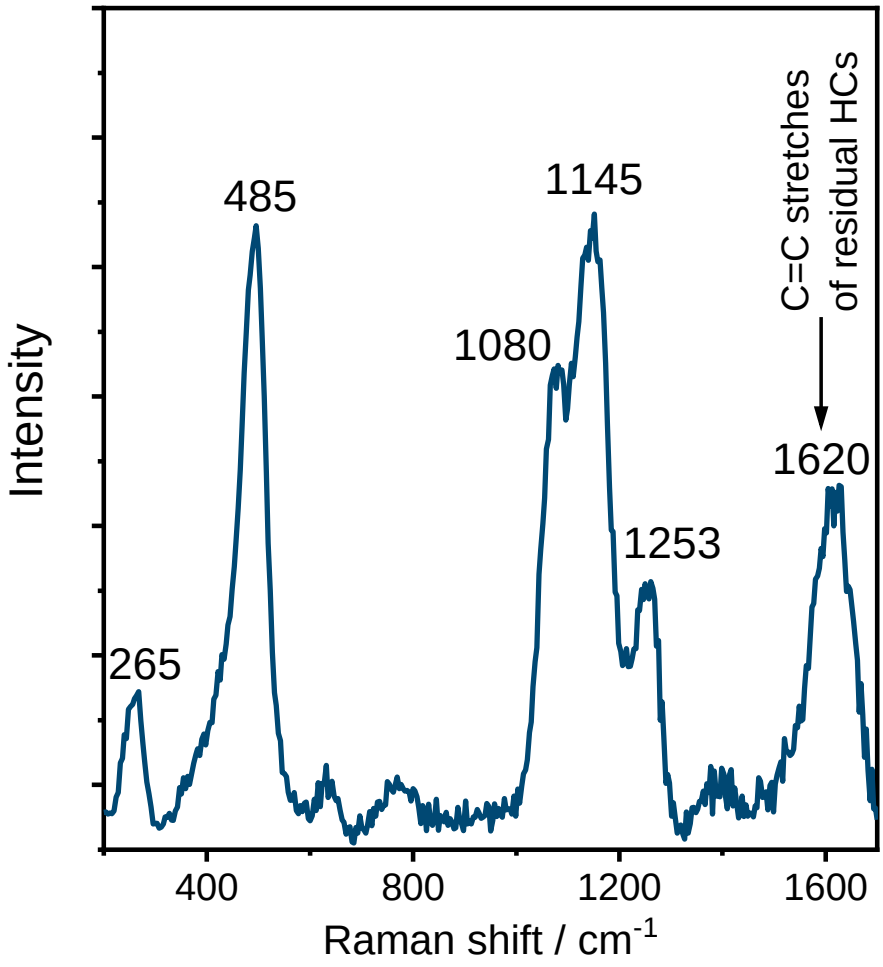

Figure 36 Kerr-gated Raman spectrum of H-SAPO-34. 400 nm probe, 10 mW power, 20 second acquisition, 1200 lines/mm.

Figure 36 shows the Kerr-gated Raman spectrum of H-SAPO-34 after calcination. The vibration at 1620 cm^{-1} is due to the C=C stretches of unburnt hydrocarbons on the surface. The band at 485 cm^{-1} corresponds to the T-O-T symmetric stretch at pore openings in chabazite, while bands at 1080 – 1253 cm^{-1} correspond to P-O-P and P-O-Al stretches in SAPO-34.[44]

Surface area and micropore analysis

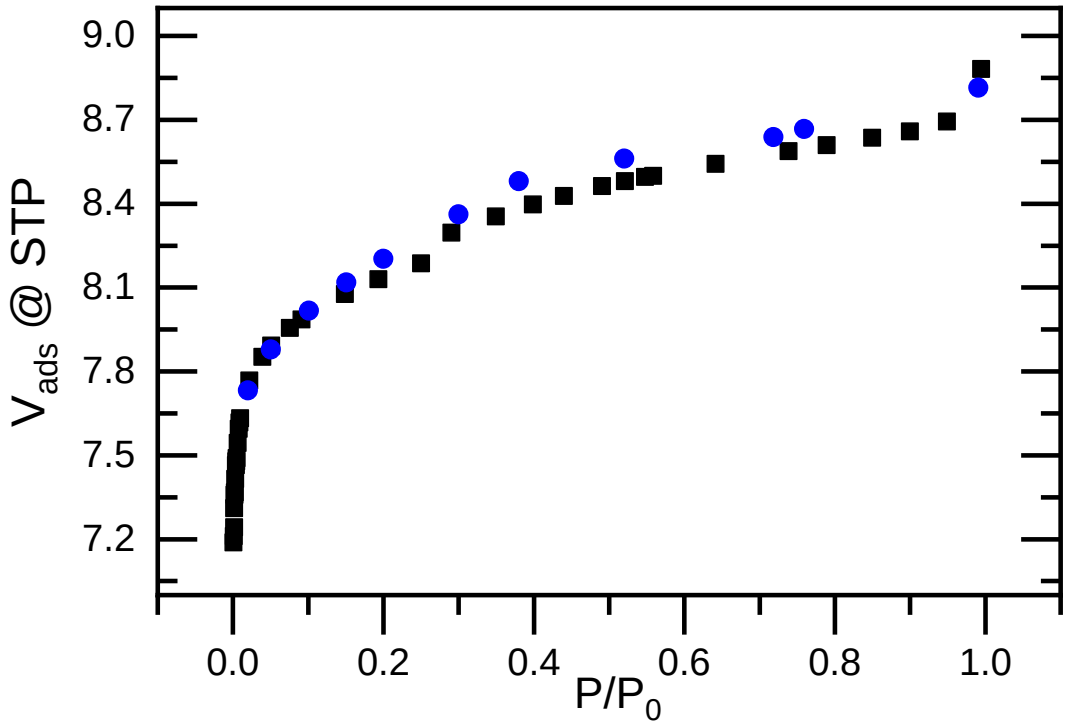

Figure 37 Nitrogen physisorption isotherms collected at 77 K of H-SAPO-34.

Figure 37 shows the nitrogen adsorption isotherm of the H-SAPO-34 material and Table 8 summarises the analysis of the surface area and micropores. The vertical increase in the volume of nitrogen adsorbed at low relative pressures <0.01 confirms the filling of micropores.

	Multipoint BET Surface Area / $m^2\ g^{-1}$	Micropore volume / cc g^{-1}	Micropore area / $m^2\ g^{-1}$	External surface area / $m^2\ g^{-1}$
H-SAPO-34	569	0.24	522	47

Table 8 A summary of the textural properties of H-SAPO-34 purchased from ACS Materials, calculated from the Multipoint BET and t-plot methods.

NH_3-Temperature Programmed Desorption

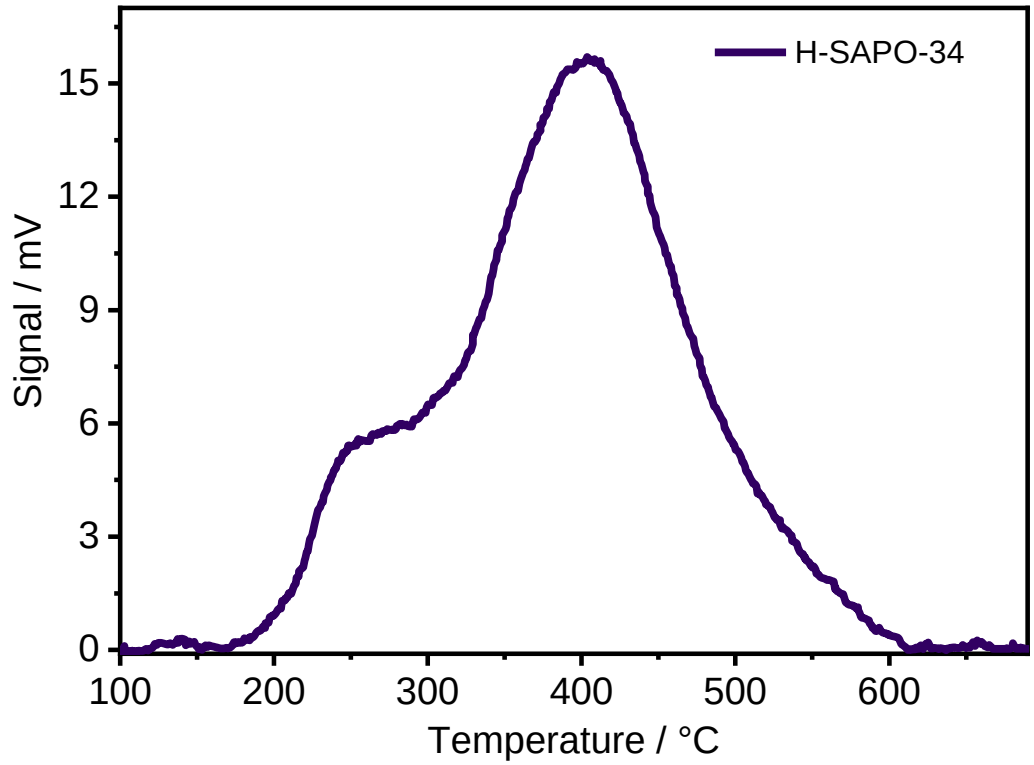

Figure 38 Temperature programmed desorption of ammonia profiles of H-SAPO-34 after adsorption of ammonia for 30 min. at 100 °C, flushing for 2 h and a temperature ramp at 10 °C min-1 from 100 to 700 °C.

Figure 38 shows that this material, akin to the aluminosilicate chabazite contains acid sites of two strengths, indicated by the desorption temperatures at ~250 °C and 405 °C. The NH_3 desorption at high temperature occurs at 86 °C lower than in the H-SSZ-13 material in line with the weaker Brønsted acidity in silicoaluminophosphate (SAPO) materials compared with their silicoaluminate counterparts.[41]

Scanning Emission Microscopy

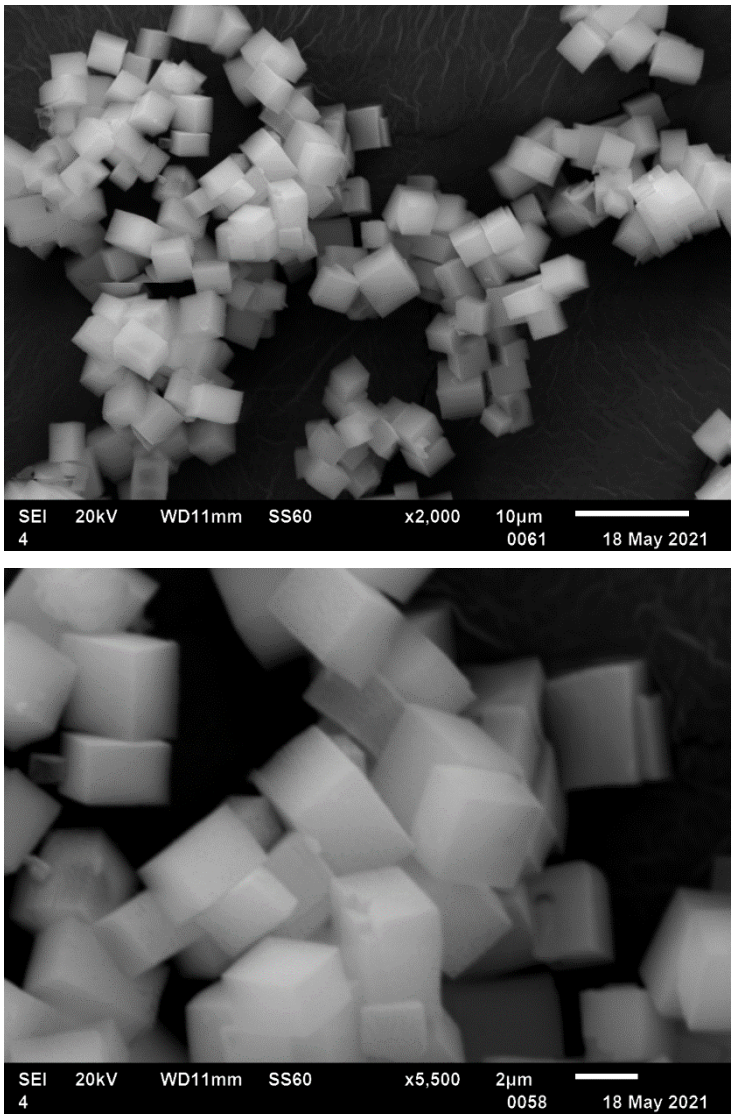

Figure 39 SEM images of H-SAPO-34 material from ACS Materials.

The SEM images of H-SAPO-34 shown in Figure 39 reveal the regular, rectangular cuboid crystals of 4 x 3 x 3 µm. The crystal shapes and sizes are smaller but comparable with those of the SSZ-13 materials in Figure 32.

2.3.4 ZSM-5 (Si/Al = 15)

ZSM-5 synthesised with a Si/Al ratio 15 according to section 2.2.1 was used in its proton form in Chapters 4 and 5 for the reaction furan and other model compounds in a modelled Catalytic Fast Pyrolysis reaction.

Powder X-Ray Diffraction

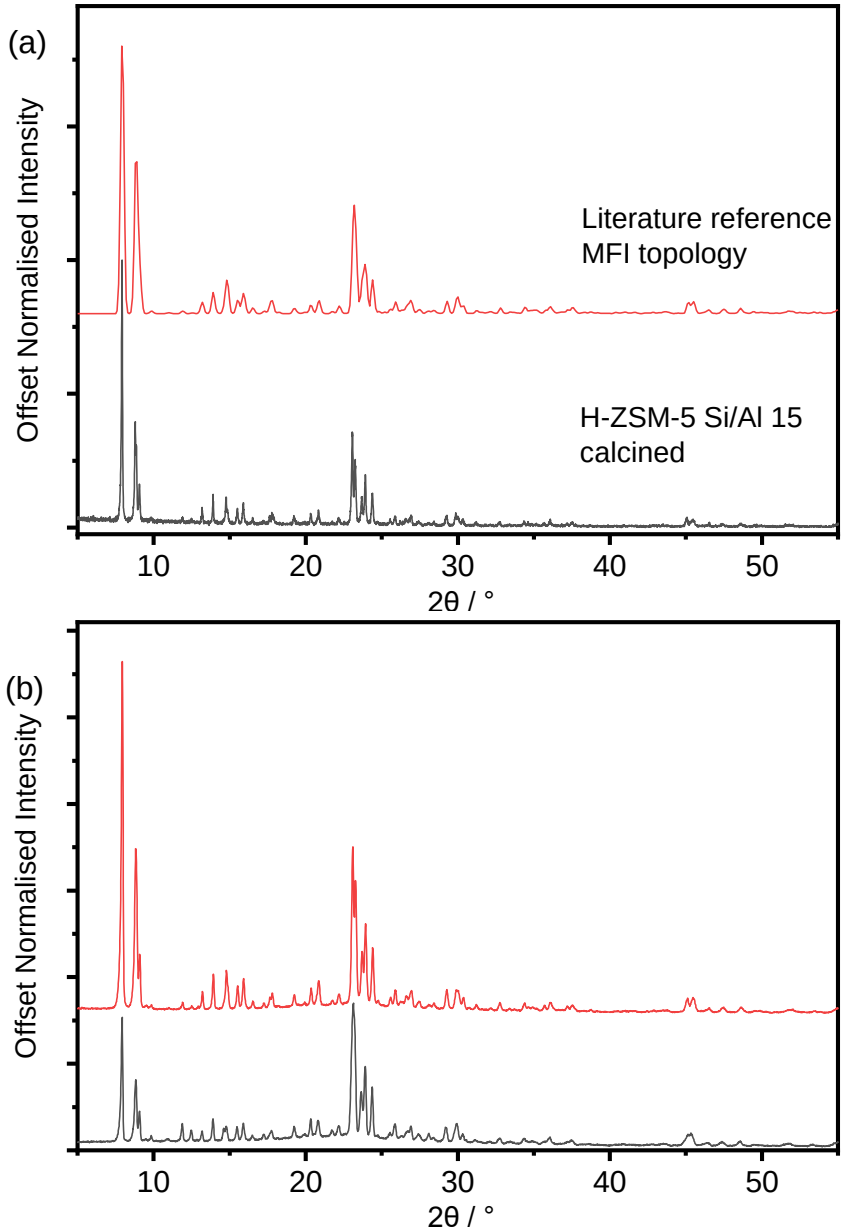

Figure 40 (a) PXRD pattern of ZSM-5 synthesised with Si/Al ratio of 15, after calcination to remove organic template and ion-exchange plotted with a literature reference from ref 29 (b) PXRD patterns before and after calcination to remove organic template collected on a Stoe Stadi P diffractometer in transmission geometry.

The PXRD pattern in Figure 40 confirm the MFI topology of the synthesised zeolite. In Figure 40b, the PXRD patterns before and after calcination are plotted, which are normalised to the reflection at 2θ=23.1°, showing a relative increase of reflections at low angle that is typical of moving from full to empty channels. The patterns in Figure 40b were collected on a different diffractometer (Stoe Stadi P) in transmission geometry and the backgrounds on the patterns are due to the silica-based grease used to hold the thin layer of powder in place in the goniometers, this was confirmed in Figure 40a when the measurement of the calcined zeolite was repeated in Bragg-Montano reflection geometry on the Rikagu SmartLab diffractometer.

Surface area and micropore analysis

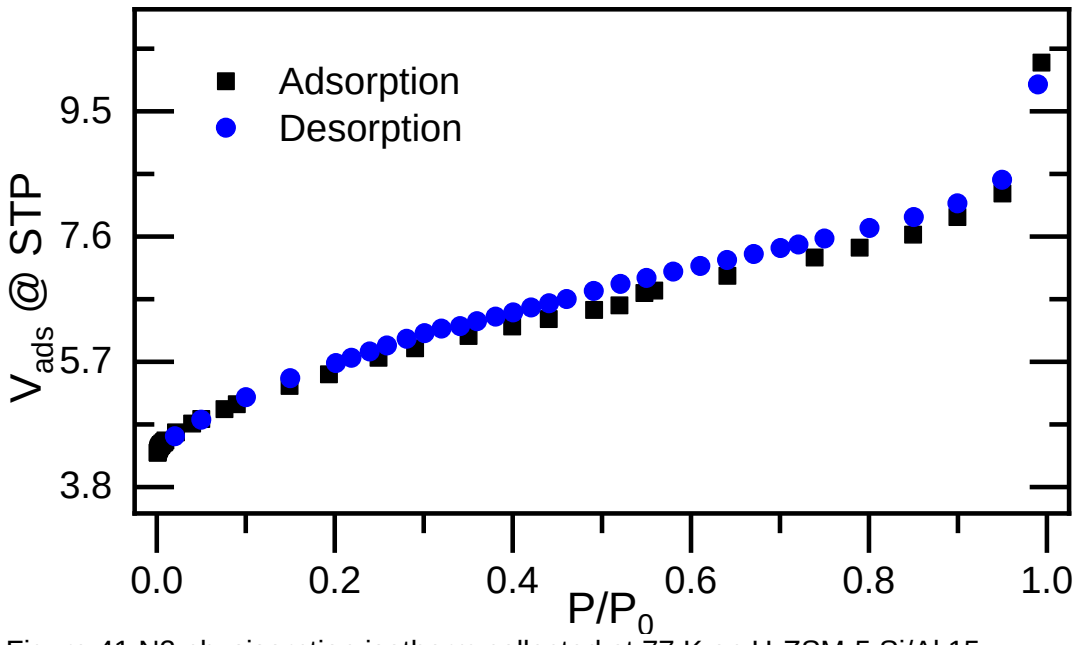

Figure 41 N2 physisorption isotherm collected at 77 K on H-ZSM-5 Si/Al 15.

The isotherm in Figure 41 indicates pore filling in the low-pressure region and an absence of mesopores by the desorption branch which closely follows the adsorption branch. Surface area and micropore properties are given in Table 9.

	Multipoint BET Surface Area / $m^2\ g^{-1}$	Micropore volume / cc g^{-1}	Micropore area / $m^2\ g^{-1}$	External surface area / $m^2\ g^{-1}$
H-ZSM-5	347	0.11	239	108

Table 9 Surface area and micropore properties determined from N2 physisorption isotherm.

NH_3-Temperature Programmed Desorption

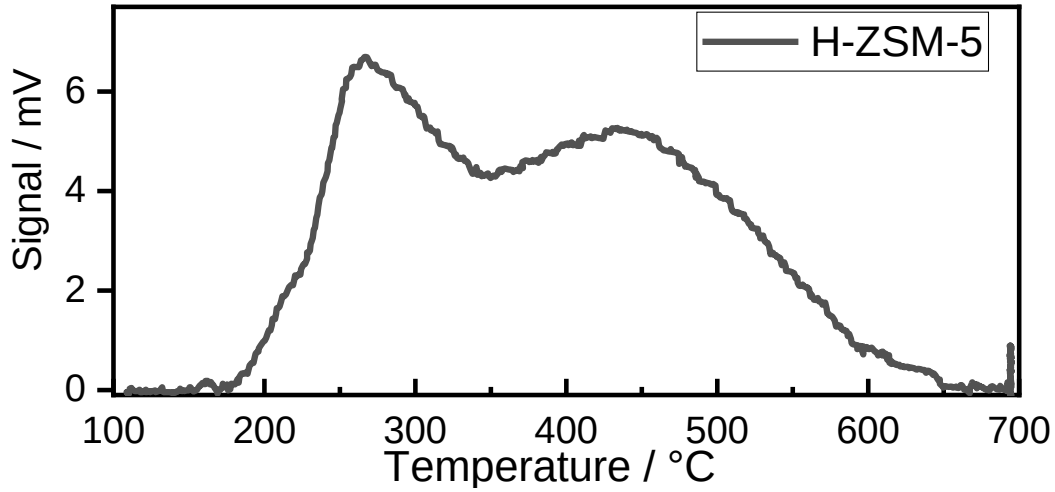

Figure 42 NH_3-TPD curve of ammonia on H-ZSM-5 synthesised with Si/Al 15.

The zeolite shows two peaks for ammonia desorption, at 265 and 440 °C relating to weak and strong acid sites, respectively.

Scanning Emission Microscopy

The SEM images in Figure 43 are poorly resolved but show clusters of particles that are approximately 300 – 500 nm in length. Due to the poor resolution and small crystal sizes, it is difficult to clearly see the crystal morphology.

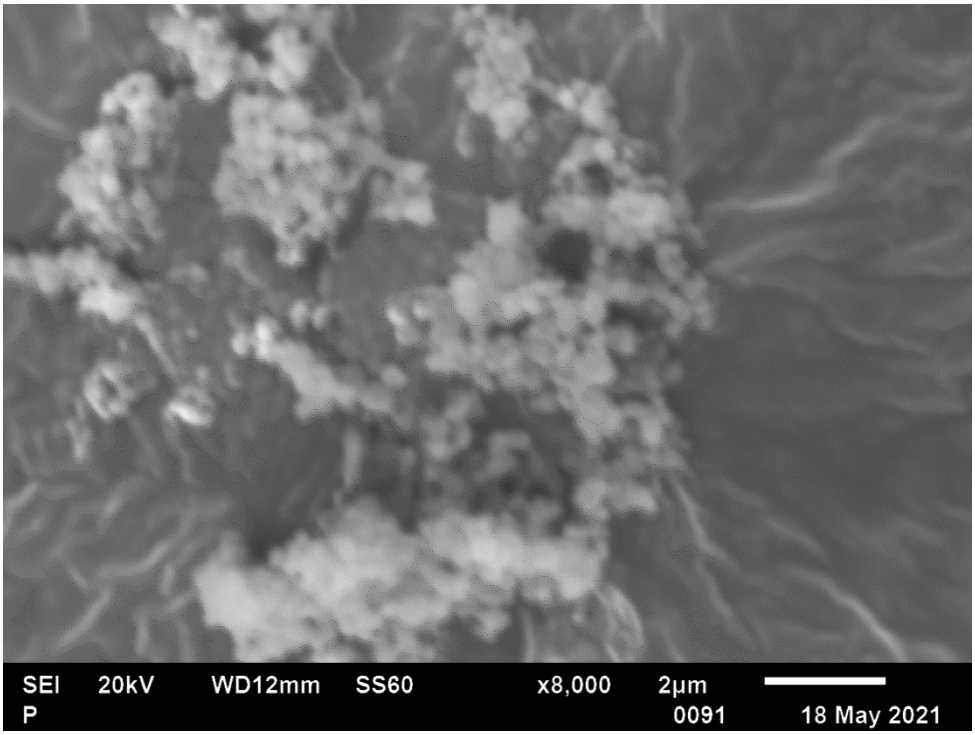

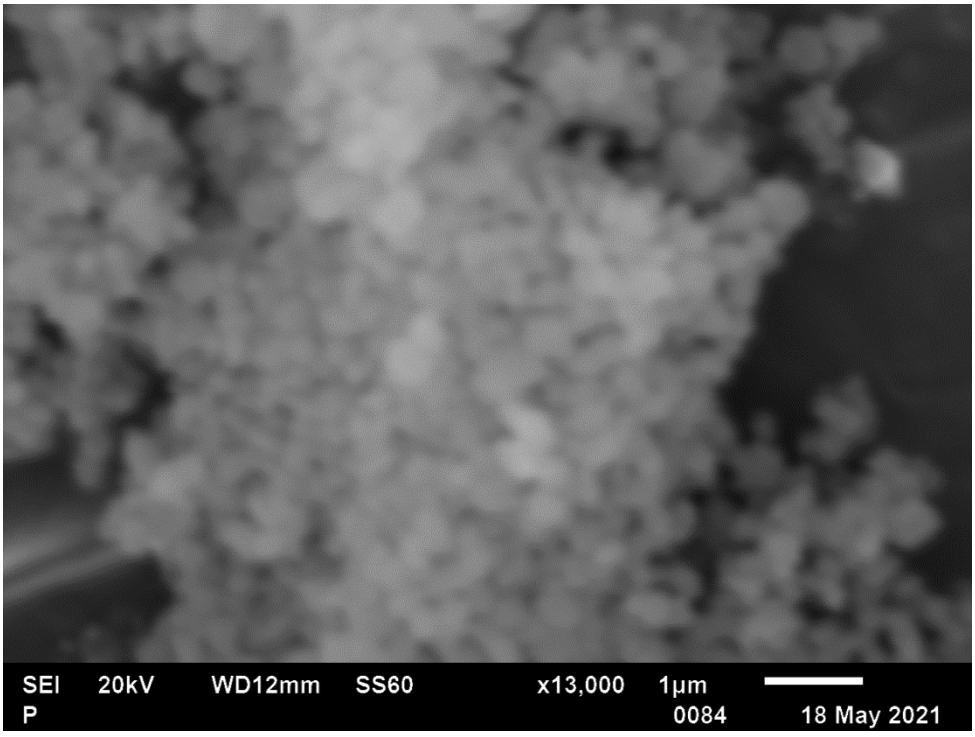

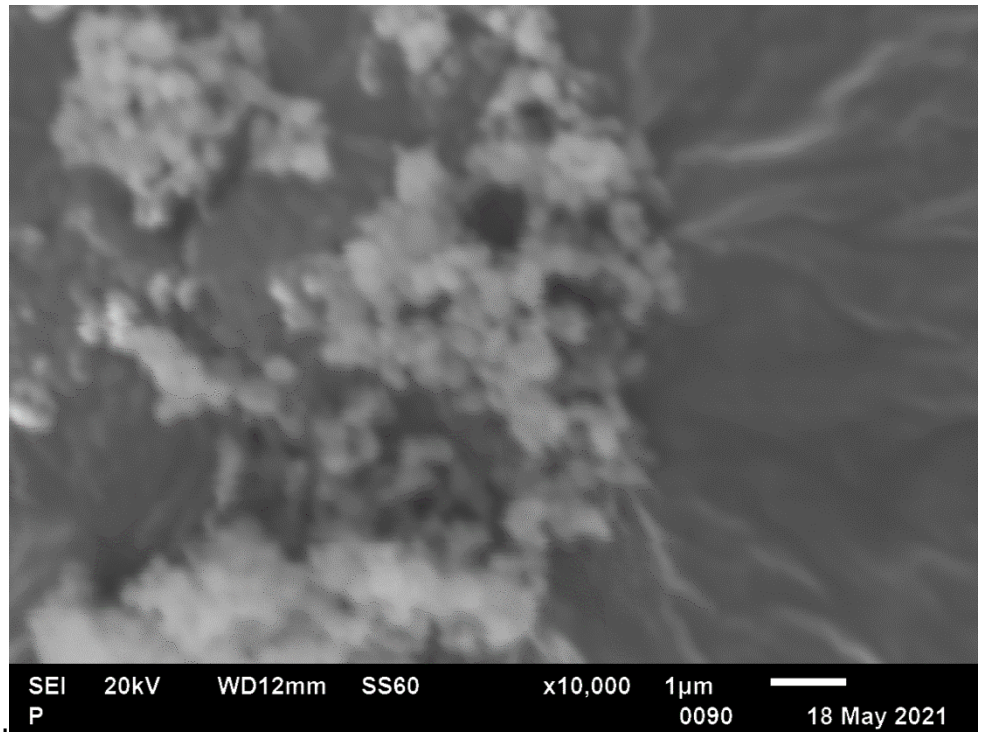

Figure 43 SEM images captures of H-ZSM-5 Si/Al 15 at 13,000, 10,000 and 8,000 x magnification.

X-Ray Fluorescence

Oxide/element	*wt. % as oxide*	*wt. % as element*
SiO_2	94.0	43.9
Al_2O_3	5.6	3.0
K_2O	0.4	0.3

Table 10 wt. % of elements detected by XRF in H-ZSM-5, presented as the metal oxides detected and converted to Wt. % of element.

XRF reveals a Si/Al molar ratio of 14.3. The data indicates some K is present as a contaminant but at very low concentrations.

2.3.5 Ferrierite, Beta and Zeolite Y from Zeolyst Int.

Surface area and micropore analysis

	Multipoint BET Surface Area / $m^2\ g^{-1}$	Micropore volume / cc g^{-1}	Micropore area / $m^2\ g^{-1}$	External surface area / $m^2\ g^{-1}$
H-ferrierite	360	0.12	308	53
H-beta	343	0.11	264	80
H-Y	745	0.25	611	134

Table 11 A summary of the textural properties of H-ZSM-5 synthesised, and ferrierite, beta and Y from Zeolyst Int., calculated from the Multipoint BET and t-plot methods.

NH_3-Temperature Programmed Desorption

	T_1 / °C	T_2 / °C
H-ferrierite	241	478
H-beta	249	429
H-Y	223	378

Table 12 A summary of the high and low temperature NH_3 desorption curves in H-ferrierite, H-beta and H-Y from Zeolyst Int.

The high temperature desorption peak is related to the acid sites of highest strength in the materials and has been shown to vary according to zeolite topology, with typically acid sites in smaller pores being stronger due to the stabilisation effect of the framework on its negative charge. This effect is shown in these results.

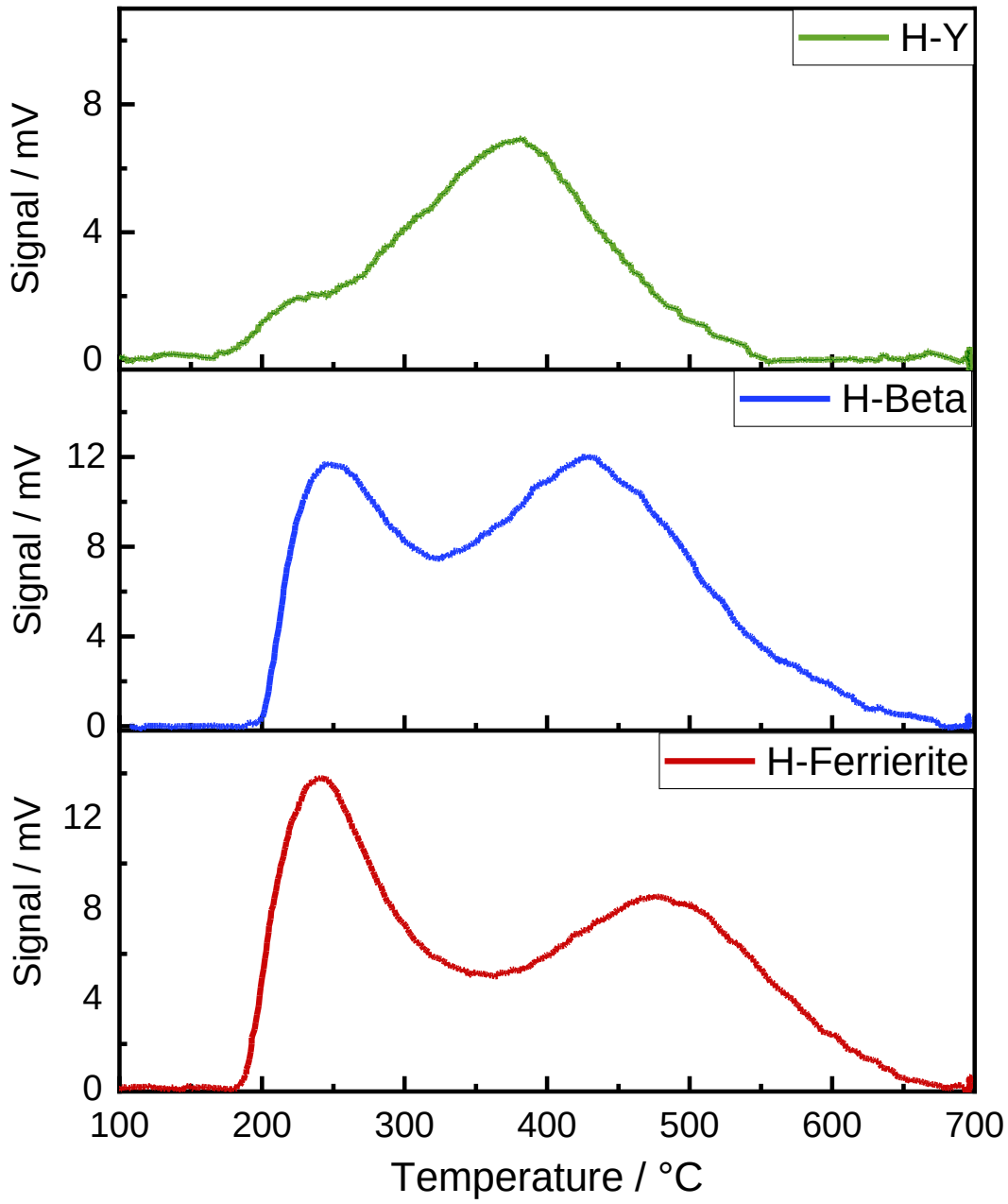

Figure 44 NH_3-TPD curves of H-ferrierite, H-beta and H-Y from Zeolyst Int.

Scanning Emission Microscopy

SEM was used in this case to see and compare rough particle/crystal size and morphology between the zeolites used in Chapter 4.

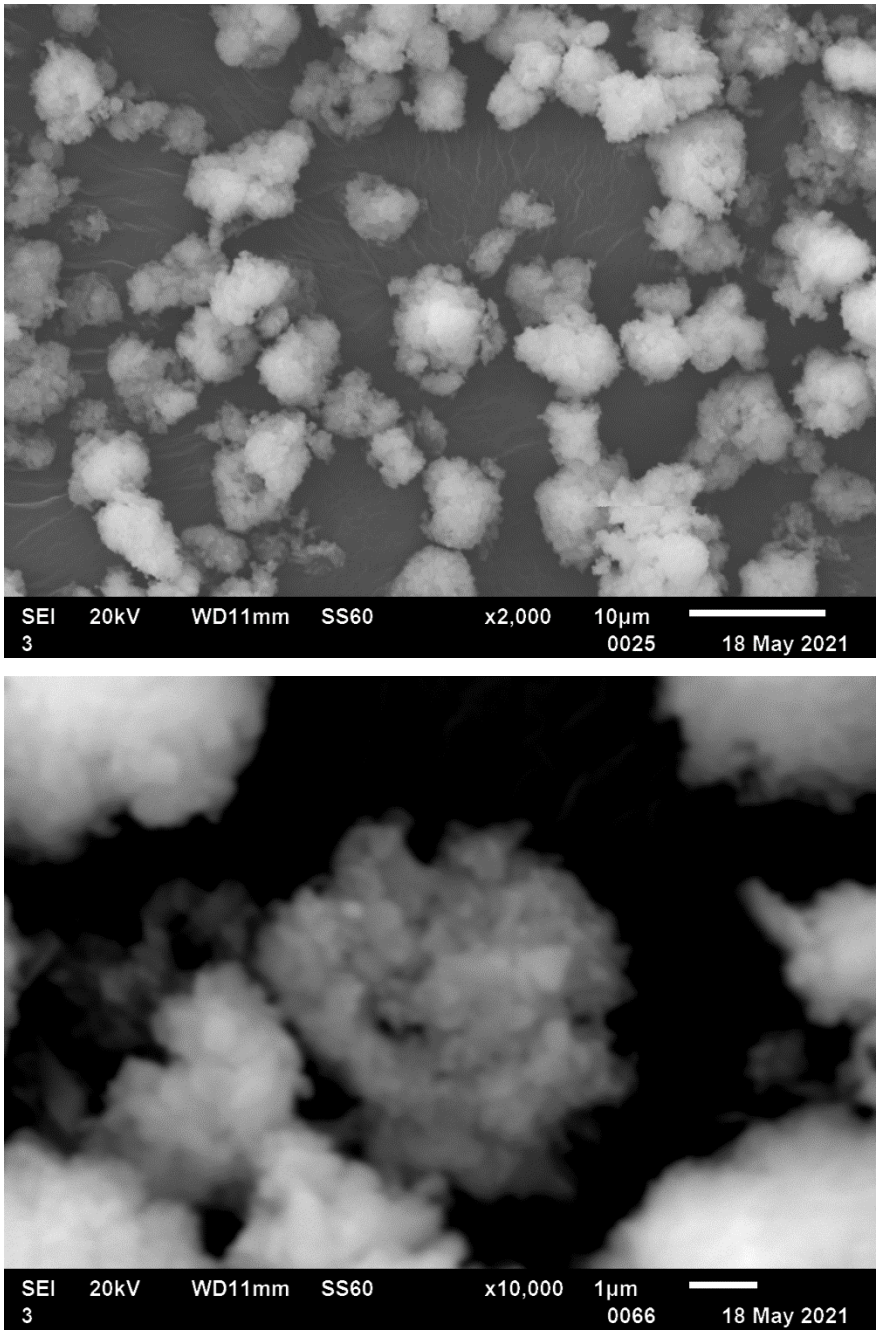

Figure 45 SEM image captures of H-ferrierite at a magnification of 2,000 and 10,000.

The image at a magnification of 2,000 in Figure 45 reveals aggregates of particles of H-ferrierite. Although the resolution is poor, at 10,000 times magnification it is possible to see that the particles consist of smaller crystals that are < 200 nm in size.

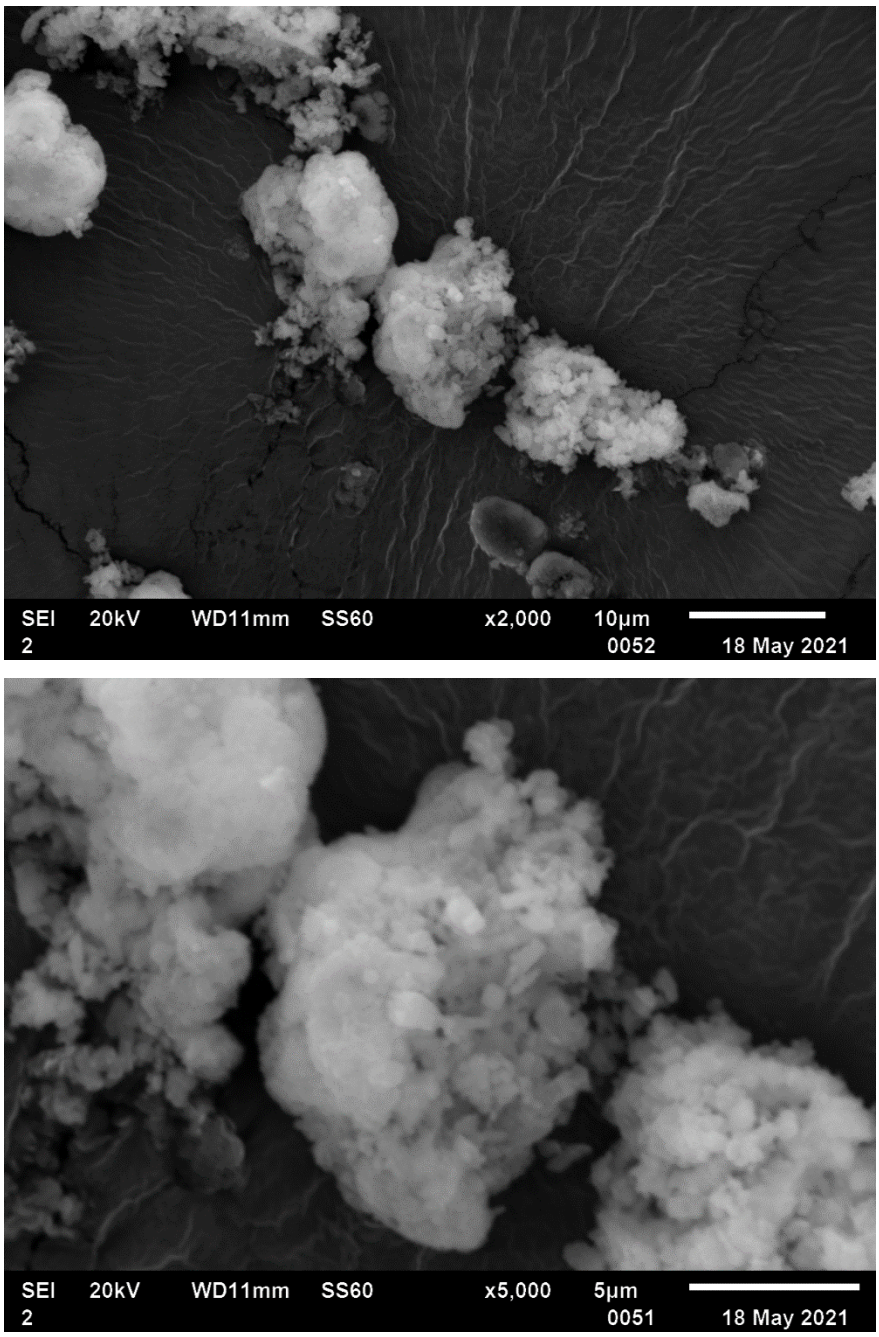

Figure 46 SEM image captures of H-beta at a magnification of 2,000 and 5,000.

The H-beta sample also consists of aggregates of smaller particles, which in Figure 46 are approximately 700 – 900 nm in size.

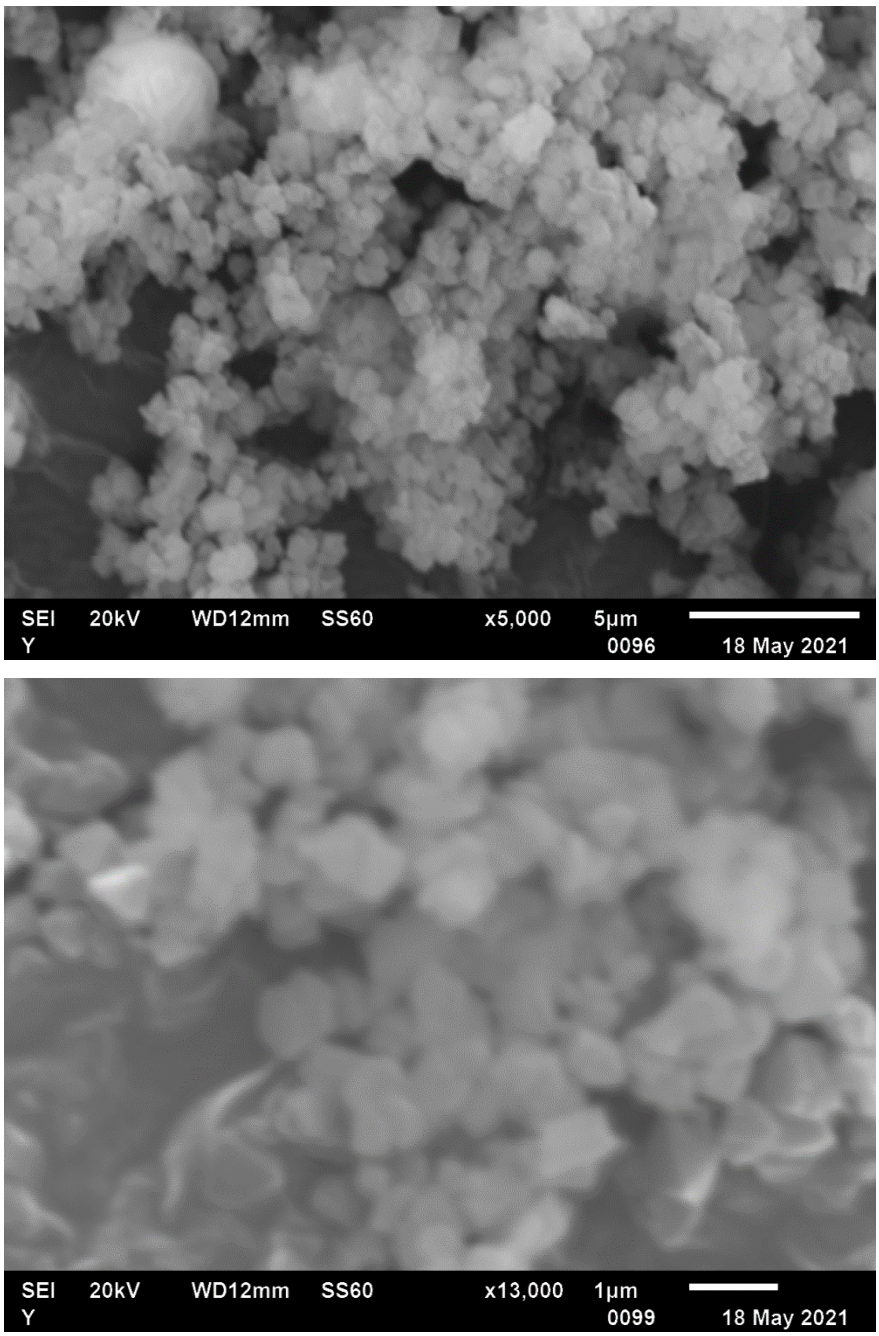

Figure 47 SEM images captures of H-Y Si/Al 15 at 5,000, 13,000 x magnification.

The images in Figure 47 show that particles of H-Y have rounded cuboid particles of approximately 600 nm size, but these particles might be made up of much smaller crystals that with the resolution on this microscope cannot be resolved.

Including the H-ZSM-5, the zeolites used in Chapter 4 have particle sizes ranging from 200 – 900 nm but consist of much smaller crystals that are too small to be resolved here. These are comparable sizes in the same order of magnitude

(compared with the large chabazite crystals for example). Significantly larger crystal sizes result in a longer path-length for reactant and product diffusion.

2.4 References

1. E. Smith and G. Dent, Modern Raman Spectroscopy: a practical approach, John Wiley & Sons Ltd., Chichester, England, 2004.
2. C. V. Raman and K. S. Krishnan, Nature, 1928, 121, 501–502.
3. C. V. Raman and K. S. Karishnan, Indian Journal of Physics, 1928, 2, 399–419.
4. W. Demtröder, Laser Spectroscopy: Basic Concepts and Instrumentation, 3rd ed. Springer, Heidelberg,Berlin, 1996.
5. John M. Chalmers and Peter R. Griffiths, Handbook of Vibrational Spectroscopy. Theory and Instrumentation, J. Wiley & Sons, Chichester, 2002.
6. S. Mosca, C. Conti, N. Stone and P. Matousek, Nature Reviews Methods Primers, 2021, 1, 1–16.
7. E. Cloutis, P. Szymanski, D. Applin and D. Goltz, Icarus, 2016, 274, 211–230.
8. H. Kim, K. M. Kosuda, R. P. V. Duyne and P. C. Stair, Chemical Society Reviews, 2010, 39, 4820–4844.
9. A. Y. Hirakawa and M. Tsuboi, Science, 1975, 188, 359–361.
10. R. J. H. Clark and T. J. Dines, Angewandte Chemie International Edition, 1986, 25, 131–158.
11. P. C. Stair, Advances in Catalysis, 2007, 51, 75–98.
12. P. Matousek, M. Towrie, A. Stanley and A. W. Parker, Applied Spectroscopy, 1999, 53, 1485–1489.
13. A. H. Tunnacliffe and A. G. Hirst, Optics, ABDO College of Education, London, 2nd ed., 2007.
14. S. Bordiga, G. Ricchiardi, G. Spoto, D. Scarano, L. Carnelli, A. Zecchina and C. Otero Areán, Journal of the Chemical Society, Faraday Transactions, 1993, 89, 1843–1855.
15. P. J. Garratt, UV-vis atlas of organic compounds, Heinz-Helmut Parkampus, Weinheim, 2nd Ed., 1992.
16. P. Wormell, in Encyclopedia of Biophysics, 1st ed., Springer, Berlin, Heidelberg, 2013.
17. 6.3 Quadrupole mass spectrometers (QMS), https://www.pfeiffer-vacuum.com/en/know-how/mass-spectrometers-and-residual-gas-analysis/quadrupole-mass-spectrometers-qms/quadrupole-mass-filter/, (accessed 24 February 2021).
18. S. N. Thomas, in Contemporary Practice in Clinical Chemistry, 4th eds. W. Clarke and M. A. Marzinke, Academic Press, 2019, pp. 171–185.
19. M. Stöcker, Zeolite Characterization and Catalysis, Springer Netherlands, 2009.
20. G. Ertl, H. Knözinger, F. Schüth and J. Weitkamp, Eds., Handbook of Heterogeneous Catalysis, VCH, Weinheim, 2008, vol. 1.
21. M. Thommes, Chemie Ingenieur Technik, 2010, 82, 1059–1073.

22. QUADRASORB EVO/SI and QuardaWin User Manual, Quantachrome Instruments, 6.0., 2013.
23. M. Niwa and N. Katada, The Chemical Record, 2013, 13, 432–455.
24. M. Niwa, M. Iwamoto and K. Segawa, BCSJ, 1986, 59, 3735–3739.
25. K. D. Vernon-Parry, III-Vs Review, 2000, 13, 40–44.
26. A. Barhoum, A. S. H. Makhlouf, Emerging Applications of Nanoparticles and Architecture Nanostructures, 4th ed., Elsevier, 2018.
27. Epsilon 3XLE spectrometer - Product support| Malvern Panalytical, https://www.malvernpanalytical.com/en/support/product-support/epsilon-range/epsilon-4/epsilon-3xle-spectrometer, (accessed 19 January 2021).
28. M. Moliner, C. Franch, E. Palomares, M. Grill and A. Corma, Chemical Communications, 2012, 48, 8264–8266.
29. IZA Structure Commission, Database of Zeolite Stuctures, http://www.iza-structure.org, (accessed 13 June 2017).
30. P. K. Dutta and M. Puri, Journal of Physical Chemistry, 1987, 91, 4329–4333.
31. S. Mintova, B. Mihailova, V. Valtchev and L. Konstantinov, Journal of the Chemical Society, Chemical Communications, 1994, 0, 1791–1792.
32. J. Socrates, Infrared and Raman characteristic group frequencies tables and charts, John Wiley and Sons, Chichester, 3rd ed., 2001.
33. T. Schmid and P. Dariz, Journal of Raman Spectroscopy, 2015, 46, 141–146.
34. M. Galván-Ruiz, J. Hernández, L. Baños, J. Noriega-Montes and M. Rodriguez-Garcia, Journal of Materials in Civil Engineering, 2009, 21, 625–708.
35. I. Yarulina, S. Bailleul, A. Pustovarenko, J. R. Martinez, K. D. Wispelaere, J. Hajek, B. M. Weckhuysen, K. Houben, M. Baldus, V. Van Speybroeck, F. Kapteijn and J. Gascon, ChemCatChem, 2016, 8, 3057–3063.
36. G. Taglieri, C. Mondelli, V. Daniele, E. Pusceddu and A. Trapananti, Advances in Materials Physics and Chemistry, 2013, 3, 108–112.
37. Y. T. Chua, P. C. Stair, J. B. Nicholas, W. Song and J. F. Haw, Journal of the American Chemical Society, 2003, 125, 866–867.
38. C. L. Angell, Journal of Physical Chemistry, 1973, 77, 222–227.
39. Calcium Carbonate Nanoparticles, https://www.americanelements.com/calcium-carbonate-nanoparticles-471-34-1, (accessed 17 March 2021).
40. D. Kim, J. Lee, S. Lee and J. Lim, Colloids and Surfaces A: Physicochemical and Engineering Aspects, 2018, 536, 213–223.
41. M. E. Potter, ACS Catalysis, 2020, 10, 9758–9789.
42. E. Borodina, H. Sharbini Harun Kamaluddin, F. Meirer, M. Mokhtar, A. M. Asiri, S. A. Al-Thabaiti, S. N. Basahel, J. Ruiz-Martinez and B. M. Weckhuysen, ACS Catalysis, 2017, 7, 5268–5281.
43. D. S. Wragg, R. E. Johnsen, P. Norby and H. Fjellvåg, Microporous and Mesoporous Materials, 2010, 134, 210–215.
44. J. Tan, Z. Liu, X. Bao, X. Liu, X. Han, C. He and R. Zhai, Microporous and Mesoporous Materials, 2002, 53, 97–108.

3 Methanol to Hydrocarbons

3.1 Introduction

The Methanol-to-Hydrocarbons reaction can be further classified to Methanol-to-Gasoline (MTG) or Methanol-to-Olefins (MTO). Small pore zeolites are good for production of light olefins due to product shape selectivity, and therefore chabazite is often a chosen topology to employ as an MTO catalyst, with H-SAPO-34 currently industrially employed.[1–3] ZSM-5 with its MFI topology has also shown success in MTH, targeted towards MTG. The internal pore structures of zeolites allow for the formation of bulky alkenes and alkylated aromatic hydrocarbons from a methanol feed. These hydrocarbons make up the Hydrocarbon Pool (HCP) which is itself autocatalytic, remaining inside the pores and reacting with methanol to give the products.[2–4] The HCP species continuously undergo methylation, contraction, side chain elimination and expansion to split off small olefins. The HCP speciation directly determines the product distribution in this ship-in-a-bottle style mechanism, so the zeolite structure plays an important role in the catalyst mechanism, and in its lifetime.[2]

In H-SSZ-13 or H-SAPO-34 with chabazite topology, the 3.8 x 3.8 Å openings allow for the diffusion of methanol, dimethyl ether (DME) and small olefins such as ethene, propene and butene.[5,6] At the same time, the large *cha* cages of the topology allow formation of bulky hydrocarbons internally, with active species consisting of penta- and hexamethyl benzenium ions for example.[7,8] The build-up of hydrocarbons that are too large within pores limits diffusion of products and reactants, and renders some cages inactive, deactivating the catalyst.[9]

In ZSM-5, the wider pore openings of 5.4 x 5.4 Å allow the diffusion of larger products including monocyclic aromatics and linear and branched paraffins and olefins, in the gasoline boiling point range.[4,10,11] This was the original zeolite employed by Mobil in 1977 when MTH technology and research began.[10] At channel intersections, the voids contain enough space to hold even higher methylated benzenes such as hexa- and pentamethylbenzene – despite tetramethylbenzene being the largest species able to diffuse through the

channel.[12] While MTH mechanisms in the CHA topology are expected to mainly work *via* aromatic based cycles, the aliphatic cycle is also facilitated in MFI such that both cycles work simultaneously.[13] The deactivation mechanism in ZSM-5 is more likely related to the formation of graphitic coke external to the zeolite particles.[4]

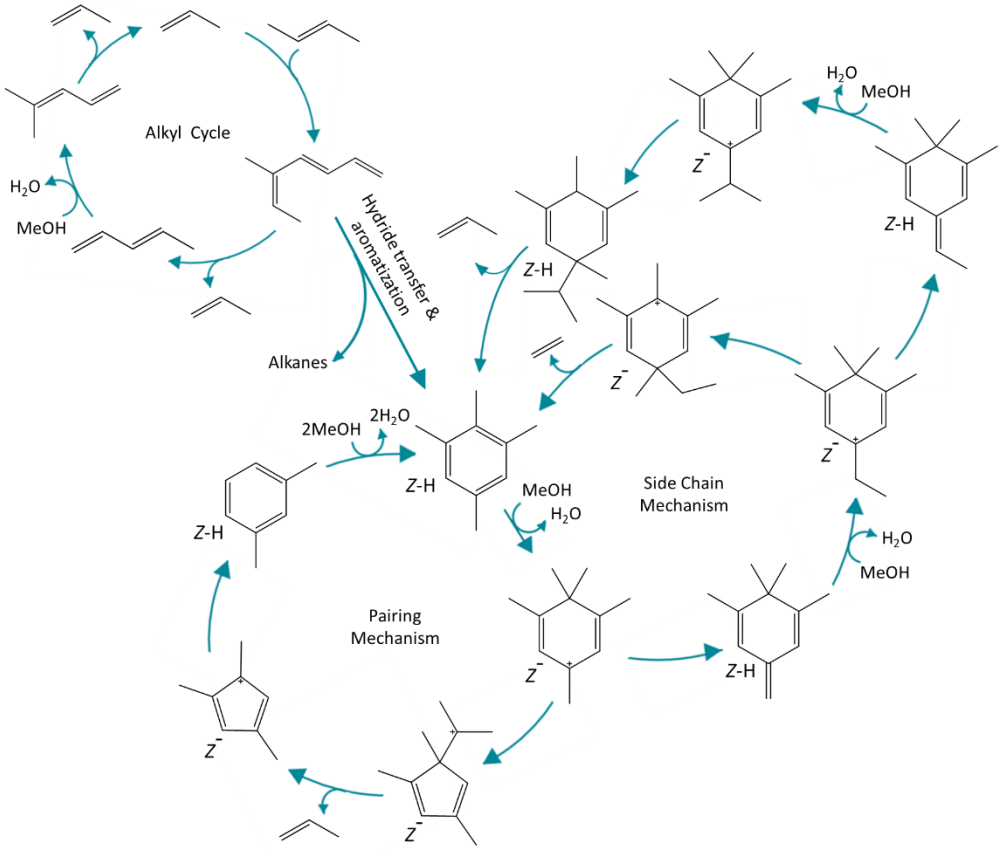

Figure 48 Summary of reaction mechanisms in MTH including the link between the "alkyl cycle" and "aromatic cycle".

In ZSM-5, attempts have been made to alter the acid sites both during and post synthesis; during synthesis by modification of the acid site density or sitting, and post synthesis by incorporation of metal ions to create greater Lewis acidity and lessen Brønsted acidity.[13–16] Specifically, modification by impregnation of calcium has been used as a method of inhibiting the aromatic cycle of the dual cycle mechanism, thereby allowing the aliphatic cycle to dominate, giving much higher yields of propene and butene and a nine-times prolonged catalyst lifetime.[14] Characterisation of the material indicated a significant increase in Lewis acidity – due to the presence of the alkali earth metal – and decreased Brønsted acidity in

terms of site density and strength. A decreased acid site strength decreases the rate of hydride transfer reactions – which link the alkene cycle with the aromatic cycle – so that methylation of alkenes should dominate the mechanism.[14] The two chemical pathways are outlined in the literature review in Chapter 1, and a fuller figure is shown below in Figure 48.

Modification of chabazite materials has also been reported for MTO by reduction of crystal size for improved diffusion, or by altering the materials acidity by metal impregnation.[17,18] These works focused on increasing ethene yield while decreasing methane formation, which was successful for some metals, such as potassium, cerium and unsuccessful for others, such as molybdenum.[17,19] Work has also included metals incorporation into the framework of SAPO-34 during synthesis, affecting the lifetime and selectivity of catalysts.[20] Little has been done to specifically separate the two cycles in chabazite to date.

3.2 Prior work

Prior to the beginning of the project, some data was collected by Kerr-gated Raman which acted as a proof of principle for its application to this system. Analysis of results was ongoing and crossed with the studentship, so work was invested on my part in the analysis and discussion, with additional results collected during the studentship published as part of the supporting information.

In these experiments, methanol was fed continuously over H-SSZ-13 and H-ZSM-5 catalysts under a temperature ramping program, while the catalyst was probed by the 400 nm laser probe of the Kerr-gated spectrometer system. Supporting calculations were also performed by a collaborating group at Ghent University, Belgium to simulate the Raman spectra of some hydrocarbon species inside the zeolite, and DFT calculations were performed to simulate their behaviour.

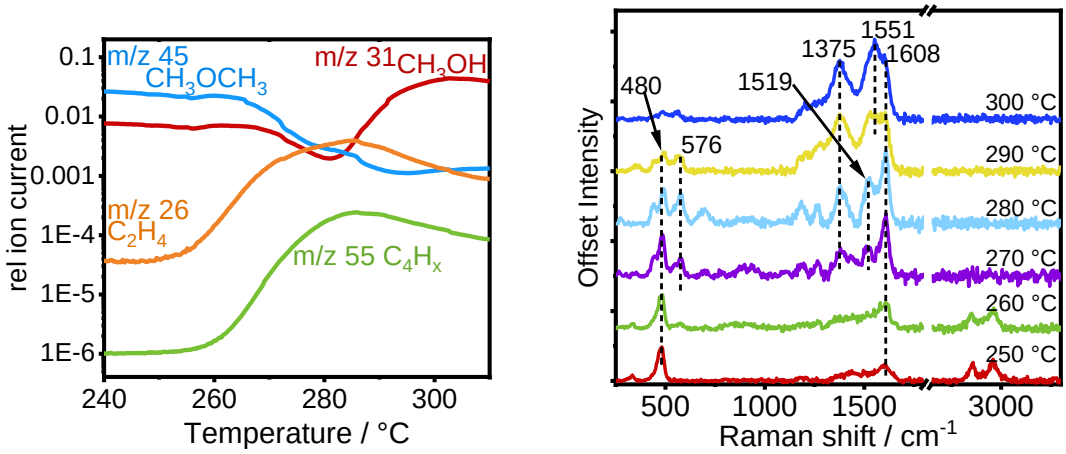

Figure 49 *Operando* Kerr-Gated Raman of SSZ-13 zeolite during the MTO reaction. Methanol was fed continuously over H-SSZ-13 (Si/Al = 15) the temperature was increased by 1 °C/min from 100 to 450 °C. (a) MS data acquired at the reaction outlet between 240 and 310 °C collected by Pfeiffer Omnistar Mass Spectrometer (b) Kerr-gated Raman measurements at 10 °C intervals from 250 to 300 °C.

At low temperature (100 to 250 °C) during reaction over H-SSZ-13 catalyst, apart from the dropping intensity of methanol bands, at 2954, 2855, 1455 and 1006 cm^{-1} for which the C-H asymmetric and symmetric stretches, CH_3 deformation and C-O stretch in methanol are responsible, the main change observed was a small growth at 1600 – 1625 cm^{-1} assigned to stretching modes of non-conjugated C=C bonds such as small alkenes, indicating a build-up of small hydrocarbons prior to the commencement of the hydrocarbon pool.[21,22] By 270 and 280 °C it can be confidently said that the hydrocarbon pool had built up, with bands between 1250 and 1400 cm^{-1} characteristic of C-H rock and CH_2 and CH_3 deformation modes that can be exhibited by methylated aromatic species or dienylic carbocations, and at 1608 and 1519 cm^{-1} assigned to the symmetric and asymmetric stretches of aromatic C=C bonds, at 1182 cm^{-1} the aromatic C-C stretching modes and at 576 cm^{-1} the C-C deformations such as those seen in methylated aromatics and dienylic carbocations.[22] The band at 1375 cm^{-1} is intense and broad and so may also contain a ring breathing mode of naphthalenes.[21,22] At this temperature, where catalytic activity is high, the species identified on the catalyst are in strong agreement with recognized hydrocarbon pool species in literature, including methylated benzenium ions and possibly methylated naphthalenic species along with alkenes and dienylic

carbocations.[2,9,23,24] In this temperature period the catalyst becomes much more active, methanol reaches its point of maximum consumption and olefin production begins, in line with the establishment of autocatalytic species allowing the aromatic and alkene cycles to take place in the pores.[7,8,23]

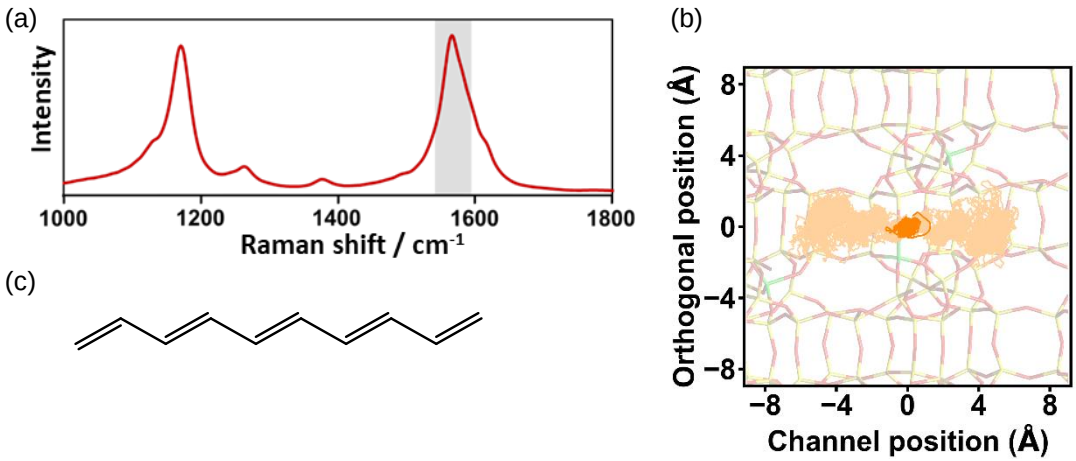

Figure 50 Results of molecular modelling calculations (a) Simulated Raman spectrum of decapentaene via ab initio molecular dynamics simulations, the grey highlighted region indicates the peak corresponding to the stretching of the extended π structure of decapentaene (b) Molecular dynamics calculations of the paths of carbon atoms of decapentaene in chabazite during 40 ps trajectory, the centre of mass of this long chain linear molecule as shown in dark orange to have very little mobility, while the light orange region desribes the movement of all carbon atoms in the molecule. The molecule sits through an 8-membered ring in two cages (c) The chemical structure of decapentaene.

When the temperature is further increased to 290 and 300 °C, a decrease in methanol conversion is observed by MS. By Raman, the most significant difference in this period is a new band growing at 1551 cm^{-1}, a band that has been previously recorded during methanol, dimethyl ether and olefin conversion in zeolites and tentatively assigned to conjugated polyenes.[21,25,26] The coincidence of the evolution of this species with slowing methanol consumption recorded here evokes a relationship between the two events, and gives extended polyenes a likely significant role in the process of catalyst deactivation, for the first time.

To further investigate the relationship of extended polyenes and catalyst deactivation, first principle molecular dynamics simulations were performed by a

collaborating group at Ghent University, to understand their mobility in the zeolite pores. While the mobilities of small alkenes – propene and butadiene – were not shown to be particularly hindered, the longer length polyene decapentaene showed almost no mobility – and needed to sit in two *cha* cages simultaneously, through the 8 membered-ring windows connecting them – where it remained – thereby inhibiting further molecular diffusion between the pores. Figure 50b demonstrates this – showing the centre of movement of the molecule in dark orange, and the positions of carbon atoms in light orange as they move during the 40 ps molecular dynamics trajectory.[22] Furthermore, molecular dynamics simulations also put the C=C stretch of the conjugated π system of this species in good agreement with experimental data, the simulated spectrum is shown in Figure 50a where the grey region highlights the peak corresponding to the C=C stretch. The assignment of the band at 1551 cm^{-1} to extended polyenes is strongly supported, and the correlation of this species with deactivation is proven, giving a key piece of data in understanding the deactivation mechanism in this material.[22]

Molecular dynamics simulations predicted that polyene-type species can undergo intramolecular cyclization to form aromatics, and progressive increase in reaction temperature saw the growth of low frequency bands at 629 and 817 cm^{-1} which are related to the formation of polyaromatic hydrocarbons. The band growth is shown in Figure 51a which shows some Raman spectra collected from 340 to 450 °C – the bands at mid-frequencies remain about constant, while the intensities of lower frequency bands at 629 and 813 cm^{-1} increase. Figure 51b shows a potential candidate for a source of the low frequency vibrations, protonated anthracene, and Figure 51c shows its simulated Raman spectrum, where the band at low frequency indicated by the star is caused by the ring opening vibration of the protonated molecule. Interestingly, at this stage of the reaction the shoulder at 1608 cm^{-1} related to methylated benzenes drops in relative intensity to other signals in the spectra, which may offer an alternative route to polyaromatic formation through the consumption of methylated aromatics.

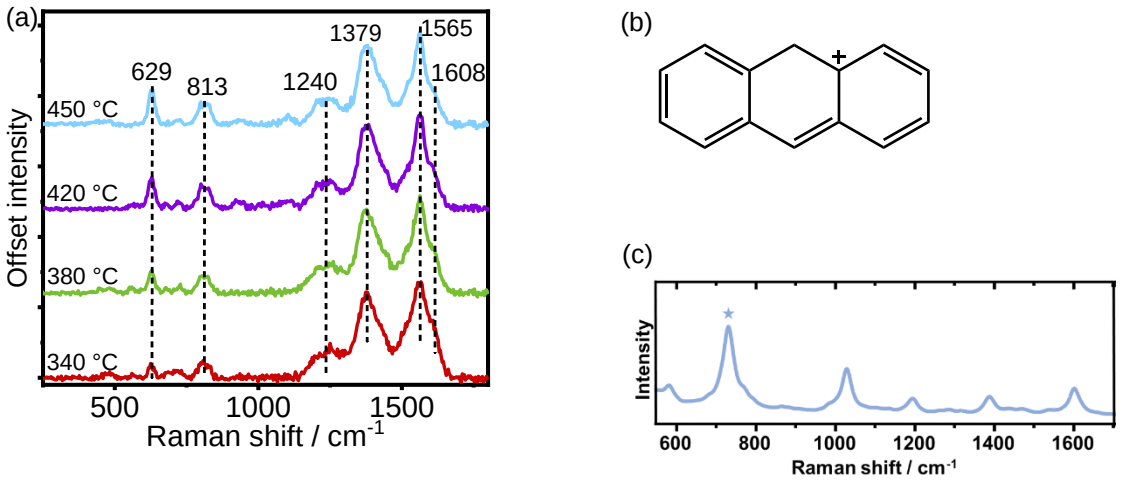

Figure 51 (a) *Operando* Kerr-gated Raman of H-SSZ-13 zeolite during MTO reaction at higher temperatures from 340 to 450 °C from 250 to 300 °C (b) Molecular Dynamics calculated Raman spectrum of protonated anthracene, as an example of a polyaromatic species exhibiting strong low frequency band assigned to the ring opening vibration of the molecule (c) Chemical structure of protonated anthracene molecule.

Investigating methanol conversion over H-ZSM-5 (in Figure 52) showed some similarities with the H-SSZ-13 catalyst – with a rapid increase in methanol conversion above 300 °C occurring simultaneously with a growth in the Raman signals characteristic of methylated benzenium ions and dienylic carbocations. With further increase in temperature to 340 °C, polyenes were observed to form with a Raman signal at 1552 cm^{-1}, though the band at 1605 cm^{-1} remained dominant and methanol consumption did not cease. This would suggest that polyene species are still able to form during the reaction on this material, but their presence does not result in deactivation. Further into the experiment, polyaromatic species (of greater size than naphthalene) were not observed to form, suggesting that the polyene formation in ZSM-5 does not cause cyclization to larger polyaromatic species. The larger channel diameter likely does not hinder polyene mobility, while the channel intersection maintains enough steric constraint as compared with SSZ-13 to inhibit polyene cyclisation.[22]

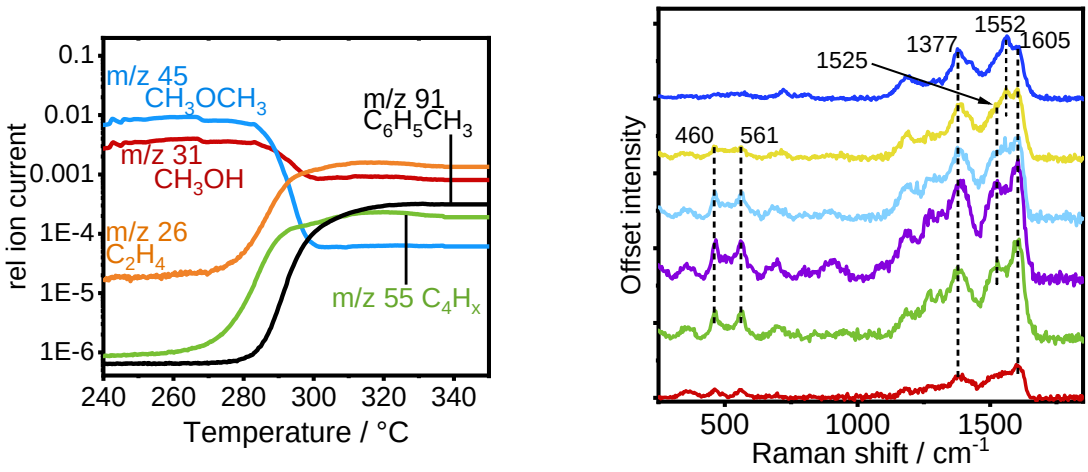

Figure 52 *Operando* Kerr-Gated Raman of H-ZSM-5 zeolite during the MTH reaction. Methanol was fed continuously over H-ZSM-5 (Si/Al = 15, Zeolyst Inc.) as the temperature was increased from 100 to 450 °C. (a) MS data acquired at the reaction outlet between 240 and 310 °C collected by Pfeiffer Omnistar Mass Spectrometer (b) Kerr-gated Raman measurements collected at intervals between 280 and 430 °C.

3.3 Methanol -to-Olefins H-SSZ-13

These results of the methanol-to-olefins study in H-SSZ-13 under temperature ramping conditions proved that polyene species are the first to begin inhibiting reaction chemistry, appearing with the onset of slowing catalytic activity, while at higher temperatures cyclization occurs, yielding polyaromatic hydrocarbons. These results are heavily insightful, although the temperature ramping reaction conditions are not typically representative of standard operating conditions. We therefore continued the study with experiments under isothermal conditions, selecting temperatures to extract different chemical behaviours observed and for comparison to prove the validity of the results of the temperature ramp experiment.

The two temperatures chosen for running the reaction isothermally were 280 and 350 °C. The motivation for choosing these two temperatures originates from the previous observations during temperature ramping where 280 °C the catalyst is observed to be in its most active state as indicated by the point of maximum methanol consumption, and at 350 °C polyenes have formed and polyaromatics begin to appear.

During these experiments, H-SSZ-13 catalyst with Si/Al ratio of 15 was used as in the experiment described in the previous section. 50 mg of catalyst was used in each experiment. The catalyst was pre-treated by heating to 550 °C at 8 °C min^{-1} in 20 % O_2/He mix and holding for 1 h. The catalyst was then cooled to reaction temperature under flowing He and methanol was introduced to the catalyst by means of a syringe pump for 1 hour at a rate of 1.7 µl min^{-1} methanol flow in 30 ml min^{-1} He, giving a WHSV of 1.62 h^{-1}.

3.3.1 Isothermal reaction at 280 °C

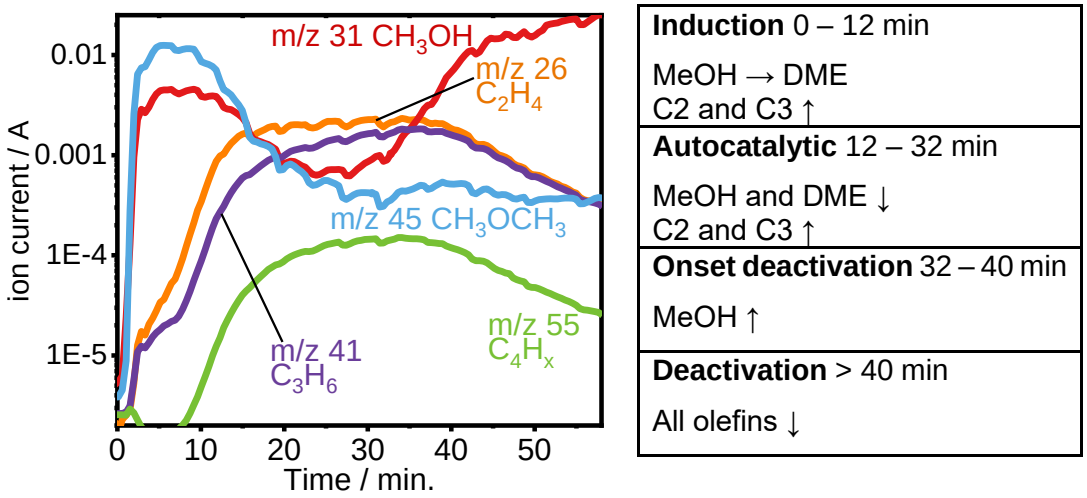

Figure 53 Mass spectrometry data acquired during the reaction of methanol over H-SSZ-13 at 280 °C for 1 hour, WHSV 1.62 h^{-1}. m/z 31 (red) methanol, m/z 45 (blue) dimethylether, m/z 26 (orange) ethene, m/z 41 (purple) propene, m/z 55 (green) butene.

As methanol is introduced to the catalyst, its conversion is initially low as the reaction enters an induction period. Figure 53 shows MS data collected during the reaction, the red line shows the mass trace of methanol with *m/z* 31, and the blue of DME *m/z* 45, which are both high initially, dropping after 12 min. indicating a faster consumption of methanol and DME as the reaction enters is autocatalytic period.[24] The reaction products detected are small olefins; ethene and propene (*m/z* 26 in orange and 41 in purple respectively) and butene/pentene isomers (*m/z* 55). Initially ethene is produced more rapidly than propene, though during the autocatalytic period as the ethene signal remains stable, propene continues to climb. Methanol conversion decreases at 30 min., indicating the onset of

catalyst deactivation, and as olefin production slows after 40 min., we enter the deactivation period.

As the MS data can be described in 4 sections; the induction period, autocatalytic period, onset of deactivation and the deactivation, so too can the interpretation of the Raman spectra. Figure 54 shows the Raman spectra collected during the first 24 min. of reaction, including the induction period, and entering the autocatalytic period. Upon the introduction of methanol, methanol Raman bands are observed; the C-H symmetric and asymmetric stretches at 2853 and 2963 cm^{-1} and C-O stretch and CH_3 deformation at 1006 and 1465 cm^{-1} respectively are easily distinguished in the Raman spectra at 0 and 8 min. of reaction shown in Figure 54.[27,28] Their intensity is much lower when compared with the results of the temperature ramp experiment where methanol was introduced at 100 °C, due its faster consumption at 280 °C. The spectra at short times on stream are mainly dominated by the Si-O bending vibration of the zeolite framework at 473 cm^{-1}, with smaller peaks at 329 cm^{-1} characteristic of pore openings, 808 cm^{-1} due to the T-O-T symmetric stretch and at 1050 cm^{-1} and 1200 cm^{-1} due to the T-O-T asymmetric stretch.[29,30]

At 8 min., broad growth in the C=C stretching region at 1603 cm^{-1} is consistent with the in-phase stretching of C=C bonds of aromatic rings,[31] and also short olefinic species can exhibit C=C stretching frequencies between 1600 and 1620 cm^{-1}, which may contribute to the broadness of the peak.[22] This time coincides with the induction period of the catalyst and the build-up of the hydrocarbon pool, and while olefinic species may be expected associated with the hydrocarbon pool build-up,[24] due to the resonance enhancement effect and given that methylated aromatics absorb at the 400 nm excitation wavelength, if methylated aromatic species are already present they would be detectable in very low concentrations.[32] Here it is not possible to distinguish between aromatic or olefinic species.

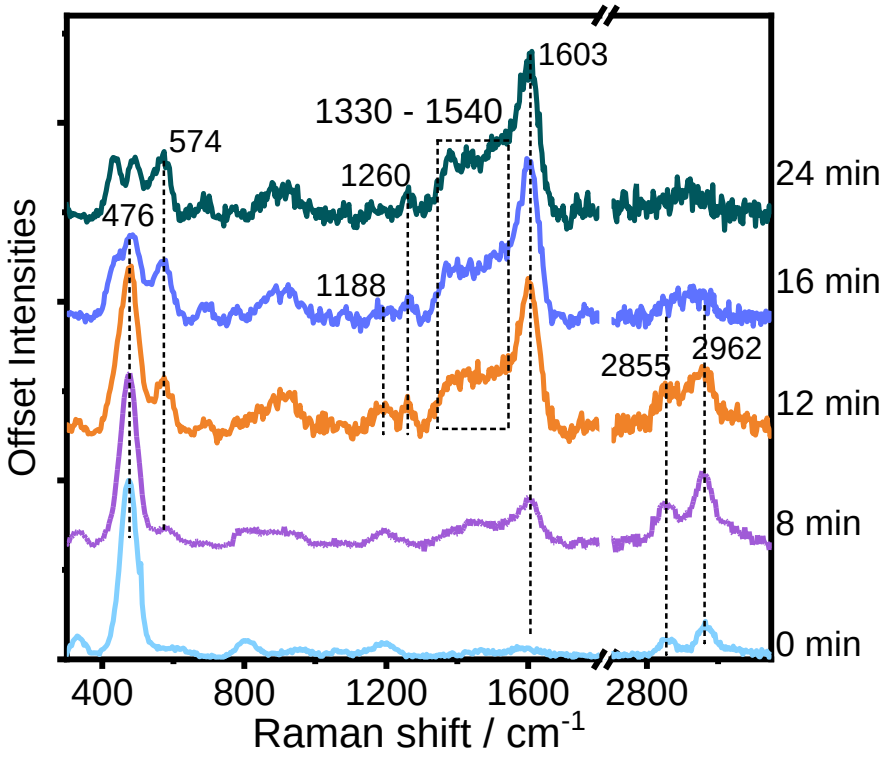

Figure 54 Kerr-gated Raman spectra collected during reaction of methanol over H-SSZ-13 catalyst at 280 °C, spectra collected at 0, 8, 12, 16 and 24 min. of reaction, during the induction period and entering the autocatalytic period.

With increasing time on stream to 12 minutes, the band at 1603 cm^{-1} significantly grows in intensity, with a very broad shoulder in the 1330 – 1540 cm^{-1} region. Bands also grow in the low frequency region at 433 cm^{-1}, 572 cm^{-1}, 692 cm^{-1} and a broad band around 900 cm^{-1}. Some of these bands can confirm the presence of methylated benzenium ions, which exhibit alkyl aromatic ring stretches, C-H rock and aromatic C-C stretching modes around 574, 1260 and 1188 cm^{-1} respectively.[22] The growth in intensity below 1540 cm^{-1} is very broad, and due to the lack of defined structure from 1330 – 1540 cm^{-1} it is difficult to identify any particular species responsible here. Dienylic carbocations show C=C stretching vibrations at 1500 cm^{-1},[33] while CH_2 and CH_3 groups exhibit deformation modes from 1350 – 1410 cm^{-1},[22,34] indicative of the presence of olefinic species and methyl groups.[21,29,35] Naphthalenic species exhibit their breathing modes from 1360 – 1390 cm^{-1} and therefore may also be responsible for the Raman intensity in this region.[21,36] Protonated naphthalenic species show an electronic transition in the region of the wavelength laser used in our experiment at 400 nm, the signals from their breathing modes should therefore be resonance enhanced, and

if present these species would be detectable in low concentrations.[24,37] The zeolite framework vibrations become weaker and are barely observable beyond 16 min. of reaction, possibly because the hydrocarbon species are strongly absorbing at 400 nm, their signals therefore being intense due to resonance enhancement and obscuring the zeolite vibrations.

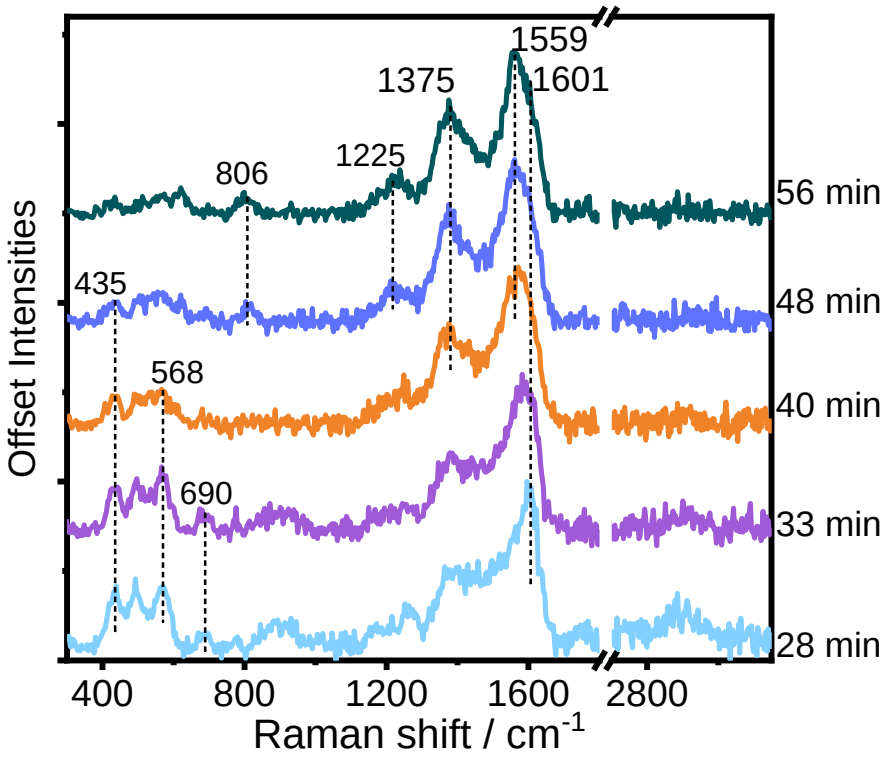

Figure 55 Kerr-gated Raman spectra collected during reaction of methanol over H-SSZ-13 catalyst at 280 °C, spectra collected at 28, 33, 40, 48 and 56 minutes of reaction, during the autocatalytic period and entering the onset of deactivation and then deactivation.

As methanol consumption is slowed at 30 min., the most intense Raman peak in the C=C stretching region changes from 1603 cm^{-1} to 1580 cm^{-1} shown in Figure 55, probably as a result of the presence of additional contributions which appear overlapped. A vibration in this region was observed by Pazé *et al.* and attributed to allylic carbocations,[33] however this peak shift is likely due to the contribution of a growing band at 1559 cm^{-1} which is initially overlapped and not well defined, and as it grows, dominates the spectrum at longer time on stream.

By 40 min., the deactivation period is reached. The lower frequency vibration at ~570 cm^{-1} belonging to the alkylated aromatic species are consumed, and a strong and sharp band growing at 1375 cm^{-1} is observed, while the band in the C=C stretch region looks highly asymmetrical, with the most intense peak at 1559 cm^{-1} and a shoulder still at 1601 cm^{-1}. Here we see a change in speciation, a stronger presence of naphthalenic species is indicated by the sharp growth at 1375 cm^{-1}, owing to their ring breathing modes, whose vibrations would be enhanced at 400 nm excitation wavelength to give the intensity observed here. While the C=C stretching frequency at 1559 cm^{-1} corresponds to the same long chain polyene species that was observed during the temperature ramp experiment, and proven to inhibit diffusion in the zeolite.[22]

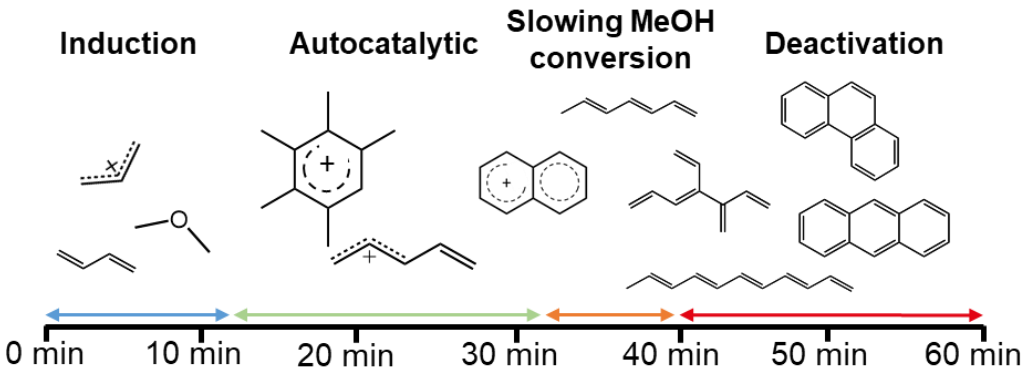

Figure 56 A visual summary of the intermediates detected throughout the periods of the reaction that were defined in Figure 53; the induction period where methanol is more slowly converted, and the main product is dimethylether with small amounts of olefins detected, the autocatalytic period where olefins are rapidly produced and methanol is rapidly consumed, the onset of deactivation where methanol conversion slows, and the deactivation period where products are no longer formed.

From this experiment we can identify that alkylated benzenium ions are responsible for the period of high activity from bands in the low and mid frequency region. This has been well documented in literature and so comes as no surprise.[2,12,24,38,39] With the onset of deactivation, we see adjustment in the C=C stretching region as the most intense peak becomes that centred at 1580 cm^{-1}, resulting from a combination of different Raman modes, including that at 1559 cm^{-1} – this change is caused by the formation of long chain polyenylic species. In this period, ethene is still steadily formed while propene production continues to steadily increase. It has also been documented that it is not

thermodynamically favourable for ethene to be formed outside of the aromatic cycle of the mechanism, through cracking of longer chain hydrocarbons, whereas propene can form through cracking reactions and from ring contraction and expansion of highly methylated aromatic species.[4,11] This fact further supports the idea that as we enter the period of deactivation onset, the species that form are of unsaturated, long chain aliphatic character, which might crack to give preference to propene formation over ethene. The deactivation period is in line with the consumption of single ring alkylated benzenium ions, proven by the consumption of their lower frequency vibrations. As shown in the previous section, long chain polyenes straddle the 8 membered ring window between two *cha* cages, blocking the diffusion of reactant or product within the catalyst particle.[22] This then explains why the onset of deactivation, indicated by the increasing methanol signal measured by MS, occurs simultaneously with the shift in the C=C stretching frequency at 33 minutes of reaction. The species identified are summarised in Figure 56, put into the context of the periods of the reaction defined in Figure 53.

3.3.2 Isothermal reaction at 350 °C

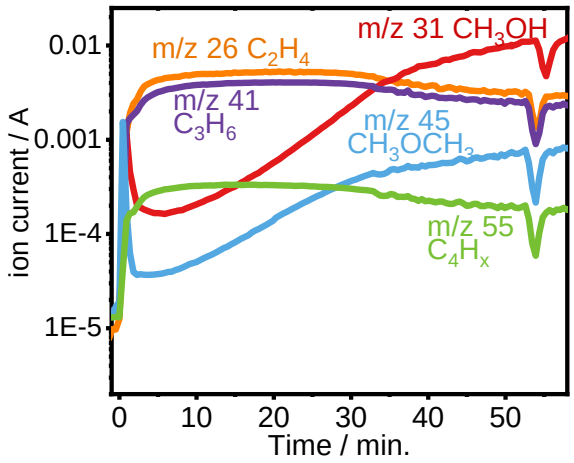

Autocatalytic period 0 – 7 minutes MeOH and DME ↓ C2 and C3 ↑
Onset of deactivation 7 – 30 minutes MeOH & DME ↑
Deactivation > 30 minutes Slight ↓ olefins

Figure 57 Mass spectrometry data acquired during the reaction of methanol over H-SSZ-13 at 350 °C for 1 h, WHSV 1.62 h^{-1}. m/z 31 (red) methanol, m/z 45 (blue) dimethylether, m/z 26 (orange) ethene, m/z 41 (purple) propene, m/z 55 (green) butene.

The activity data measured by MS in the reaction at 350 °C takes a significantly different shape than at 280 °C. Firstly, there is not a notable induction period,

which has been confirmed in studies by Bleken and Borodina as an effect of increasing the reaction temperature.[24,40] The period of maximum methanol consumption, indicated by the red line *m/z* 31, is reached quickly at 3 min. on stream, while ethene and propene (m/z 26 in orange and 41 in purple respectively) are produced simultaneously. Methanol consumption is slowed after 7 min., however, note that ethene and propene traces remain stable up to 30 min., after which point, they slowly begin to decline. One further difference in this data is that as methanol consumption is slowed, the DME signal (*m/z* 45) also increases, indicating that methanol is still being dehydrated and therefore acid sites must still be accessible and the rate of DME consumption is dropping.

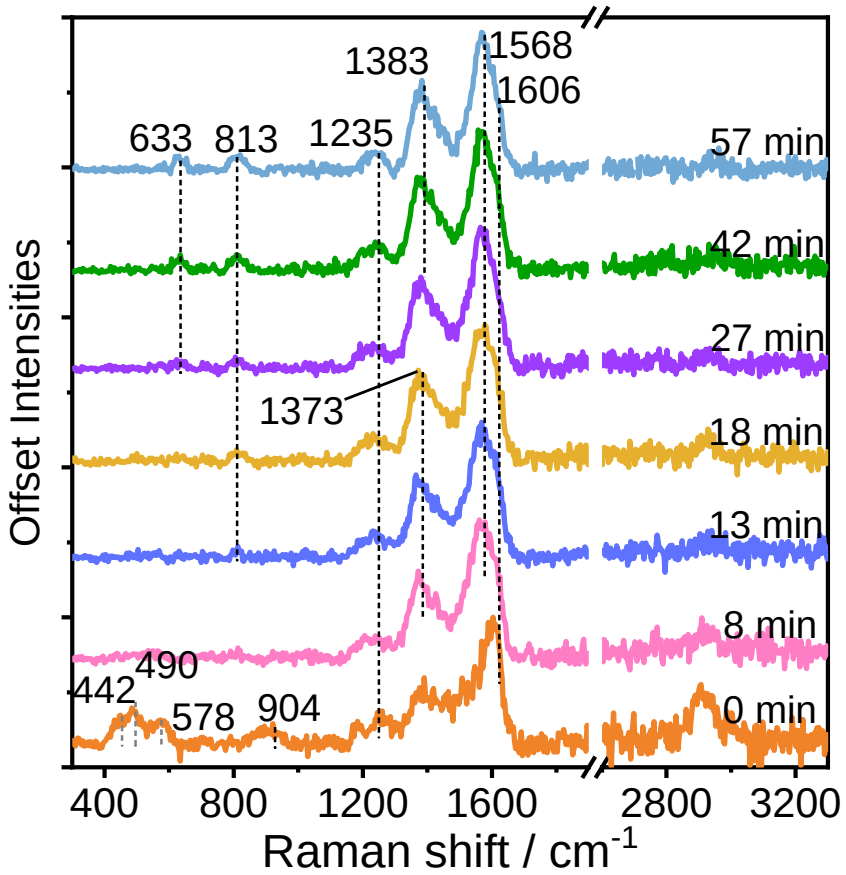

Figure 58 Kerr-gated Raman spectra collected during reaction of methanol over H-SSZ-13 catalyst at 350 °C for 1 h, spectra collected at 0, 8, 13, 18, 27, 42 and 57 min. from the autocatalytic period and entering the deactivation.

At the initial introduction of methanol to the catalyst, at 0 min in Figure 58, the hydrocarbon pool rapidly builds up due to a very fast induction period in line with the observations made from MS data shown in Figure 57. Vibrations at 578, 1265, 1186, and 1605 cm^{-1} which form quickly can be attributed to the alkyl aromatic

ring stretches, C-H rock, aromatic C-C stretching modes and C=C in phase stretching modes of methylbenzenium ions as above.[22] The zeolite band is still present at 487 cm^{-1}, and a small bump centred at 2915 cm^{-1} may be an average of the CH symmetric and asymmetric stretches of methanol, but is low in intensity due to rapid methanol reaction.

By 8 minutes of reaction, the speciation has changed – the most intense band in the C=C stretch region is at 1565 cm^{-1} (although the band is asymmetric with a shoulder at 1605 cm^{-1} and so likely contains the C=C stretching vibration of methylbenzenium ions).[22,35] Again, this change is coincident with a decrease in methanol consumption as shown by MS, although as previously mentioned the production of ethene and propene is still high, and so the catalyst has not yet entered its period of deactivation. A sharp peak at 1376 cm^{-1} confirms the presence of naphthalenic species at such a short time on stream.[21]

At longer reaction time, at 18 min. we see the evolution of a band at 815 cm^{-1}. From 32 min. onwards a band at 631 cm^{-1} grows in intensity. These low frequency bands are likely related to the formation of polyaromatic species as shown in the prior work,[22] and continue to grow in intensity, as the band at 1566 cm^{-1} becomes sharper and narrower. Beyond the slowing of methanol consumption, these later changes are in line with a slowing product formation, as the olefin signals start to drop.

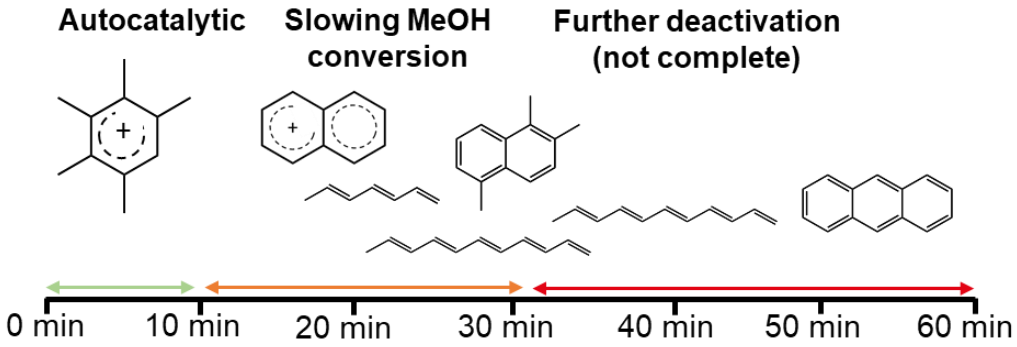

Figure 59 A visual summary of the intermediates detected throughout the periods of the reaction defined in Figure 9; the autocatalytic period where olefins are rapidly produced and methanol and DME are rapidly consumed, the onset of deactivation where methanol conversion slows, and further deactivation where product formation is slowed.

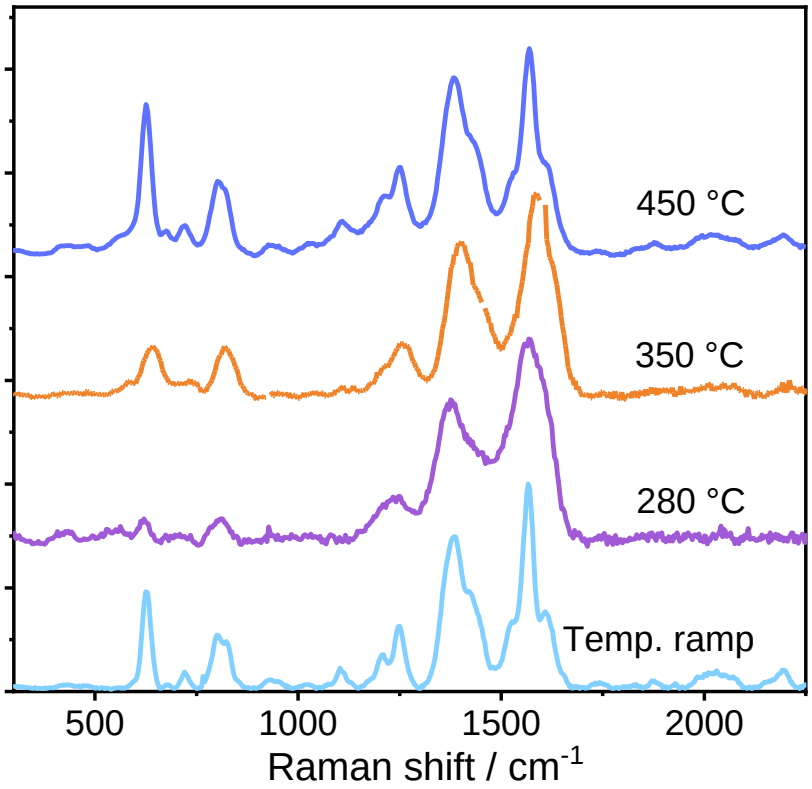

Figure 60 Raman spectra collected after reaction of methanol on H-SSZ-13 catalyst after temperature ramp experiment, and after 1 h at 280, 350 and 450 °C. Spectra were acquired for 5 times the acquisition time during *operando* study (for a total 100 s), 400 nm probe beam at 10 mW power.

Figure 59 gives a visual comparison of the species identified at different times during this reaction at 350 °C. In contrast with the reaction at 280 °C, here the induction period is significantly shorter and not observable, this is echoed in literature studies by Bleken and Borodina for example where product formation starts immediately, therefore no induction period is included in the schematic.[9,14] They also generally note a longer lifetime at higher temperatures, Borodina by indicating the drop in methanol consumption from 100 % (at WHSV 0.5 h^{-1}) and Bleken by reaching methanol conversion of less than 20 % (at WHSV 6 h^{-1}). Since our gases are only analysed semi-quantitatively by MS, we are unable to measure the values of conversion, and only see trends in consumption/production, and therefore cannot compare activity figures between the experiments. In our experiment at 350 °C, methanol consumption slows down after the initial 10 min. of reaction, although product formation does not, reaching its maximum at 10 – 30 min. In this period by Raman, we observe the formation

already of polyenes, which explain the decrease in methanol consumption so early on. While the ethene and propene signals drop at later times on stream, the drop does not appear to be as significant as was at 280 °C – although again we should be careful when comparing values of ion currents between experiments. It is interesting to note that even with the presence of polyenes, we still do see an active catalyst (although drop in methanol consumption was recorded) through continued olefin production even after polyenes have formed in the reaction at 350 °C.

3.3.3 Discussion

Comparison of results of isothermal experiments with the temperature ramp discussed in section 3.2 shows good agreement. While under ramping conditions the induction takes place at lower temperatures, at 280 °C the induction period takes place during the first 12 min. of reaction. After this point and during the autocatalytic part of the reaction, the hydrocarbon species detected do reflect those observed at 280 °C during the temperature ramp. It is interesting to note that as methanol consumption starts to decrease, the main spectral difference is the red shift of the C=C stretch due to the growing intensity around 1560 cm^{-1}, earlier assigned to polyenes. So too, in the isothermal experiment, the formation of these long chain species causes a slowing methanol consumption. At longer times on stream, despite reaching a deactivation stage where olefins stop being produced (>40 min.), large amounts of polycyclic aromatic species are not detected, in the experiment their low frequency vibrations are absent. Figure 60 shows data acquired after the end of the experiments, when the reactor was cooled to room temperature under flowing helium, and the acquisition repeated 5 times (a total of 100 seconds acquisition time) to give an averaged spectrum with an improved signal-to-noise ratio. Here, some very weak low frequency bands at 630 and 810 cm^{-1} are observed to have formed during the experiment at 280 °C, but given that we needed the much longer acquisition time to observe these vibrations, the polyaromatic hydrocarbons are likely in low quantity.

The experiment at 350 °C shows no induction period, but there is evidence at short time on stream of an autocatalytic period like that observed at lower temperatures during the temperature ramp experiment. Nonetheless, the spectra

very rapidly change, showing formation of naphthalenic species and polyenes by 8 min. on stream, followed by a slowing of methanol consumption. The signal for polyenylic species sits at 1568 cm^{-1} – 10 wavenumbers higher than in the reaction at 280 °C – possibly indicating a slightly shorter chain polyene molecule,[41] or this could be due to convolution with the aromatic C=C vibrations. Despite the slowing methanol consumption, the catalyst remains active with propene and ethene produced at a stable rate until 32 min. of reaction, when their production slows. At these longer times on stream, low frequency bands at 633 and 813 cm^{-1} develop, as polyaromatic species form in the pores.[22]

Also included in Figure 60 is the result of running the reaction for 1 hour at 450 °C. Unfortunately, during this experiment there was a problem with the methanol delivery system at early times of reactions. This data is therefore included in the appendix. What is clear from these data is that even during the early stages of reaction, polyaromatics quickly form at this temperature. And the Raman spectrum acquired after cooling the reactor shows very similar speciation with the end of the temperature ramp experiment, which was run up to 450 °C, but with more intense bands at low frequency due to a greater build-up of the polyaromatic species.

3.4 Methanol-to-Olefins on H-SAPO-34

H-SAPO-34 is the industrially employed MTO catalyst and is therefore highly relevant to study.[2,42] Further to studying the reaction mechanism in H-SSZ-13 under isothermal conditions, probing the reaction mechanism in H-SAPO-34 is important for comparison of the zeolite with its silicoaluminophosphate analogue containing weaker acid sites (proven by NH_3-TPD in Chapter 2). The results of an experiment under temperature ramping conditions are shown, giving a straightforward comparison to the original H-SSZ-13 experiment.

In this experiment, the methodology was analogous to that used for the temperature ramped experiment of methanol over SSZ-13 catalyst.[22] The H-SAPO-34 was purchased from ACS Materials in proton form with (Al + P)/Si ratio 18. 50 mg was used in the experiment. The catalyst was pre-treated by heating to 550 °C at 8 °C min^{-1} in 20 % O_2/He mix and holding for 1 h. The catalyst was

then cooled to 100 °C under flowing He, when methanol was introduced to the catalyst by means of a syringe pump for 1 hour at a rate of 1.7 µl min^{-1} methanol flow in 30 ml min^{-1} He, giving a WHSV of 1.62 h^{-1}. The temperature was increased by 1 °C min^{-1} to 450 °C.

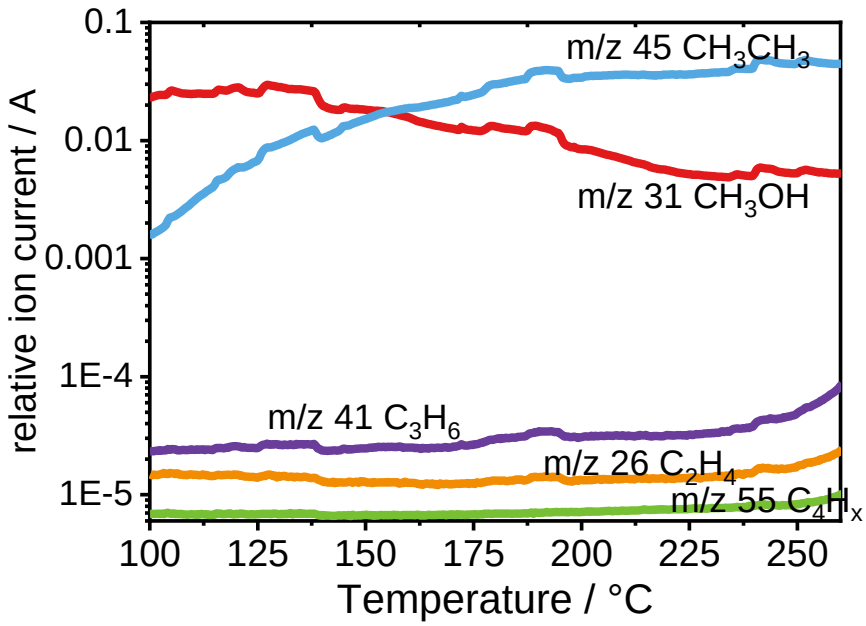

Figure 61 MS data acquired during the low temperature region from 100 – 250 °C of the reaction of methanol over H-SAPO-34 under temperature ramping conditions. WHSV 1.62 h^{-1}. *m/z* 31 (red) methanol, *m/z 45* (blue) dimethylether, *m/z 26* (orange) ethene, *m/z 41* (purple) propene, *m/z 55* (green) butenes.

Figure 61 shows the MS data acquired during the temperature ramp from 100 to 260 °C, whilst feeding methanol over H-SAPO-34 catalyst. In this period, methanol becomes increasingly consumed as *m/z* 31 decreases, and DME forms as *m/z* 45 increases. Little to no hydrocarbon products are formed up to 240 °C at which point ethene, propene and butene/pentene as indicated by *m/z* 26, 41 and 55 respectively, start to slightly grow, propene most rapidly.

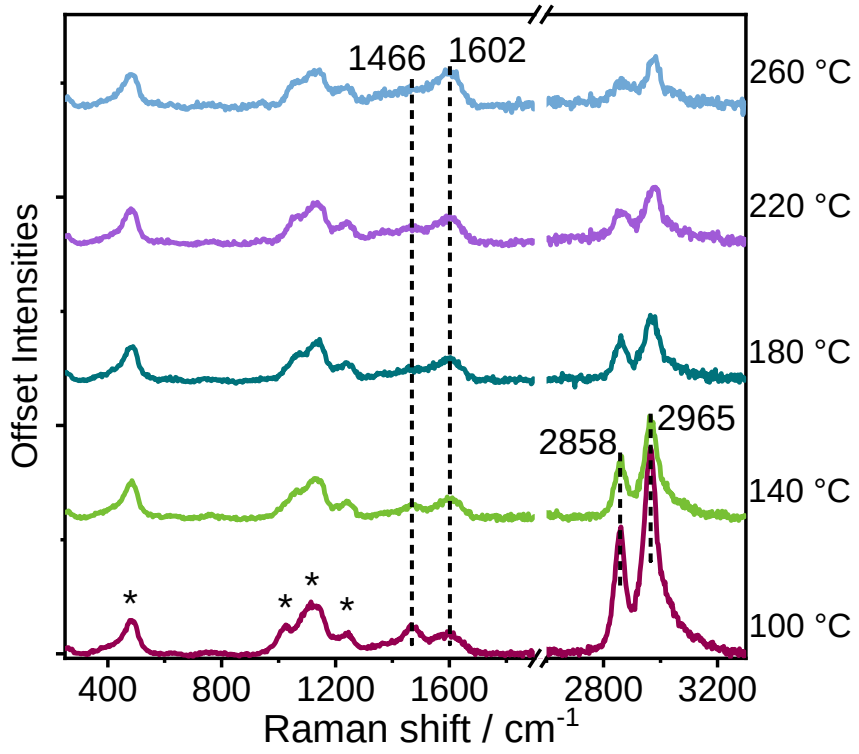

Figure 62 Kerr-gated Raman spectra collected during reaction of methanol over H-SAPO-34 catalyst under temperature ramping conditions at low temperatures from 100 – 260 °C. The methanol bands are attenuated with increasing temperature, as the signal in the C=C stretching region increases. The framework vibrations of the catalyst are indicated by the asterisks in the spectrum at 100 °C.

In Figure 62, Raman spectra are displayed corresponding to the period of increasing the temperature from 100 to 260 °C. At 100 °C, methanol is observed adsorbed by the intense bands at 2858 and 2965 cm^{-1} (CH_3 symmetric and asymmetric stretches) and by a smaller band at 1466 cm^{-1} (CH_3 deformation mode).[27,28] The C-O stretch expected at 1006 cm^{-1} is hidden by the vibrational modes of the catalyst. With increasing temperature to 260 °C, the CH_3 and C-O stretches of methanol decrease in intensity, in line with the methanol consumption observed by MS in Figure 63. The framework vibrations stay constant throughout this temperature ramping period, at 485 cm^{-1} corresponding to the T-O-T symmetric stretch at pore openings, and at 1025, 1122 and 1243 cm^{-1} to asymmetric P-O-P and P-O-Al stretches.[43] A small bump at 1602 cm^{-1} at 100 °C, may be due to hydrocarbon impurities on the catalyst surface, which are known to require long calcinations at high temperature in pure oxygen to entirely combust.[44] The bridging hydroxyl groups on zeolites were also shown through theoretical calculations to give a signal around 1600 cm^{-1} and might contribute

here.[22] However, the growing intensity of this signal – which is fairly broad – with increasing temperature can be explained by an increased concentration of carbonaceous species as the hydrocarbon pool builds up in the pores, the growth continues with further temperature increase as illustrated by the spectra in Figure 64 and described later.

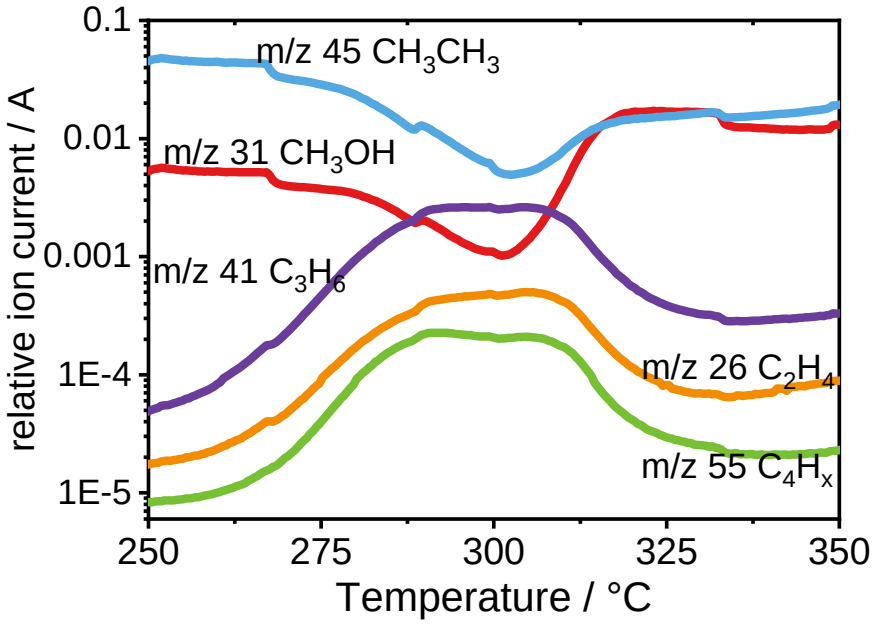

Figure 63 MS data acquired during the mid-temperature period of the reaction where the maximum catalyst activity is observed, from 250 – 350 °C in the reaction of methanol over H-SAPO-34 under temperature ramping conditions. WHSV 1.62 h^{-1}. m/z 31 (red) methanol, m/z 45 (blue) dimethylether, m/z 26 (orange) ethene, m/z 41 (purple) propene, m/z 55 (green) butenes.

In Figure 63, a dynamic system is observed by MS where the catalyst enters and leaves its most active period. With increasing temperature to 302 °C, the methanol signal continues to drop. This higher temperature for the maximum methanol conversion when compared with the analogous H-SSZ-13 experiment is in line with previous reports that higher temperatures are required due to the weaker acid strength of the silicoaluminophosphate material.[24,45] Hydrocarbon products, ethene, propene and butene/pentene (*m/z* 26 in orange, 41 in purple and 55 in green) are formed at increasing rates up to 290 °C, reaching a plateau for the next 20 °C of the reaction before the signals again drop, due to decreasing catalytic activity. The catalyst does not completely deactivate with this drop in hydrocarbon signals, as the ion current signals do not drop to as low as before

the period of high activity and, in fact, the ethene signal begins to climb again after 335 °C.

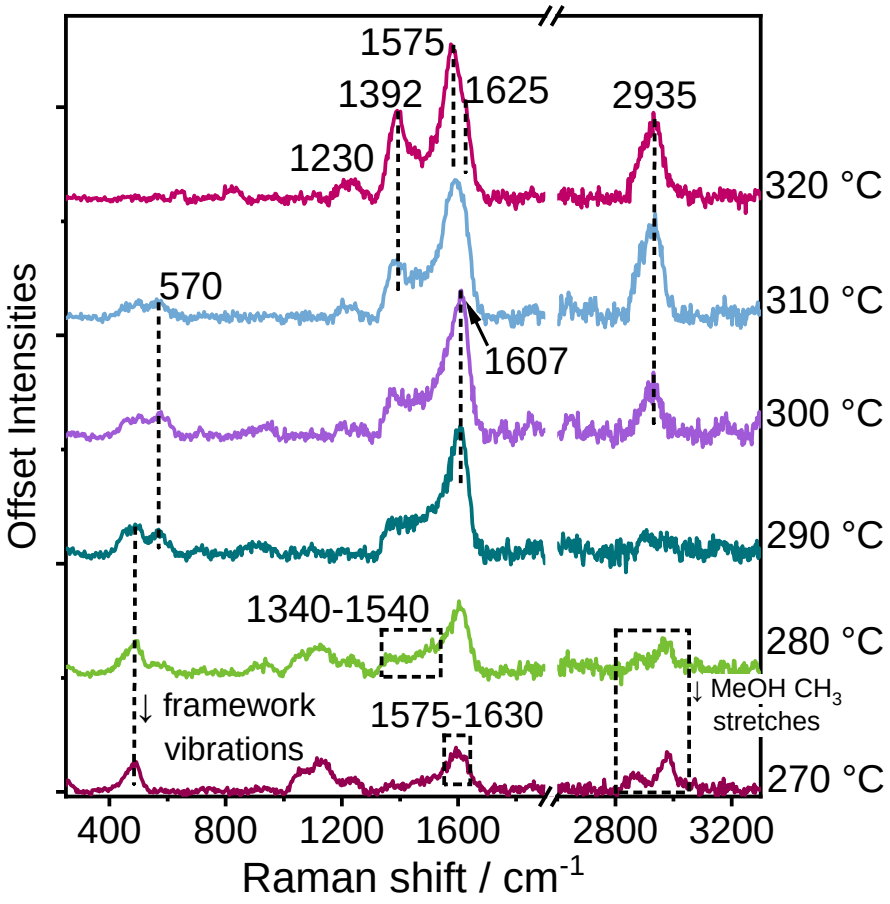

Figure 64 Kerr-gated Raman spectra collected during reaction of methanol over H-SAPO-34 catalyst under temperature ramping conditions during the autocatalytic period of the reaction from 270 – 320 °C.

The Raman data in Figure 64 accompanying the activity data is equally dynamic, with changes in speciation at each 10 °C interval. At 270 °C we can classify the end of the induction period. The small bump at 1602 cm^{-1} which was observed to grow during the induction period in Figure 62 reaches intensity as high as the framework vibrations. This broad feature reaching from 1575 – 1630 cm^{-1} likely encompasses a wide range of hydrocarbon species from isolated olefins which show C=C bond stretching frequencies at 1620 – 1630 cm^{-1} to monoenylic carbocations exhibiting C^{+}-C=C stretching frequencies at 1580 cm^{-1} and aromatic C=C ring stretches around 1590-1605 cm^{-1}.[22,33,35]

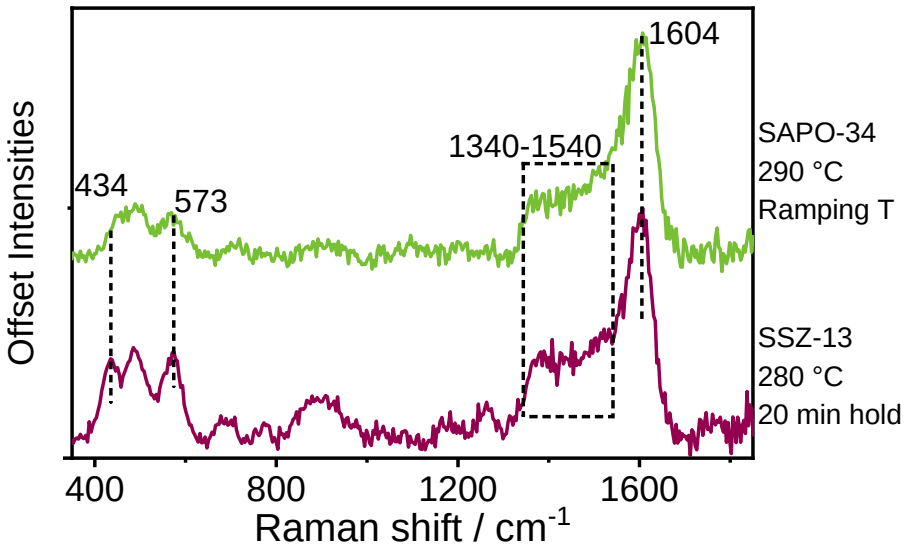

Figure 65 Comparison of Raman spectrum acquired at 290 °C during the reaction of methanol over SAPO-34 under temperature ramping conditions, with that acquired at 20 minutes on stream during the autocatalytic period of the reaction of methanol over SSZ-13 whilst holding at 280 °C.

By 280 °C this band grows again significantly and towers over the framework vibrations, and the methanol bands are barely discernible from the noise level of the spectrum, in line with rapid methanol consumption observed by MS. A strong vibration at 1607 cm^{-1} dominates the spectrum with a broad shoulder reaching far down to 1350 cm^{-1}. The spectrum holds many similarities to those measured during the autocatalytic period of the reaction in H-SSZ-13 at 280 °C, a comparison is given in Figure 65. While the band at 1604 cm^{-1} is characteristic of the C=C stretches in aromatics,[35] and the shoulder at lower frequency is broad. In this region, as observed in the autocatalytic period of the SSZ-13 catalyst, the broad shoulder from 1340 – 1540 cm^{-1} may contain contributions from dienylic carbocations at 1500 cm^{-1}, and CH_3 and CH_2 deformation modes at 1330 – 1440 cm^{-1} and possibly the breathing modes of naphthalenic species at 1360 – 1390 cm^{-1}.[21,29,34–36] Small bands grow at lower frequency, one at 570 cm^{-1} belonging to C-C stretching modes of planar carbon atoms bonded to 3 neighbouring carbon atoms, such as those in alkyl aromatic species.[22] The growth of these peaks is coincident with olefins reaching their maximum production as detected by MS, reiterating the important role of methylbenzenium ions in the reaction mechanism in this material. The similarities drawn from the Raman spectra so far reinforce the importance of topology in this reaction mechanism,

where despite differences in acidity, the species detected indicate similar reaction pathways.

With increase in temperature to 300 °C, the band at 1607 cm^{-1} again grows in intensity, as the concentration of species builds up. Interestingly a high frequency band at 2935 cm^{-1} grows which was not observed in the previous H-SSZ-13 experiments, in the region of H-C stretching frequencies of sp^3 bonded carbon species such as those in methyl groups on substituted aromatic species.[33,34] With increasing the temperature to 310 °C and 320 °C, most intense peak in the C=C stretching region frequency now sits at 1580 cm^{-1}. While species with vibrations in this region could be caused by monoenylic carbocations,[33] these species absorb below 300 nm and are therefore unlikely to be resonance enhanced by the 400 nm excitation wavelength used here to probe the sample, and this vibration towers over all others. Rather, as in the SSZ-13 experiments, this maximum is a combination of the peaks at ~1560 and 1620 cm^{-1} which is seen more clearly at higher temperatures, these vibrations are both caused by C=C stretching but the former belonging to polyenes and the latter to aromatic species, both of which would be resonance enhanced using this excitation wavelength.[22,37,45] The aromatic species here may be protonated naphthalenic species to have ring stretching vibrations at such high frequency.[21] A sharp peak at 1392 cm^{-1} and a small bump around 1230 cm^{-1} develop. The sharp peak at 1392 cm^{-1} is possibly caused by greater presence of naphthalenic species, which show an intense ring breathing mode of frequency ranging from 1360 to 1390 cm^{-1} depending on the degree of methylation.[21] C-H rock vibrations occur in the 1230 cm^{-1} region. The lower frequency band at 570 cm^{-1} which was earlier attributed to alkyl groups on methylated benzenium ions is no longer present.[22]

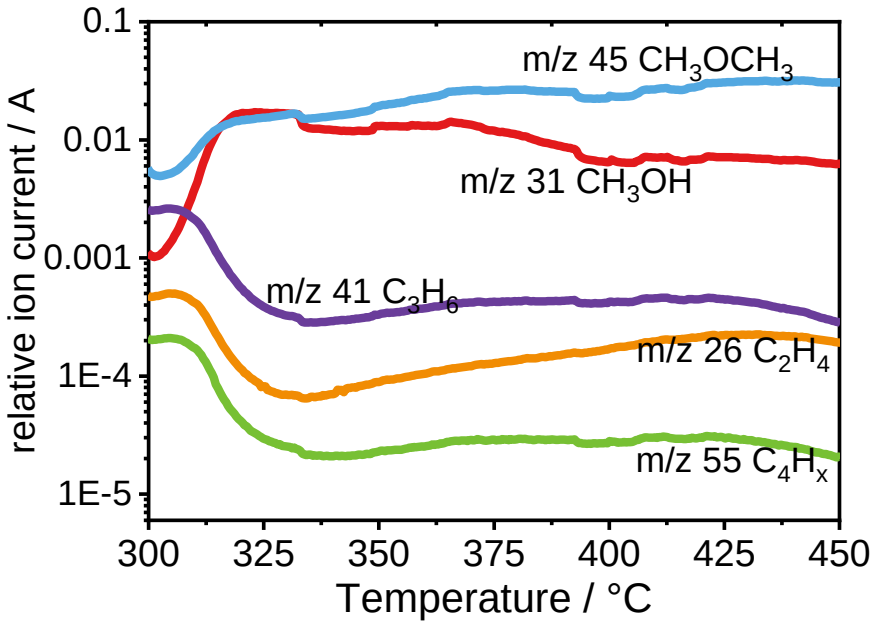

Figure 66 MS data acquired at high temperatures 300 – 450 °C in the reaction of methanol over H-SAPO-34 under temperature ramping conditions. WHSV 1.62 h^{-1}. m/z 31 (red) methanol, m/z 45 (blue) dimethylether, m/z 26 (orange) ethene and some contribution from propene, m/z 41 (purple) propene, m/z 55 (green) butenes.

As we enter the final temperature stage of the reaction, after the initial drop in methanol conversion, the methanol ion signal (*m/z* 31) again begins a gradual decline, while small olefin signals – particularly ethene (*m/z* 26) – slightly increase. This has been noted in previous literature and is known as the reanimation period; at low temperature, bulky species (for example highly methylated benzenium ions and methylated naphthalenic species) become unreactive in the pores due to steric hindrance, thereby deactivating the catalyst. As the temperature is increased, dealkylation reactions become thermodynamically favourable, and the large hydrocarbons can again partake in hydrocarbon pool chemistry.[46]

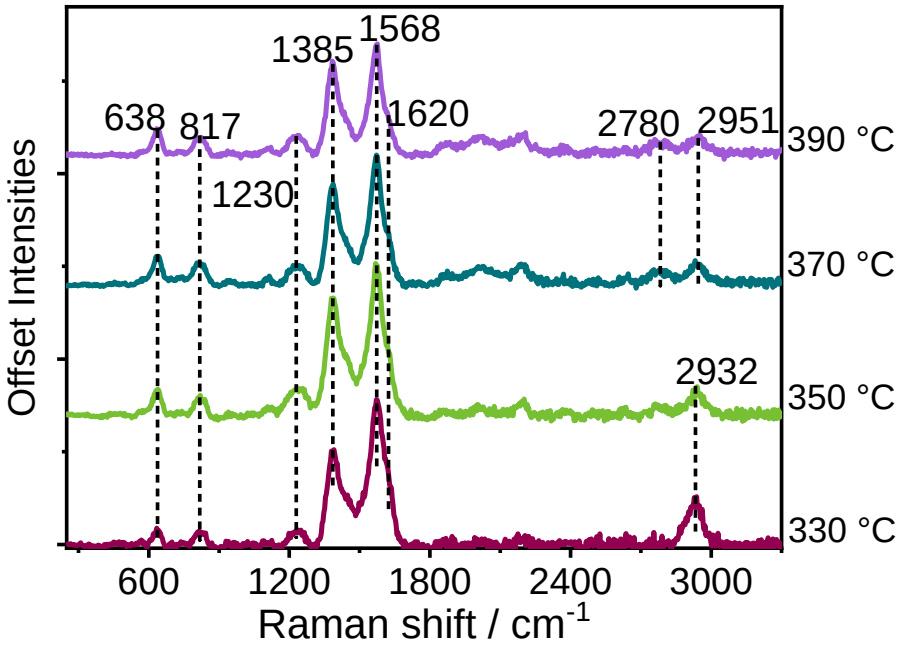

Figure 67 Kerr-gated Raman data acquired between 330 and 390 °C during temperature programmed reaction of methanol over H-SAPO-34.

By 330 °C all signals are very intense, implying a large resonance enhancement effect of the present species. Intense C=C stretching at 1568 cm^{-1} infers a dominance of polyene species, which were also observed in H-SSZ-13.[22] The aromatic C=C stretch is still present as a shoulder, around 1620 cm^{-1}, decreasing in intensity relative to the other peaks in the spectrum as the reaction progresses. A very strong band at 1385 cm^{-1} is unlikely to be caused by CH_3 deformations, but rather by a vibration which is resonance enhanced at 400 nm, such as breathing modes of protonated naphthalenic species and some other polyaromatic hydrocarbons.[37,45] The intensifying breathing mode at 1385 cm^{-1} is accompanied by bands at lower frequency at 638 and 817 cm^{-1} assigned to alkyl groups on polyaromatic hydrocarbons and ring-breathing modes of polyaromatic hydrocarbons, respectively.[22] Further temperature increase to 390 °C does not induce the formation of new bands in the low and mid frequency regions, only further intensification of bands attributed to polyaromatic species, as the lower frequency peaks become more obvious and the breathing modes around 1385 cm^{-1} grow to almost an equivalent height with the C=C stretching vibration of the polyene species.

At higher frequency, the intense peak attributed to sp^3 bonded carbonaceous species drops significantly, which could be in line with the dealkylation of

aromatics with increasing temperature as discussed on the previous page. Two small peaks at 2780 and 2950 cm^{-1} exist instead, which could possibly be described as overtones and combination bands, as well as others at 1870, 2011 and 2196 cm^{-1}. These higher order vibrations may be consistent with the formation of more ordered, graphitic hydrocarbon structures.[47]

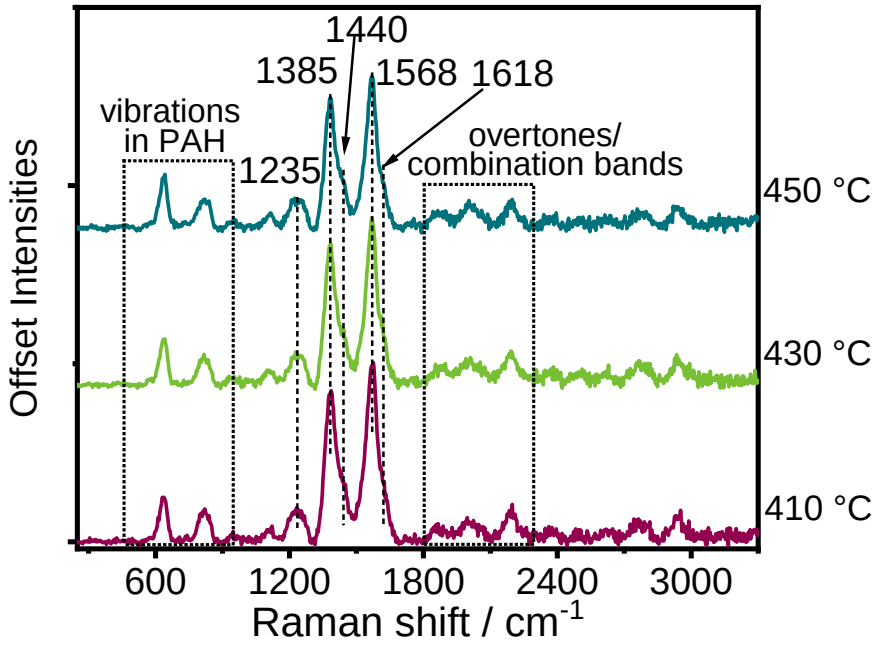

Figure 68 Kerr-gated Raman data acquired between 410 and 450 °C during temperature programmed reaction of methanol over H-SAPO-34.

With again further temperature increase, the band positions remain constant, with a high signal-to-noise ratio which indicates strong Raman scattering, given by resonance enhancement or possibly by the high polarizability of ordered hydrocarbon structures present. A shoulder grows at 1440 cm^{-1} which was shown by Stair to be due to polyaromatic hydrocarbons containing 5-membered rings such as fluorene or polyaromatics such as phenanthrene with rings in a bent chain configuration.[21] Otherwise, the low frequency vibrations of polyaromatics at 638 and 817 cm^{-1}, ring breathing modes of bi- or polycyclic aromatic hydrocarbons at 1383 cm^{-1}, C=C stretching of polyenylic species at 1568 cm^{-1}, overtones and combination bands only intensify further.

3.4.1 Discussion

The main conclusion to be drawn from the work on H-SAPO-34 is that the speciation throughout the experiment, as observed by Raman spectroscopy, is very similar to that observed during the experiment in H-SSZ-13. This has been observed previously, by UV-Vis by the group of Weckhuysen, who concluded that the nature of both the active and the deactivating species are similar in both catalysts which share the CHA topology.[24,45] In the temperature ramping experiment, at lower temperatures the induction period is observed, and only the small growth at 1602 cm^{-1} hints that a hydrocarbon pool is building, a signal possibly comprising isolated olefins, monoenylic carbocations and small amounts of aromatic species. By 280 °C the dramatic growth of this band along with others confirm the presence of alkylated aromatics, as well as possibly dienylic and naphthalenic species, these are responsible for the sudden increase in small olefins production and reaching the maximum methanol conversion. The maximum methanol conversion is reached at 302 °C, 20 °C higher than recorded for the maximum methanol conversion in H-SSZ-13. This has been documented in literature, where the effect of the higher acid site strength in H-SSZ-13 in the MTO reaction creates a lower reaction barrier to protonation and subsequent methylation reactions of hydrocarbon pool species, allowing the reaction to take place at lower temperatures.[45,48]

As the reaction proceeds and the methanol conversion and olefin production drop, this may again be attributed to the formation of polyenes in the *cha* cages, due to the new C=C stretch emerging at 1568 cm^{-1}. This polyene having C=C stretches in its conjugated π-system at a frequency 10 cm^{-1} higher than any observed in the H-SSZ-13 experiments can be due to a shorter chain length, giving a lesser degree of conjugation,[41] or alternatively, a higher signal intensity from the aromatic C=C stretching is more convoluted with this band in H-SAPO-34.

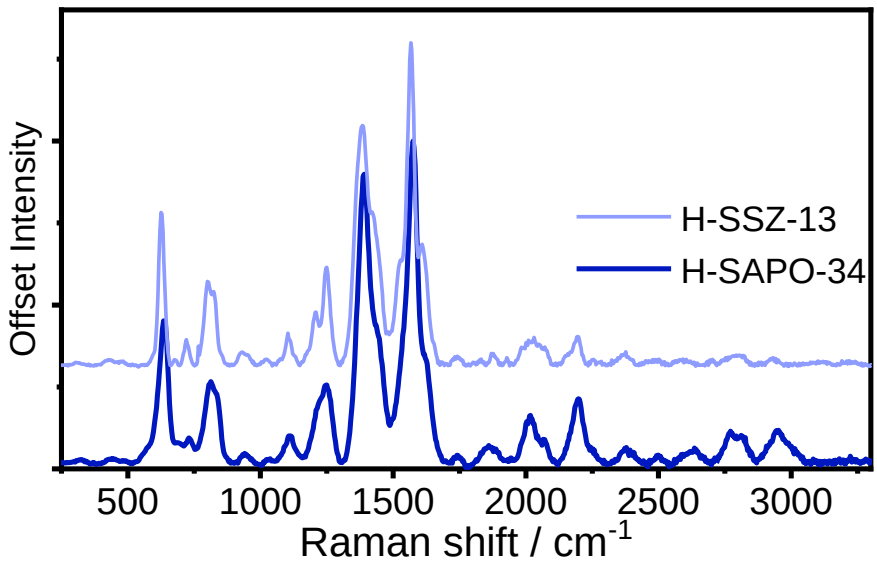

Figure 69 Kerr-gated Raman spectra of (top) H-SAPO-34 and (bottom) H-SSZ-13 after MTO reaction under temperature ramp from 100 - 450 °C. Spectra normalised to the highest intensity peaks for ease of comparison.

In Figure 69, the spectra acquired at the end of the temperature ramped MTO reactions in H-SAPO-34 and H-SSZ-13 can be compared. While there are some differences in relative peak intensities, the spectral overlap is very strong, with the band positions at the same frequencies confirming that overall, the species of hydrocarbons on the catalyst are the same. The intensity differences are in line with a lower degree of deactivation in H-SAPO-34, including a relatively lower peak for polyene species indicated by the C=C stretch as compared with the ring breathing mode of naphthalene, and less intense low frequency vibrations due to a lesser build-up of polyaromatic species.

The differences in terms of degree of deactivation were discussed previously and attributed to the weaker acid site strength in H-SAPO-34 than in H-SSZ-13.[24,45] Despite this difference, the same hydrocarbon species are observed to form and show similar reactivity behaviour.

3.5 Methanol-to-Olefins Ca/H-ZSM-5

Although the MFI topology of ZSM-5 is well known in MTH chemistry to allow or promote the formation of aromatics (MTG), its greater coking resistance than chabazite make it attractive as a catalyst for alkene production. Several studies exist where metal impregnation into zeolite pores is used to separate the two cycles (aromatic vs alkene), altering product distribution giving higher aromatic and ethene yields from the aromatic cycle or higher propene/butene yields from the alkene cycle. By impregnation of calcium, Yarulina *et al.* showed that the aromatic cycle could be inhibited, to give up to 90 % selectivity to light olefins.[14]

In this work, the mechanism of the MTH reaction was probed in H-ZSM-5 with Si/Al ratio 40 and impregnated with 6 wt. % Ca^{2+}, to prove the presence or absence of an aromatic cycle. The full synthesis method and characterisation data are given in Chapter 2. During the experiment, 50 mg of catalyst was pre-treated by heating to 550 °C at 8 °C min^{-1} in 20 % O_2/He mix and holding for 1 h. The catalyst was cooled to 100 °C under flowing He, when methanol was introduced into the 30 ml min^{-1} He feed by a syringe pump at 1.7 µl min^{-1} giving a WHSV of 1.62 h^{-1}. The temperature was increased by 1 °C min^{-1} to 525 °C.

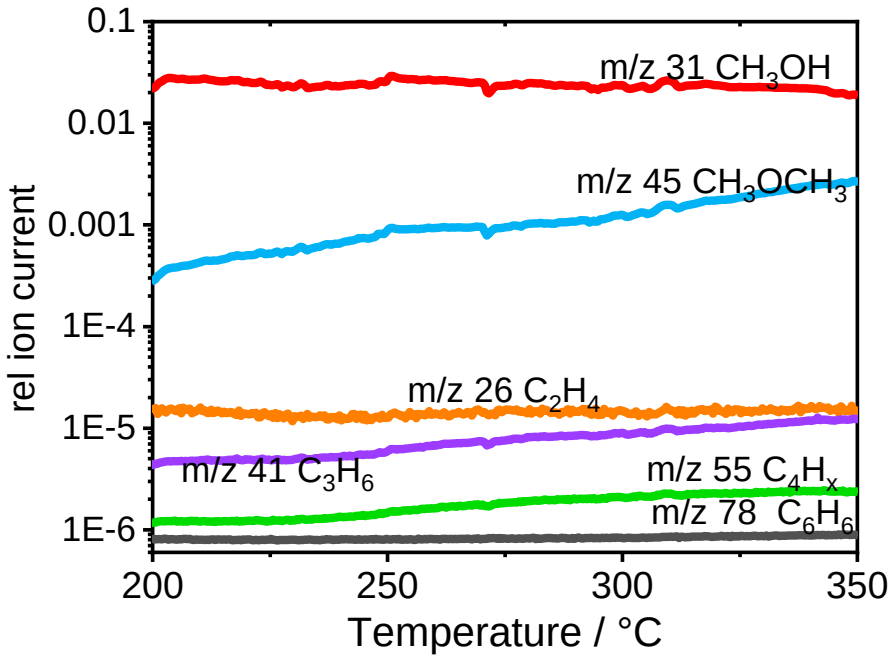

Figure 70 MS data during methanol reaction over Ca-ZSM-5, from 200 to 350 °C. m/z 31 (red) methanol, m/z 45 (blue) dimethylether, m/z 26 (orange) ethene, m/z 41 (purple) propene, m/z 55 (green) butenes and m/z 78 benzene.

The MS data shown in Figure 70 collected at low temperature during the temperature ramped experiment, shows little catalytic activity, apart from some dehydration of methanol to DME and from 230 °C and upwards some propene and butene/pentene products are formed, indicated by the ion signals *m/z* 41 and 55, respectively. The ethene signal at *m/z* 26 does not increase at all in this period, in line with ethene being formed from a mechanism separate from propene which requires aromatic reaction centres in catalyst pores.[11]

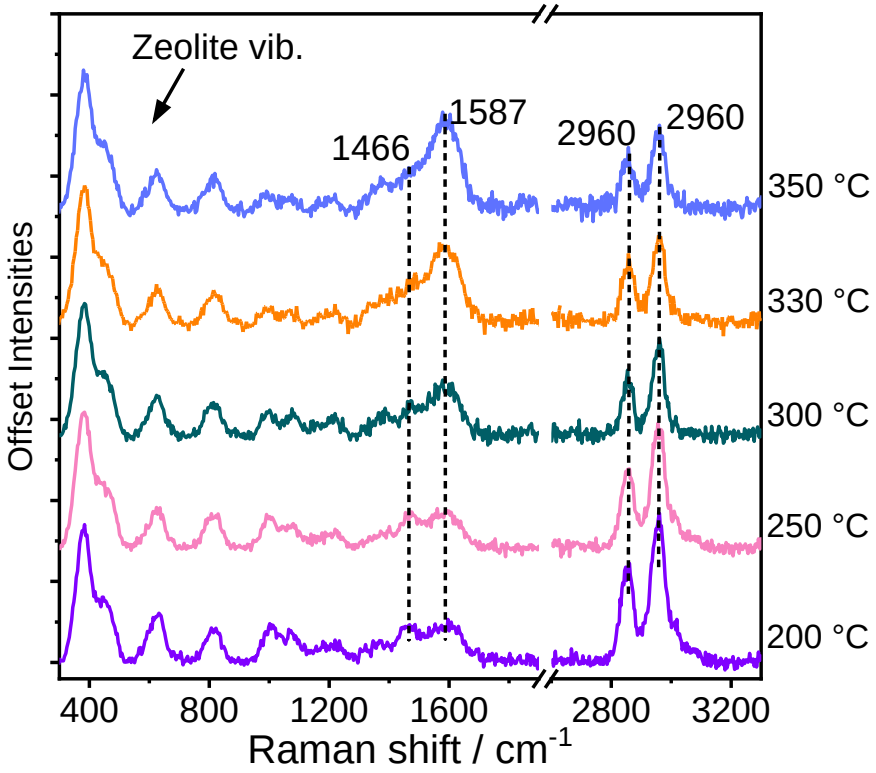

Figure 71 Kerr-gated Raman spectra collected during reaction of methanol over Ca-ZSM-5 catalyst under temperature ramping conditions from 200 – 350 °C.

During this low temperature period, the Raman signals of methanol observed clearly at 2960, 2855 and 1466 cm^{-1} decrease, in line with its consumption. There is broad growth in the mid frequency region, around 1587 cm^{-1}. This growth indicates a growing concentration of C=C bond containing species, and more specifically monoenylic carbocations with C=C-C^{+} frequencies at 1580 cm^{-1}, dienylic carbocations at 1500 cm^{-1}, and short chain olefins at 1600-1625 cm^{-1}.[22,33] Interestingly, the zeolite vibrations do not lose intensity, which likely signifies that the hydrocarbon signals detected are not given by a resonance enhancement effect, and therefore the species detected do not absorb at 400 nm, in comparison to the build-up of strongly resonance enhanced species in H-SSZ-13 or

H-SAPO-34 where the zeolite vibrations were weakened. The formation of benzenium ions in this period can therefore be ruled out, because although they also exhibit a C=C stretching frequency at 1595-1615 cm^{-1},[34,35] they would give very strong signals that would swamp the catalyst vibrations in comparison due to their strong absorbance at 400 nm.[24,37]

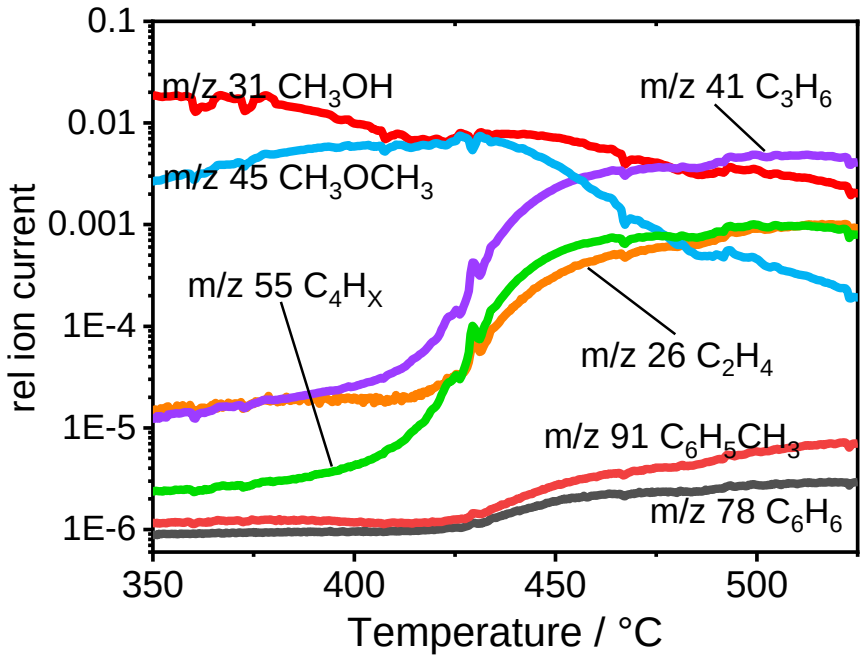

Figure 72 MS data of mid-high temperature region of methanol reaction over Ca-ZSM-5 catalyst from 200 to 350 °C. WHSV 1.62 h^{-1}. *m/z* 31 (red) methanol, *m/z* 45 (blue) dimethylether, *m/z* 26 (orange) ethene, *m/z* 41 (purple) propene, *m/z* 55 (green) butene, *m/z* 78 (dark grey) benzene, *m/z* 91 (dark red) toluene.

At higher temperatures we observe a drastic difference in catalytic activity by MS. Figure 72 demonstrates that above 400 °C, in the first place there is rapid increase in propene and butene/pentene production as indicated by *m/z* 41 and 55, respectively. This is followed shortly by the production of ethene and monocyclic aromatics – benzene and toluene – at 425 °C as indicated by m/z 25, 78 and 91. Since ethene has been proven to be formed through the aromatics cycle and is unfavourably formed by alkene cracking,[11] this would suggest that despite Ca^{2+} impregnation with an intention of suppression of the aromatic cycle, some aromatic mechanism can still take place. Note however, that the production of aromatics is still significantly lower than for H-ZSM-5 (Si/Al = 15), where m/z 91 is 2 orders of magnitude higher,[22] in agreement with previous works.[14] Dimethyl ether

is consumed above 425 °C, while increase in methanol consumption continues at a similar rate to prior to the higher production of olefins. There is a complicated equilibrium between methanol and DME in any form of the MTH reaction. Here, at lower temperatures below 425 °C there is mainly consumption of methanol to DME shown by dropping methanol signal *m/z* 31 and growing DME *m/z* 45, but at this temperature the reaction nature changes and DME becomes a strong methylating agent in the reaction for the hydrocarbon pool species that have formed, which would lead to methanol as a side product.

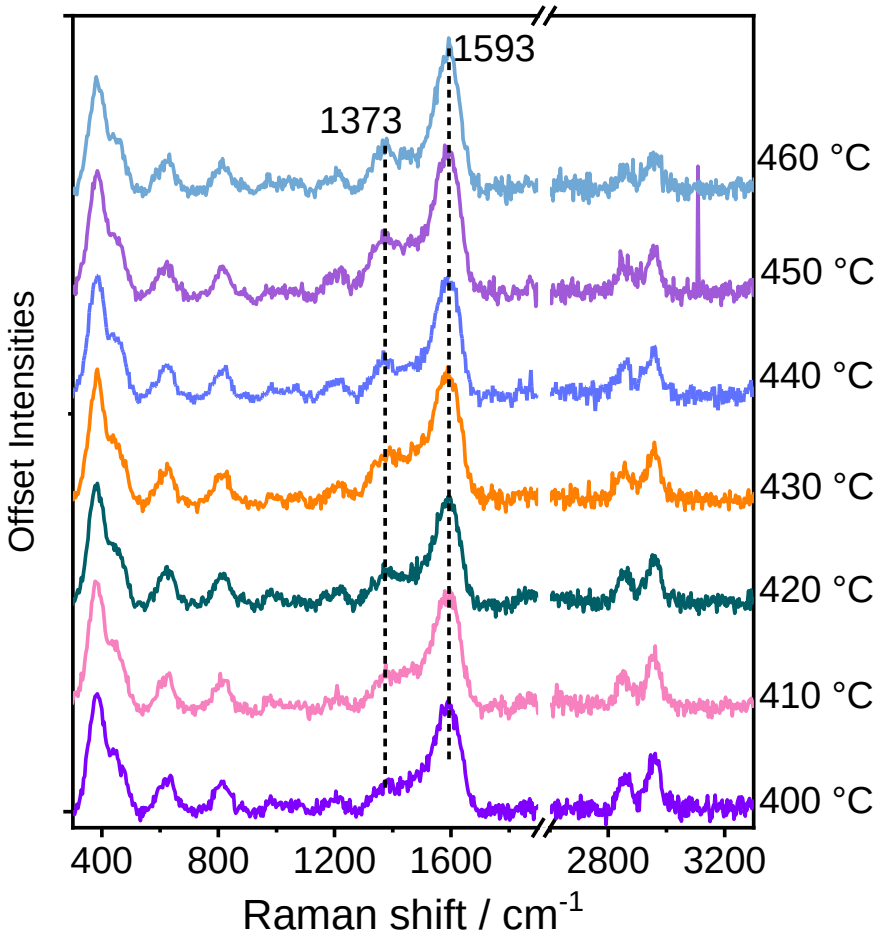

Figure 73 Kerr-gated Raman spectra collected during reaction of methanol over Ca-ZSM-5 catalyst under temperature ramping conditions from 400 – 460 °C.

Spectra recorded at 400 and 460 °C are shown in Figure 73 as growth continues in the broad C=C stretching region from as low as 1560 up to 1615 cm^{-1}. At 420 °C, the C=C stretch sharpens, and a band at 1365 cm^{-1} becomes more prominent. These changes could signify the formation of methylated aromatic

species, with their methyl group bending at 1365 cm^{-1}. Again, in this temperature region there is no drop in intensity of zeolite bands – since the species formed are not resonance enhanced, it may be that methyl benzenes but not the benzenium ions have formed.

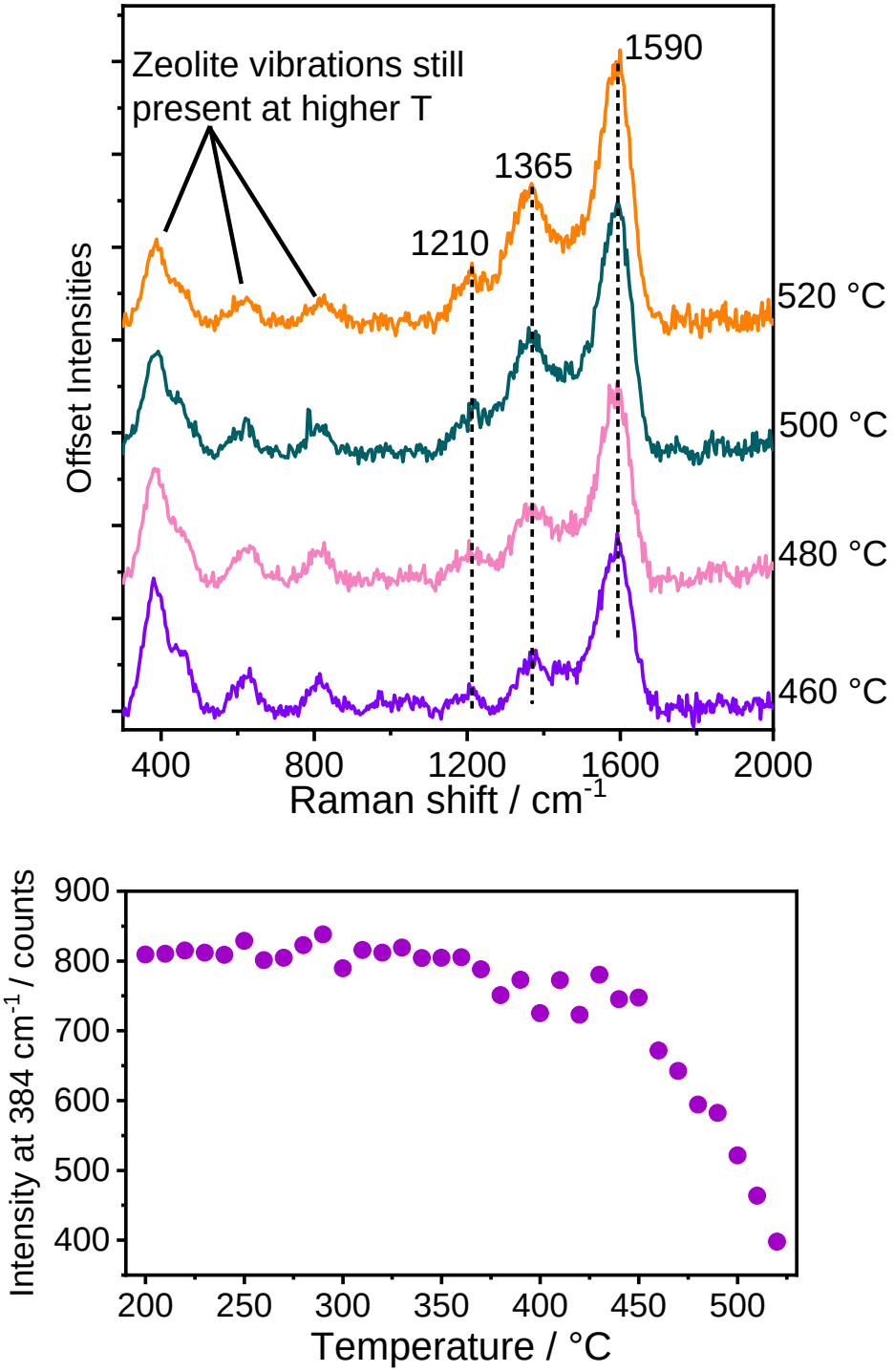

Figure 74 (a) Kerr-gated Raman spectra collected during reaction of methanol over Ca-ZSM-5 catalyst from 460 to 520 °C and (b) and plot of intensity of the Si-O-Si framework vibration of the zeolite against temperature indicating the drop in its intensity above 440 °C.

Progressive heating results in increased activity, and an increasing degree of methylation of the species on the catalyst surface, as indicated by the growth at 1372 cm^{-1} in Figure 73. Above 440 °C, the intensity of the catalyst vibrations starts dropping and this is demonstrated in Figure 74b which plots the intensity of the most intense framework vibration at 384 cm^{-1} with changing temperature. Throughout this experiment the framework vibration is not lost, which could occur because of a lack of strongly absorbing hydrocarbon species in the zeolite pores.

3.5.1 Diffuse Reflectance UV-Vis Spectroscopy

In a complementary DR-UV-Vis experiment where methanol was reacted over Ca-ZSM-5 zeolite during temperature ramping from 200 to 525 °C, the data is shown in Figure 75, which was to help in identifying the groups hydrocarbons involved at each stage of the reaction. A higher temperature of reactivity was observed by MS as compared with the Raman experiment, this is unusual and probably due to a different CCR1000 Linkam Cell used (same model). The trends of the reactions are the same and the data is discussed in terms of this.

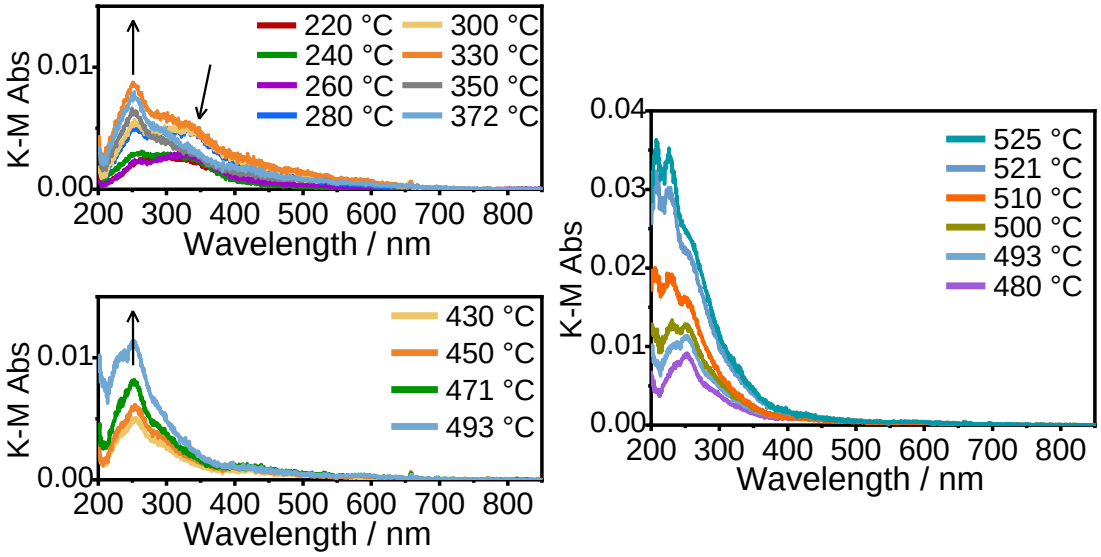

Figure 75 DR-UV-Vis spectra collected during conversion of methanol on Ca-ZSM-5 catalyst at (a) 220 – 370, (b) 430 – 493 and (c) 480 – 525 °C.

At lower temperatures, up to 270 °C, absorbance is recorded at very low intensity as a broad bump centred at 300 nm, but the breadth that may include also peaks at 260 and 340 nm. Peaks in this region are attributed to neutral olefins or

aromatics,[24,49] and the very low absorbance values indicate very low concentrations. This is consistent with only small amounts of hydrocarbons forming that was observed by Kerr-gated Raman in the early stages of reaction.

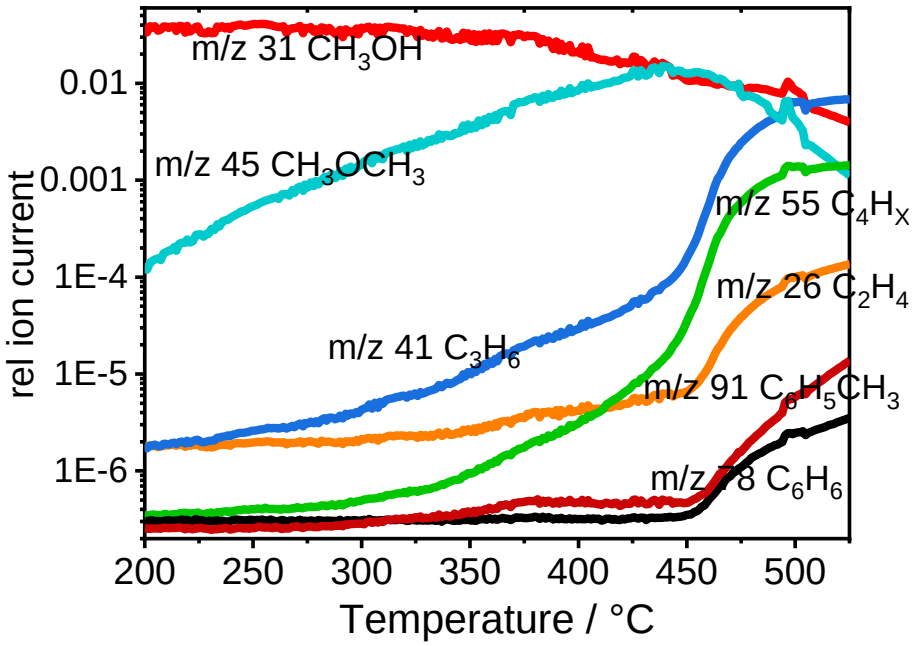

Figure 76 DR-UV-Vis spectra collected during conversion of methanol on Ca-ZSM-5 catalyst (top) and accompanying MS data (bottom) from 200 to 525 °C.

This signal slightly increases in intensity with increasing temperatures until about 250 °C when the components of the signal separate, with separate peaks arising at 260 and 325 nm. As the propene signal increases by MS, so too does the signal at 325 nm. Above 310 °C, growth occurs at 250 nm while at 340 °C the signal at 330 nm is attenuated. Apart from slight increasing in signal intensity, there are then very few changes amongst spectra until much higher temperatures above 480 °C which according to the MS data is the point where a great increase in activity occurs, with the DME signal (*m/z* 45) suddenly dropping with its consumption and drastic increase in olefins (C_2 – C_4) as well as some aromatic products at above 450 °C.

It is important to note, however, the absence of a band in the 380 – 400 nm region, confirming that protonated aromatic species – which are often said to be the main driving force of the reaction – are not present here. This agrees with the Kerr-gated Raman data where the constant intensity of the Raman bands of the

carbonaceous species to the zeolite framework vibrations suggested that no resonance enhancement was taking place below 400 °C, and therefore no species were absorbing at 400 nm. Although at very high temperatures, when aromatic species are detected, there is a very weak tail into the visible region which would explain the slight loss of zeolite framework vibrations at high reaction temperature because there is some resonance enhancement effect.

3.5.2 Discussion

Between the Kerr-gated Raman and DR-UV-Vis data, it appears likely that aromatic formation was hindered until very high temperatures of reaction. Ca impregnation did completely prevent the detection of any aromatic products until up to 420 °C. That ethene did not form as a product until after the zeolite vibrations were attenuated is strong evidence that the aromatic cycle was inhibited until this point. When aromatics did form, there was a sudden increase in activity as the MS signals for ethene, propene and aromatic hydrocarbons rose sharply. It is important to note that the aromatic species detected on the surface were not protonated, as confirmed by DR-UV-Vis by the lack of absorbance bands at 380 – 400 nm.[24,50]

This Kerr-gated Raman data also serves as a helpful example of how similar aliphatic and aromatic species can appear by Raman, consisting of C=C stretches of conjugated systems and methyl group deformations. However, from this data it appears as though polyenes do not form, where they were shown to form in H-ZSM-5 (Si/Al = 15) previously.

3.6 Methanol-to-Olefins Ca/H-SSZ-13

The work by Yarulina *et al.* in inhibiting the aromatic cycle is an interesting idea for the prevention of polyene cyclization, discussed earlier in this chapter. Could Ca^{2+} impregnation allow us to improve catalyst lifetime through preventing cyclisation of polyenes to polycyclic aromatic hydrocarbons?[14,22]

Here, H-SSZ-13 with Si/Al ratio 15 was impregnated with 6 wt. % Ca^{2+}, and Kerr-gated Raman employed to probe the MTO mechanism. 50 mg of catalyst was

pre-treated by heating to 550 °C at 8 °C min^{-1} in 20 % O_2/He mix and holding for 1 h. The catalyst was cooled to 200 °C under flowing He, and the masses recorded by MS allowed to equilibrate after methanol was introduced to the catalyst by means of a syringe pump at a rate of 1.7 µl min^{-1} giving a WHSV of 1.62 h^{-1}. Gas flows were constant at 30 ml min^{-1} He. The temperature was increased by 1 °C min^{-1} to 525 °C.

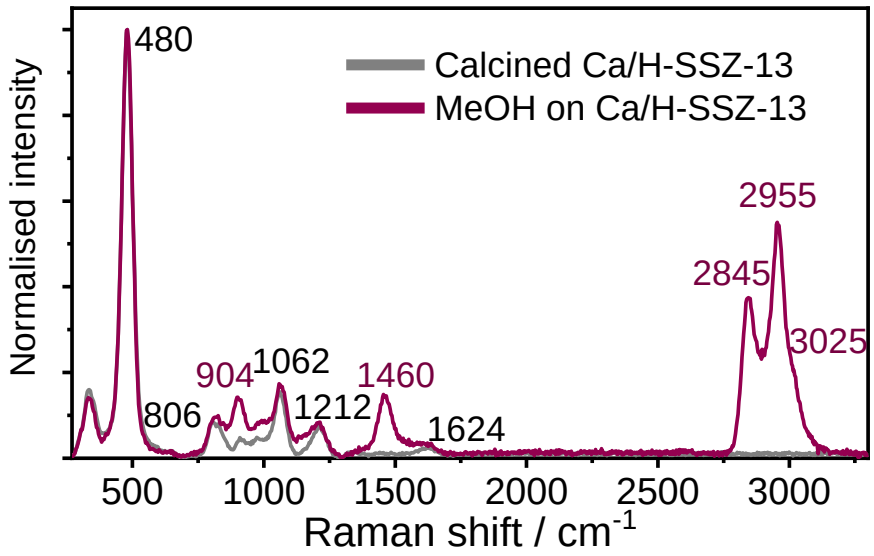

Figure 77 Calcined zeolite (Ca impregnated SSZ-13) before and after methanol adsorption.

In Figure 77, Raman spectra are compared before and after methanol was introduced to the calcined sample at 200 °C. The SSZ-13 framework vibrations are present; 334 cm^{-1} (pore openings), 480 cm^{-1} (T-O bend), 806 cm^{-1} (T-O-T symmetric stretch), and the intense band at 1062 cm^{-1} is attributed to calcium species.[51] As compared with other catalysts in this chapter when methanol is introduced, the bands in the CH stretching region are broader and more overlapped. After methanol is introduced, clear bands with peaks at 904 and 1460 cm^{-1}, and 2845 and 2955 cm^{-1} emerge. During methanol adsorption on H-SSZ-13 at 100 °C, bands at 1006, 1455, 2855 and 2954 cm^{-1} were assigned to the C-O stretching vibration, CH_3 deformation and CH symmetric and asymmetric stretches.[22,27] The differences observed may be due to a significant formation of DME on this catalyst due to higher temperature. Gaseous DME shows bands at 2989, 2881 and 2813 cm^{-1} but when adsorbed on ZSM-5 bands were observed at 3011, 2971 and 2842 cm^{-1},[52] and similar observations have

been published by other groups.[53] DME also exhibits CH_3 deformation vibration at 1460 cm^{-1} and C-O stretching at 930 cm^{-1},[54] which might be expected to move to lower wavenumbers after adsorption on an acid site.[55] Methanol to DME takes place easily at 200 °C, while the catalyst was held at this temperature to allow the signals to stabilise before starting the ramp, as shown in Figure 78 which shows *m/z* 45 increase by two orders of magnitude after methanol introduction at the expense of water release at *m/z* 18.

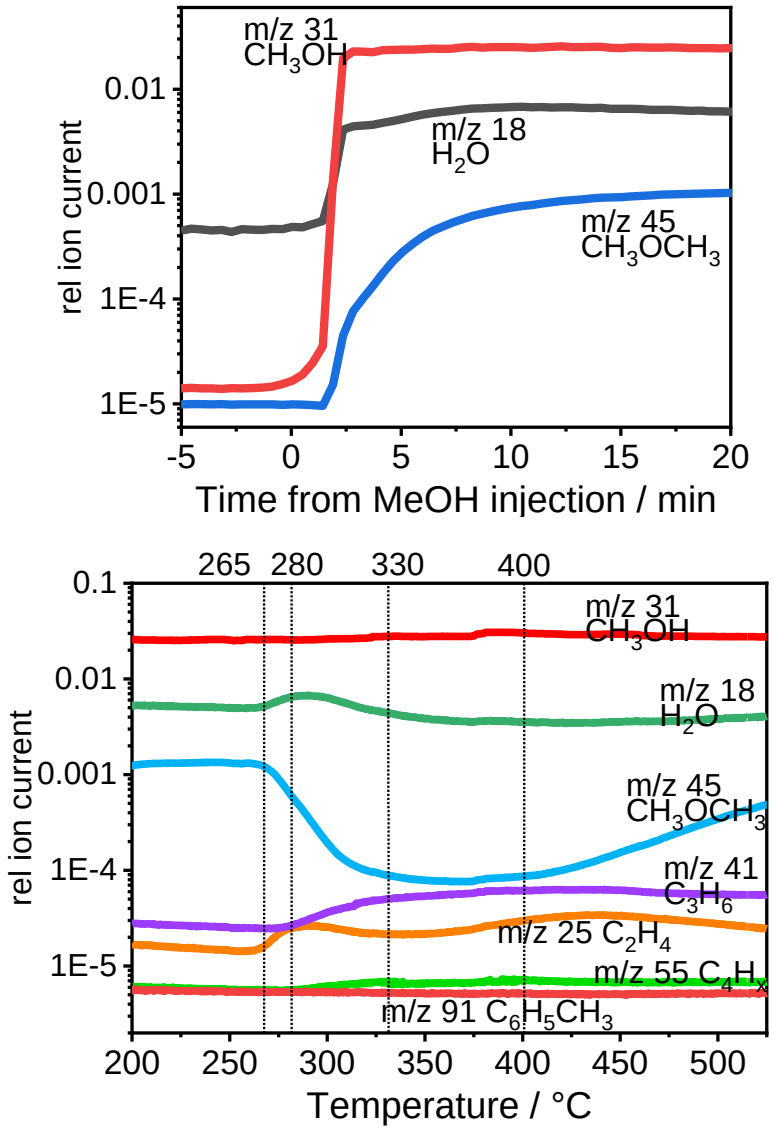

Figure 78 (a) MS data recorded upon introduction of methanol to Ca-SSZ-13, holding temperature at 200 °C and (b) MS data of MTH reaction on Ca-SSZ-13 from 200 to 525 °C. WHSV 1.62 h^{-1}. m/z 31 (red) methanol, m/z 45 (blue) dimethyl ether, m/z 26 (orange) ethene, m/z 41 (purple) propene, m/z 55 (green) butene, m/z 91 (dark red) toluene.

Apart from DME production, further reaction takes place only above 265 °C, where initially ethene is formed, shown here by *m/z* 26, while DME is rapidly consumed. There is no drop in the methanol signal *m/z* 31, the products here are therefore formed from reaction of DME. 15 minutes later at 280 °C, propene is formed, indicated by the increase in *m/z* 41. DME consumption increases rapidly to 330 °C where its signal stabilises, increasing again after 400 °C, indicating drop in consumption rather than increased formation. This signal increase not only signifies a drop in methanol to hydrocarbons activity, but also shows that the methanol to DME equilibrium is still at play, and acid sites for the dehydration of methanol are still at work. No aromatics are detected by MS during any point of the reaction as expected in chabazite catalysed MTO.

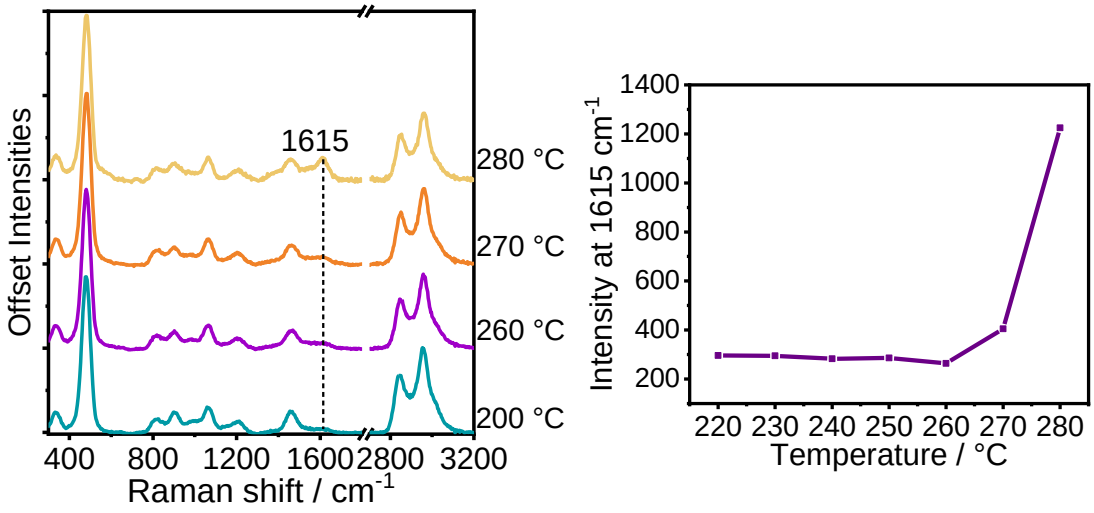

Figure 79 (a) Kerr-gated Raman spectra collected during reaction of methanol over Ca-SSZ-13 catalyst under temperature ramping conditions from 200 – 290 °C and (b) plot of the intensity of the C=C signal at 1615 cm^{-1} against temperature from 220 – 280 °C to correlate its growth with activity.

From 200 to 270 °C, there is little to no change observed amongst the spectra, the zeolite framework bands remain strong as do the CH stretching vibrations of adsorbed methanol or DME in the high frequency region and the C-O stretching vibration at 908 cm^{-1}. The only spectral change to accompany the increase in catalytic activity – observed by sudden DME consumption – is an increased intensity at 1615 cm^{-1} which is emphasised by the plot on the right side of Figure 79. Signal intensity at 1615 cm^{-1} is stable up to 260 °C where it is probably caused by residual carbon not burned during calcination, after which point its intensity

increases from ~300 up to 400 counts and then at 280 °C to 1200 counts. Growth in this region as stated previously can be caused by C=C stretches of monoenylic carbocations, aromatic ring stretches and olefins,[22,33,35] strongly indicating that the induction period of the catalyst has been reached which rationally explains the formation of small olefins above 260 °C.

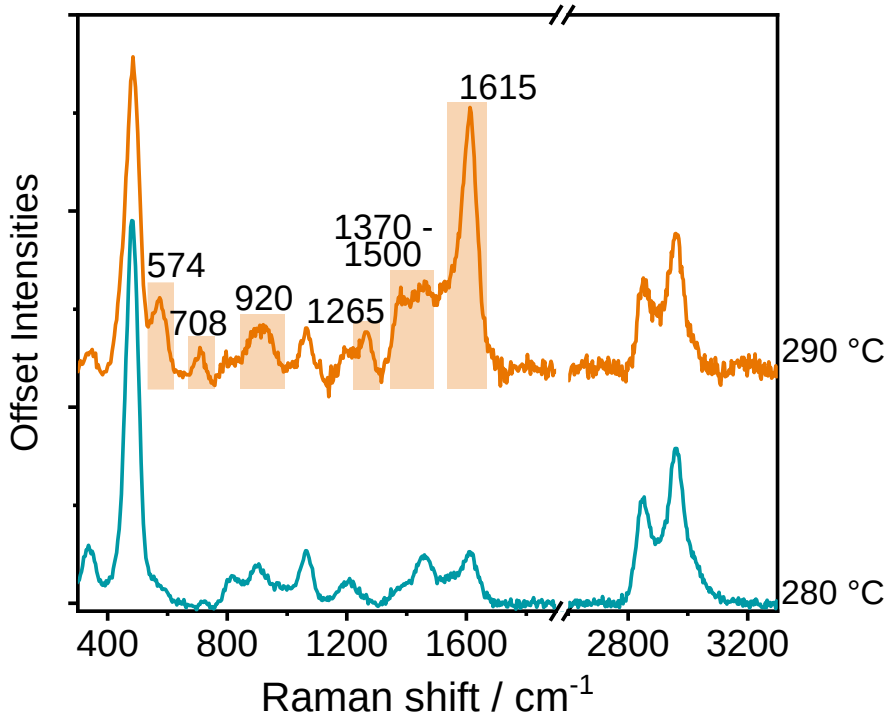

Figure 80 Kerr-gated Raman spectra collected during methanol reaction over Ca-SSZ-13 at 290 and 300 °C.

At 290 °C, the spectrum suddenly contains a lot of new information. The strongest peak at 1615 cm^{-1} is likely an indication of C=C stretches of protonated methylated aromatic species,[31] which would strongly absorb at the 400 nm wavelength probe used here to give very intense signals.[24,37] The 1330 – 1500 cm^{-1} region may include C=C stretches of dienylic carbocations at 1500 cm^{-1},[33] CH_2 and CH_3 group deformations at 1370 – 1410 cm^{-1} of olefinic species or of alkyl groups on aromatics,[22,34] and possibly naphthalenic breathing modes at 1360 – 1390 cm^{-1}.[21,36] The signal at 574 cm^{-1} was observed previously and further confirms the presence of alkylated aromatics, belonging to C-C stretching modes of planar carbon atoms bonded to 3 neighbouring carbon atoms.[22] The band at 1265 cm^{-1} can be attributed to symmetric C-C stretches in aromatic rings. [22]

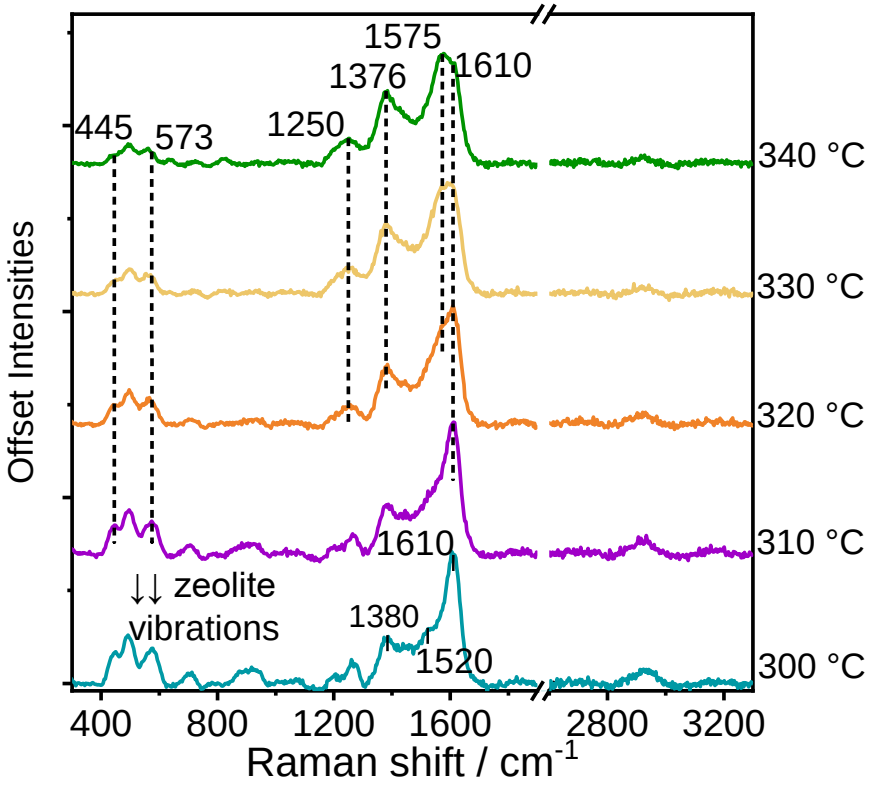

Figure 81 Kerr-gated Raman spectra collected during reaction of methanol over Ca-SSZ-13 catalyst under temperature ramping conditions from 300 – 340 °C.

With further temperature increase by just 10 °C, at 300 °C as shown in Figure 81, a significant drop in the catalyst framework vibrations is in line with pore filling of species which are resonance enhanced, therefore inhibiting the signals of the zeolite. Methylated benzenium ions are the primary species present, with a C=C stretch at 1610 cm^{-1}, CH_3 group deformations at 1380 cm^{-1}, stretch of trivalent planar C atoms at the carbon methylated in the ring at 574 cm^{-1}, CH rock of aromatics at 1198 and the C-C stretch of aromatic rings at 1265 cm^{-1}.[22] There is also a bump now at 1520 cm^{-1} which is in the region of C=C stretching of protonated dienylic species, or of polyenes which show stretching of their conjugated π-system from 1520 – 1580 cm^{-1},[33] however a polyene with a stretch at 1520 cm^{-1} should be on the longer side containing more than 7 conjugated double bonds – and therefore this makes an unlikely assignment here.[22] Rather, a peak in this region is caused by protonated dienes.[33]

At 320 °C, growth does start in what might be the region of conjugated π-systems of polyenes, from 1520 – 1580 cm^{-1}. By 330 °C this growth results in a band at

1575 cm^{-1} – assigned to C=C stretching in polyenylic species, this becoming the most intense band at 340 °C, while the lower frequency vibrations of methylated benzenium ions are attenuated. The peak at 1376 cm^{-1} became more prominent at 320 °C, and growth relative to other signals in the spectrum continues with increasing temperature. This strong signal implies the formation of naphthalenic species which would exhibit strong signals for their breathing vibrations in this region.[21,36]

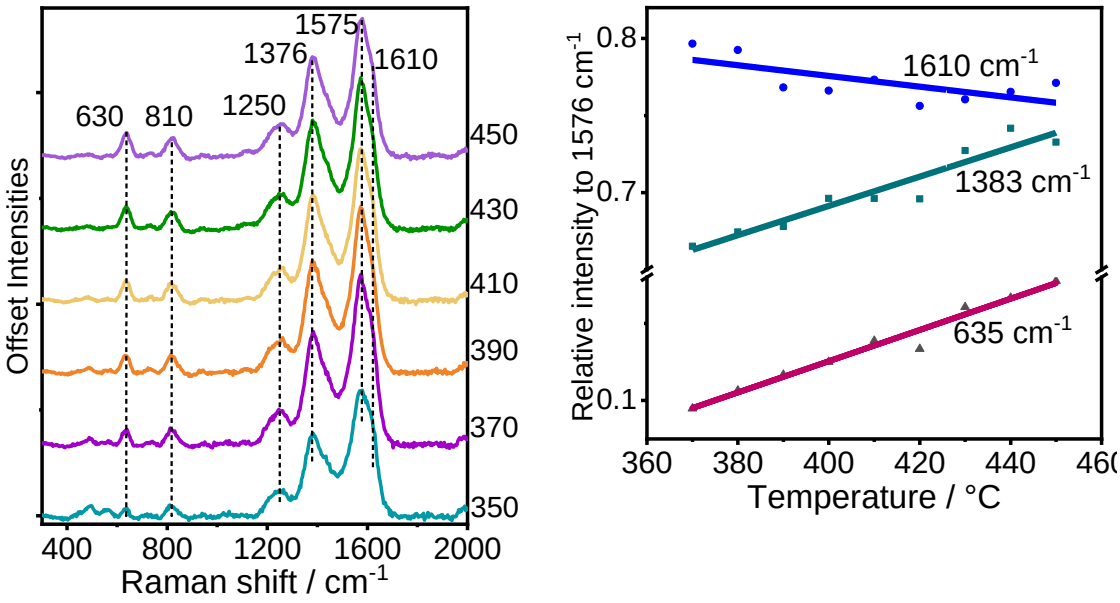

Figure 82 (a) Kerr-gated Raman spectra collected during reaction of methanol over Ca-SSZ-13 catalyst under temperature ramping conditions from 350 – 450 °C and (b) plots of relative intensities of 3 major peaks in the Kerr-gated Raman data at 638, 1382 and 1610 cm^{-1} relative to the most intense peak in the spectrum (at 1576 cm^{-1}).

Above 350 °C the zeolite framework vibrations are not distinguishable from the noise of the spectrum and new bands grow at 638 cm^{-1} and 818 cm^{-1} which are associated with the vibrations of polycyclic aromatic hydrocarbons. The plots of relative intensities of some peaks in the Raman spectra are shown in Figure 82, which demonstrates that with respect to the most intense peak at 1576 cm^{-1}, the intensity at 635 and 1383 cm^{-1} increase while that at 1610 cm^{-1} decreases. This indicates an increase in temperature and reaction progress leads to an accumulation of polycyclic aromatic hydrocarbons (peaks at 638 and 1383 cm^{-1}) as monocyclic aromatics are consumed (1610 cm^{-1}).

3.6.1 Diffuse Reflectance UV-Vis experiment

Ca^{2+} impregnated H-SSZ-13 was reacted under the same conditions as above, and the sample probed by UV-Vis spectroscopy. The initial spectrum of the catalyst was collected with a $BaSO_4$ background in the Linkam Cell, and then after the catalyst pre-treatment, a new background was acquired using the Ca/H-SSZ-13 before any methanol was introduced to the catalyst. In this way, the bands which develop are caused by the hydrocarbon species on the catalyst and are not from the zeolite. Spectra were collected in reflectance mode and converted to absorbance through the Kubelka-Munk theorem. Gases were analysed by a Pfeiffer mass spectrometer as before.

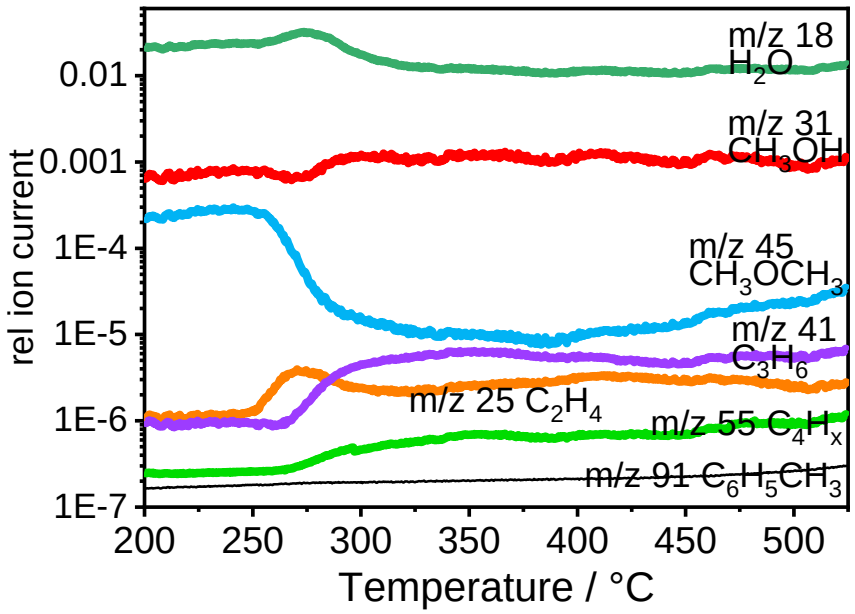

Figure 83 MS data collected during methanol reaction over Ca/H-SSZ-13 catalyst during diffuse reflectance UV-Vis spectroscopy.

The general trends shown in the MS data in Figure 83 are the same as those in Figure 78 where the same reaction was followed by Kerr-gated Raman, although there is some discrepancy in the temperature at which some events occurred. The formation of ethene for the first time as indicated by the sharp rise in *m/z* 26 takes place at 252 °C rather than at 265 °C and the drop in dimethyl ether signal *m/z* 45 at 257 °C rather than 280 °C. In general, the events take place 13 °C lower in temperature in the DR UV-Vis experiments, although they occur in the same order.

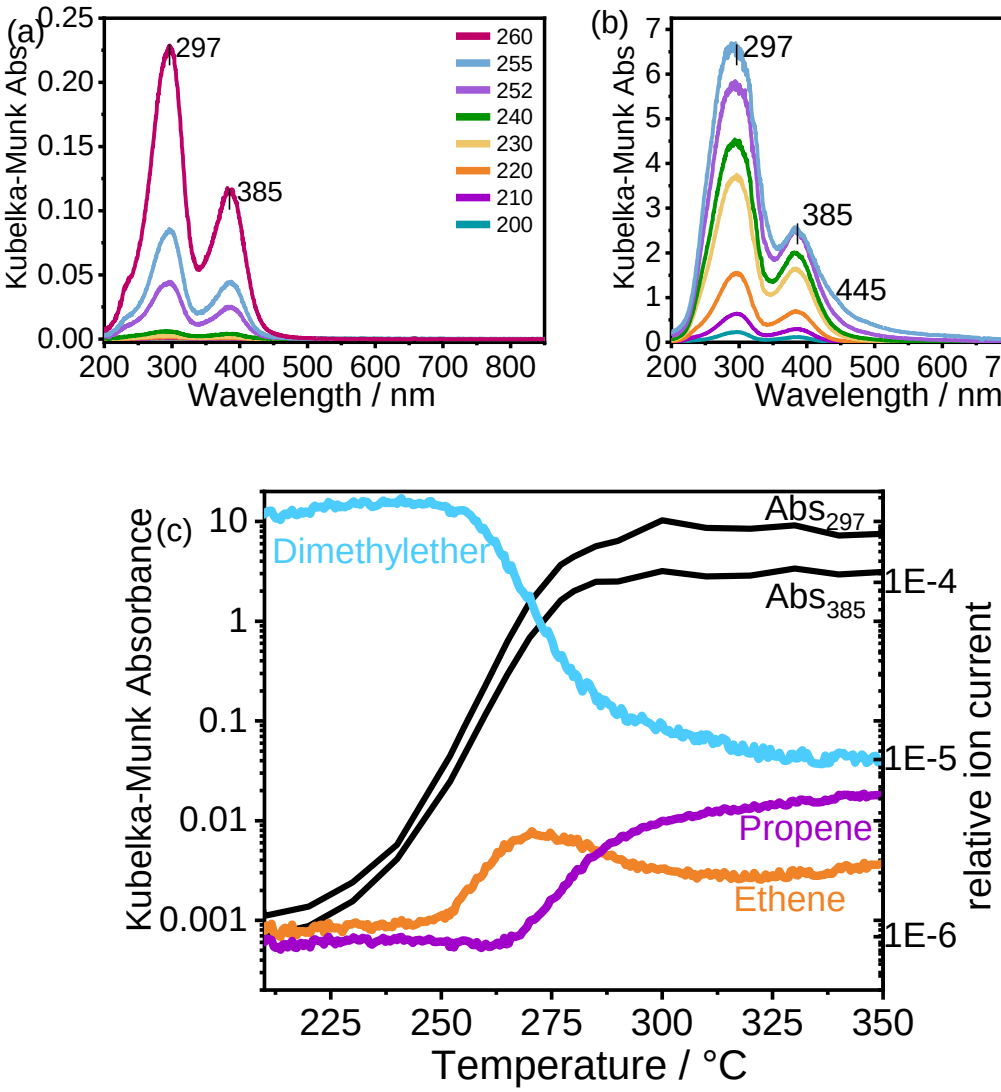

Figure 84 DR-UV-Vis spectra collected during methanol reaction on Ca-SSZ-13 catalyst during temperature ramp from (a) 200 to 260 and (b) 260 to 290 °C and (c) plot of intensity at λ 297 and 385 nm, together with the relative intensities of *m/z* 25 and 41 collected by MS to illustrate the formation of ethene and propene being produced after this increase in absorbance.

UV-Vis data did confirm the presence of protonated cyclic species. Growing absorbance at 385 and 297 nm from 200 to 260 °C indicate an increasing concentration of dienylic carbocations or protonated methylated aromatics, which show their π→π* transition around 385 nm, and monoenylic carbocations or protonated cyclopentadienyl ions at 297 nm.[24,35,50,56] Although methylated benzenium ions would also exhibit an electronic transition around 270 – 300 nm, it would be less intense than that at ca. 390 nm, and therefore we can infer also contribution from the protonated monoenylic species.[35,56] The growth of these

bands coincides with the production of ethene and propene, which is illustrated by the plot at the bottom of Figure 84, once absorbance reaches approximately 0.02 ethene is formed, and propene production stabilises as absorbance stops increasing.

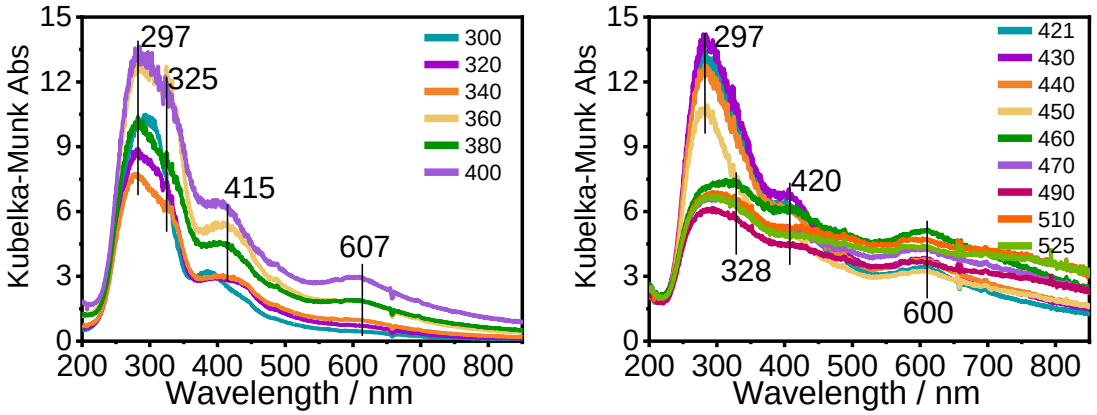

Figure 85 DR-UV-Vis spectra collected from 300 to 525 °C during conversion of methanol on Ca/H-SSZ-13.

With increasing temperature above 300 °C, some new absorbance bands in the lower energy region start to grow at around 488 and 607 nm. A change in λ_{max} from 385 to 418 nm has also occurred, which according to Borodina *et al.* is associated with the formation of protonated bicyclic (naphthalenic) species, and absorbance around 600 nm is related to the formation of larger protonated polyaromatic species such as phenanthrenes.[24,45] The very high absorbance overall and particularly at low energies beyond 700 nm are indicative of large graphitic structures, which Borodina concluded were able to form on the outer surface of H-SSZ-13 due to its high acidity.[24,45] The strong increase in overall absorbance is accompanied by the decreased conversion of DME at higher temperatures, and might occur due to pore blockage by these large graphitic hydrocarbons.

3.6.2 Thermogravimetric analysis of coke

A comparison of coke content through combustion is shown in Figure 86 of the samples from the Kerr-gated Raman experiments. In H-SSZ-13, a coke content of 12% burns off at maximum 550 °C compares with 5% at 545 °C in Ca/H-SSZ-13. The peak temperature is similar in both catalysts indicating similar

characteristics of the coke species, in agreement with the Raman data collected towards the end of reactions. The higher coke content of H-SSZ-13 will be caused by the higher reactivity of the catalyst due to the higher density of strong acid sites (as proven by NH_3-TPD in Chapter 2).

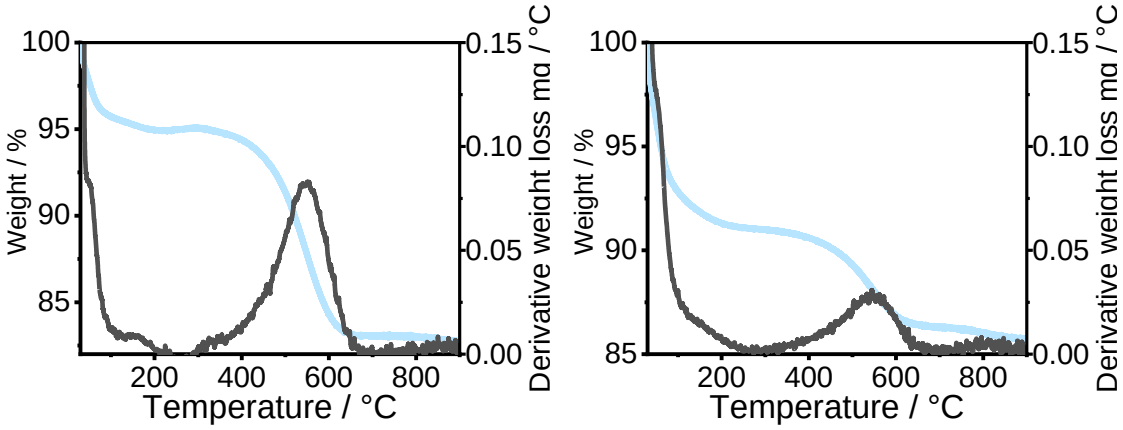

Figure 86 Plots of changes in weight of (a) H-SSZ-13 and (b) Ca/H-SSZ-13 after MTO in flowing oxygen with increasing temperature from 20 to 950 °C at a rate of 5 °C min^{-1}, derivatives in weight change are shown in grey.

3.6.3 Discussion

Both Kerr-gated Raman and DR-UV-Vis indicate that aromatics form in the Ca/H-SSZ-13 catalyst, and at high temperatures polyaromatics are even able to form which were identified by their ring opening vibrations in the low frequency region of the Raman spectra and by their absorbance at high wavelength in DR-UV-Vis. This unfortunately means that Ca impregnation was not successful in preventing the cyclization of aromatics as was hoped. In Chapter 2, Section 2.3.2, ammonia temperature programmed desorption experiments showed that Ca impregnation removed some of the strong Brønsted acidity but not all, as the high temperature desorption of ammonia peak was merely reduced and not removed. SEM-EDX in the same section showed that Ca was mainly located externally to the crystal rather than distributed homogeneously throughout the material, and therefore much of the Brønsted acidity inside the pores of the catalyst would not have been removed. The external surface area of the catalyst was decreased most significantly by Ca impregnation, again in agreement with most Ca having been deposited outside of the crystals. Working with smaller crystals may have helped to distribute Ca more homogeneously and a parent material with lower

aluminium content would also help to ensure lesser Brønsted acidity, since the Si/Al ratio here at 15 is lower than in H-ZSM-5 used at 40.

One unusual feature of the MTO reaction on Ca/H-SSZ-13 catalyst, the MS data recorded during the Kerr-gated Raman and DR-UV-Vis studies both show that ethene is formed before propene – in all studies in this chapter it is the only reaction where this happens. The mechanism of ethene formation has been determined in literature as part of the aromatic cycle, where alkylated aromatic molecules contract to cyclopentenyl species with an ethene leaving group.[4,11,57] The formation of ethene directly at 265 °C in Figure 78, without the aromatics cycle, which according to Raman data in Figure 80 does not form until between 280 and 290 °C, and prior to propene formation, is difficult to explain. This observation requires further investigation.

3.7 Conclusions

Running MTO experiments under isothermal conditions over H-SSZ-13 yielded results that agreed with MTO run under temperature ramping conditions, the aim of running additional experiments under isothermal conditions was to determine whether this would be the case. At the lowest temperature tested isothermally, an induction period was associated with the building hydrocarbon pool in the zeolite pores, followed by an autocatalytic period where methyl benzenium ions dominate the spectrum, with evidence too of dienylic carbocations as small olefins are detected by MS as products. Eventually after 30 minutes of reaction, methanol conversion slows down and after 40 minutes olefin formation slows down. By Raman, a shift in C=C stretch frequency after 33 minutes reveals that polyenes have started to form, which become clear at 40 minutes. At higher temperature of 350 °C, no induction period is observed as the catalyst immediately enters the autocatalytic period upon the introduction of methanol to the catalyst where methyl benzenium ions immediately dominate the Raman spectrum and olefin production starts. After only 7 minutes of reaction methanol conversion again slows down, as the C=C stretch shifts to reveal the formation of polyenes, and after 30 minutes of reaction the olefin products recorded by MS decrease as low frequency vibrations of polyaromatic hydrocarbons form.

The H-SAPO-34 catalyst shows a similar trend in reactivity as H-SSZ-13 – although it appears as though the polyenes formed are shorter with a C=C stretch at 1570 cm^{-1} compared with the 1551 cm^{-1} frequency recorded in H-SSZ-13. Further comment on this is made in Chapter 6.

Kerr-gated Raman and DR-UV-Vis are used to prove that Ca-impregnation onto H-ZSM-5 does alter the reaction mechanism, favouring the alkene cycle until high temperature (>425 °C) when monocyclic aromatic hydrocarbons and ethene do also form. For the most part, the aromatic cycle can be “switched off” by the reduction in Brønsted acidity. When aromatic hydrocarbons do form at higher temperature, UV-Vis confirms that these species are not protonated.

From the Kerr-gated Raman study of Ca-SSZ-13, as well as the formation of monocyclic aromatics which were evident to have formed at 290 °C, it was apparent that polyenylic hydrocarbons were still able to form by their C=C stretching frequency at 1570 cm^{-1}. In Chapter 2, SEM-EDX revealed that Ca species were located on the surface, and so the Ca impregnation should be optimised so ensure better diffusion of Ca into the zeolite pores.

3.8 References

1. M. Yang, D. Fan, Y. Wei, P. Tian and Z. Liu, Advanced Materials, 2019, 31, 1902181.
2. U. Olsbye, S. Svelle, M. Bjørgen, P. Beato, T. V. W. Janssens, F. Joensen, S. Bordiga and K. P. Lillerud, Angewandte Chemie International Edition, 2012, 51, 5810–5831.
3. B. P. C. Hereijgers, F. Bleken, M. H. Nilsen, S. Svelle, K.-P. Lillerud, M. Bjørgen, B. M. Weckhuysen and U. Olsbye, Journal of Catalysis, 2009, 264, 77–87.
4. M. Bjørgen, S. Svelle, F. Joensen, J. Nerlov, S. Kolboe, F. Bonino, L. Palumbo, S. Bordiga and U. Olsbye, Journal of Catalysis, 2007, 249, 195–207.
5. S. Nawaz, S. Kolboe, S. Kvisle, K.-P. Lillerud, M. Stocker and H. M. Øren, in Studies in Surface Science and Catalysis, eds. A. Holmen, K.-J. Jens and S. Kolboe, Elsevier, 1991, 61, 421–427.
6. I. M. Dahl and S. Kolboe, Catalysis Letters, 1993, 20, 329–336.
7. B. Arstad and S. Kolboe, Journal of the American Chemical Society, 2001, 123, 8137–8138.
8. B. Arstad and S. Kolboe, Catalysis Letters, 2001, 71, 209–212.
9. J. F. Haw and D. M. Marcus, Topics in Catalysis, 2005, 34, 41–48.
10. C. D. Chang and A. J. Silvestri, Journal of Catalysis, 1977, 47, 249–259.

11. S. Svelle, F. Joensen, J. Nerlov, U. Olsbye, K.-P. Lillerud, S. Kolboe and M. Bjørgen, Journal of the American Chemical Society, 2006, 128, 14770–14771.
12. D. Lesthaeghe, B. De Sterck, V. Van Speybroeck, G. B. Marin and M. Waroquier, Angewandte Chemie, 2007, 119, 1333–1336.
13. T. Liang, J. Chen, Z. Qin, J. Li, P. Wang, S. Wang, G. Wang, M. Dong, W. Fan and J. Wang, ACS Catalysis, 2016, 6, 7311–7325.
14. I. Yarulina, S. Bailleul, A. Pustovarenko, J. R. Martinez, K. D. Wispelaere, J. Hajek, B. M. Weckhuysen, K. Houben, M. Baldus, V. Van Speybroeck, F. Kapteijn and J. Gascon, ChemCatChem, 2016, 8, 3057–3063.
15. I. Yarulina, K. D. Wispelaere, S. Bailleul, J. Goetze, M. Radersma, E. Abou-Hamad, I. Vollmer, M. Goesten, B. Mezari, E. J. M. Hensen, J. S. Martínez-Espín, M. Morten, S. Mitchell, J. Perez-Ramirez, U. Olsbye, B. M. Weckhuysen, V. V. Speybroeck, F. Kapteijn and J. Gascon, Nature Chemistry, 2018, 10, 804–812.
16. Y. J. Du, W. D. Hu, C. M. Wang, J. Zhou, G. Yang, Y. D. Wang and W. M. Yang, Catalysis Science & Technology, 2021, 11, 2031–2046.
17. D. L. Obrzut, P. M. Adekkanattu, J. Thundimadathil, J. Liu, D. R. Dubois and J. A. Guin, Reaction Kinetics and Catalysis Letters, 2003, 80, 113–121.
18. E. Aghaei and M. Haghighi, Journal of Porous Materials, 2015, 22, 187–200.
19. D. R. Dubois, D. L. Obrzut, J. Liu, J. Thundimadathil, P. M. Adekkanattu, J. A. Guin, A. Punnoose and M. S. Seehra, Fuel Processing Technology, 2003, 83, 203–218.
20. H. A. Salih, O. Muraza, B. Abussaud, T. K. Al-Shammari and T. Yokoi, Industrial & Engineering Chemical Research, 2018, 57, 6639–6646.
21. P. M. Allotta and P. C. Stair, ACS Catalysis, 2012, 2, 2424–2432.
22. I. Lezcano-Gonzalez, E. Campbell, A. E. J. Hoffman, M. Bocus, I. V. Sazanovich, M. Towrie, M. Agote-Aran, E. K. Gibson, A. Greenaway, K. De Wispelaere, V. Van Speybroeck and A. M. Beale, Nature Materials, 2020, 19, 1081–1087.
23. U. Olsbye, M. Bjørgen, S. Svelle, K.-P. Lillerud and S. Kolboe, Catalysis Today, 2005, 106, 108–111.
24. E. Borodina, F. Meirer, I. Lezcano-González, M. Mokhtar, A. M. Asiri, S. A. Al-Thabaiti, S. N. Basahel, J. Ruiz-Martinez and B. M. Weckhuysen, ACS Catalysis, 2015, 5, 992–1003.
25. Y. T. Chua and P. C. Stair, Journal of Catalysis, 2003, 213, 39–46.
26. R. F. Howe, Suwardiyanto, D. J. Price, M. Castro, P. A. Wright, A. Greenaway, M. D. Frogley and G. Cinque, Topics in Catalysis, 2018, 61, 199–212.
27. J. Li, G. Xiong, Z. Feng, Z. Liu, Q. Xin and C. Li, Microporous and Mesoporous Materials, 2000, 39, 275–280.
28. Y. Yu, Y. Wang, K. Lin, N. Hu, X. Zhou and S. Liu, Journal of Physical Chemistry A, 2013, 117, 4377–4384.
29. Y. T. Chua, P. C. Stair, J. B. Nicholas, W. Song and J. F. Haw, Journal of the American Chemical Society, 2003, 125, 866–867.
30. C. L. Angell, Journal of Physical Chemistry, 1973, 77, 222–227.
31. J. H. Hibben, Chemical Reviews, 1936, 18, 1–232.
32. M. J. Wulfers and F. C. Jentoft, ACS Catalysis, 2014, 4, 3521–3532.

33. C. Pazè, B. Sazak, A. Zecchina and J. Dwyer, Journal of Physical Chemistry B, 1999, 103, 9978–9986.
34. J. Socrates, Infrared and Raman characteristic group frequencies tables and charts, John Wiley and Sons, Chichester, 3rd ed., 2001.
35. M. Bjørgen, F. Bonino, S. Kolboe, K.-P. Lillerud, A. Zecchina and S. Bordiga, Journal of the American Chemical Society, 2003, 125, 15863–15868.
36. M. Signorile, F. Bonino, A. Damin and S. Bordiga, Journal of Physical Chemistry C, 2015, 119, 11694–11698.
37. K. Hemelsoet, Q. Qian, T. De Meyer, K. De Wispelaere, B. De Sterck, B. M. Weckhuysen, M. Waroquier and V. Van Speybroeck, Chemistry – A European Journal, 2013, 19, 16595–16606.
38. W. Song, H. Fu and J. F. Haw, Journal of the American Chemical Society, 2001, 123, 4749–4754.
39. W. Song, J. F. Haw, J. B. Nicholas and C. S. Heneghan, Journal of the American Chemical Society, 2000, 122, 10726–10727.
40. F. Bleken, M. Bjørgen, L. Palumbo, S. Bordiga, S. Svelle, K.-P. Lillerud and U. Olsbye, Topics in Catalysis, 2009, 52, 218–228.
41. A. Baruya, D. L. Gerrard and W. F. Maddams, Macromolecules, 1983, 16, 578–580.
42. D. Chen, K. Moljord and A. Holmen, Microporous and Mesoporous Materials, 2012, 164, 239–250.
43. J. Tan, Z. Liu, X. Bao, X. Liu, X. Han, C. He and R. Zhai, Microporous and Mesoporous Materials, 2002, 53, 97–108.
44. W. Song, D. M. Marcus, H. Fu, J. O. Ehresmann and J. F. Haw, Journal of the American Chemical Society, 2002, 124, 3844–3845.
45. E. Borodina, H. Sharbini Harun Kamaluddin, F. Meirer, M. Mokhtar, A. M. Asiri, S. A. Al-Thabaiti, S. N. Basahel, J. Ruiz-Martinez and B. M. Weckhuysen, ACS Catalysis, 2017, 7, 5268–5281.
46. H. Schulz, Z. Siwei and H. Kusterer, Studies in Surface Science and Catalysis, 1991, vol. 60, pp. 281–290.
47. A. Sadezky, H. Muckenhuber, H. Grothe, R. Niessner and U. Pöschl, Carbon, 2005, 43, 1731–1742.
48. V. Van Speybroeck, K. Hemelsoet, K. De Wispelaere, Q. Qian, J. Van der Mynsbrugge, B. De Sterck, B. M. Weckhuysen and M. Waroquier, ChemCatChem, 2013, 5, 173–184.
49. P. J. Garratt, UV-vis atlas of organic compounds, 2nd ed., Heinz-Helmut Parkampus, Weinheim, 1992.
50. Q. Qian, C. Vogt, M. Mokhtar, A. M. Asiri, S. A. Al-Thabaiti, S. N. Basahel, J. Ruiz-Martínez and B. M. Weckhuysen, ChemCatChem, 2014, 6, 3396–3408.
51. M. Galván-Ruiz, J. Hernández, L. Baños, J. Noriega-Montes and M. Rodriguez-Garcia, Journal of Materials in Civil Engineering, 2009, 21, 625–708.
52. R. Osuga, T. Yokoi and J. N. Kondo, Molecular Catalysis, 2019, 477, 110535.
53. T. R. Forester and R. F. Howe, Journal of the American Chemical Society, 1987, 109, 5076–5082.

54. Y. Kanazawa and K. Nukada, Bulletin of the Chemical Society of Japan, 1962, 35, 612–618.
55. H. An, F. Zhang, Z. Guan, X. Liu, F. Fan and C. Li, ACS Catalysis, 2018, 8, 9207–9215.
56. E. D. Hernandez and F. C. Jentoft, ACS Catalysis, 2020, 10, 5764–5782.
57. J. F. Haw, J. B. Nicholas, W. Song, F. Deng, Z. Wang, T. Xu and C. S. Heneghan, Journal of the American Chemical Society, 2000, 122, 4763–4775.

4 Furan conversion: a comparison of topology

4.1 Introduction

Catalytic Fast Pyrolysis (CFP) is a process that can convert raw biomass directly into high value products including gasoline and light olefins and is one of many technologies that if harnessed properly could enable us to move towards carbon neutrality.[1–3] The aim of CFP is to give a final product with reduced oxygenates, through removal of CO, CO_2, and H_2O, to avoid the common problem of bio-oils which typically contain oxygenated molecules, making the oils acidic, unstable and miscible with water – undesirable properties for transportation fuels – and giving oils low heating values.[3–5] After solid biomass is pyrolyzed, the resulting volatile organic vapours undergo complicated mechanisms involving oligomerisation, cracking, alkylation, dealkylation and cyclization reactions on the catalyst as well as dehydration, decarbonylation and decarboxylation.[6,7]

Catalysts employed for CFP include zeolites, and some studies already demonstrate well that the zeolite topology plays an important role in determining the reaction products.[8–11] ZSM-5 has been consistently reported to give the highest aromatic yield,[8–10] with Jae *et al.* having shown that despite other zeolites having similar pore size or dimensionality to ZSM-5, none showed as high an aromatic selectivity at 35 %.[8] 3-dimensional, larger pore zeolites such as zeolite beta and Y show the highest selectivity towards specifically monocyclic aromatics but overall aromatic selectivity of 4.3 and 1.6 %, while smaller pore zeolites tend to produce more oxygenated species and no aromatics.[8–10] Clearly, the pore systems of the zeolites are imposing restrictions on the chemical reactions, promoting some pathways over others. Zeolite pores create confined spaces that can promote or inhibit some multi-molecular reactions through a confinement or solvation effect.[12] While ZSM-5 has to date shown the most promising behaviour in terms of selectivity and lifetime,[8,9,13] in this study we compare and contrast the nature of the intermediates formed in the ZSM-5 architecture with those formed in 3 other typically-studied zeolites; ferrierite, zeolite beta and zeolite Y.

Ferrierite is a medium pore zeolite containing 10-MR pores in one direction only, with 8-MR pores running perpendicular direction,[14] therefore for long-chain molecules the zeolite is a one-dimensional zeolite.[15] Beta is a large pore zeolite containing 12-MR pore openings, with straight channels running in three-dimensions, with channel intersections similar in size at 6.68 Å to those in ZSM-5 of 6.36 Å.[14] Zeolite Y is a large pore zeolite where the three-dimensional channel system contains large internal voids known as sodalite cages of 11.24 Å in diameter.[14] We note that in small pore zeolites (where maximum ring size contains less than 8 T sites) the pore openings are too small to interact with most molecules typical of biomass vapours, which is why they typically produce high yields of oxygenates,[8] and we chose not to study small pore zeolites here. The textural properties of these zeolites are again presented in Table 13. Strong acid site strength increases in the order of H-Y < H-beta < H-ferrierite < H-ZSM-5, as determined by NH_3-TPD, data is presented in Chapter 2.

	Largest no. of T-atoms at pore opening[14]	*Dimensionality of pore system*[14]	*Largest pore opening / Å*[14]	*Largest spherical volume that can be included / Å*^{3}	*Total surface area / cm*^{3} *g*$^{-1}$	*Micropore area / cm*^{3}	*High T desorption peak of ammonia / °C*
ZSM-5	10	3	5.6 x 5.3 5.5 x 5.1	6.36	347	239	440
Ferrierite	10	2	5.4 x 4.2 4.8 x 3.5	6.31	360	308	478
Beta	12	3	6.7 x 6.6 5.6 x 5.6	6.68	343	264	429
Y	12	3	7.4 x 7.4	11.24	745	611	378

Table 13 Summary of textural properties of the 4 zeolites studied in this Chapter; ZSM-5, Ferrierite, Zeolite Y and Zeolite Beta.

Furanic species make up a significant proportion of pyrolysis vapours from pyrolysis of lignocellulosic biomass, and Huber showed that furfural, furan,

glucose and cellulose gave similar aromatic product distributions for CFP.[16] This, combined with their high thermal stability make them useful and popular candidates as model compounds for simplifying this reaction for mechanistic analysis.[6,16–20] We therefore use furan as a model compound for studying this reaction.

An interesting study by Cheng and Huber analysed the reaction of furan on ZSM-5 under temperature programmed conditions for thermogravimetric analysis, with analysis of reaction products by online mass spectrometry (MS).[18] Other groups have also employed this method as a way to investigate the step-wise mechanisms for the formation of primary and secondary products.[21–23] At low temperatures they observed the removal of H_2O, CO and CO_2, and at intermediate temperatures olefins and aromatics production was observed.[18] We adopted this method for our study by Kerr-gated Raman Spectroscopy (KGRS), allowing us to apply controlled conditions to the reactions, using furan as a model compound to analyse why aromatic formation occurs. As well as KGRS, measurements were also performed using Diffuse Reflectance UV-Vis spectroscopy (DR-UV-Vis), recording changes in light absorption as the temperature ramp progresses. Through running experiments in this way, we were able to observe primary products, the intermediates and secondary products whilst separating from the rapid deactivation that occurs in furan reaction over zeolite catalysts. Although by KGRS we are able to collect data at extremely short timescales, multiple acquisitions are needed for reasonable signal-to-noise ratio and therefore the rapid deactivation (in around 5 minutes)[18] of zeolites by furan reaction remains a challenge in spectroscopic mechanistic studies. Some of our studies in MTH discussed in Chapter 3 highlight the benefit of running experiments under temperature ramping conditions to observe the earlier stages of reaction at low temperature which would otherwise happen too quickly, and in these cases, we also observed that similar species formed at all temperatures tested during non-ramping experiments but at different rates.

During these experiments, 50 mg of zeolite catalyst was pre-treated by heating at 10 °C min^{-1} in a flow of 20 % O_2/He to 600 °C and holding for 1 h in the Linkam CCR1000 cell. The catalyst was then cooled to 30 °C in He, and then furan was adsorbed by injection by a syringe pump at 6 µl min for 1 h, followed by flushing

for 1 h to remove much of the weakly adsorbed species. The temperature was linearly increased by 5 °C min^{-1} from 30 to 600 °C, and recordings taken every 25 °C; i.e. every 5 minutes. The MS data was normalised with respect to the flow of the carrier gas, to account for fluctuations in gas velocity or chamber pressure.

Since the samples were highly absorbing, to avoid laser damage to the sample, a low power of 1 mW was employed for the Raman measurements, and measurements taken for 2 x 4 second acquisitions. The laser wavelength for probing the sample was 400 nm. For UV-Vis experiments, spectra were recorded over a total of 20 seconds in reflectance mode and then converted to absorbance using the Kubelka-Munk formula. Experimental setup is described in Chapter 2.

4.2 Room temperature adsorption

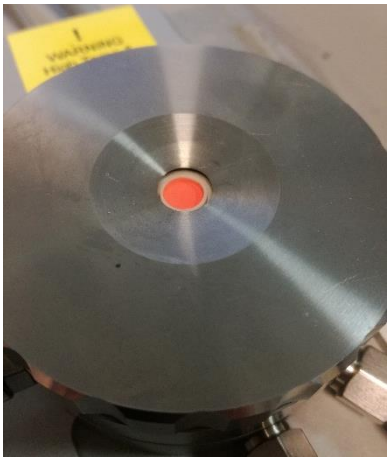

Figure 87 Image of the Linkam Cell holding 50 mg of H-ferrierite after furan adsorption for 1 hour at 30 °C showing the bright red/orange colouration of the sample.

The figures in this section illustrate the Raman signals and UV-Vis spectra observed after 1 hour of flowing furan over the 4 zeolites followed by flushing for 1 hour, at room temperature. Bordiga previously reported the oligomerization of 5-membered heterocycles, including furan, at room temperature and after contact with Brønsted the acid sites in zeolites, the colour immediately turns deep red or orange.[24] This has been also observed in our work as shown in the picture in Figure 87 which displays a picture of ferrierite in the Linkam Cell after furan adsorption, showing a bright orange colour.

Amongst all Raman spectra there is an intense band in the C=C stretch region from 1590 – 1630 cm^{-1} and then commonly there are 3 – 4 weaker bands at lower frequencies, near 1510, 1200 and 1400 cm^{-1} due to more conjugated C=C stretches, CH_3 deformations or CH_2 wag, twist, or deformation vibrations.[25,26] The DR-UV-Vis spectra also show similarities in the positions of the bands measured after furan adsorption and are linked to the level of conjugation in the surface species, these are compared in Table 1 below. The vibrational frequencies measured after room temperature adsorption on zeolites do not correspond to those observed experimentally or calculated theoretically in previous literature for furan in the gas or liquid phase.[24,27] Raman bands characteristic of free furan molecules have been identified by Spoto *et al.* at 1384, 1460, 1490 and 1586 cm^{-1}.[24] The Raman spectra described below differ from the Raman spectra of free or adsorbed furan, and combined with the DR-UV-Vis data, we confirm that oxygenated polymeric species formed after protonation.

Level of conjugation	π→π* / nm
1 double bond	< 190
2 conjugated double bonds	220 - 245
3 conjugated double bonds	250 - 290
5 conjugated double bonds	280 - 350
1 double bond and +ve charge	280 - 330
2 double bonds and +ve charge	360 - 380
3 double bonds and +ve charge	430 - 470
4 double bonds and +ve charge	485 - 515
5 double bonds and +ve charge	> 540

Table 14 Approximate absorbance wavelengths as a function of degree of conjugation of an organic molecule, summarised from refs.[24,28–32]

The Raman spectrum of furan adsorbed on H-ZSM-5 is shown in Figure 88a, the most intense band sits at 1620 cm^{-1}, a relatively high frequency for a C=C double bond stretch, that might suggest either isolated C=C bonds or small olefins,[26,33] or possibly confined C=C bonds in the larger polymeric structure. This vibrational frequency was observed by the groups of Zecchina and Chen when working on the transformation of furfuryl alcohol, and assigned to polymers of the 2,3-disubstituted furan rings.[34,35] Linear polyfuran which consists of furan

monomers linked by C atoms in the 2 and 5 positions are also recorded to show C=C stretch modes of the ring around 1620 cm^{-1}.[36,37] An assignment to polymeric furan rings that remain intact supports the polymer structures put forward by Bordiga.[24] The asymmetry of this band would indicate that a different C=C stretch is also present vibrating at lower frequency, which might be related to free or adsorbed furan molecules having a C=C stretch frequency at 1585 – 1590 cm^{-1}.[24,27,38] A sharp peak at 1500 cm^{-1} is characteristic of C-C=C^+ stretches in unsaturated carbocations.[32,39–42] A broad band from 1370 – 1410 cm^{-1} might be assigned to free and adsorbed furan molecules since a strong ring stretching vibration would be expected at 1385 cm^{-1},[24,25,38] but is also in the region of CH_2 and CH_3 deformations,[33,38,43] while a band at 1160 cm^{-1} can be attributed to CH rock vibrations.[43] CH_2 groups must exist for the formation of furan polymers of any length, formed through intramolecular hydrogen transfer after protonation.[24]

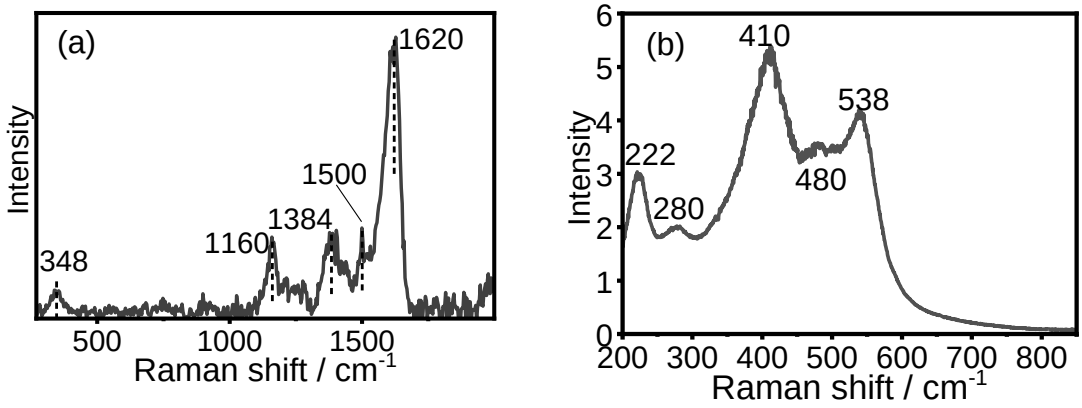

Figure 88 (a) Kerr-gated Raman spectrum and (b) DR-UV-Vis absorbance spectrum recorded after adsorption of furan at 30 °C on H-ZSM-5, followed by 60-minute flush in He.

The corresponding UV-Vis spectrum in Figure 88b shows clear, distinct bands at 220, 280, 410, 480 and 538 nm. The band at 220 nm is due to neutral, adsorbed furan species as confirmed by Spoto *et al.* who studied the adsorption of pure furan vapour as well as adsorbed on the surface of silicalite and zeolites,[24] and this also corresponds to liquid furan.[31] The bands near 280 nm are attributed to monoenylic carbocations,[24,28,29] 410 nm due to a species containing 2 – 3 double bonds and a positive charge,[29] and that at 538 nm to a species containing 5 double bonds and a positive charge.[24,29] From this data, a mixture of adsorbed neutral furan, protonated furan, and protonated polymers the length of 2 and 3

furan monomers are proposed to have formed already on the zeolite at room temperature.

Since these species also contain oxygen, they would likely contain n→π* transitions at lower energies which might be observed by UV-Vis, although their extinction coefficients (ε) should be low compared with the π→π* and they are therefore not observed in this data. For example, the $\varepsilon_{n\rightarrow\pi^*}$ transition in furan is ~10^6 times lower than $\varepsilon_{\pi\rightarrow\pi^*}$.[31]

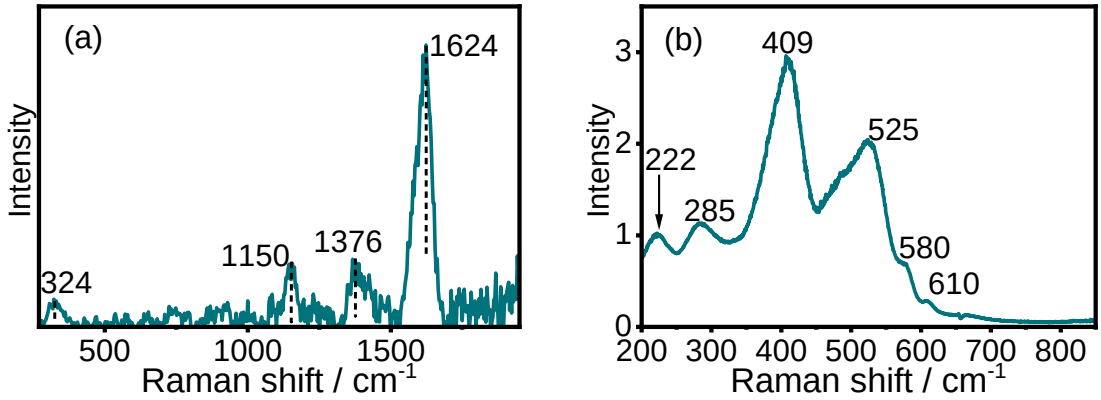

Figure 89 (a) Kerr-gated Raman spectrum and (b) DR-UV-Vis absorbance spectrum recorded after adsorption of furan at 30 °C on H-Ferrierite, followed by 60-minute flush in He.

In Figure 89 the Raman and DR-UV-Vis spectra are shown after the same experiments performed in H-Ferrierite. By Raman, the most intense band is again seen in the C=C stretch region at 1624 cm^{-1} – in the region of either isolated C=C bonds,[26,39] or of large polymeric-type species.[36,37] This band is again asymmetric, it therefore likely contains some vibrations at a lower frequency also in the C=C stretch region. The band at 1376 cm^{-1} could be allocated to the ring stretching modes in furan molecules or to CH_2 deformations,[24,33] and that at 1150 cm^{-1} to CH_2 twist.[43]

In the corresponding UV-Vis spectrum in Figure 89b there are 4 distinct bands at 222, 284, 409 and 525 nm. The spectrum is dominated by the band at 409 nm which we previously assigned to the presence of a charged polymer containing 2 – 3 double bonds, while the absorbance of charged polymers containing 5 double bonds is weaker in H-Ferrierite relative to those seen in H-ZSM-5.[24,29] The less

intense bands at 222 and 284 nm with respect to the maximum indicate that adsorbed furan and protonated furan are less prevalent.[24,29]

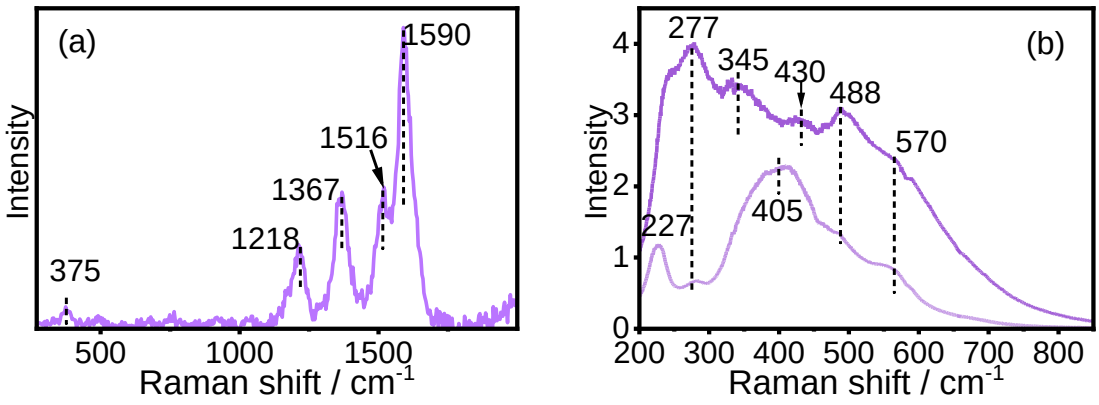

Figure 90 (a) Kerr-gated Raman spectrum and (b) UV-Vis spectra recorded after adsorption of furan at 30 °C on H-Y, for 15 minutes in lighter purple and for 1 hour followed by 60-minute flush in He in darker purple.

In contrast in Zeolite Y, the most intense band in the Raman spectrum (shown in Figure 90) lies at 1590 cm^{-1}, in the C=C stretch region, which is likely due to adsorbed furan molecules.[24] Another band at 1516 cm^{-1} can be attributed to the C-C=C^+ stretches in alkyl carbocations,[42] possibly such as those in protonated furan. Bands at 1368 and 1212 cm^{-1} are characteristic of CH_2 deformation and twisting vibrations.[25,26]

The UV-Vis data is highly convoluted in the case of furan adsorbed on zeolite Y – unlike in the medium pore zeolites where the spectra contained well-defined and separate bands owing to the confinement of the zeolite framework on the size and shape of the polymers that would form – the large and open structure of Zeolite Y does not impose such spatial constrains on the polymerising furan. Still, the spectrum can be interpreted in terms of the presence of a range of species including; adsorbed furan at 227 nm, monoenylic carbocations at 277 nm, dienylic carbocations at 345 nm, trienylic carbocations at 430 nm and cations containing 4 – 6 double bonds at 488 and 570 nm.[24,33,44]

Both Raman and UV-Vis data in this case are consistent with the observation that the zeolite contains more furan monomers. In Figure 4b, the DR-UV-Vis spectrum of furan adsorbed on the surface after just 15 minutes is also shown, where the spectrum looks more comparable to the other zeolites, containing a band of highest intensity at 405 nm showing that during the initial stages of reaction there is strong evidence for the formation of protonated dimers.

In Figure 5a we see the Raman spectrum recorded after furan adsorption on zeolite Beta; in the C=C stretch region, the strongest band sits at 1586 cm^{-1} with a strong shoulder near 1620 cm^{-1}, which can be attributed respectively to physisorbed furan,[24] and large polymers.[36,37] A broad shoulder at lower frequencies (1490 – 1530 cm^{-1}) can again be attributed to the C-C=C^{+} stretches in alkyl carbocations.[42] Bands are also observed at 1360, 1206 and 1159 cm^{-1}, in addition to very small bands at 740 and 906 cm^{-1}. Again, UV-Vis data in Figure 5b provide evidence of adsorbed furan, monoenylic carbocations, dienylic carbocations, trienylic carbocations, and more extended structures containing up to 6 double bonds.[24,28–32]

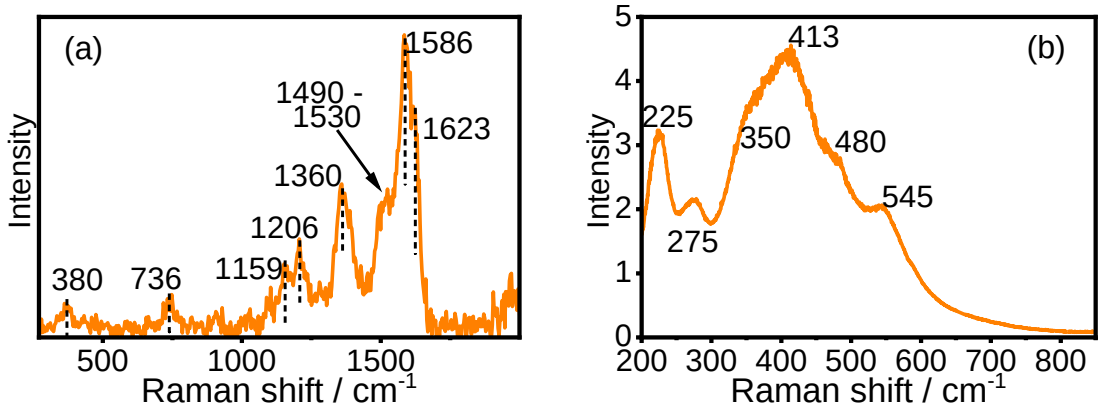

Figure 91 (a) Kerr-gated Raman spectrum and (b) UV-Vis spectrum recorded after adsorption of furan at 30 °C on H-Beta, followed by 60-minute flush in He.

The intense bands at around 410 nm & 540 nm in the UV-Vis data of furan adsorbed on H-ZSM-5 and H-Ferrierite indicate from Table 1 the formation of distinct cationic hydrocarbons which contain mostly 2 - 3 double bonds and is positively charged in addition to species containing 5 double bonds and a positive

charge i.e., 2 or 3 furan monomers. In the larger pore zeolites, however, bands at 350 nm indicate the presence of dienylic carbocations which are not present in the medium pore zeolites, in line with the Raman signal at around 1510 cm^{-1} which was attributed to the protonated C-C=C^{+} structure.[42] In both large pore zeolites the UV-Vis band around 220 nm which was assigned to physisorbed furan is more intense when compared with the medium pore zeolites, and by Raman C=C stretches observed around 1586 cm^{-1} which is indicative of C=C stretches in furan,[24] providing strong evidence that more physisorbed furan exists in the large pore structures, probably due to the higher pore volume of the large pore zeolites, and perhaps due to lesser special restrictions forcing polymerization.

Even at room temperature, the interaction of furan with different zeolites yields polymeric species to different degrees on the surface, which is evidenced by distinct DR-UV-Vis bands at wavelengths well into the visible region and Raman bands revealing CH_2 character. CH_2 groups need to exist for polymerisation to have occurred, resulting from a hydride transfer step to give the more conjugated species.[24]

4.3 H-ZSM-5 Temperature programmed reaction

4.3.1 Kerr-gated Raman

Consistent with previous observations by Cheng and Huber,[18] upon heating the zeolites after furan adsorption, water, carbon dioxide, hydrogen, and aromatic and olefinic hydrocarbons are produced. This was determined from analysis of the following masses by MS: *m/z* 2, 18, 25, 28, 41, 43, 44, 78 and 91, to represent: hydrogen, water, ethene, carbon monoxide, propene, $C_{4\text{-}5}$ paraffins, carbon dioxide, benzene, and branched aromatics toluene/xylene, respectively.

For the experiment in H-ZSM-5 zeolite, MS data is shown in Figure 92. From 60 °C, water is released, reaching a maximum at 140 °C. CO_2 is released from the start of the ramp to a maximum at 375 °C. Above 275 °C the evolution of hydrocarbon products is observed with firstly propene production, reaching a maximum at 420 °C. Benzene and toluene production begins at 300 – 325 °C,

with toluene reaching its maximum at 455 °C and benzene at 500 °C, which is consistent with benzene being the more thermodynamically stable product. Above 350 °C, *m/z* 2 climbs, indicating H_2 production which continues to the end of the experiment at 600 °C.

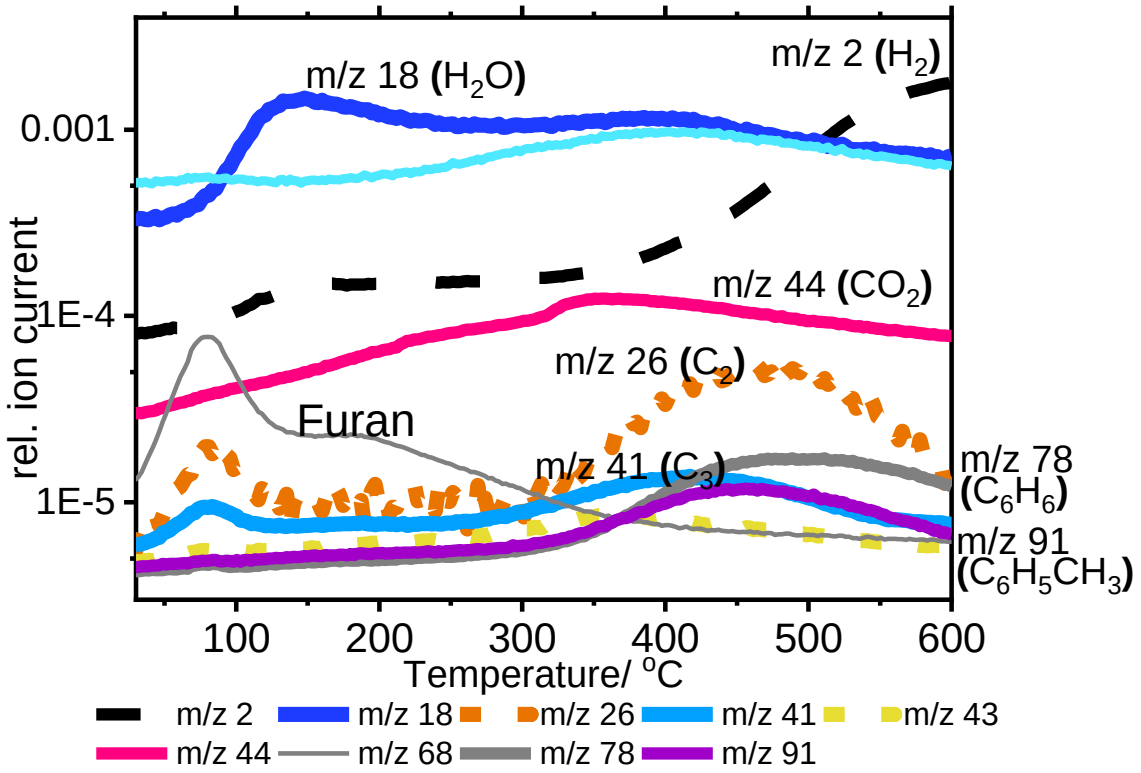

Figure 92 MS data acquired during temperature programmed reaction of furan over H-ZSM-5 catalysts, during temperature ramp from 30 to 600 °C.

Figure 93 shows Raman spectra collected during the first half of the temperature ramp. During these temperature ramp experiments, an overall drop in signal intensity is observed with time, which is partly caused by the loss of some structure of the polymeric species formed at 30 °C. UV-Vis data (shown later in Figure 96) indicates an increasing absorbance of the sample i.e., samples darkening, which can also be responsible for an overall decrease in signal intensity by Raman.

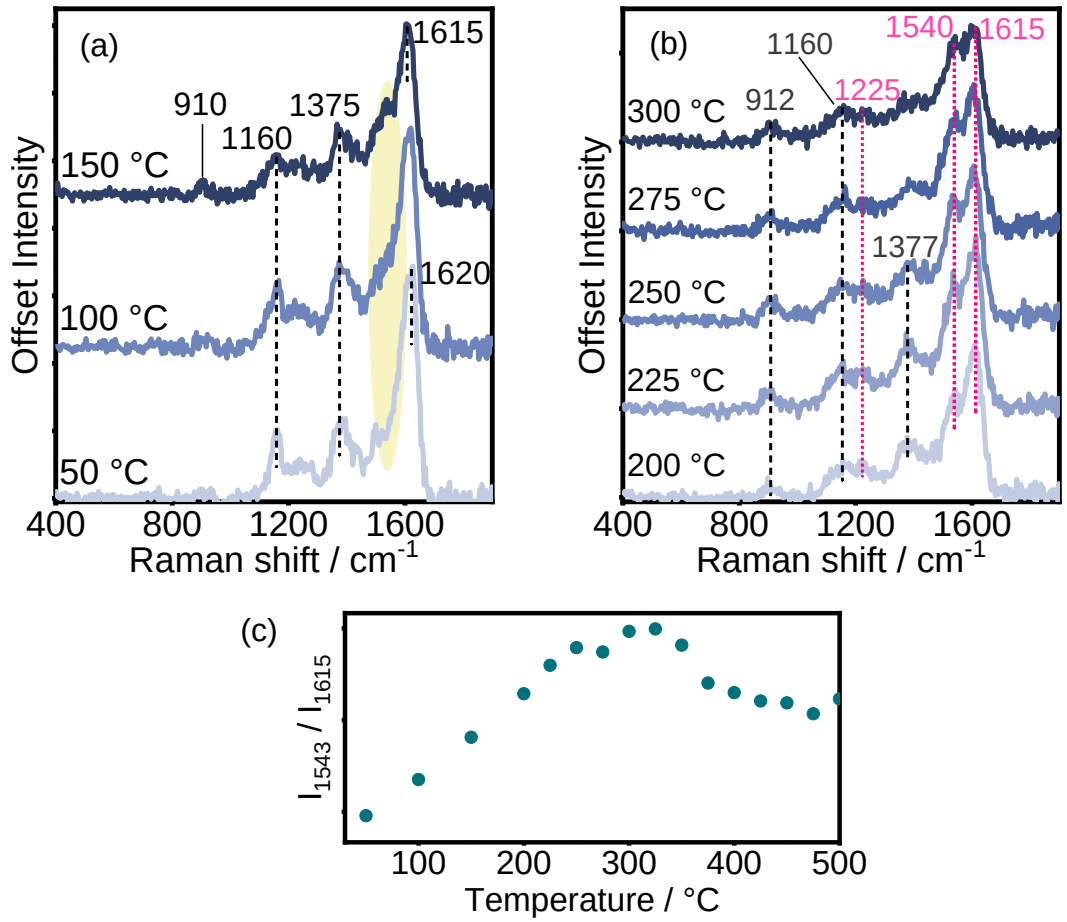

Figure 93 Kerr-gated Raman spectra recorded during temperature programmed reaction of furan over H-ZSM-5 at (a) 50 – 150 °C, (b) 200 – 300 °C and (c) a plot of the relative intensity at 1543 cm^{-1} with respect to that at maximum intensity at 1620 cm^{-1}

On increasing temperature to 150 °C, a new, broad band emerges at 1530 – 1550 cm^{-1} which is highlighted in yellow in Figure 93a, and while a band at 1620 cm^{-1} is still very intense, it appears as though a new component to this spectrum at 1615 cm^{-1} grows, becoming the band of highest intensity by 150 °C. The distinct band at 1160 cm^{-1} drops in intensity and becomes broader, which may be due to the loss of the structured polymer which had formed at room temperature.

The most prominent spectral change from 200 to 300 °C, is the growing band at 1540 cm^{-1} which we assign to the C=C stretch of the 5-membered ring of benzofuran. The assignment of this band to benzofuran is further supported by a small band at 1225 cm^{-1} which can be attributed to the C-O stretch and the strong intensity at 1620 cm^{-1} where the C=C stretch in the benzene ring of benzofuran

would lie,[45] (although the signal in the 1610 – 1630 cm^{-1} region could more generally correspond to C=C containing aromatic species overall, in line with Huber's observations by FTIR).[18] These bands are highlighted by the pink dotted droplines in Figure 93b. As shown in Figure 93c, the relative intensity of this band increases linearly up to 325 °C when the relative intensity of the bands at 1540 to that at 1615 cm^{-1}, I_{1543}/I_{1615}, reaches 0.9. Relative intensity is plotted here rather than absolute intensity to account for the overall signal decrease across the spectrum with increasing reaction co-ordinate/temperature.

Benzofuran has been discussed as a product or intermediate in this reaction in literature, forming through the Diels-Alder condensation of two furan molecules, which can explain the production of water by MS.[19,46,47] However, benzofuran was not detected as a product by MS in this experiment.

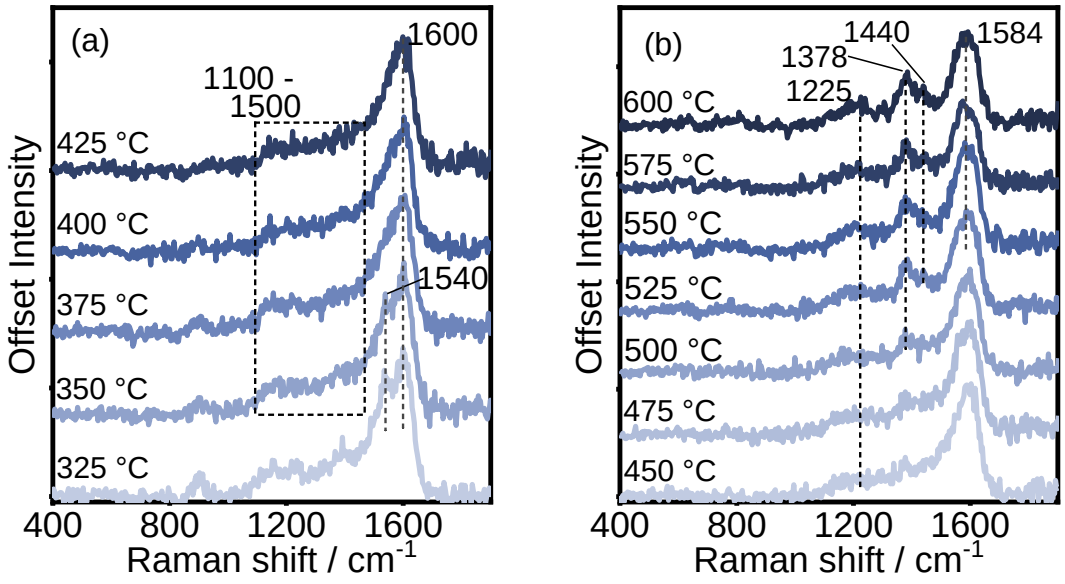

Figure 94 Kerr-gated Raman spectra recorded during temperature programmed reaction of furan over H-ZSM-5 at 25 °C intervals at (a) 325 – 425 °C and (b) 450 – 600 °C.

As the temperature is further increased beyond 325 °C, the band at 1540 cm^{-1} drops in relative intensity, becoming indistinguishable as a broad shoulder by 375 °C, indicating the consumption of benzofuran at this stage. Benzofuran may be decarbonylated to yield aromatic products and CO, this process may be responsible for the aromatics observed by MS.[6,18] At 425 °C, one broad band sits

from 1605 – 1625 cm^{-1}, which could correspond to C=C vibrations of trapped monocyclic aromatic species which were unable to diffuse out of the zeolite as a product. Some weaker bands from 1000 – 1500 cm^{-1} are unfortunately too weak to be resolved from the spectral noise, but likely contain a mixture of signals corresponding to CH_2 and CH_3 deformations, C-C stretches and C-H twists.[25,26] The poor signal intensity could be because of an array of different species here where the bonds involved in the vibrations are not resonance enhanced.

Increasing the temperature further from 450 to 600 °C leads to the formation of polycyclic aromatic species. Firstly, at 450 °C we start to observe a growing band at 1380 cm^{-1} where bicyclic aromatics exhibit ring-breathing modes.[25,39] This band continues to grow while from 525 °C and above, a shoulder at 1440 cm^{-1} grows, which has been observed during studies of methanol conversion and attributed to polyaromatic species bent structure for example those containing 5-membered rings – such as fluorene.[39,48] In the C=C stretch region, a strong band centred at 1584 cm^{-1} is very broad encompassing vibrations between 1575 and 1620 cm^{-1}, the latter being related to C=C stretching in naphthalenic species.[39,48]

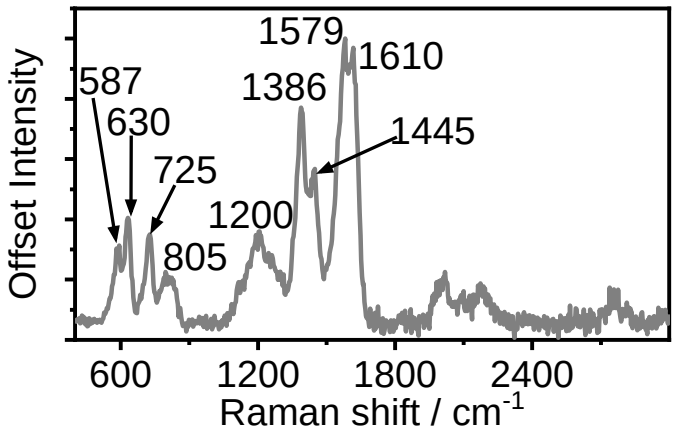

Figure 95 Kerr-gated Raman spectrum of quenched H-ZSM-5 after furan adsorption and temperature ramp to 600 °C, recorded at room temperature. The reactor was cooled at 20 °C min^{-1} under flowing He. Spectra collected in 5 acquisitions of 8 seconds with 1 mW power.

The spectrum acquired after quenching the catalyst in the reactor reveals some intense bands in the low frequency region at 587, 630, 725 and 805 cm^{-1}, which were not observed at high temperature most likely due to the lower signal-to-noise ratio which improved after cooling, as well as due to the 5 times longer

acquisition. The band at 630 cm^{-1} was demonstrated to be due to ring-opening vibrations of polycyclic aromatic hydrocarbons, as discussed in Chapter 3.[26] Branched species containing carbon atoms tetrahedrally coordinated to 3 other carbon atoms give rise to C-C vibrations at 575 cm^{-1} very close here to 587 cm^{-1} – revealing the presence of branched aromatic species in the zeolite.[26]

4.3.2 UV-Vis Spectroscopy

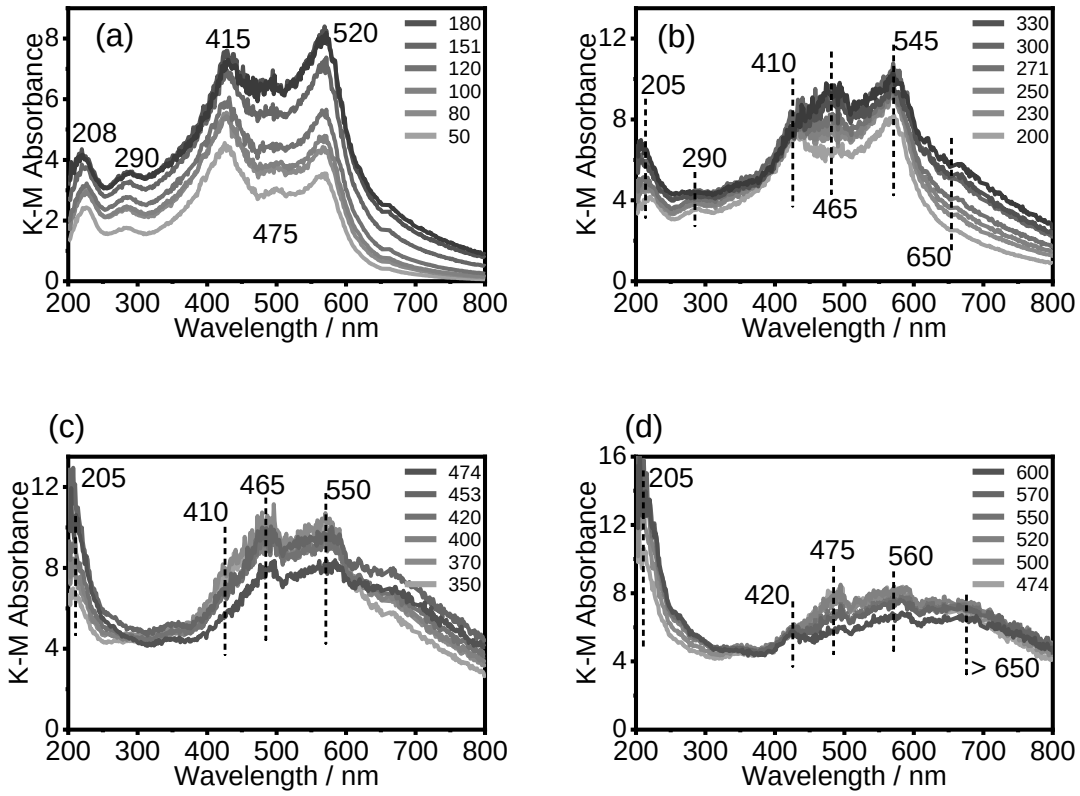

Figure 96 DR-UV-Vis spectra collected during temperature programmed ramp on H-ZSM-5 at (a) 50 – 200, (b) 220 – 360, (c) 370 – 480, and (d) 500 – 600 °C.

The experiment repeated with a DR-UV-Vis probe gave more general structural information about the chemical species. Upon increasing temperature to 200 °C, as shown in Figure 96a, there is an overall increase in absorption across the spectrum but the band at 545 nm grows most significantly – this has been previously assigned to the furan trimer containing 6-conjugated double bonds by Spoto *et al.*,[24] with the heating inducing more hydride transfer reactions which would be necessary for forming the species with 6-conjugated double bonds.[24] Above 220 °C, a band emerges at 465 nm which would signify a species

containing 3 double bonds and a positive charge,[29,33] which could include protonated benzofuran. This band is at its most intense at 330 – 350 °C. Increasing temperature to 350 °C also induces growth of bands at higher wavelengths centred around 650 nm, indicating the formation of protonated and conjugated structures containing as many as 8 double bonds.[24,29] Further temperature increase beyond 350 °C leads to a decrease in absorbance at 410, 465 and 550 °C but an overall increase at 650 nm as conjugated species tend towards small, graphite-like polyaromatics.[28]

At low wavelengths, an increased absorbance below 200 nm is observed which might be explained by the higher energy transitions of the aromatic species present. The π→π* transitions given in Table 14 are given for the lowest energy transitions in the molecule, defined by excitation from the HOMO to LUMO, which has typical extinction coefficients (ε) of 10^2. In aromatic species, transitions are possible from the HOMO to higher unoccupied orbitals at energies equivalent to 190 – 220 nm in aromatic species with ε of approximately 10^4.[31] This might explain the very high absorbance at < 230 nm in Figure 96d due to the aromatic character of the surface hydrocarbons.

4.4 Ferrierite Temperature Programmed Reaction

4.4.1 Mass Spectrometry

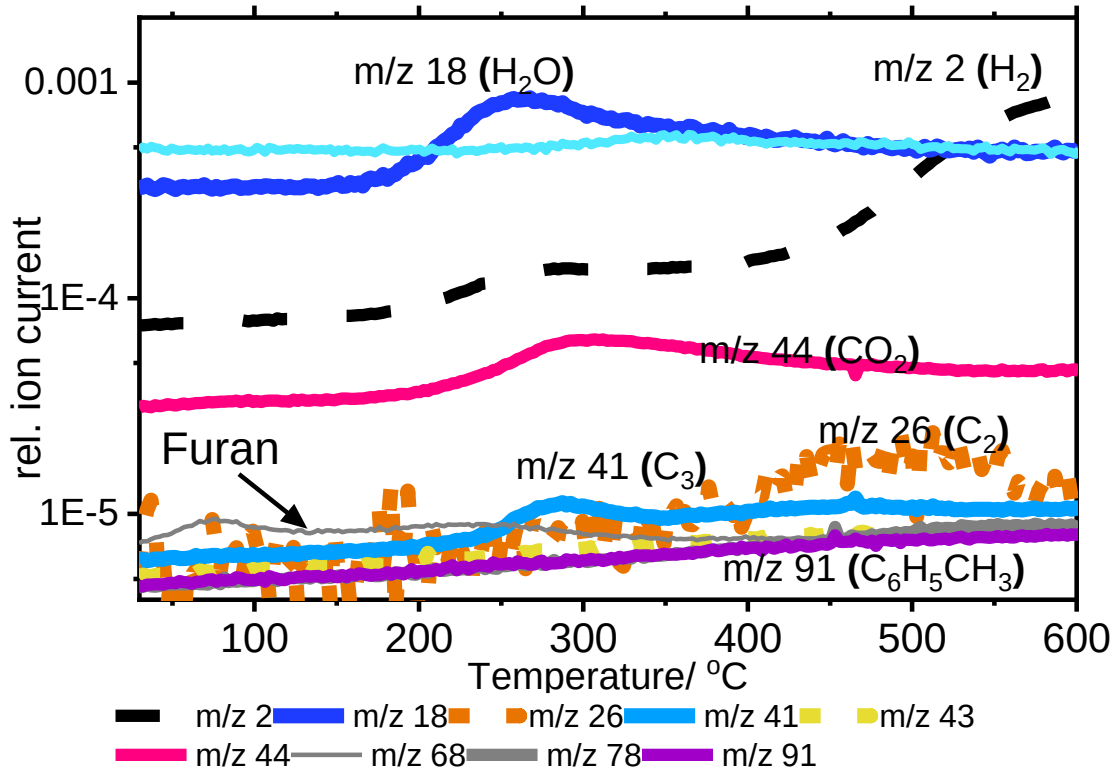

Figure 97 MS data acquired during temperature programmed reaction of furan over H-ferrierite catalyst, from 30 to 600 °C at 5 °C/min.

The activity of this zeolite revealed by MS in Figure 97 is significantly different to that observed in the H-ZSM-5 experiment. The desorption of furan at temperatures below 100 °C is far less than the response recorded for H-ZSM-5; the relative ion current reaches an order of magnitude lower here, which is rationalised by the lesser accessibility to the internal volume of the zeolite.[8,15] Water is released at higher temperature than in H-ZSM-5, above 180 °C with maximum at 260 °C. Some propene and CO_2 are released at 220 °C, which may be explained by the decarboxylation of furan to produce propene, a process demonstrated by Huber *et al.*[49,50] At high temperatures ethene is formed and hydrogen evolves from 430 °C. No aromatics are observed as products at any stage of reaction.

4.4.2 Kerr-gated Raman

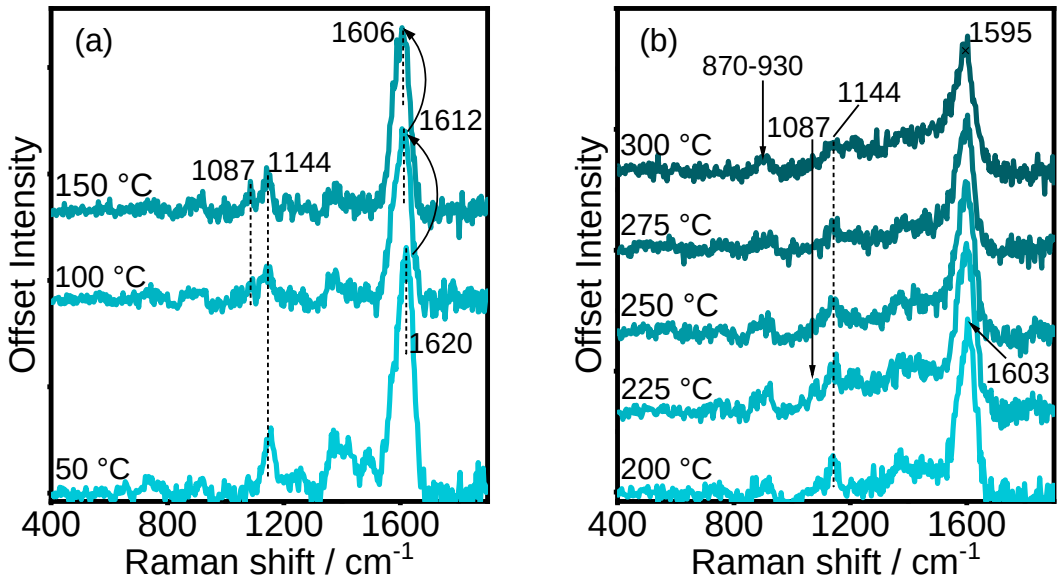

Figure 98 Kerr-gated Raman spectra recorded during temperature programmed reaction of furan on H-ferrierite at (a) 50 – 150 °C and (b) 200 – 300 °C.

Increasing the temperature from 50 to 150 °C sees a red shift in the C=C bond stretching frequency from 1620 to 1606 cm^{-1} (Figure 98a). The starting polymeric species undergoes a change in composition resulting in a C=C stretching vibration at the frequency of monocyclic aromatic species or conjugated olefins containing 2 or 3 conjugated double bonds.[26,51] The band at 1144 cm^{-1} appears to be stable with increasing temperature, as does a weak and broad band at 870 – 930 cm^{-1}. A new band develops at 1087 cm^{-1} which could indicate a new C-O-C vibration. This band at 1087 cm^{-1} drops again after 200 °C in Figure 98b and is completely diminished by 250 °C. Above 250 °C, a small new feature appears at 1214 cm^{-1}; previously a band in this region was assigned to a C-O stretching mode.[45] With further temperature increase to 300 °C, there is general growth in the 1320 – 1500 cm^{-1} region, but no intense bands that can be resolved.

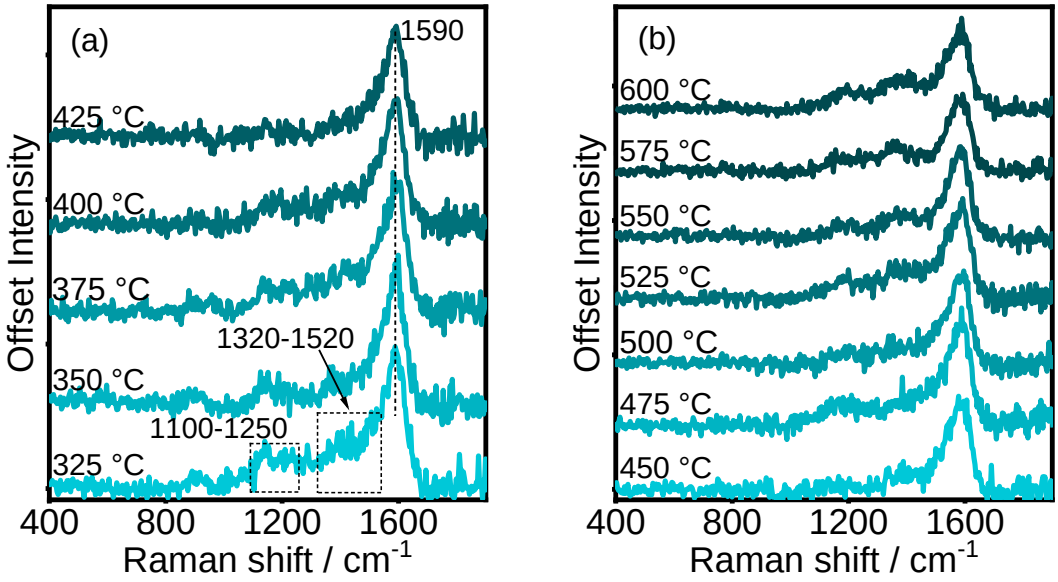

Figure 99 Kerr-gated Raman spectra collected from (a) 325 to 425 and (b) 450 to 600 °C during temperature programmed reaction of furan on H-ferrierite.

The poor signal-to-noise ratio makes it difficult to isolate specific vibrations in this dataset shown in Figure 99, but generally the spectra in the 325 – 425 °C temperature window consist of an intense band at 1590 cm^{-1} assigned to C=C stretching modes, and weaker convoluted signals in the 1320 – 1520 cm^{-1} and 1100 – 1250 cm^{-1} regions. The band at 800 cm^{-1} which was present at all lower temperatures is now attenuated above 350 °C.

As the temperature is increased from 525 to 600 °C, in the period where ethene formation ceases, three bands form which are typical of amorphous carbon.[52,53] These can more clearly be seen after the reactor has been cooled and a spectrum collected with a longer acquisition time, improving the signal-to-noise ratio, as shown in Figure 100.

With less noise, it is now easier to observe that the spectrum contains a clear band at 1365 cm^{-1} due to CH_2 or CH_3 deformations,[25,26] or possibly due to the ring breathing modes of bicyclic aromatic species,[39] although the band is at a lower relative intensity than would be expected for bicyclic aromatic hydrocarbons. Another band at 1190 cm^{-1} has been described in terms of amorphous carbon as C-C stretching between pairs of single and double bonds.[52]

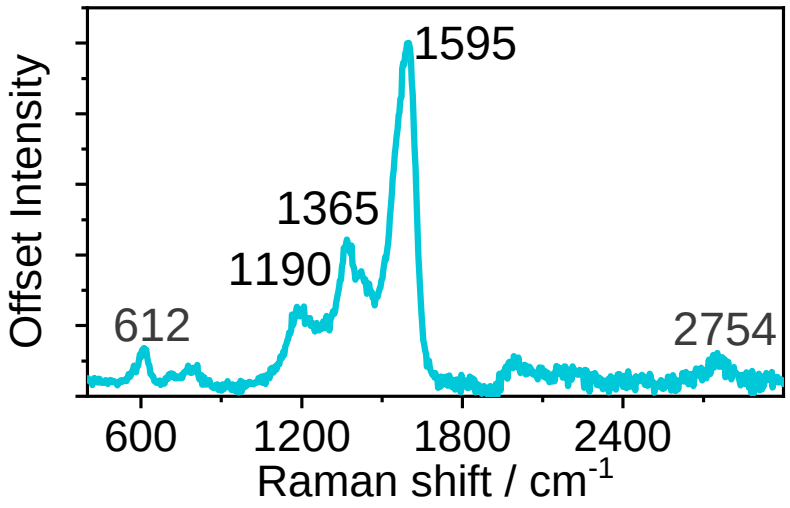

Figure 100 Kerr-gated Raman spectrum of quenched catalyst after temperature programmed reaction of ferrierite with furan up to 600 °Cs. The reactor was cooled at 20 °C min^{-1} under flowing He. Spectra collected in 5 acquisitions of 8 seconds with 1 mW power.

A small band at 612 cm^{-1} is an indicator of branched aromatic species.[26] Although it wasn't possible to identify any aromatics during the reaction, if the mechanism of this reaction can be compared with methanol-to-hydrocarbons at all, for the formation of ethene at temperatures between 400 – 500 °C, there must be contraction of branched aromatic species, leading to ethene formation through dealkylation reactions, since ethene is not a favoured product of cracking reactions.[54,55]

4.4.3 UV-Vis Spectroscopy

From the DR-UV-Vis data, with increasing temperature to 200 °C as shown in Figure 101a, there is some decrease in the absorption band at 416 nm and some overall increase at 585 nm, again indicating transformation to the more conjugated species due to the occurrence of hydride transfer reactions. Further increase to 350 °C induces the complete loss of the band at 416 nm and growing and broadening of the band at a higher wavelength (520 nm), which signals the condensation of trienylic carbocations to longer species containing 4 – 5 double bonds and positive charge. The band at 290 nm where adsorbed and charged furan absorbs disappears, coincident with the formation of CO_2 and propene as seen by MS in Figure 97, the latter proposed to form via the direct decarboxylation

of furan after hydrolysis.[50] At longer wavelengths (600 – 800 nm), absorption increases which indicates formation of larger, more extended structures. Increasing the temperature beyond 350 °C results in the loss of the 517 nm band, and by MS at 400 °C ethene is formed – these two events might be a result of dealkylation reactions, such as those observed in MTH to produce ethene.[55,56] Overall, the absorbance remains low throughout the experiment as compared with the results obtained from ZSM-5, and there is little evidence of polyaromatic hydrocarbon formation.

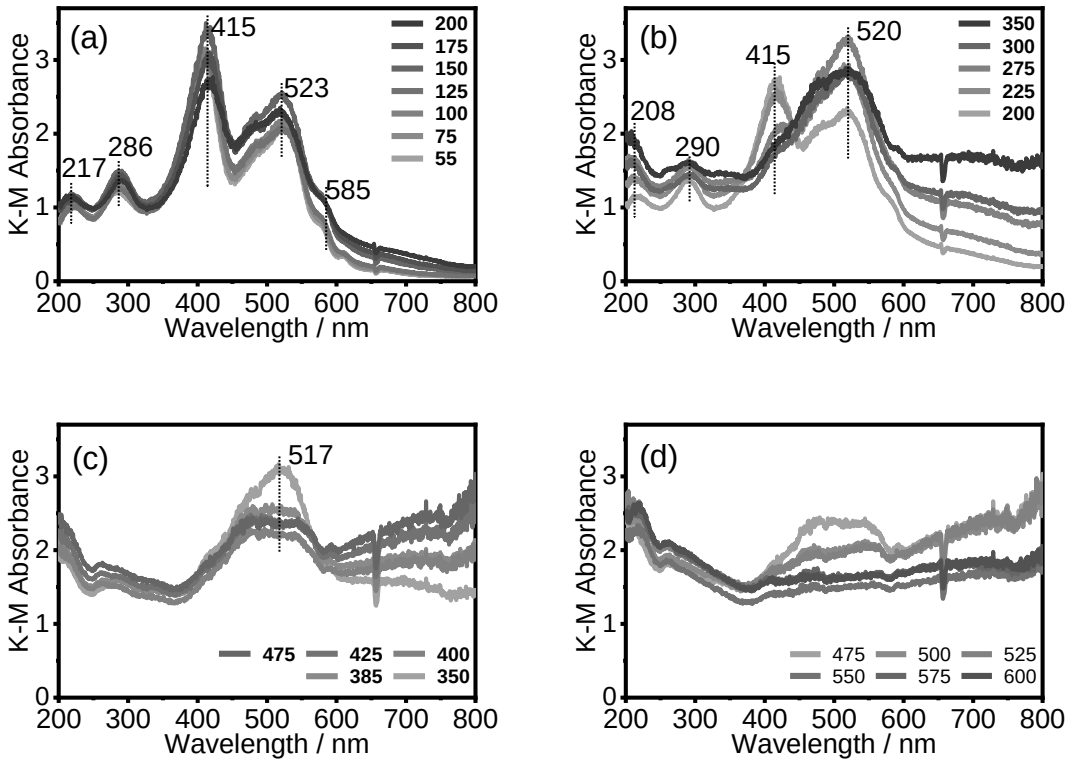

Figure 101 DR-UV-Vis data recorded during temperature ramp data furan conversion on ferrierite between 5 and 600 °C.

4.5 H-Y Temperature programmed reaction

4.5.1 Kerr-gated Raman

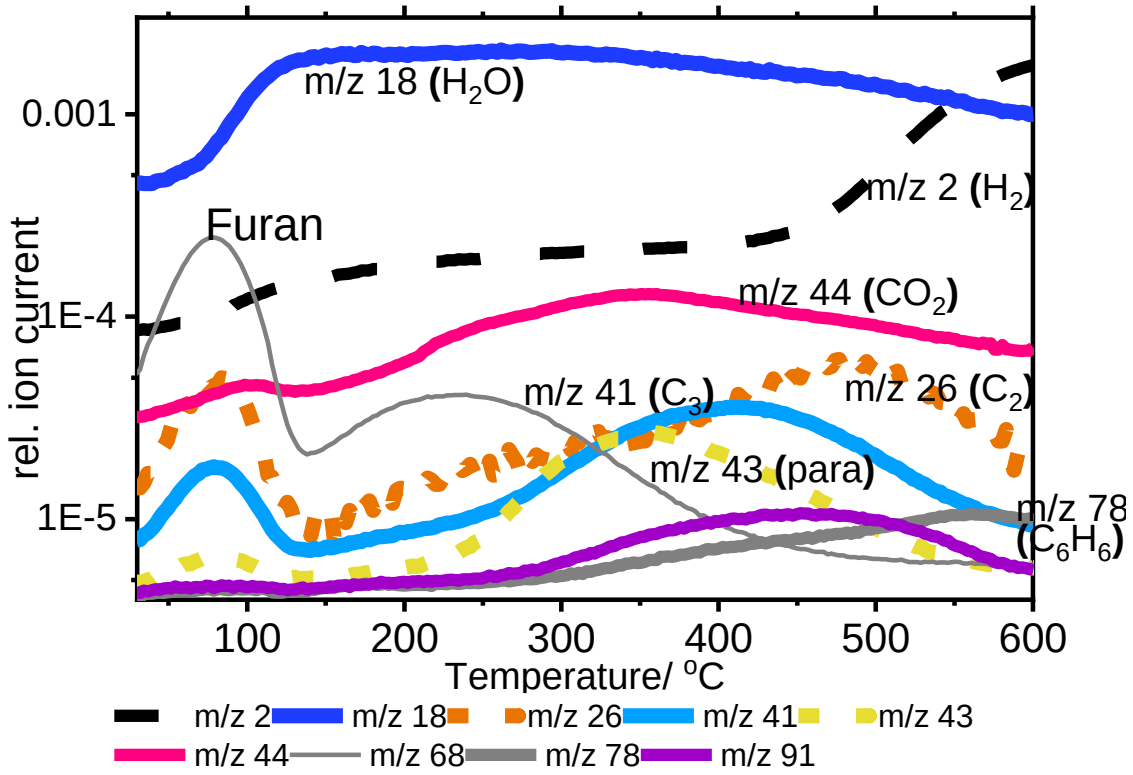

Figure 102 MS data acquired during temperature programmed reaction of furan over H-Y catalyst, from 30 to 600 °C at 5 °C min^{-1}.

In the reaction of furan on H-Y as shown in Figure 16, water release occurs at lower temperatures from 50 °C and the signal plateaus at 120 °C, remaining high before dropping later in the reaction at 340 °C, indicating that dehydration occurs over a longer temperature period. The CO_2 signal climbs throughout the ramp to a maximum at 350 °C. Propene production, shown by increasing *m/z* 41, increases slowly from 120 °C to 250 °C when its rate of production suddenly increases to a maximum at 405 °C. In contrast to the reaction in H-ZSM-5, here in H-Y, from 250 °C, we observe a high increase of *m/z* 43, which contains high contribution for C_4 and C_5 paraffins. Paraffin production peaks here at a maximum at 355 °C. Toluene and xylene production (*m/z* 91) starts at 275 °C and decreases after 450 °C, while benzene production (*m/z* 78) is favoured at higher temperatures from 300 °C to 560 °C. Maximum ethene production (*m/z* 26) is at 485 °C. Hydrogen (*m/z* 2 with some contribution from water) evolution starts at 450 °C without reaching a maximum before 600 °C.

Increasing the temperature from 50 to 150 °C in Figure 103a induces broadening of all bands whilst intensity drops, again, in line with furan desorption. The C=C stretching band remains constant at 1594 cm^{-1} but its breadth at 150 °C might suggest growing bands at 1630 and 1534 cm^{-1}. Peaks at 1215 and 1365 cm^{-1} are attenuated.

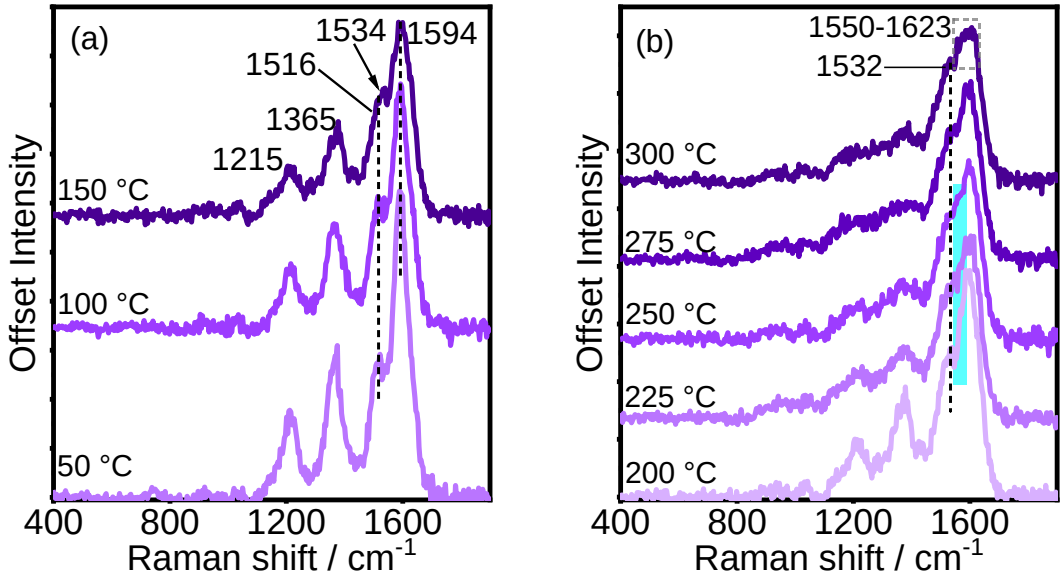

Figure 103 Kerr-gated Raman spectra collected during temperature programmed reaction of furan on H-Y at (a) 50, 100 and 150 °C and (b) 200 – 300 °C.

From 200 to 225 °C there is increasing intensity between 1540 and 1580 cm^{-1} as highlighted by the blue section in Figure 103b. By 250 °C, the spectrum consists of a C=C stretch at 1595 cm^{-1} and a very strong shoulder at lower frequency around 1530 cm^{-1}. Signals here can again be ascribed to C=C stretches of cyclic species such as benzofuran. This changes by 300 °C as growth in the region of 1550 and upwards creates a strong and broad band with highest intensity ranging from 1550 to 1623 cm^{-1} which is outlined in the grey box. In Chapter 3, Raman bands around these frequencies from 1540 to 1580 cm^{-1} were assigned to conjugated olefinic species of various chain lengths, which may or may not be protonated.[26] One possible explanation for the formation of conjugated olefinic species in this temperature region would be that they form as the hydrogen deficient species on the zeolite which results from bi-molecular hydride transfer process, explaining the observed formation of paraffins seen in the MS. This process has been discussed in the field of fluid catalytic cracking, where

increasing catalyst content of Zeolite Y gives higher paraffin yields (and also higher selectivity to coke).[57,58] Due to the interactions between acid sites of zeolites and the π electrons of olefins, they remain on the catalyst surface where they might undergo further reaction, while paraffins with weak zeolite interactions leave the microporous structure as products without further reaction.

Further heating sees changes around 1100 – 1470 cm^{-1}, (pink dashed box in Figure 104a); these signals encompass overlapping CH, CH_2 and CH_3 vibrations.[25,26] With increasing temperature from 325 to 400 °C, a narrowing of the broad band at 1580 – 1620 cm^{-1} occurs, as paraffin production declines after 355 °C, and propene production increases, this might be due to the cracking of olefinic species proposed here to have remained on the surface.

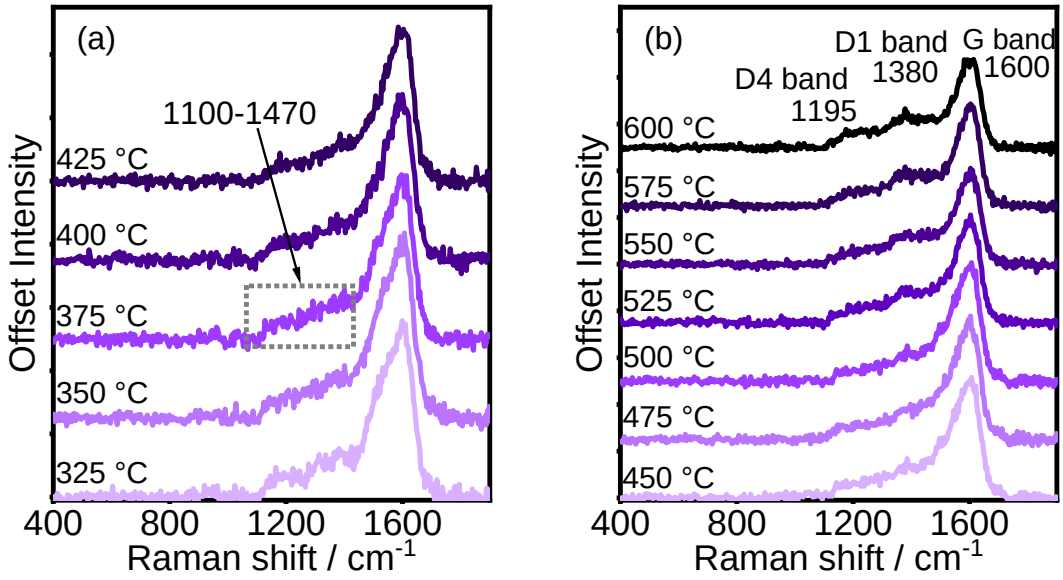

Figure 104 Kerr-gated Raman spectra collected during temperature programmed reaction of furan on H-Y at (a) 325 – 425 °C and (b) 450 – 600 °C.

With further temperature increase from 450 to 600 °C, in Figure 104b, the most intense band remains that at 1602 cm^{-1} but in addition, two broad and flat bands grow at 1380 cm^{-1} and 1200 cm^{-1}. These three bands are more clearly seen in the quenched spectrum shown in Figure 105, and could be described as the G, D1 and D4 bands respectively of coke, where the low intensity of the D1 band compared with the G band indicates amorphous carbon since the D1 band is usually intense when associated with the breathing modes of aromatic rings, and

the D4 band at 1200 cm^{-1} indicates stretching between sp^2 and sp^3 hybridised carbon atoms seen between double and single CC bonds.[52,53]

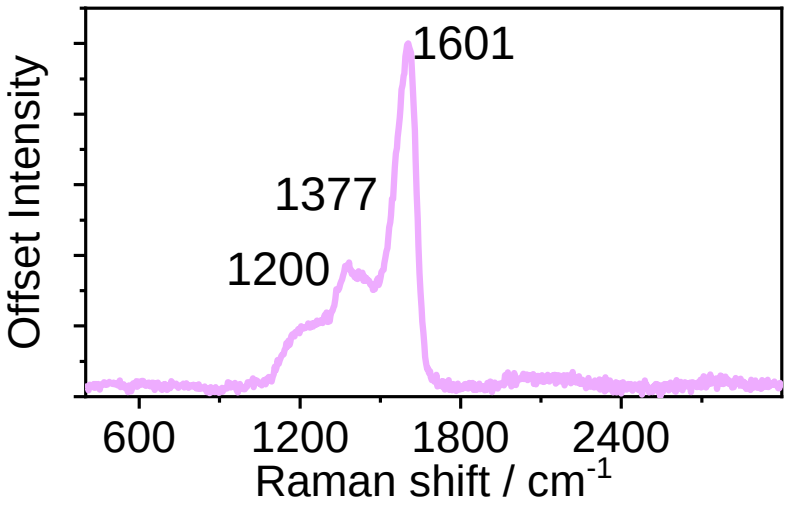

Figure 105 Kerr-gated Raman spectrum of quenched catalyst after temperature programmed reaction of Zeolite Y with furan up to 600 °C. The reactor was cooled at 20 °C min^{-1} under flowing He. Spectra collected in 5 acquisitions of 8 seconds with 1 mW power.

4.5.2 UV-Vis spectroscopy

In the early stages, up to 200 °C, the overall absorbance increases, and particularly at 550 – 600 nm as indicated by the arrow in Figure 106a due to the formation of more conjugated species. From 200 to 325 °C the changes are characterised by an increasing overall absorbance across the spectrum, as bands become less distinct. The broadening of the bands here supports the observation by Raman that conjugated species have formed containing an indistinct number of conjugated bonds. In this zeolite the structure in the DR-UV-Vis spectra is quickly lost when compared with ZSM-5 and ferrierite, which is explained by the lack of compartmentalisation in zeolite Y. Further increasing the temperature to 600 °C as shown in Figure 106d leads to increased absorbance over the entire spectrum.

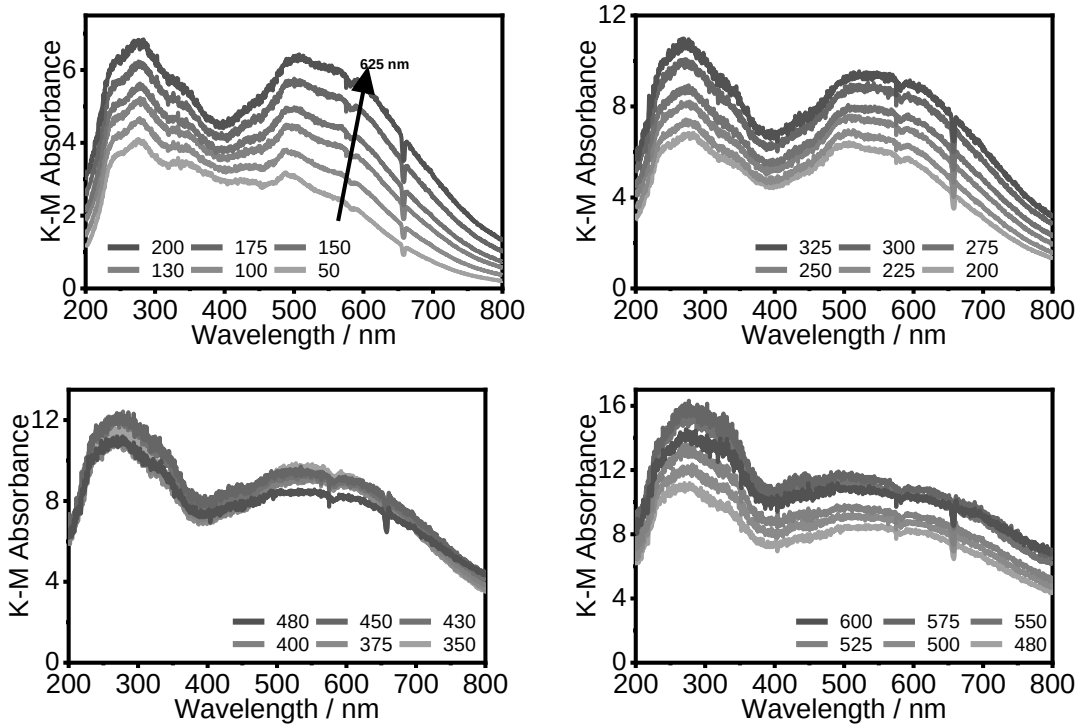

Figure 106 DR-UV-Vis spectra recorded during temperature programmed reaction of furan over H-Y zeolite from (a) 50 to 200, (b) 200 to 325, (c) 350 to 480 and (d) 480 to 600 °C.

4.6 H-Beta Temperature Programmed Reaction

4.6.1 Mass Spec

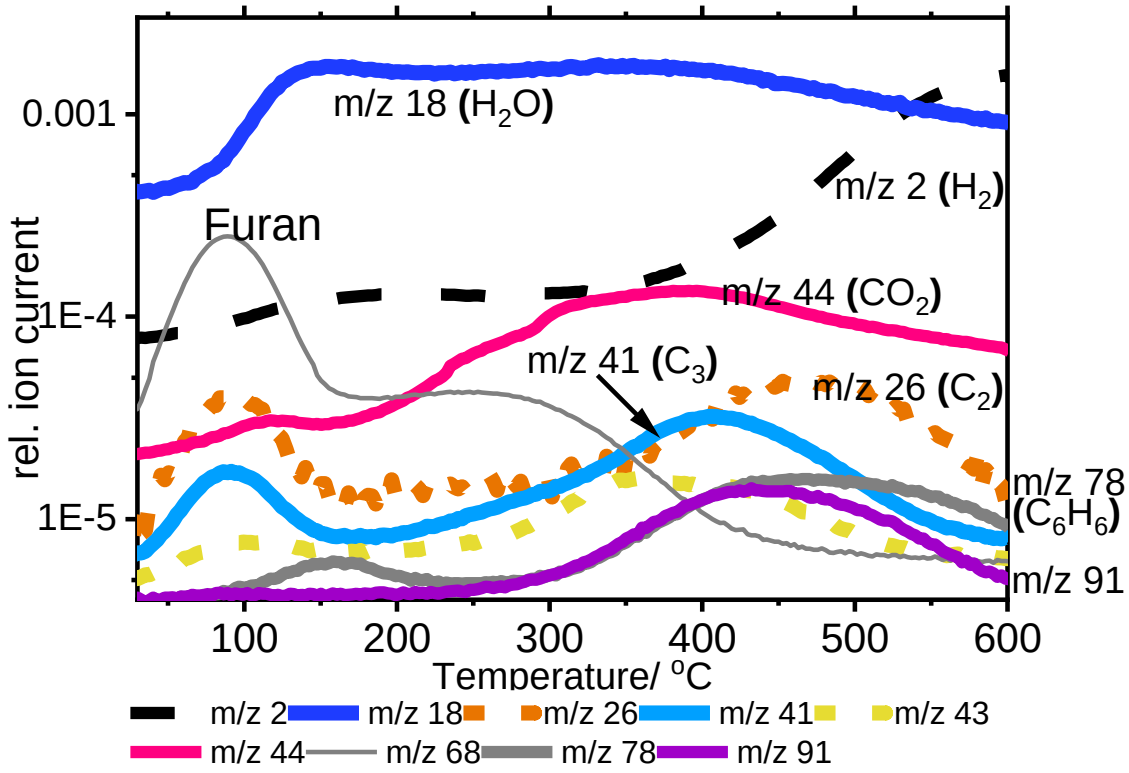

Figure 107 MS data collected during temperature programmed reaction of furan on zeolite H-Beta from 30 to 600 °C at 5 °C min^{-1}.

Shown in Figure 21 by MS, are data for the reaction on H-Beta, water evolution starts from 100 °C with the *m/z* 18 signal only slowly dropping off above 400 °C. Meanwhile the CO_2 signal is seen to climb to a maximum at 400 °C. Production of propene starts gradually at 200 and up to 405 °C, while ethene production reaches its highest at 475 °C. Paraffin production also occurs. The signal at *m/z* 43, increases initially in line with the *m/z* 41 signal, but finishes at 360 °C. Benzene and toluene/xylene production start simultaneously at 275 °C, with benzene reaching its maximum at 475 °C and toluene again at lower temperature 440 °C. Hydrogen evolution takes place from 400 °C.

4.6.2 Kerr-gated Raman

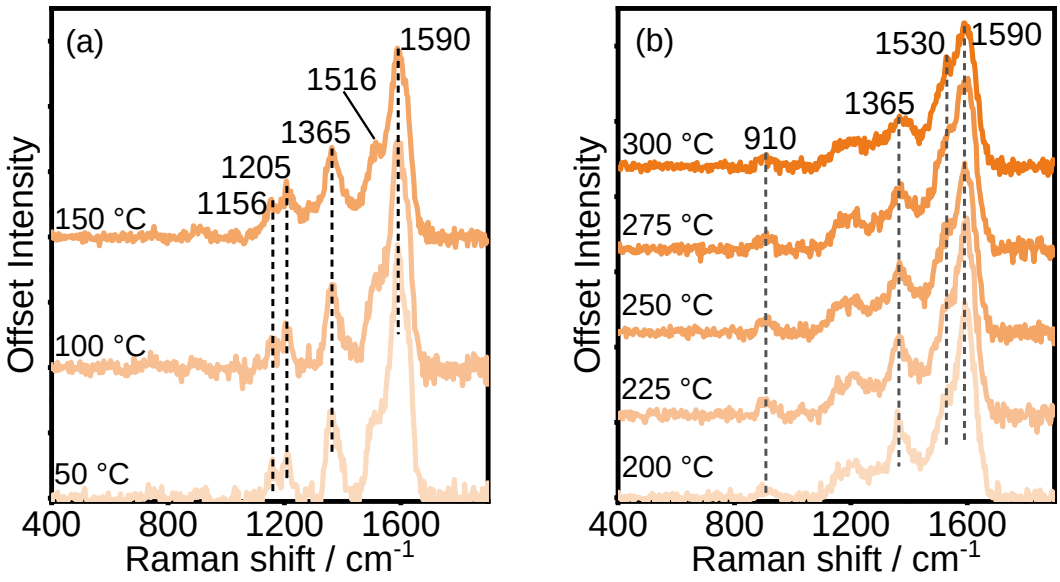

Figure 108 Kerr gated Raman spectra collected during temperature programmed reaction of furan on H-Beta at (a) 50, 100 and 150 °C and (b) 200 – 300 °C.

Upon increasing the temperature from 50 to 150 °C, an overall decreased intensity is observed in Figure 108a. Most signals broaden, although the band at 1520 cm^{-1} becomes more distinct and increases in relative intensity. Since the start of the ramp, a band at 910 cm^{-1} began to grow, and continues to grow up to 300 °C. The band at 1592 cm^{-1} which was assigned to the C=C stretching in furan is gradually attenuated as temperature is increased and furan desorbed, but it remains the strongest band in the spectrum. The band at 1365 cm^{-1} becomes broad and rounded and the distinct 1160 and 1208 cm^{-1} bands merge.

The band at 1530 cm^{-1} continues to grow until 300 °C. The vibrational frequency is lower than the C=C bond of the 5-membered ring of benzofuran at 1543 cm^{-1},[45] which was assigned as a species observed in H-ZSM-5, but this may be due to its lower intensity relative to the C=C stretch at 1592 cm^{-1} and the bands being more convoluted. Given that the band grows in a similar region of the spectrum and during water release observed by MS, it seems sensible to tentatively assign the vibration again to benzofuran.[45]

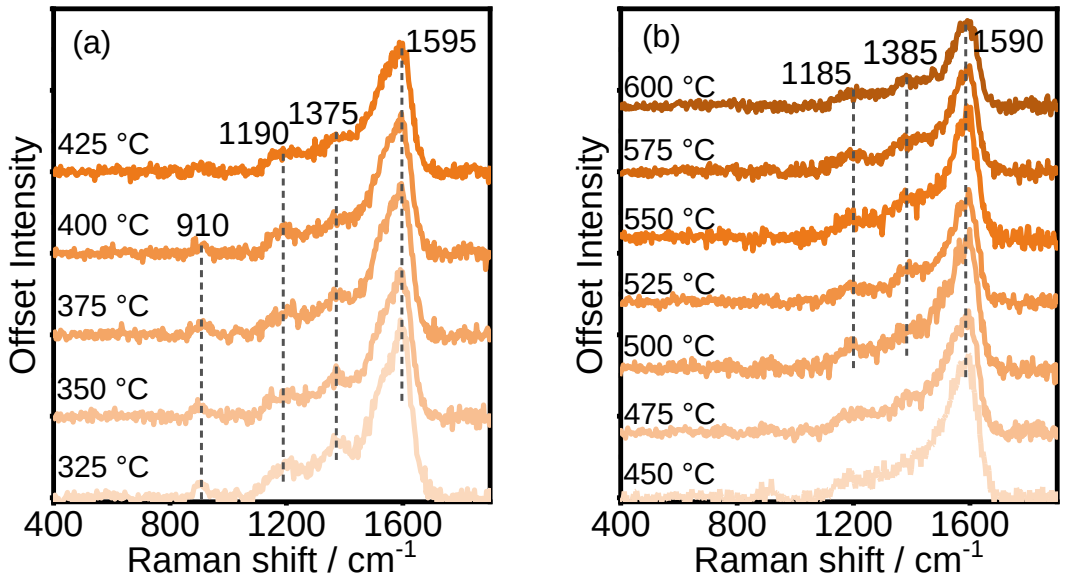

Figure 109 Kerr-gated Raman spectra collected during temperature programmed reaction of furan on H-Beta from (a) 325 to 425 and (b) 450 to 600 °C.

With increasing temperature, although the 1530 cm^{-1} band is not clear, the broad shoulder of the band at 1592 cm^{-1} would suggest it is still present. From 325 to 425 °C, bands at 905, 1190 and 1378 cm^{-1} are attenuated until at 450 °C they cannot be distinguished. By 600 °C, the growth of bands in the region of 1185 and 1385 cm^{-1} occurs again. After quenching the reactor and collecting a spectrum with a longer acquisition time, the bands become much clearer and sharper. In Figure 110, for the most part, bands can be compared again to amorphous carbon, the G band at 1602 cm^{-1} and D1 band and 1380 cm^{-1}, similarly to the spectrum collected of zeolite Y. However, in contrast to that observed in zeolite Y, there are also weak bands at 610 and 726 cm^{-1} which indicate that some branched aromatic species have formed and polyaromatic hydrocarbons.[26]

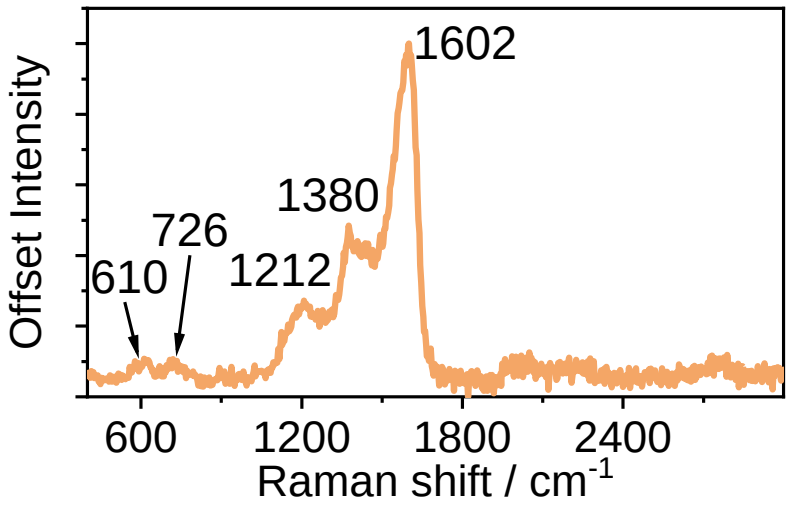

Figure 110 Kerr-gated Raman spectrum of quenched catalyst after temperature programmed reaction of H-Beta with furan up to 600 °Cs. The reactor was cooled at 20 °C min^{-1} under flowing He. Spectra collected in 5 acquisitions of 8 seconds with 1 mW power.

4.6.3 UV-Vis spectroscopy

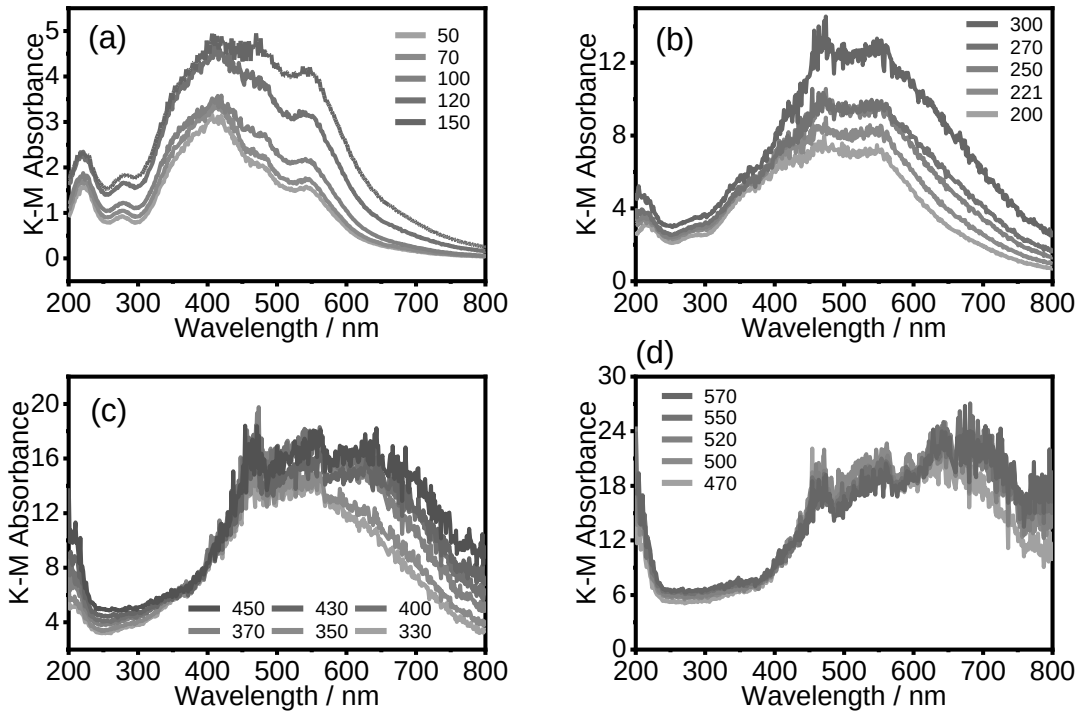

Figure 111 DR-UV-Vis spectra collected during the temperature programmed reaction of furan with H-Beta from (a) 60 – 160, (b) 200 – 300, (c) 330 – 430 and (d) 470 – 600 °C.

By DR-UV-Vis, in Figure 111a, we can see that the species that form on zeolite Beta during this reaction are strongly absorbing. In the early stages of the reaction up to 150 °C, the main changes are an almost doubling in overall absorbance, and most significant growth in the band at 450 nm – this was also observed in H-ZSM-5 and attributed to the growing concentration of trienylic carbocations,[24,29] including possibly protonated benzofuran. By Raman in zeolite Beta, the growth of a band at 1530 cm^{-1} hinted at the formation of a species like benzofuran and this further supports the assignment.

Further temperature increase beyond 200 °C in Figure 111b sees the consumption of bands at 217 and 280 nm which were related to adsorbed neutral and protonated furan, respectively,[24,31] while bands at higher wavelengths grow in intensity at 550 and 650 nm – indicating the formation of highly conjugated and likely charged species. The high absorbance below 200 nm towards the end of the experiment might, as in H-ZSM-5, indicate the higher energy transitions in aromatic species.[31] It should be noted that the Kubelka-Munk theorem becomes inaccurate as a means of quantifying absorbance from reflectance when reflectance is less than 10%. In this experiment since reflectance was less than 5% the absorbance values need to be treated more arbitrarily.

4.7 Thermo-gravimetric Analysis of coked zeolites

Thermogravimetric analysis (TGA) reveals information about the characteristics of coke species present in the samples by revealing the temperature required for combustion.[59] Through deconvoluting the asymmetric curve of the differential of the weight change, two curves are revealed that indicate two types of coke in each zeolite. The values of the peaks of these curves indicate the “hardness” of the coke present. For all zeolites, the greater curve has a maximum at around 544 °C, this is the temperature at which most weight is lost. Ferrierite, zeolite Y and zeolite Beta have a maximum at lower temperature around 500 °C, while ZSM-5 shows a second maximum at higher temperature at 580 °C. This indicates that ZSM-5 contains a “harder” type of coke which is more dehydrogenated,[60] in line with the results of Raman which indicate that ZSM-5 is the only zeolite on which significant polyaromatic species form. Ferrierite, zeolite Y and Beta contain a more hydrogenated coke-type.[60]

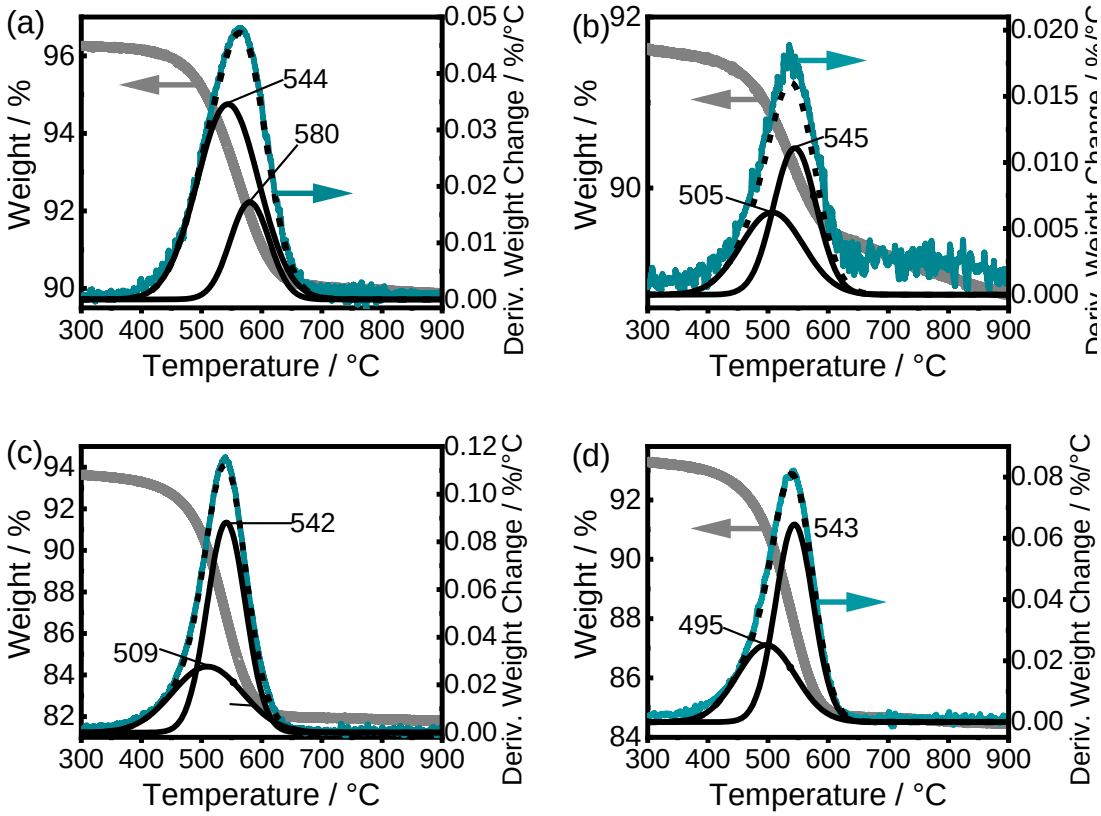

Figure 112 TGA data presented between 300 and 900 °C of (a) ZSM-5, (b) ferrierite, (c) zeolite Y and (d) Beta. Samples heated in air after reaction with furan during Kerr-gated Raman study. Grey line indicates the weight % of the sample during heating, green line the derivative of the weight lost, and the black lines are deconvolution curves of this derivative.

In terms of quantity, the larger pore zeolites contain the most deposited carbon by weight at 11.6 % in zeolite Y and 8.6 % in Beta, ZSM-5 contains 6.5 % and ferrierite (being the zeolite with the internal volume most difficult to access)[15] contains just 2.8 % coke. The differences in weight might also be explained by the amount of furan adsorbed at room temperature before the temperature ramp, due to the different adsorption properties of the zeolite.

Zeolite	Total % wt. lost	Temperature highest weight lost / °C	Low temperature peak (T_1) / °C	High temperature peak (T_2) / °C
ZSM-5	6.5	564	544	580
Ferrierite	2.8	543	505	545
Zeolite Y	11.6	542	509	542
Beta	8.6	543	495	544

Table 15 Results of TGA of carbon deposit on zeolites after temperature programmed reaction with furan. T_1 and T_2 values are determined from the deconvolution of the weight loss curve.

4.8 Comparison and discussion

The differences in reactivity of furan on each zeolite topology becomes clear even at room temperature during the adsorption of furan. In larger pore zeolites there is a larger contribution to adsorbed furan, and in zeolite Y the bands become very convoluted and are more overlapped in-line with a greater array of species formed on the surface. This contrasts with the medium pore zeolites, ZSM-5 and ferrierite where distinct bands in DR-UV-Vis indicate species containing mainly 3 and 5 conjugated double bonds, indicative of polymers containing 2 or 3 furan monomers and a positive charge, and Raman indicates the formation of a polyfuran-type species. Medium pore zeolites offer a degree of compartmentalisation that larger pore zeolites, and especially zeolite Y, cannot.

In running this type of temperature-programmed reaction, Huber observed firstly water loss below 200 °C, then the release of some unreacted furan and CO, CO_2 and water beginning at 200 °C most at 400 °C.[18] Finally, after 400 °C up to maximum at 500 °C they observe ethene, benzene and toluene. By FTIR, they observed the formation of new, aromatic C=C-H vibrations up to 300 °C, that decreased at 400 °C.[18] From our results we can say that the species they observed would have likely been benzofuran, as the signals follow a similar trend in our work (see the plot of benzofuran signal intensity plotted with *m/z* 78 and 91 in Figure 113).

The observation of benzofuran formation and consumption in H-ZSM-5 is very clear. There might be evidence of a species similar to benzofuran in zeolite Beta by the vibration at 1530 cm^{-1} and the growing absorbance band at 450 nm,[45] but this is far less clear than in H-ZSM-5 where benzofuran formation dominates the Raman spectrum up to 325 °C. Some works have postulated that benzofuran is a precursor to coke species,[47] this is particularly found during low temperature reactions after dissolution-extraction experiments to study the coke species.[47,50] Other studies have focused on the species as an intermediate of the reaction.[46,61] Gancedo *et al.* studied the catalytic pyrolysis of benzofuran on ZSM-5 to identify deactivation pathways,[6] and even highlighted a reaction pathway where naphthalenic species are formed from the Diels-Alder condensation of benzofuran with propene.[6] While we cannot rule this out under different reaction

conditions to ours, we can say confidently that it does not explain the consumption of benzofuran nor the formation of naphthalene in our work. Benzofuran is consumed above 325 °C and naphthalene does not start to form until 450 °C, both events are observed by Raman, separated by time and temperature in our experiment, despite detection of propene by MS while benzofuran is present.

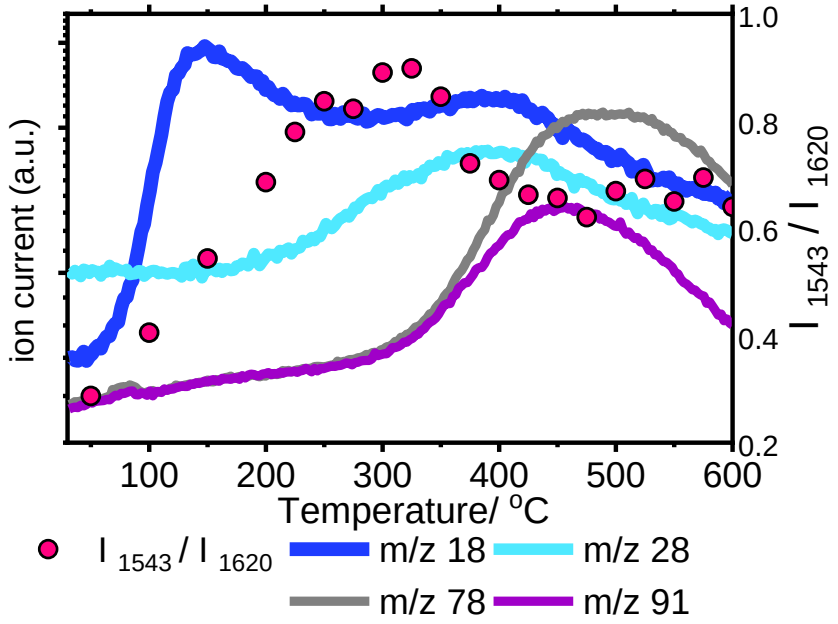

Figure 113 Figure illustrating water and CO produced by MS and the relative intensity of the benzofuran signal at 1543 cm^{-1} observed by Raman during temperature-programmed reaction over H-ZSM-5 catalyst.

Perhaps, while at lower temperatures benzofuran is deemed a deactivating species, at higher temperatures it is reactive, its consumption in our experiments coincides with both decarbonylation and dehydration reactions occurring at 300 – 400 °C, as illustrated in Figure 113. This is analogous to parts of the MTH reaction mechanism, where higher reaction temperatures are required to promote dealkylation of bulky intermediates.[28,56] The decarbonylation of benzofuran has been discussed in literature as a likely route to monocyclic aromatics,[6,18] which would correlate well with our data being around the same temperature that benzene and toluene form. While the direct decarbonylation of benzofuran gives toluene, disproportionation reactions allow benzene and xylenes also to be formed. Dehydration might also occur from further Diels-Alder condensation, but we do not see spectroscopic evidence to explain the dehydration at high

temperature. The schematic in Figure 114 gives an overview of the reactions that we can observe by Kerr-gated Raman in this chapter during the temperature-programmed reaction of furan on H-ZSM-5.

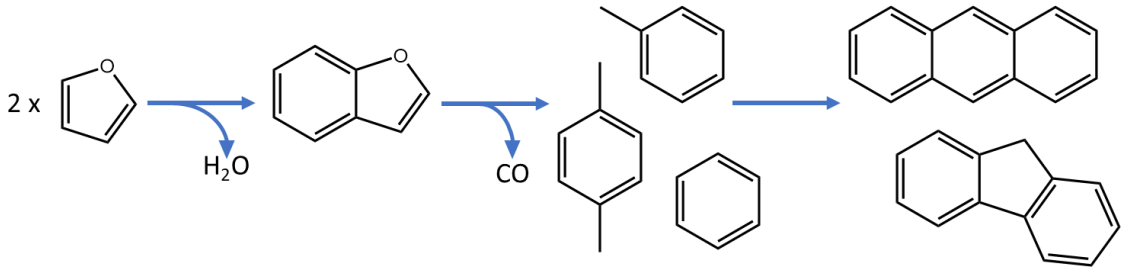

Figure 114 Schematic of species observed in reaction of furan on H-ZSM-5 as observed by Kerr-gated Raman spectroscopy.

From our Raman results, small polycyclic aromatic hydrocarbons including naphthalene and fluorene only form in ZSM-5 catalyst, despite there being a large enough internal volume for these species to form in zeolite Y and Beta.[14] This is further confirmed by TGA which reveals a high temperature maximum weight loss at 580 °C in ZSM-5, which is not present in the 3 other zeolites, where polyaromatic hydrocarbons do not form. In MTH there is a consensus that in H-ZSM-5, the polyaromatic hydrocarbons that are typically blamed for catalyst deactivation form on the external catalyst surface. It would be interesting to understand whether this is also the case during the conversion of furan. These polyaromatic hydrocarbons may form internally, since the hydrocarbon pool involved is more hydrogen deficient, and ring-condensation might be easier.

In ferrierite, MS data indicated only the formation of some olefinic products, and even dehydration reactions seem more inhibited in this material since water is released at 200 °C compared with 50 – 100 °C in the other zeolites. By DR-UV-Vis, after water was released, the loss of the band assigned to adsorbed furan cations occurred simultaneously with the formation of propene and CO_2 recorded by MS. This pathway is given in Figure 115, and has been demonstrated to occur by Gilbert *et al.* over H-ZSM-5 catalyst through co-feeding water experiments.[50] At higher temperatures, aromatics may form on the surface but are not released as products, they would be likely responsible for the formation of ethene through condensation, if the mechanism of ethene formation through aromatic contraction can be applied from MTH.[54] By Raman it is not possible to distinguish the

presence of any reactive intermediates, but by DR-UV-Vis the formation of a large conjugated system upon increasing temperature is observed by the growing band at 570 nm that may experience diffusion limitation in the zeolite.[15]

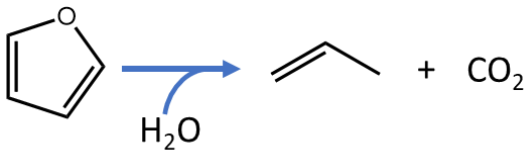

Figure 115 Reaction scheme of furan hydrolysis to result in propene and CO_2 as observed by DR-UV-Vis and MS during reaction of furan on ferrierite.

In larger pore zeolites, zeolite Y and Beta, by MS, the formation of C_{4-5} paraffins were observed to form which indicates hydride transfer reactions on these materials. Only in the large pore zeolites are bi-molecular hydride reactions possible, which can also explain why the lifetime of these catalysts are typically lower, since as a result of hydride transfer reactions, a hydrogen deficient species is left on the surface at intermediate temperatures.[8,11]

Comparisons have been made in literature between CFP and the hydrocarbon pool chemistry of MTH.[62] In Figure 116, spectra are shown which were collected after the reaction of furan and methanol with H-ZSM-5 which show marked similarities in the species present. This further strengthens the argument that the CFP reaction proceeds via a hydrocarbon pool-type mechanism which is especially stable in this zeolite topology.[54,63] After reaction with furan a greater number of low frequency vibrations show that more polyaromatic hydrocarbons have formed, in line with the use of a reactant molecule with lower effective hydrogen to carbon ratio compared with methanol, and the higher reaction temperature reached (600 °C compared with 450 °C in methanol).

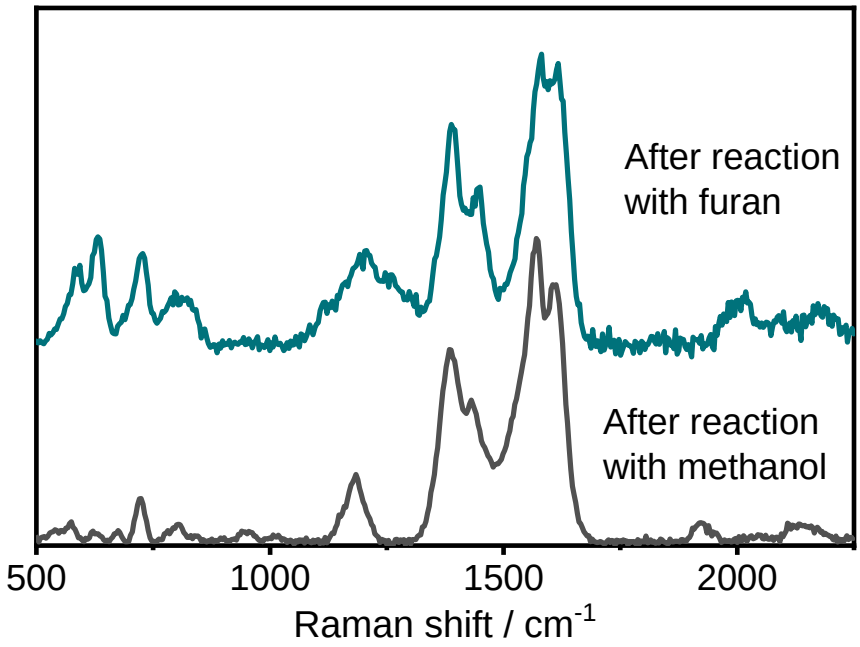

Figure 116 Comparison of data acquired after reaction of methanol on H-ZSM-5 from ref 26 (our work) and furan, by Kerr-gated Raman spectroscopy.

In large pore zeolites, by UV-Vis we observed an increasing absorbance across the spectrum, compared with the medium pore zeolites where the limited internal voids lend the catalysts to distinct molecular level species. As a comment to the very high Kubelka-Munk absorbance values, due to the exaggerated absorbances at reflectance < 10%, for zeolite beta in particular, absorbance values seem extremely high. The overall backgrounds can be explained by carbon laydown on the zeolites. While in the ferrierite experiment, the absorbance reaches a maximum intensity of > 3.5, this is a reasonable value due to the lower carbon laydown on the zeolite surface. In large pore zeolites, there is greater carbon laydown as confirmed by TGA, and absorbance values are therefore very high.

4.9 Conclusions

By Kerr-gated Raman we have identified benzofuran as an intermediate in H-ZSM-5, and this assignment is supported by UV-Vis data where a species of similar conjugation is formed in the same temperature period. Consumption of this peak coincides with CO and H_2O release and is followed shortly by aromatic production, which would suggest it is a very important hydrocarbon pool species

in furan conversion on H-ZSM-5. There is evidence of a benzofuran intermediate in H-beta, but the identifying Raman band is far weaker. Generally, the large pore zeolites H-beta and H-Y allow the formation of more extended polymers early in the reaction which are easily observed by UV-Vis spectroscopy. Reactions in H-ferrierite were hindered, only olefins were formed and no aromatics. No key intermediates were detected by Raman in the reaction of furan with H-ferrierite and even intermediate temperatures were required for the direct decarboxylation of furan to propene and CO_2. Of the zeolites tested, the 3-dimensional medium pores of ZSM-5 offer a compromise between the inhibited diffusion limitations in ferrierite and the lacking compartmentalization of Y and Beta that allow the formation of bulky “intermediates” that lead to coke.

4.10 References

1. T. Dickerson and J. Soria, Energies, 2013, 6, 514–538.
2. A. Zheng, L. Jiang, Z. Zhao, Z. Huang, K. Zhao, G. Wei and H. Li, Wiley Interdisciplinary Reviews: Energy and Environment, 2017, 6, 234.
3. C. Liu, H. Wang, A. M. Karim, J. Sun and Y. Wang, Chemical Society Reviews, 2014, 43, 7594–7623.
4. S. Yaman, Energy Conversion and Management, 2004, 45, 651–671.
5. A. V. Bridgwater, D. Meier and D. Radlein, Organic Geochemistry, 1999, 30, 1479-149 3.
6. J. Gancedo, L. Faba and S. Ordóñez Applied Catalysis A: General, 2021, 611, 117980.
7. S. Vitolo, B. Bresci, M. Seggiani and M. G. Gallo, Fuel, 2001, 80, 17–26.
8. J. Jae, G. A. Tompsett, A. J. Foster, K. D. Hammond, S. M. Auerbach, R. F. Lobo and G. W. Huber, Journal of Catalysis, 2011, 279, 257–268.
9. D. J. Mihalcik, C. A. Mullen and A. A. Boateng, Journal of Analytical and Applied Pyrolysis, 2011, 92, 224–232.
10. T. R. Carlson, G. A. Tompsett, W. C. Conner and G. W. Huber, Topics in Catalysis, 2009, 52, 241.
11. C. Mukarakate, M. J. Watson, J. ten Dam, X. Baucherel, S. Budhi, M. M. Yung, H. Ben, K. Iisa, R. M. Baldwin and M. R. Nimlos, Green Chemistry, 2014, 16, 4891–4905.
12. E. G. Derouane, Journal of Molecular Catalysis A: Chemical, 1998, 134, 29–45.
13. A. Aho, N. Kumar, K. Eränen, T. Salmi, M. Hupa and D. Yu. Murzin, Fuel, 2008, 87, 2493–2501.
14. IZA Structure Commission, Database of Zeolite Stuctures, http://www.iza-structure.org, (accessed 13 June 2017).
15. A. Bonilla, D. Baudouin and J. Pérez-Ramírez, Journal of Catalysis, 2009, 265, 170–180.

16. T. R. Carlson, J. Jae, Y.-C. Lin, G. A. Tompsett and G. W. Huber, Journal of Catalysis, 2010, 270, 110–124.
17. J. L. Grandmaison, P. D. Chantal and S. C. Kaliaguine, Fuel, 1990, 69, 1058–1061.
18. Y. T. Cheng and G. W. Huber, ACS Catalysis, 2011, 1, 611–628.
19. S. Vaitheeswaran, S. K. Green, P. Dauenhauer and S. M. Auerbach, ACS Catalysis, 2013, 3, 2012–2019.
20. E. A. Uslamin, N. A. Kosinov, E. A. Pidko and E. J. M. Hensen, Green Chemistry, 2018, 20, 3818–3827.
21. A. C. Psarras, C. M. Michailof, E. F. Iliopoulou, K. G. Kalogiannis, A. A. Lappas, E. Heracleous and K. S. Triantafyllidis, Molecular Catalysis, 2019, 465, 33–42.
22. Y. Ji, J. Pan, P. Dauenhauer and R. J. Gorte, Applied Catalysis A: General, 2019, 577, 107–112.
23. A. Gumidyala, T. Sooknoi and S. Crossley, Journal of Catalysis, 2016, 340, 76–84.
24. G. Spoto, F. Geobaldo, S. Bordiga, C. Lamberti, D. Scarano and A. Zecchina, Topics in Catalysis, 1999, 8, 279.
25. J. Socrates, Infrared and Raman characteristic group frequencies tables and charts, 3rd ed., John Wiley and Sons, Chichester, 2001.
26. I. Lezcano-Gonzalez, E. Campbell, A. E. J. Hoffman, M. Bocus, I. V. Sazanovich, M. Towrie, M. Agote-Aran, E. K. Gibson, A. Greenaway, K. De Wispelaere, V. Van Speybroeck and A. M. Beale, Nature Materials, 2020, 19, 1081–1087.
27. A. Mellouki, J. Liévin and M. Herman, Chemical Physics, 2001, 271, 239–266.
28. E. Borodina, F. Meirer, I. Lezcano-González, M. Mokhtar, A. M. Asiri, S. A. Al-Thabaiti, S. N. Basahel, J. Ruiz-Martinez and B. M. Weckhuysen, ACS Catalysis, 2015, 5, 992–1003.
29. S. Bordiga, G. Ricchiardi, G. Spoto, D. Scarano, L. Carnelli, A. Zecchina and C. Otero Areán, Journal of the Chemical Society, Faraday Transactions, 1993, 89, 1843–1855.
30. Q. Qian, C. Vogt, M. Mokhtar, A. M. Asiri, S. A. Al-Thabaiti, S. N. Basahel, J. Ruiz-Martínez and B. M. Weckhuysen, ChemCatChem, 2014, 6, 3396–3408.
31. P. J. Garratt, UV-vis atlas of organic compounds, Vol. 5, Heinz-Helmut Parkampus, Weinheim, 2nd Ed., 1992.
32. S. Yang, J. N. Kondo and K. Domen, Chemical Communications, 2001, 19, 2008–2009.
33. G. Spoto, S. Bordiga, G. Ricchiardi, D. Scarano, A. Zecchina and E. Borello, Journal of the Chemical Society, Faraday Transactions, 1994, 90, 2827–2835.
34. Z. Wang, Z. Lu, X. Huang, R. Xue and L. Chen, Carbon, 1998, 36, 51–59.
35. S. Bertarione, F. Bonino, F. Cesano, A. Damin, D. Scarano and A. Zecchina, Journal of Physical Chemistry B, 2008, 112, 2580–2589.
36. S. Şen, B. Bardakçı, A. G. Yavuz and A. U. Gök, European Polymer Journal, 2008, 44, 2708–2717.
37. O. Ninis, M. Abarkan and M. Bouachrine, 2014 International Renewable and Sustainable Energy Conference (IRSEC), 2014, 593–595.

38. F. Billes, H. Böhlig, M. Ackermann and M. Kudra, Journal of Molecular Structure: THEOCHEM, 2004, 672, 1–16.
39. P. M. Allotta and P. C. Stair, ACS Catalysis, 2012, 2, 2424–2432.
40. C. Pazè, B. Sazak, A. Zecchina and J. Dwyer, Journal of Physical Chemistry B, 1999, 103, 9978–9986.
41. M. Fabbiani, G. Confalonieri, S. Morandi, R. Arletti, S. Quartieri, M. Santoro, F. Di Renzo, J. Haines, R. Fantini, G. Tabacchi, E. Fois, G. Vezzalini, G. Ricchiardi and G. Martra, Microporous and Mesoporous Materials, 2021, 311, 110728.
42. I. Kiricsi and H. Förster, Journal of the Chemical Society, Faraday Transactions 1: Physical Chemistry in Condensed Phases, 1988, 84, 491–499.
43. K. Tamagawa and R. L. Hilderbrandt, Journal of the American Chemical Society, 1984, 106, 20–25.
44. I. Kiricsi, I. Pálinkó and T. Kollár, Journal of Molecular Structure, 2003, 651–653, 331–334.
45. V. B. Singh, Spectrochimica Acta Part A: Molecular and Biomolecular Spectroscopy, 2006, 65, 1125–1130.
46. C. Liu, T. J. Evans, L. Cheng, M. R. Nimlos, C. Mukarakate, D. J. Robichaud, R. S. Assary and L. A. Curtiss, Journal of Physical Chemistry C, 2015, 119, 24025–24035.
47. S. Shao, H. Zhang, R. Xiao, D. Shen and J. Zheng, Bioenergy Research, 2013, 6, 1173–1182.
48. M. Signorile, F. Bonino, A. Damin and S. Bordiga, The Journal of Physical Chemistry C, 2015, 119, 11694–11698.
49. H. Yang, R. J. Coolman, P. Karanjkar, H. Wang, Z. Xu, H. Chen, T. J. Moutziaris and G. W. Huber, Green Chemistry, 2015, 17, 2912–2923.
50. C. J. Gilbert, J. S. Espindola, W. C. Conner, J. O. Trierweiler and G. W. Huber, ChemCatChem, 2014, 6, 2497–2500.
51. M. Bjørgen, F. Bonino, S. Kolboe, K.-P. Lillerud, A. Zecchina and S. Bordiga, Journal of the American Chemical Society, 2003, 125, 15863–15868.
52. A. Sadezky, H. Muckenhuber, H. Grothe, R. Niessner and U. Pöschl, Carbon, 2005, 43, 1731–1742.
53. A. C. Ferrari and J. Robertson, Physics Review B, 2000, 61, 14095–14107.
54. S. Svelle, F. Joensen, J. Nerlov, U. Olsbye, K.-P. Lillerud, S. Kolboe and M. Bjørgen, Journal of the American Chemical Society, 2006, 128, 14770–14771.
55. M. Bjørgen, S. Svelle, F. Joensen, J. Nerlov, S. Kolboe, F. Bonino, L. Palumbo, S. Bordiga and U. Olsbye, Journal of Catalysis, 2007, 249, 195–207.
56. J. Goetze, F. Meirer, I. Yarulina, J. Gascon, F. Kapteijn, J. Ruiz-Martínez and B. M. Weckhuysen, ACS Catalysis, 2017, 7, 4033–4046.
57. E. T. C. Vogt and B. M. Weckhuysen, Chemical Society Reviews, 2015, 44, 7342–7370.
58. F. N. Guerzoni and J. Abbot, Journal of Catalysis, 1993, 139, 289–303.
59. J. M. Ortega, A. G. Gayubo, A. T. Aguayo, P. L. Benito and J. Bilbao, Industrial Engineering & Chemical Research, 1997, 36, 60–66.

60. P. Castaño, G. Elordi, M. Olazar, A. T. Aguayo, B. Pawelec and J. Bilbao, Applied Catalysis B: Environmental, 2011, 104, 91–100.
61. X. Hu, S. Jiang, S. Kadarwati, D. Dong and C.-Z. Li, RSC Advances, 2016, 6, 40489–40501.
62. T. R. Carlson, Y.-T. Cheng, J. Jae and G. W. Huber, Energy & Environmental. Sciience, 2010, 4, 145–161.
63. U. Olsbye, S. Svelle, M. Bjørgen, P. Beato, T. V. W. Janssens, F. Joensen, S. Bordiga and K. P. Lillerud, Angewandte Chemie International Edition, 2012, 51, 5810–5831.
64. S. A. Ali, K. E. Ogunronbi and S. S. Al-Khattaf, Chemical Engineering Research and Design, 2013, 91, 2601–2616.

5 Conversion of oxygenated hydrocarbons on H-ZSM-5: Acetaldehyde, acetic acid, furan and 2,3-dihydrofuran

5.1 Introduction

The upgrading of bio-oils over zeolite catalysts is a complicated process to study mechanistically in part due to the many components that constitute bio-oils or biomass vapours. Using model compounds to simplify the reactions to be studied can be helpful to understand how the different functional groups of components play their role in the mechanism, leading to desired pathways to high-value products or to coke formation that ultimately leads to catalyst deactivation.[1] During the catalytic upgrading of biomass feedstocks, several researchers noted a high dependence of the deactivation rate on the effective H/C ratio (H/C_{eff}),[2,3] and similarity in product distribution for feeds with similar values. Specifically using H-ZSM-5 as a catalyst, Zhang *et al.* found a correlation between increasing H/C_{eff} and an increase in overall olefin and aromatic yield, with decreased coke formation.[2] Mentzel *et al.* compared the conversion of oxygenates with low H/C_{eff} ratios ($H/C_{eff} < 1.5$) to methanol ($H/C_{eff} = 2$) conversion under the same conditions, and found that lifetime decreased dramatically from 65 h to the order of minutes.[3] The similarity in product distribution that is observed converting different feeds using H-ZSM-5 catalyst is thought to be due to a hydrocarbon pool (HCP) within zeolite pores that is responsible for the formation of aromatic and olefinic products. The composition of the HCP of methanol in H-ZSM-5 is fairly well-established,[4,5] but biomass or model compounds thereof, would form HCPs that are expected to be hydrogen deficient and therefore deactivate more quickly, due to rapid coke formation.[1,2]

The model compounds used in this study are furan, 2,3-dihydrofuran, acetic acid and acetaldehyde. The chemical structures of these compounds and their H/C_{eff} ratios are shown in Figure 117. Furanic species make up a large proportion of lignocellulosic biomass pyrolysis vapours and are therefore a common model compound used (as discussed in the previous chapter). 2,3-dihydrofuran is used to compare the reactivity of a compound with similar structure to furan but with

higher H/C_{eff} and without the aromaticity. Acetic acid in bio-oils might be typically derived from the acetyl groups of hemicellulose or from the decomposition of sugars,[6] and is one of the most abundant compounds found in bio-oils.[7–9] Acetic acid has been studied as an acetylating agent over zeolites of other biomass-relevant hydrocarbons, to understand its roles in biomass upgrading reactions.[10–12] Acetaldehyde is an interesting compound to study due to the presence of small oxygenates such as aldehydes and ketones in biomass pyrolysis vapours. Despite the higher H/C_{eff} of acetaldehyde than acetic acid, Ramasamy *et al.* found that the deactivation of H-ZM-5 from aqueous solutions of small hydrocarbons was faster with acetaldehyde, this was attributed to the ease of acetaldehyde condensation followed by cyclization to benzene which condenses easily to form coke.[13]

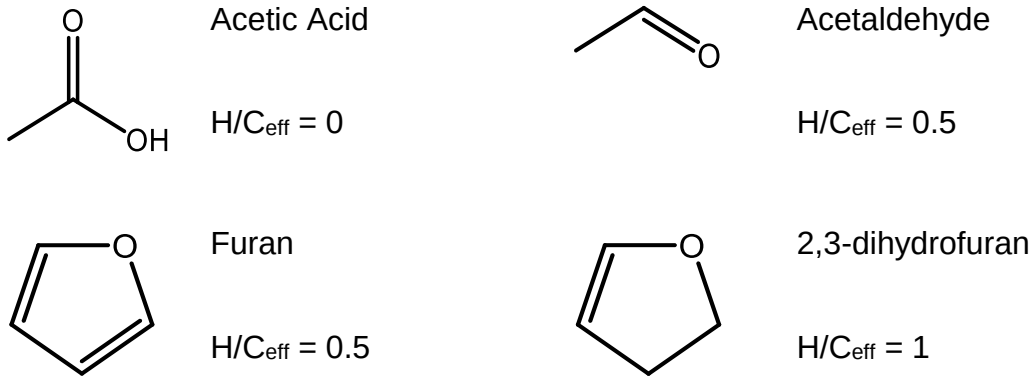

Figure 117 Chemical structures of the model compounds used to study their reaction over H-ZSM-5 in this chapter, furan, acetic acid, acetaldehyde and 2,3-dihydrofuran.

In this work, we studied the interaction of H-ZSM-5 with acetaldehyde, acetic acid, 2,3-dihydrofuran and furan as model compounds for lignocellulosic biomass. A similar experimental methodology as in Chapter 4 was used, where the zeolite was saturated with the model compound at room temperature and temperature-programmed reaction carried out. Due to some issues with the reaction cell, during these experiments, only 30 mg of zeolite catalyst was used in these experiments, and gas flows were adjusted accordingly to maintain the same GHSV. Compared with Chapter 4, lower partial pressures of liquids were injected into the gas stream because acetic acid was prone to condensation in the lines and on the walls of the reaction cell (1 µl min^{-1} of liquid was vapourised in 23 ml min^{-1} of He, rather than 6 µl min^{-1} in 30 ml min^{-1}) The H-ZSM-5 catalyst was pre-

treated by heating at 10 °C min^{-1} in a flow of 20 % O_2/He to 600 °C and holding for 1 h in the Linkam CCR1000 cell. The catalyst was then cooled to 30 °C in He, and then either furan, acetic acid, acetaldehyde or 2,3-dihydrofuran (DHF) was adsorbed by injection of a syringe pump at 1 µl min^{-1} for 1 h into the He stream, followed by flushing with He for 1 h to remove much of the weakly adsorbed species. The temperature was linearly increased by 5 °C/min from 30 to 600 °C, and recordings taken every 25 °C, every 5 min. The mass spectrometry (MS) data was normalised with respect to the flow of He, the carrier gas, to account for any changes in chamber pressure. Kerr-gated Raman spectra were collected with a 10 s acquisition time, using 2 mW power, and a 1200 lines/mm grating.

5.2 Room temperature adsorption

5.2.1 Acetaldehyde

The Kerr-gated Raman spectrum of H-ZSM-5 after adsorption of acetaldehyde for 1 h is shown in Figure 118, and contains a strong C=C stretch at 1608 cm^{-1}, broad bands at 1174 – 1260 cm^{-1} and a small band at 1425 cm^{-1}. There is no C=C stretch in acetaldehyde itself, but it is known to readily condense to form crotonaldehyde, with a C=C stretch frequency at 1649 cm^{-1} as recorded in gas phase measurements by both IR and Raman.[14] Liu *et al.* studied the conversion of acetaldehyde and furan by experimental and computational methods and found that acetaldehyde easily self-reacts, undergoing aldol condensation to give crotonaldehyde.[15] The structure of crotonaldehyde is shown in Figure 120a, and is the product of condensation of two acetaldehyde molecules. The strong signal measured here at 1608 cm^{-1}, however, would indicate a more conjugated species formed from a greater degree of condensation. The maximum at 1174 cm^{-1} can be assigned to a C-C stretching vibration in aliphatic aldehydes,[14,16] 1260 cm^{-1} to the C=C-H bend of crotonaldehyde,[14] and 1425 cm^{-1} near to the symmetric CH_3 deformation of either crotonaldehyde or acetaldehyde, which are both reported in literature at near 1450 cm^{-1}.[14,17]

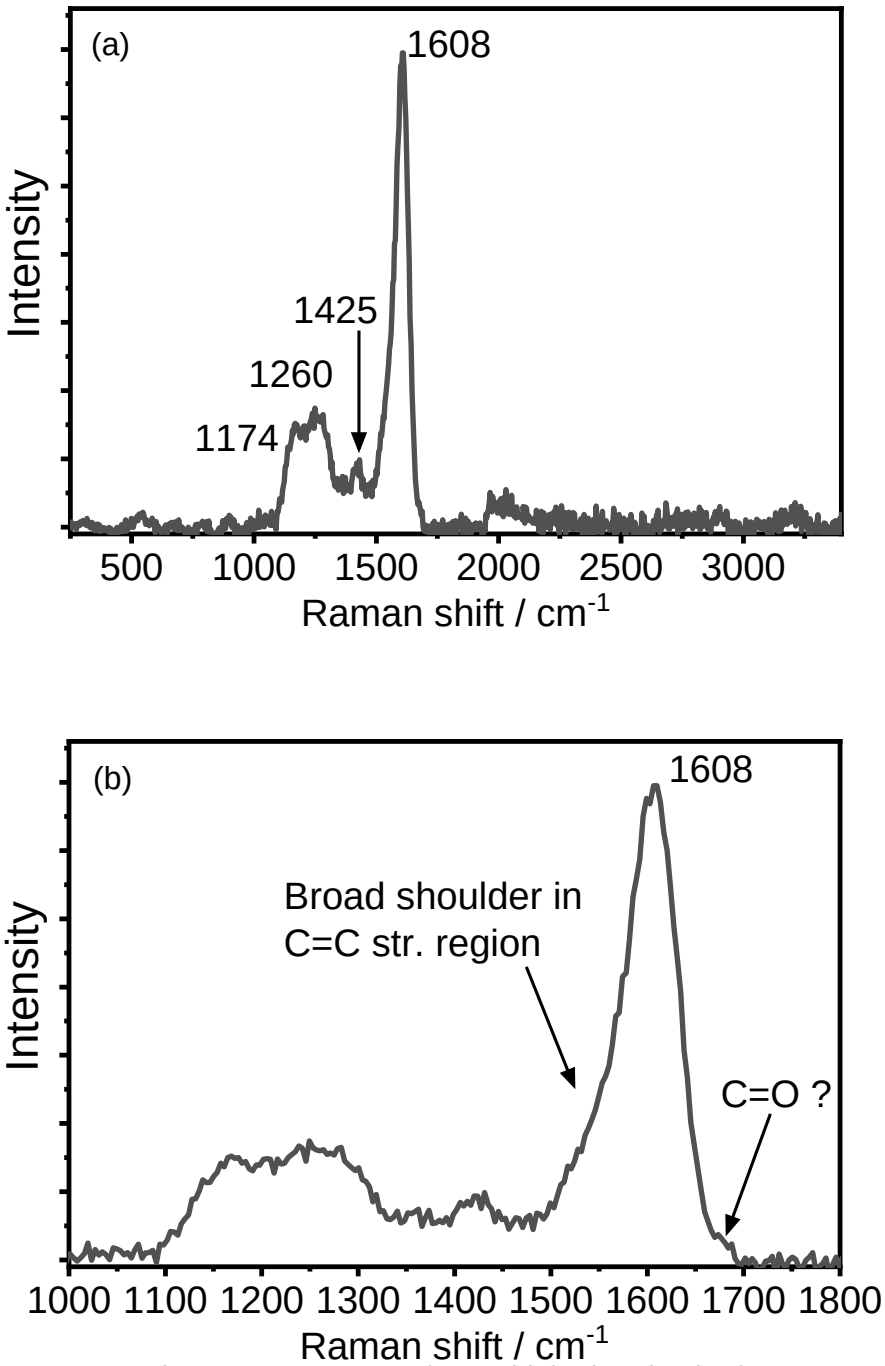

Figure 118 Kerr-gated Raman spectrum of acetaldehyde adsorbed on H-ZSM-5 at 30 °C for 1 h followed by 1 h of flushing with inert gas. Displayed (a) between 250 and 3350 cm^{-1} and (b) between 1000 and 1800 cm^{-1}.

A closer look at the bands from 1000 to 1800 cm^{-1} as shown in Figure 118b shows clearly the maximum at 1608 cm^{-1} but also a broad shoulder to the lower frequency side of this band, which would indicate the C=C stretches of more conjugated species,[16,18] but no clear shoulder at higher frequency which would have indicated some shorter chain species with C=C stretches. A very, very weak band at 1680 cm^{-1} is in the region of a C=O stretch of aliphatic aldehydes.[14,16]

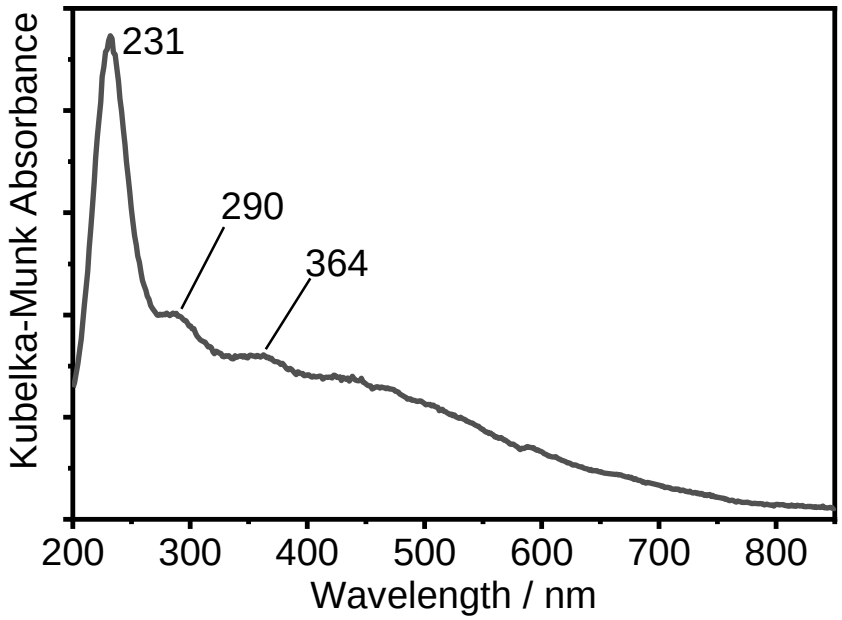

Figure 119 UV-Vis spectrum acquired after acetaldehyde adsorption on H-ZSM-5 followed by 1 h of flushing with helium to remove weakly adsorbed species.

The UV-Vis data after adsorption, shown in Figure 119, would also agree with greater degrees of polymerisation having taken place, with absorbance bands at 231, 290 and 364 nm and a broad absorbance at high wavelengths from 400 – 700 nm. A band at 231 nm is in line with the formation of conjugated species containing 2 double bonds, at 290 nm to 1 double bond and a positive charge, at 364 nm to 2 double bonds and positive charge.[19–24] The broad band which tails to high wavelengths above 600 nm can be assigned to species with up to 5 double bonds with a positive charge.[19–24] The three highest energy bands might therefore account for crotonaldehyde, protonated crotonaldehyde and further condensed and similar species as shown in Figure 120c. The UV-Vis and Raman data together do agree that a resonance enhanced species is being detected by Raman; a charged species with 3 conjugated double bonds.

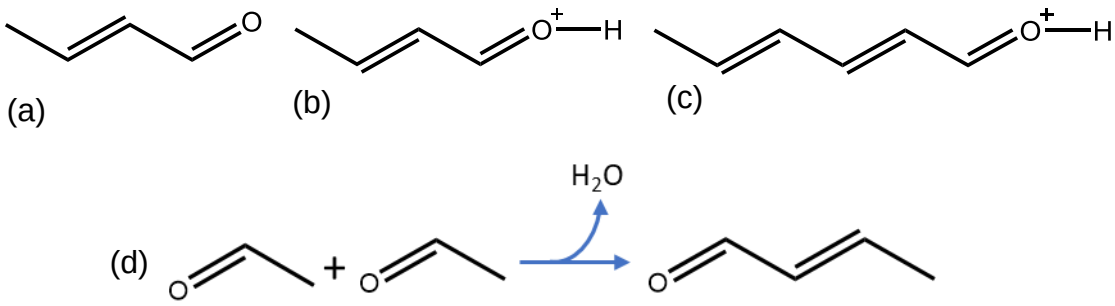

Figure 120 Chemical structures of (a) crotonaldehyde, (b) protonated crotonaldehyde at the preferred site of protonation and (c) protonated acetaldehyde trimer. (d) The overall reaction of two acetaldehyde molecules to give crotonaldehyde and water.

5.2.2 Acetic Acid

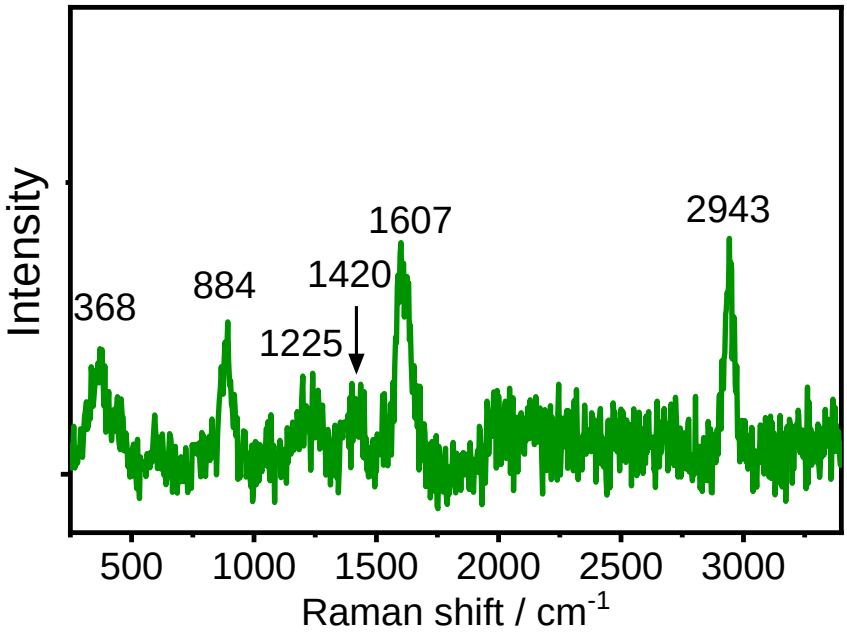

Figure 121 Kerr-gated Raman spectrum of acetic acid adsorbed on H-ZSM-5 at 30 °C for 1 h followed by 1 h of flushing with inert gas.

Upon adsorption of acetic acid to the zeolite, acetic acid remains intact and unreacted on the surface exhibiting weak but distinct bands which are shown in Figure 121. Bands appear at 2943, 1410, 1225 and 884 cm^{-1}, corresponding to the C-H stretch, the CH_3 deformation, C-O stretch and C-C stretch of acetic acid, which are recorded in literature as being of very strong, medium, medium, and very strong intensity respectively.[25,26] The assignment to adsorbed acetic acid is

in line with studies which show that acetic acid at low temperatures remains only hydrogen bonded to H-ZSM-5, its proton affinity being too low for protonation to occur which might lead to reaction.[27,28]

Two extra bands remain unassigned in the spectrum, at 368 and 1607 cm^{-1}. The low frequency band is related to the zeolite Si-O-Si vibration.[29,30] The band at 1607 cm^{-1} is most likely, unfortunately, a C=C stretch vibration related with impurities in the acetic acid, being the only band in the spectrum that does not belong to acetic acid, as it was not present prior to acetic acid injection and according to Psarras *et al.*, the self-condensation of acetic acid does not occur at such low temperatures.[6] Despite the overall indication from the spectrum that acetic acid remains intact, we are still unable to detect the C=O stretching vibration near 1700 cm^{-1} due to its weak Raman scattering, being a highly polar group and hence having weak polarizability.

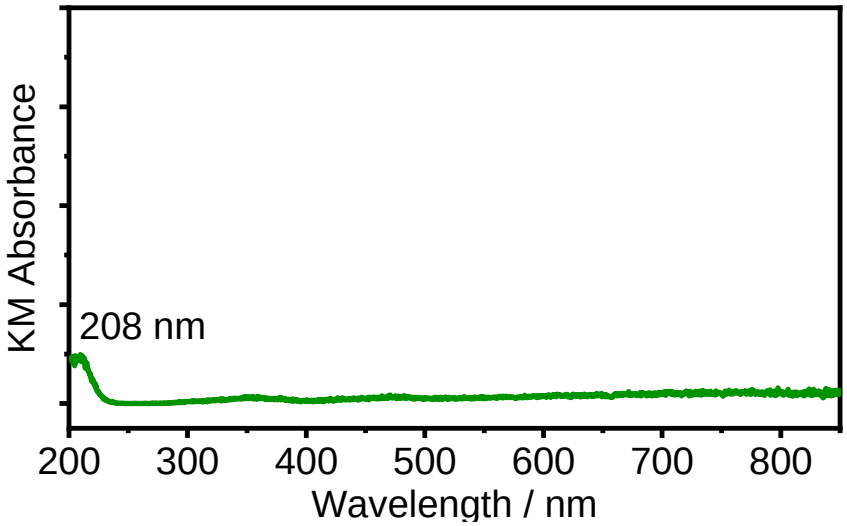

Figure 122 UV-Vis spectrum of acetic acid adsorbed to H-ZSM-5 for 1 h followed by 1 h of flushing. Calcined H-ZSM-5 was used as a background/reference material, to display only bands belonging to acetic acid.

The UV-Vis spectrum of adsorbed acetic acid, in Figure 122, shows only low absorbance at below 210 nm, in-line with the forbidden n→π* transition of the C=O bond of acetic acid.[23,31] This further confirms that no polymerisation reactions have taken place at room temperature, and that there is no resonance enhancement effect, which explains the low signal-to-noise ratio in Figure 121.

5.2.3 Furan

In Figure 123, the Kerr-gated Raman spectrum of furan adsorbed on H-ZSM-5 is shown and the UV-Vis spectrum in Figure 124. The adsorption of furan was carried out under slightly different conditions to those measured in a previous chapter, with lower partial pressures of vapours and less catalyst, this warranted the repeated reaction of furan in this chapter.

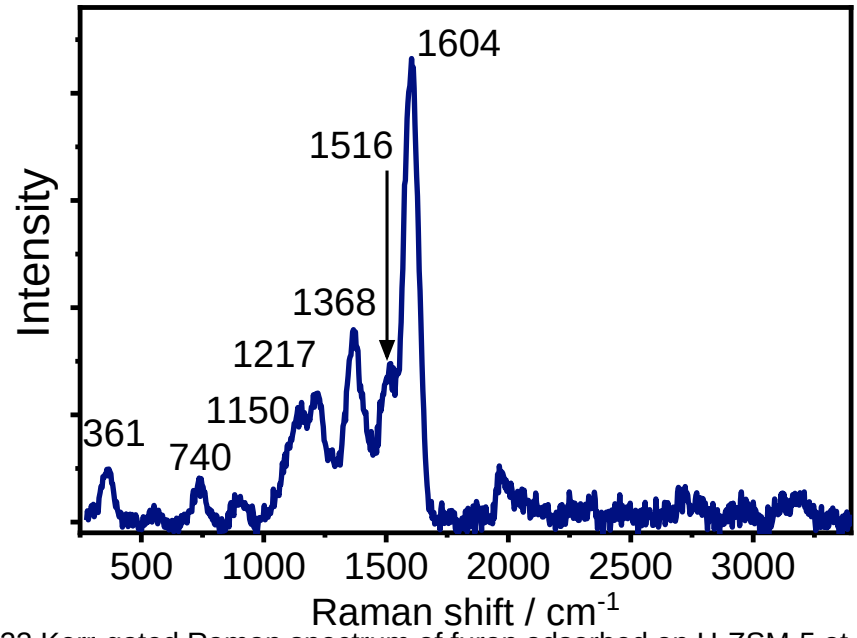

Figure 123 Kerr-gated Raman spectrum of furan adsorbed on H-ZSM-5 at 30 °C for 1 h followed by 1 h of flushing with inert gas.

The C=C stretch at 1604 cm^{-1} is ambiguous to assign, but generally relates to carbonaceous species containing 2 – 3 conjugated double bonds, while the band at 1368 cm^{-1} is connected to CH_2 vibrations which must be formed from hydride transfer reactions to give the more conjugated species with some C atoms hydrogenated. The shoulder at 1516 cm^{-1} is typical of the stretching of C-C=C^+ bonds in unsaturated carbocations.[24,32–35] The band at 1150 cm^{-1} could be related to CH rock vibrations and at 1217 cm^{-1} to CH_2 deformations.[16] The small band at low frequency, 740 cm^{-1}, is in a region where ring deformation vibrations and out-of-plane C-H deformations have been measured for furan and its hydrogenated derivatives.[16,36]

By UV-Vis, the main differences compared with the spectrum after furan adsorption on H-ZSM-5 in Chapter 4, are the lessened intensity of the bands at 540 nm due to relatively fewer conjugated species containing 5 double bonds and a positive charge, and at 220 nm due to neutral and adsorbed furan.[19,21] These differences can be rationalised by the lower partial pressure of furan in the gas feed, which lead to a lesser degree of polymerization and a lesser amount of physisorbed furan on the zeolite surface. The most significant band is again that at 410 nm for which species containing 2 – 3 double bonds and a positive charge are responsible.[21]

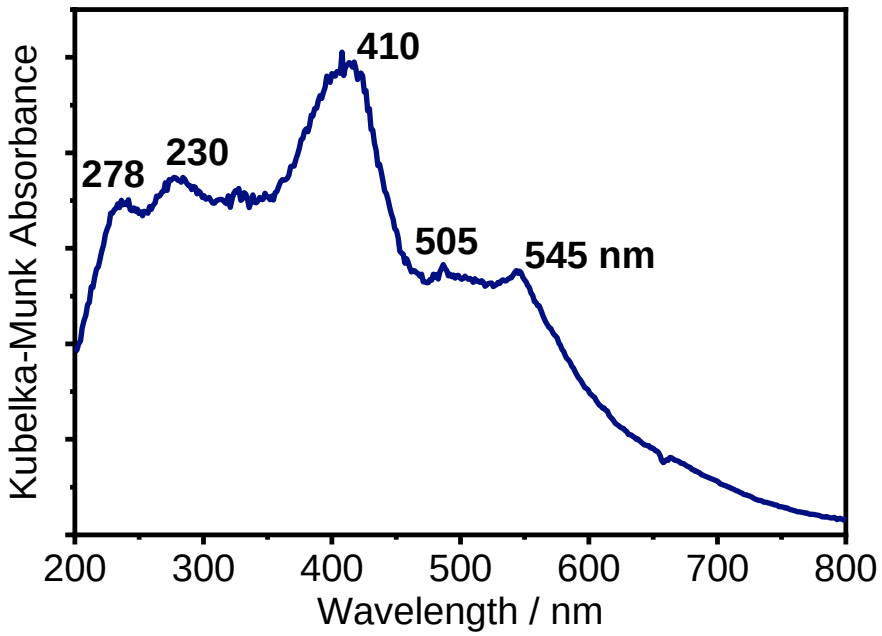

Figure 124 UV-Vis spectrum captured after furan adsorption on H-ZSM-5 under different measurement conditions to those in Chapter 4

5.2.4 2,3-dihydrofuran

The Raman spectrum of 2,3-dihydrofuran adsorbed on H-ZSM-5 is shown in Figure 125. The vibration at 1600 cm^{-1} does not correspond to the C=C stretch in 2,3-dihydrofuran which is recorded in literature at 1625 cm^{-1},[36] indicating a chemical change upon adsorption. A shoulder at 1519 cm^{-1} signifies the formation of C-C=C^{+} bonds in carbenium ion systems, and a band at 1205 cm^{-1} is often assigned to C-C stretching between sp^2-sp^3 carbon atoms,[14,16] or to the C-O stretching in furan rings.[36] The weak band at 883 cm^{-1} can be assigned to the CH_2 deformation vibrations in hydrogenated furan derivatives.[36]

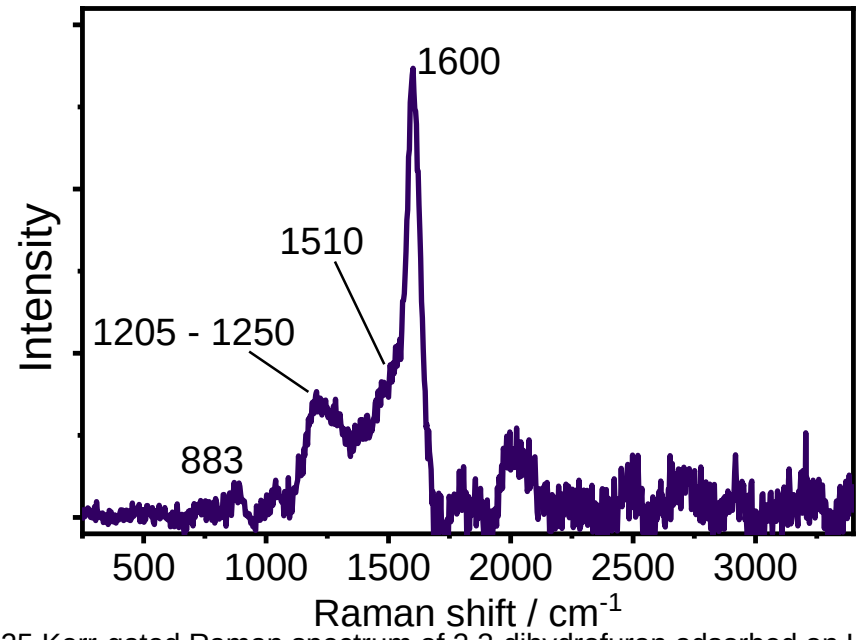

Figure 125 Kerr-gated Raman spectrum of 2,3-dihydrofuran adsorbed on H-ZSM-5 at 30 °C for 1 h followed by 1 h of flushing with inert gas.

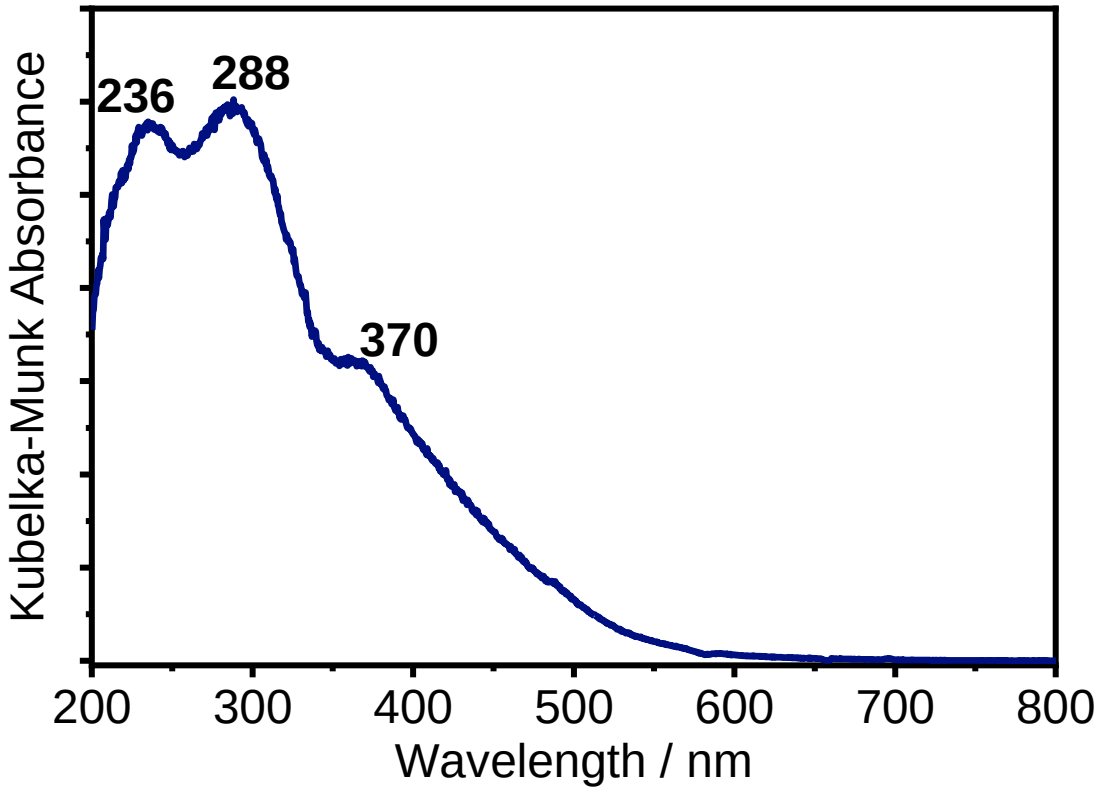

Figure 126 UV-Vis spectrum of 2,3-dihydrofuran adsorbed on H-ZSM-5 after 1 h of adsorption and 1 h of flushing in He.

In line with its high proton affinity (with respect to ammonia – having the lowest proton affinity required for protonation by H-ZSM-5),[37,38] a study on the protonation of hydrogenated furan derivatives gave evidence that upon protonation of 2,3-dihydrofuran, a carbenium ion is formed,[37] i.e. one of the carbon atoms at the double bond becomes protonated. With an excess of 2,3-dihydrofuran it is possible that the carbenium ions formed at the surface act as an electron-acceptor to form some polymers. This is in line with the UV-Vis data in Figure 126 that provides evidence of the formation of species with 2 conjugated double bonds (band at 235 nm), 1 double bond and a positive charge (band at 288 nm) and 2 double bonds and a positive charge (band at 370 nm).

5.3 Temperature programmed reaction

5.3.1 Acetaldehyde

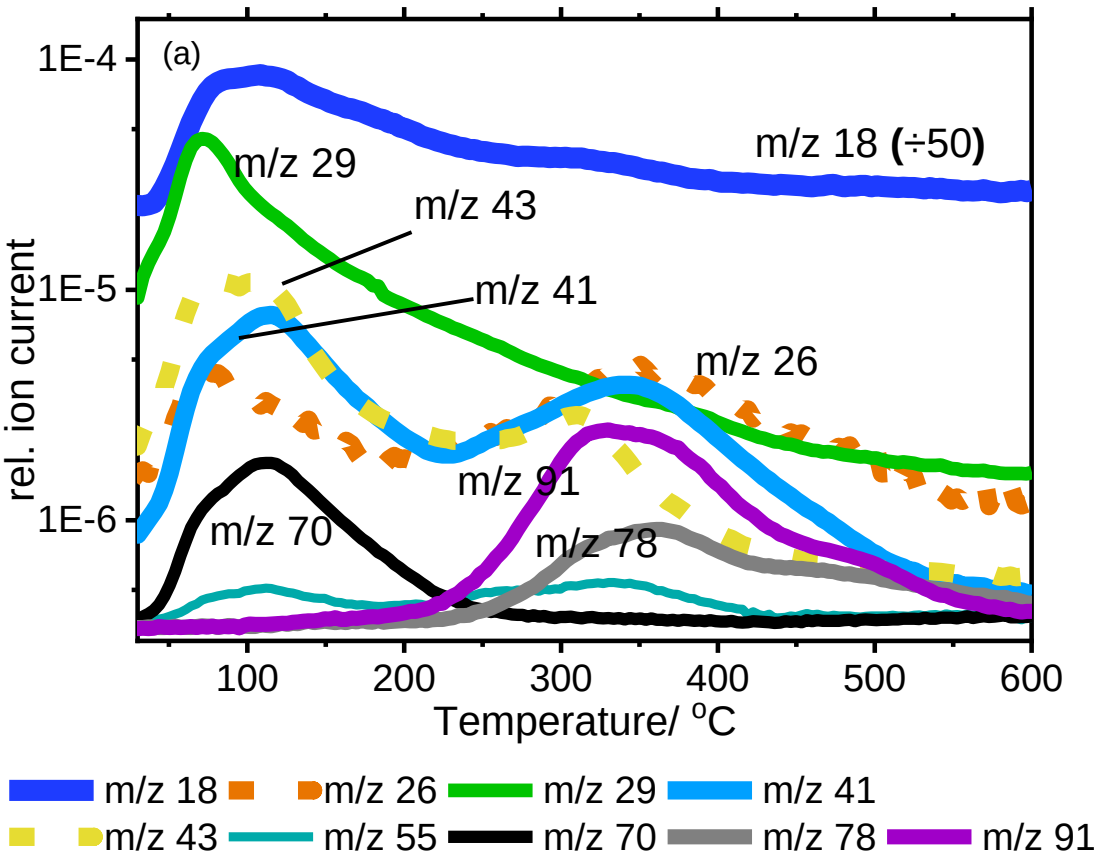

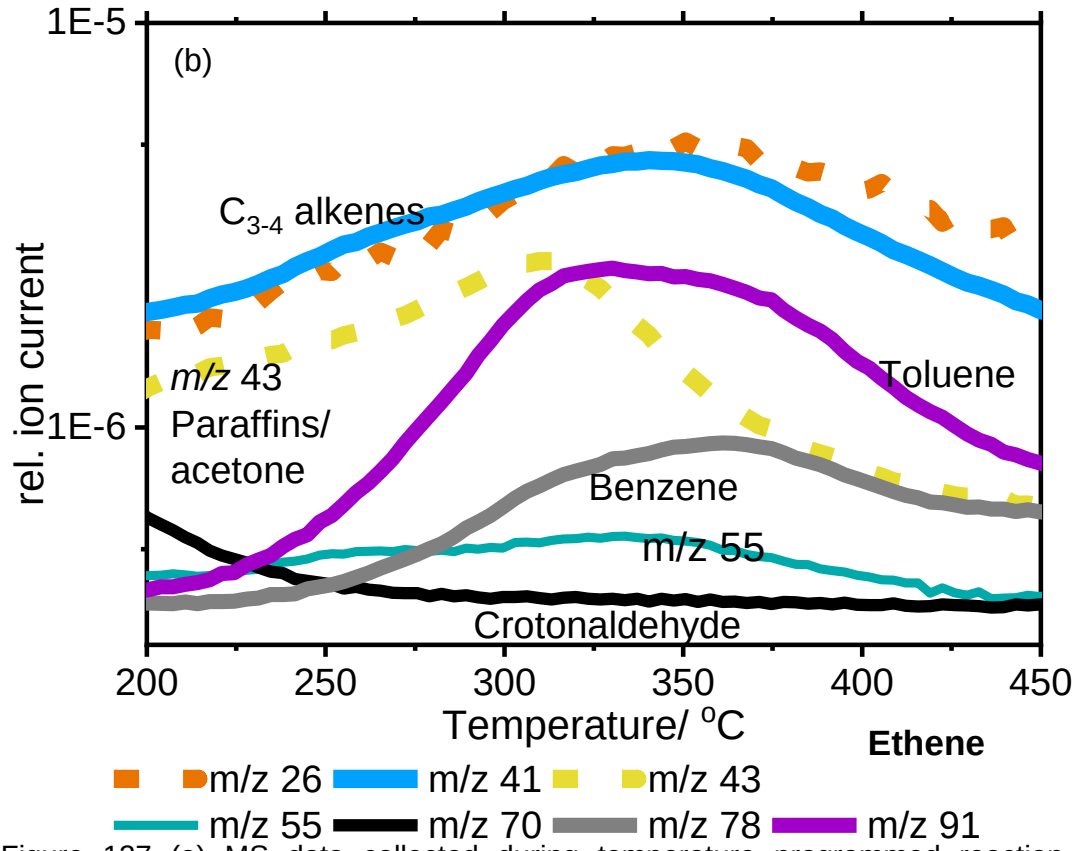

Figure 127 (a) MS data collected during temperature programmed reaction of acetaldehyde on H-ZSM-5 from 30 to 600 °C and (b) MS data with *m/z* 41, 26, and 43 corrected by removal of the contributions of acetaldehyde and crotonaldehyde to the *m/z* fragments (using fragmentation patterns reported in the NIST database)[39], from 200 to 450 °C.

The MS data recorded during the temperature ramp from 30 to 600 °C are shown in Figure 127a, which includes the recorded signals from 30 to 600 °C, as well as a plot in Figure 127b from 200 – 450 °C in which the contributions of fragments of acetaldehyde and crotonaldehyde have been removed from *m/z* 26, 41 and 43 to reveal more clear patterns of ethene, $C_{3\text{-}4}$ alkenes, and paraffins/acetone formation (both acetone and paraffins may contribute to *m/z* 43). From 30 to 200 °C, water (*m/z* 18) is detected with a maximum signal observed at 100 °C, and acetaldehyde and crotonaldehyde are desorbed, these products are followed by *m/z* 29 and 70, respectively. Other products which are typical of hydrocarbon pool products, such as olefins and aromatics, are released above 200 °C. Ethene and propene/butene are formed in this region, which are more easily shown in Figure 127b. Alkenes ($C_{3\text{-}4}$) reach a maximum at 341 °C and ethene at 354 °C. The signal at *m/z* 43 also rises again above 200 °C, which could be due to paraffin formation, or another oxygenate such as acetone or acetic acid that also

contributes ion fragments to *m/z* 43. Toluene is formed onwards of 225 °C and benzene 250 °C according to *m/z* 91 and 78, respectively.

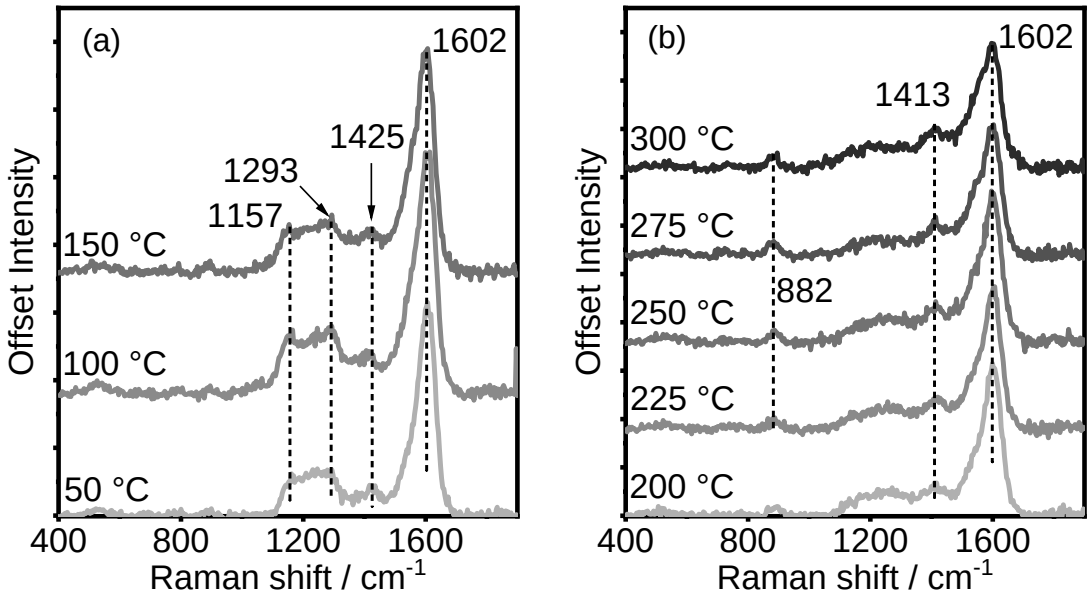

Figure 128 Kerr-gated Raman spectra acquired during temperature programmed reaction of acetaldehyde on H-ZSM-5 from (a) 50 - 150 °C and (b) 200 - 300 °C.

Figure 128 displays the Raman spectra collected from (a) 50 to 150 °C and (b) 200 to 300 °C during the temperature programmed ramp of acetaldehyde on the zeolite. From 50 to 150 °C there is little change apart from the strengthening of bands around 1155 and 1290 cm^{-1} from the previously broad band in that region. From 200 °C and onwards, the MS data in Figure 127 reveals the onset of olefin and aromatic products. During this period, a weak band grows at 882 cm^{-1}, as does a band at 1413 cm^{-1} while the broad bands at 1155 – 1290 cm^{-1} are diminished. Bands around 1410 cm^{-1} can be related to CH_3 deformation vibrations in aliphatic compounds.[16] The most intense band in the spectrum remains that at 1602 cm^{-1} with a C=C stretch that can be attributed to either aromatic or linear species, most likely containing 3 double bonds, although it becomes more broad and asymmetric, encompassing more C=C stretch vibrations at lower frequency.

As the temperature increases from 325 to 375 °C, the data in Figure 129a shows that a broad band at 1415 cm^{-1} continues to increase in intensity, correlating with

the maximum in aromatic formation. This band is in the region of vinylic CH_2 deformations,[18] which would suggest aromatic formation directly from small, branched olefin cyclization. At 400 °C a more significant band at 1370 cm^{-1}, becomes dominant over that at 1415 cm^{-1}, which remains as a shoulder. The strong band at 1370 cm^{-1} makes it clear that bicyclic or polycyclic aromatic species have been formed, as their ring-breathing modes lie here.[16,32,40]

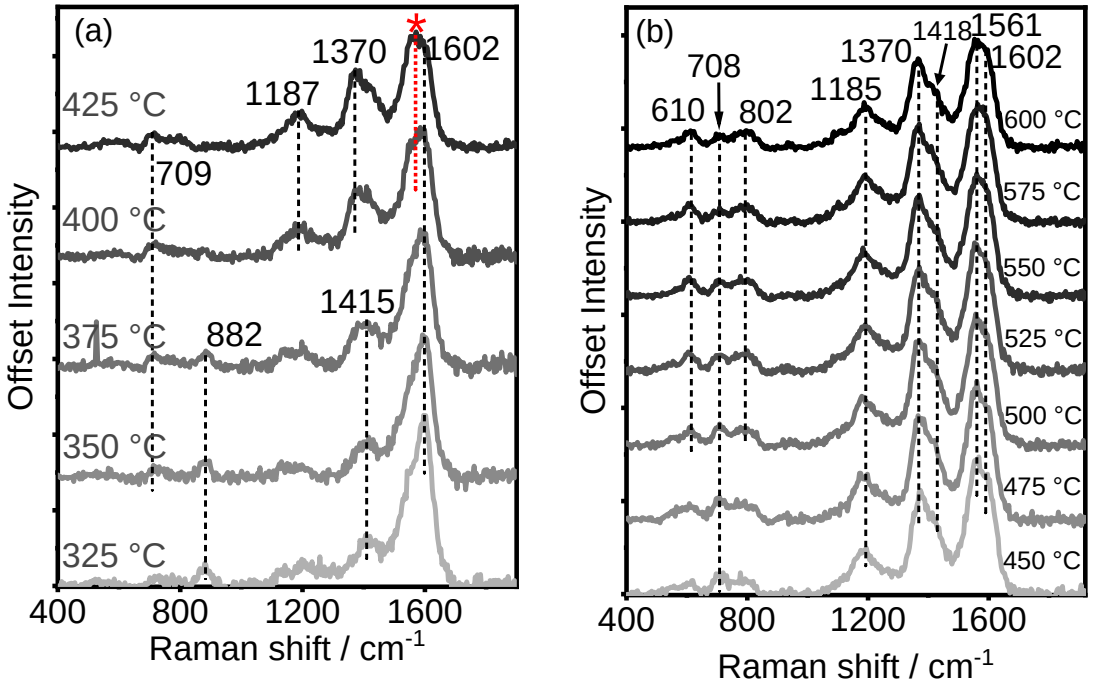

Figure 129 Kerr-gated Raman spectra acquired during temperature programmed reaction of acetaldehyde on H-ZSM-5 from (a) 325 - 425 °C and (b) 450 - 600 °C.

In the C=C stretch region at 400 °C, in Figure 129a, a new band emerges at 1566 cm^{-1}, which is indicated by the red asterisk and dropline. The asymmetry of the band at 1602 cm^{-1} may indicate that this species was growing at lower temperatures but dominate the spectrum by 425 °C. Data presented in Chapter 3 showed that polyenes have a strong C=C stretch vibration in this region and lead to catalyst deactivation through pore blocking in H-SSZ-13 during MTH.[18] Hernandez *et al.* noted the formation of a dienylic carbocation in H-ZSM-5 with a vibration at 1567 cm^{-1}, the structure of which is given in Figure 130, a trienylic polyene which became protonated leaving two double bonds and a positive charge. By 400 °C the band at 880 cm^{-1} is diminished, and a new low frequency band at 710 cm^{-1} is recorded. Meanwhile, by MS, the formation of monocyclic

aromatic and olefinic products is observed to slow at 375 °C. The slowing of product formation prior to the formation of naphthalene would suggest that polyaromatics are not solely responsible for catalyst deactivation here, linking again perhaps polyenes with slowing activity.

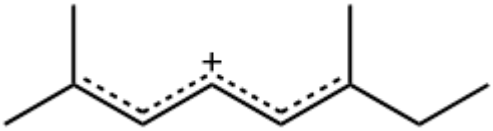

Figure 130 Chemical structure of the polyene species with C=C-C+ stretching frequency at 1567 cm^{-1}.[41]

The most intense Raman band during heating from 450 to 600 °C as shown in Figure 129b is the C=C stretch at 1561 cm^{-1}, and a strong band remains at 1602 cm^{-1}. In the lower frequency region, two further bands develop at 610 and 800 cm^{-1} which can be linked with the formation of polyaromatic hydrocarbons.[18] An intense band at 1185 cm^{-1} is attributed to sp^2-sp^3 mixing of C atoms, and is often observed in coke analysis by Raman.[42,43] In this period by MS we observe the continued drop in products, as the catalyst is in the deactivation phase.

5.3.2 Acetic Acid

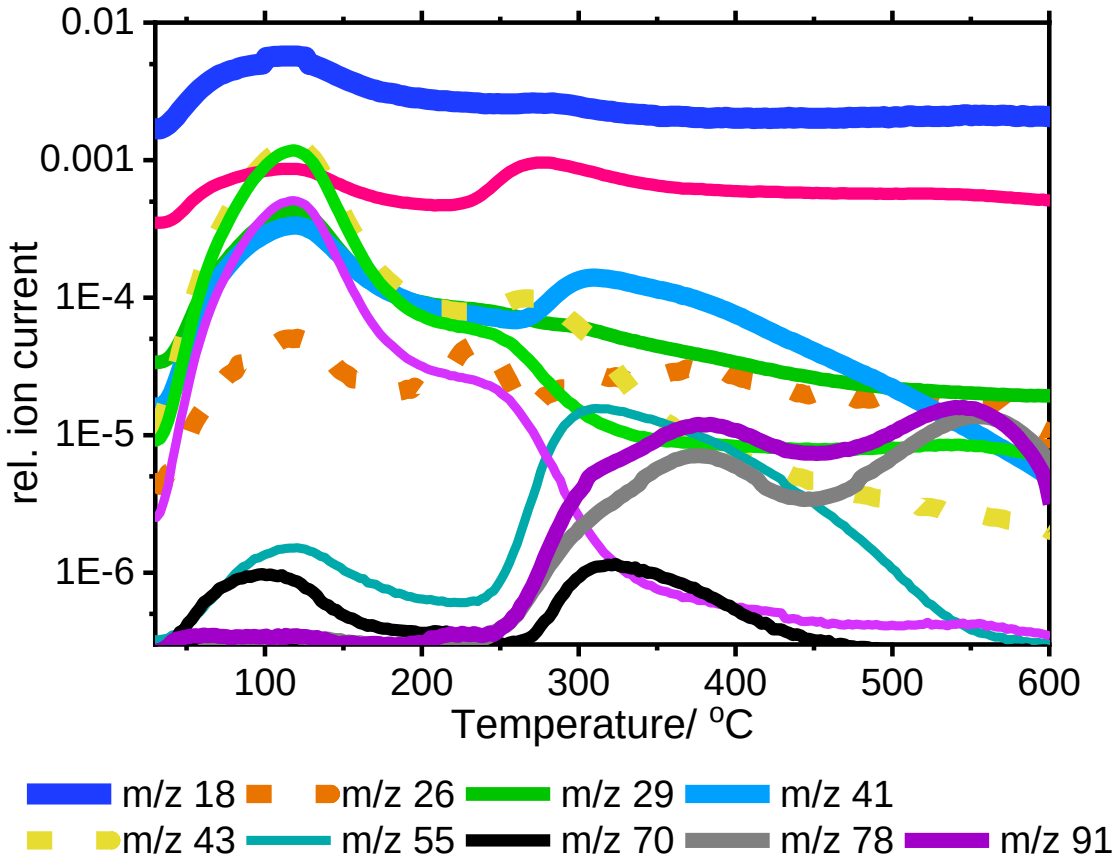

Figure 131 MS data acquired during temperature programmed reaction of acetic acid on H-ZSM-5 from 30 to 600 °C.

During the temperature programmed reaction of acetic acid, the raw MS data shown in Figure 131 shows that initially, unreacted acetic acid is desorbed, and water is released between 30 and 120 °C, then, products are formed mainly at and above 250 °C. Due to the complexity of this data owing to the number of products formed which have convoluted mass fragment patterns, a simplified plot is shown below in Figure 132 where the contributions of acetic acid to *m/z* 41 and 43 have been removed by subtracting the proportion of these ion currents in reference to *m/z* 60 (which is unique to acetic acid of these convoluted species). The major contributor to *m/z* 41 in this experiment is therefore $C_{3\text{-}4}$ alkenes and to *m/z* 43 acetone, with some possible contribution from C_4 paraffins although given the low H/C_{eff} of the acetic acid feedstock, paraffins seem unlikely.

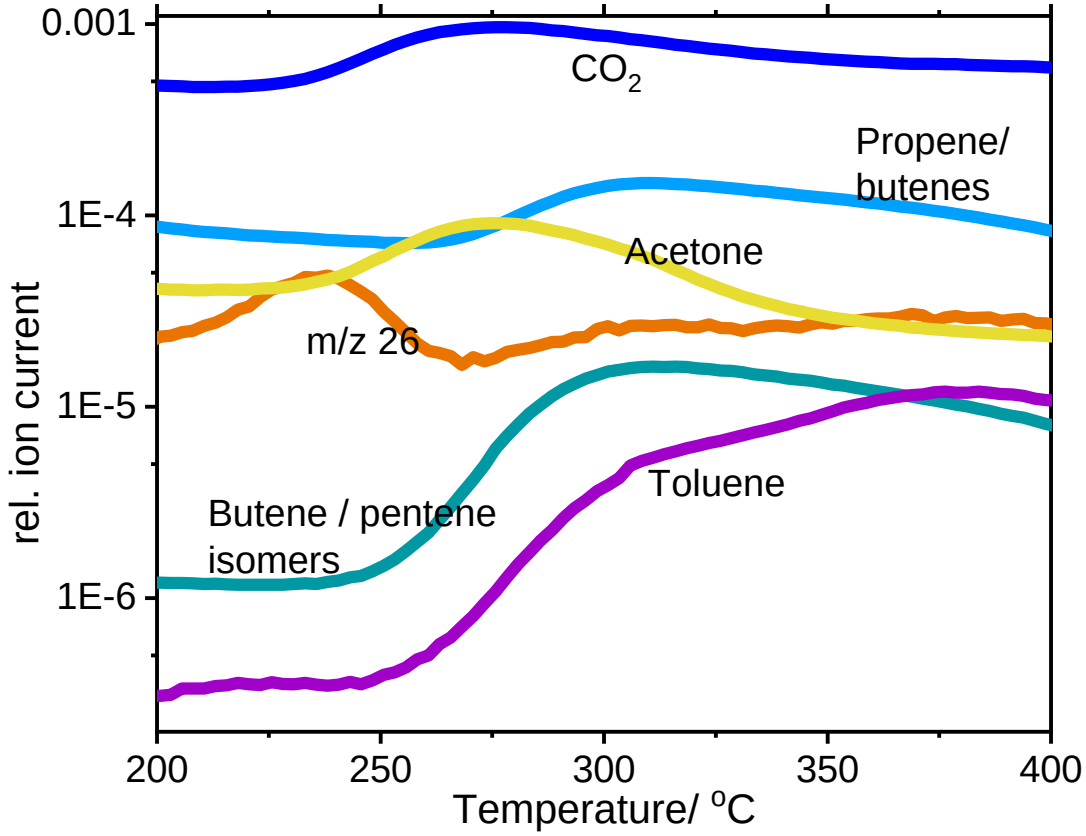

Figure 132 Simplified and deconvoluted MS data collected during temperature programmed reaction of acetic acid on H-ZSM-5, shown in the temperature period from 200 to 400 °C. The contributions of acetic acid (*m/z* 60) to *m/z* 41, 43 and 55 have been removed.

The condensation of acetic acid is described in literature to lead to a dimer as an acetyl intermediate on the zeolite acid sites – these have been observed by infra-red spectroscopy during temperature programmed reaction experiments by Parker and Gumidyala.[7,27] This intermediate can easily decompose into acetone and CO_2, which explains the simultaneous detection of CO_2 and acetone by MS at 240 °C, the reaction and acetyl intermediate is illustrated in Figure 133. In agreement with previous works, acetic acid typically undergoes dehydration and decarboxylation to easily yield acetone as a product or in this case it could be the primary product that further reacts in the pores to yield secondary reaction products – aromatics and olefins.[6,7] Soon after, at 250 °C the increasing signal at *m/z* 55 indicates the formation of butene and/or pentene isomers, closely followed by aromatic products, benzene and toluene (*m/z* 78 and 91). Aromatics might form from the cyclization of these C_4-C_5 alkenes. The aromatic formation reaches a maximum at 400 °C, and where the entire temperature range is shown in Figure

131, the aromatic production then drops to increase again later. Propene or butene isomers form at the highest temperature starting at 273 °C. The ion fragment *m/z* 26 is labelled as such, it usually corresponds to mostly ethene but in this case might be an unknown product – but it was detected at a very low temperature from 205 °C which is unusual for ethene.

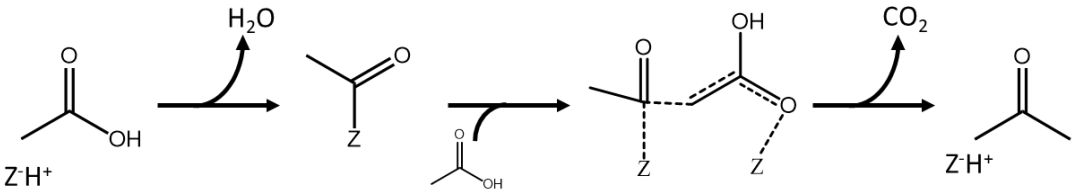

Figure 133 Overall schematic of the ketonization of acetic acid via an acetyl intermediate on the zeolite surface to give acetone, CO_2 and H_2O on Brønsted acid sites, according to ref 7.

In Figure 134, Raman spectra collected from 50 – 150 °C during reaction of acetic acid is shown. As the temperature is increased initially, signal intensity significantly increases, in contrast to other experiments included in this thesis running temperature programmed ramp experiments (without continuously feeding reactant into the catalyst), where the signal intensity typically drops with progressive heating. Most likely the difference in this experiment is the formation of resonance enhanced species where initially there was no resonance enhancement, as proven by the UV-Vis spectrum of acetic acid adsorbed on H-ZSM-5 in Figure 122, or the formation of a species with a greater Raman cross section.

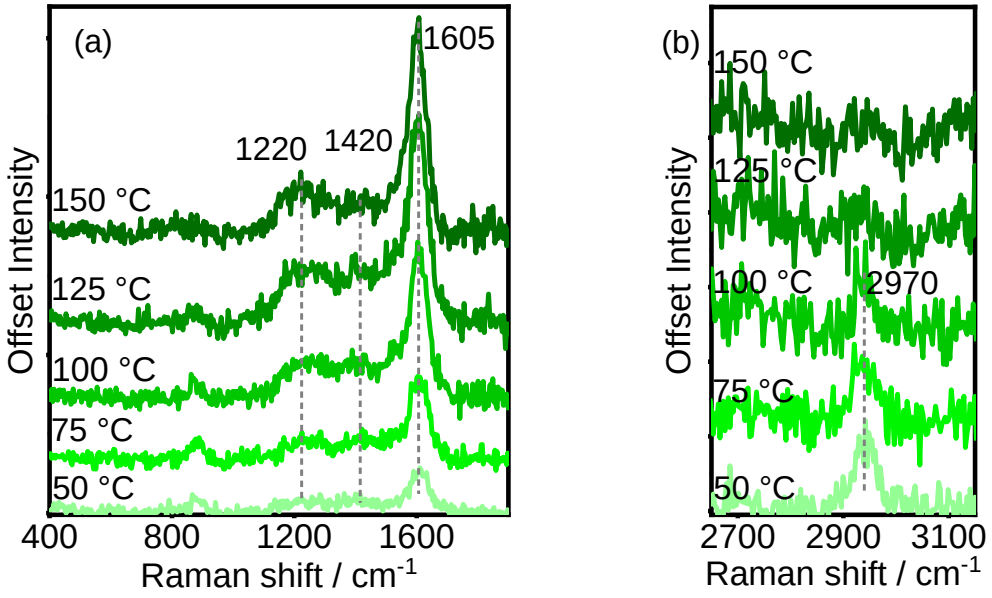

Figure 134 Kerr-gated Raman spectra acquired during temperature programmed reaction of acetic acid on H-ZSM-5 at 50 - 150 °C in the (a) low and mid-frequencies region and (b) high frequency region.

The CH_3 stretch vibration of acetic acid at high frequency that was observed at room temperature is weakened until it is consumed entirely by 125 °C. Meanwhile, the band at 1605 cm^{-1} increases by 5 times its intensity between 50 and 125 °C, and a broad band around 1220 cm^{-1} indicates that CH_2 and CH_3 deformations are becoming stronger.[16] In Figure 135a, the Raman spectra recorded during the temperature ramp between 175 and 300 °C are shown – a temperature region that the MS results in Figure 132 show is very active. The Raman spectra show bands that remain constant up to 200 °C, including the strong C=C stretch at 1600 cm^{-1}, and CH_2 and CH_3 deformations at 1200 and 1420 cm^{-1}.[16] Progressive temperature increase leads to (1) the growth of a strong band at 885 cm^{-1} from 225 to 300 °C, which becomes one of the most intense bands in the spectrum, (2) three distinct bands grow at 1190, 1300 and 1410 cm^{-1} from 225 to 300 °C and (3) a shift in the most intense peak in the C=C stretch region from 1604 to 1595 cm^{-1}, a common frequency of the C=C stretch vibration for monocyclic aromatic hydrocarbons.[16,44]

The relative intensity of the band at 885 cm^{-1} is plotted against temperature in Figure 135 b, and directly overlaying MS data between 200 – 450 °C, which helps

to demonstrate that it reaches its maximum intensity at 325 and 350 °C, before the species responsible is consumed again. Vibrations at 885 cm^{-1} might relate to C-C stretches, ring vibrations in epoxides, symmetric C-O stretching in ethers and C-H deformations in aliphatic aldehydes or carboxylic acids, but the strength of this band is unusual and indicates a very strong vibration and likely, resonance enhancement. Aliphatic aldehydes with branching at adjacent to the α-carbon show a medium-strong Raman band at 890 cm^{-1} due to symmetric skeletal stretching vibration of the quaternary carbon.[16] This medium-strong vibration combined with the resonance enhancement effect through conjugation could lead to such a strong signal.

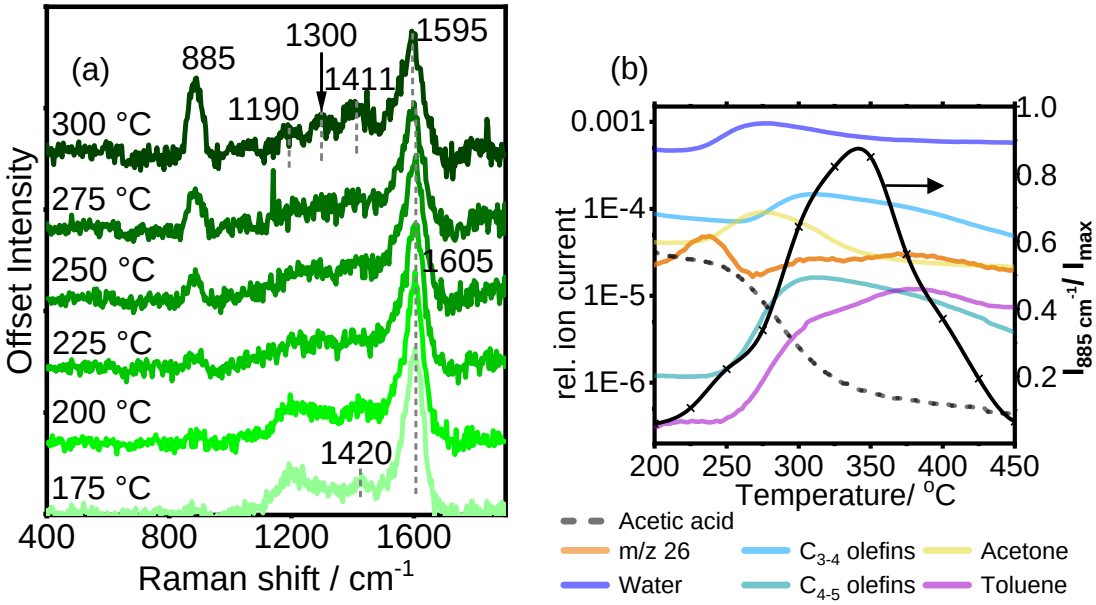

Figure 135 (a) Kerr-gated Raman spectra acquired during temperature programmed reaction of acetic acid on H-ZSM-5 at 175 - 300 °C and (b) plot of relative intensity of the Raman band at 885 cm^{-1} against temperature.

From 325 to 450 °C as shown in Figure 136a, an overall drop in Raman intensities is observed, although the signal-to-noise ratio improves. The band at 885 cm^{-1} is gradually attenuated from its maximum intensity at 325 °C until it is diminished entirely by 450 °C. The strong C=C stretch at 1590 cm^{-1} likely belongs to the monocyclic aromatic species that are detected by MS, they could form from the cyclization of olefins. The CH_3 deformations observed at 1413 cm^{-1} are overshadowed as stronger vibrations emerge at 375 °C first at 1395 and then 1370 cm^{-1} by 450 °C, which are more likely belonging to breathing modes of

naphthalenic species, based on the strength of the band. A vibration at 1188 cm^{-1} is observed, and a new, strong vibration in the C=C stretch region at 1560 cm^{-1} emerges.

The spectra in Figure 136b indicate that with increasing temperature to 600 °C, new low-frequency bands emerge at 615 and 790 cm^{-1}, which have been assigned previously to polyaromatics, and this would be further supported by the strong breathing mode at 1362 cm^{-1}.[18,32] By 500 °C, the strongest band in the spectrum is at 1570 cm^{-1} in the C=C region, although the band is sufficiently broad to contain also higher frequency vibrations at 1590 – 1610 cm^{-1}.

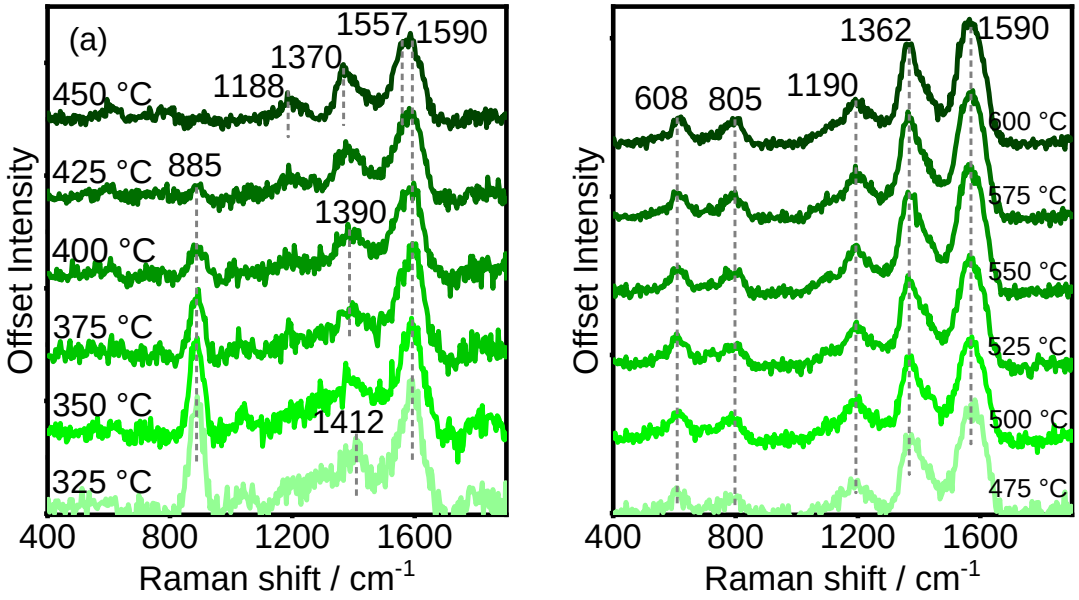

Figure 136 Kerr-gated Raman spectra acquired during temperature programmed reaction of acetic acid on H-ZSM-5 at (a) 325 - 450 °C and (b) 475 - 600 °C.

In conversion of acetic acid, the formation of products starts in the same temperature period that the strong band at 885 cm^{-1} grows. The signal intensity plotted with the MS data in Figure 135b suggests that the species formation is related to acetone, since at the maximum acetone production at 275 °C, its intensity soars, and starts to decrease when the acetone signal (*m/z* 43 with acetic acid fragments removed) peaks and drops at 350 °C. The assignment to a branched aliphatic aldehyde seems the most likely, forming from acetone polymerisation to give a C_6 species, including a carbonyl group, such as that

suggested in Figure 137. If protonated, this species contains two double bonds, the C=O and C=C and OH groups which are conjugated and would likely be resonance enhanced at 400 nm to explain the strong Raman band.[19,21] Further experiments by UV-Vis or DRIFTS, or theoretical calculations would help to draw a definite assignment which at this stage is not possible.

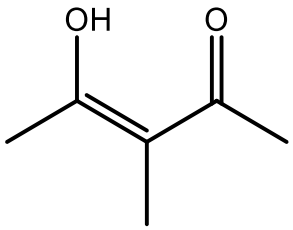

Figure 137 Suggestion of a molecular structure of species responsible for the intense C-C stretch at 885 cm^{-1} during the conversion of acetic acid.

Acetone polymerisation has been shown to result in such a species and its degradation led to acetic acid formation,[45] although acetic acid is not detected as a product by MS at this temperature period of the reaction, in fact according to MS data it appears to be still consumed at this stage, and may still react with the acetone itself.

5.3.3 Furan

The MS data acquired during furan upgrading under the new conditions are shown in Figure 138. The MS data are difficult to understand, because at low temperature, as well as the desorption of physisorbed furan, m/z 26, 41, 43, 44, 45, 55 and 91 also rise indicating the desorption of some unknown species, which would require further investigating. One possible explanation is that this is a result of some liquid condensation in the gas lines, and this reaction needs repeating.

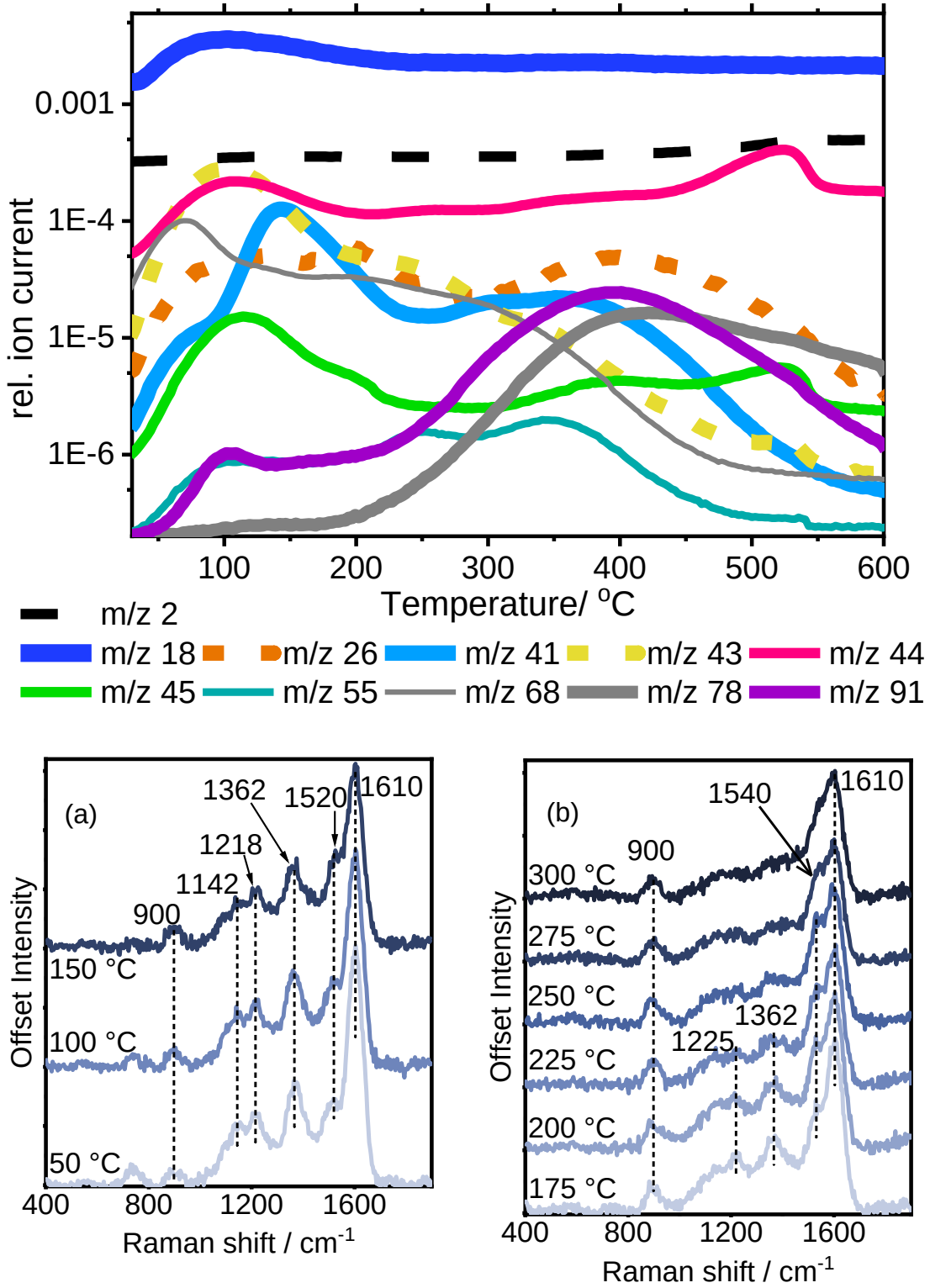

Figure 138 (a) MS data colected during temperature programmed reaction of furan over H-ZSM-5 from 30 to 600 °C and Kerr-gated Raman spectra acquired during temperature programmed reaction of furan on H-ZSM-5 from (b) 50 - 150 °C and (c) 175 - 300 °C.

At very low temperatures, furan desorption takes place with a maximum at 70 °C. As expected, water is released up to a maximum at 100 °C as condensation reactions take place on the surface. Aromatic species, benzene (*m/z* 78) and toluene (*m/z* 91) form from 200 °C onwards, with a maximum for benzene at 425 °C and for toluene at 395 °C – in a similar order to that observed in Chapter 4 – in line with benzene being the most thermodynamically stable product of the two. It is difficult to determine the temperature at which olefin formation starts, but as in the previous chapter, ethene (*m/z* 26) reaches its maximum simultaneously with toluene, here at 395 °C. Propene (*m/z* 41) reaches its maximum at 345 °C. To completely understand the MS data here and the observed differences from Chapter 4, further investigation is needed, including Gas Chromatography coupled with Mass Spectrometry to identify the unknown compounds.

The accompanying Raman spectra of the hydrocarbons on the surface during heating are shown in Figure 138. With increasing temperature from 50 to 150 °C there is an overall decreased intensity and increasing relative intensity of the shoulder at 1520 cm^{-1}. The band at 1142 cm^{-1} is gradually diminished and that at 1520 cm^{-1} grows, indicating a loss of CH_2 groups as charged carbenium ions become more prevalent. With higher temperature from 175 °C, the development of the band at 1540 cm^{-1} occurs which as in Chapter 4 was assigned to the C=C stretch of the 5-membered ring of benzofuran.[46] This strong vibration is at its highest intensity at 275 °C rather than 325 °C as recorded in Chapter 4. By 300 °C here the only remaining evidence of the signal is a broad shoulder. Two broad and weak signals around 1200 and 1350 cm^{-1} suggest a mixture of signals corresponding to CH_2 and CH_3 deformations, C-C stretches and C-H twists.[16,18] The band at 900 cm^{-1} is observed up to be consumed above 325 °C. This band has been present during the catalytically active period of all reactants which would suggest an important intermediate, it might be related to the C-O-C bonds of ethers.[16]

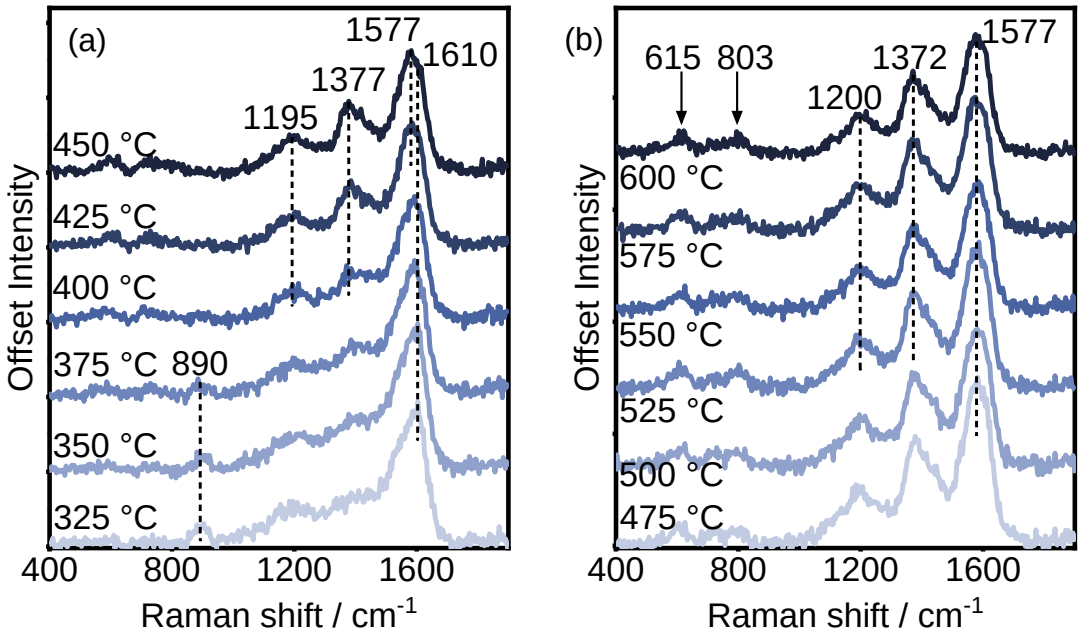

Figure 139 Kerr-gated Raman spectra acquired during temperature programmed reaction of furan on H-ZSM-5 from (a) 325 - 450 °C and (b) 475 - 600 °C.

As the temperature increase continues beyond 350 °C, the intensity of a band at 1377 cm^{-1} grows which strongly indicates the formation of naphthalenic species, since the breathing modes of bicyclic aromatic species is here.[16,32] This band is very strong by 425 °C and continues to grow in intensity with temperature increase to 600 °C, although with a blue shift to 1372 cm^{-1}. At 425 °C an additional band grows in the C=C stretch region at 1577 cm^{-1}, with still a strong shoulder at 1605 cm^{-1}. This comes as the band at 1200 cm^{-1} strengthens and weak signals at low frequencies are recorded – at 615 and 803 cm^{-1} – which are attributed to the ring opening vibrations of polyaromatic hydrocarbons.[18]

5.3.4 2,3-dihydrofuran

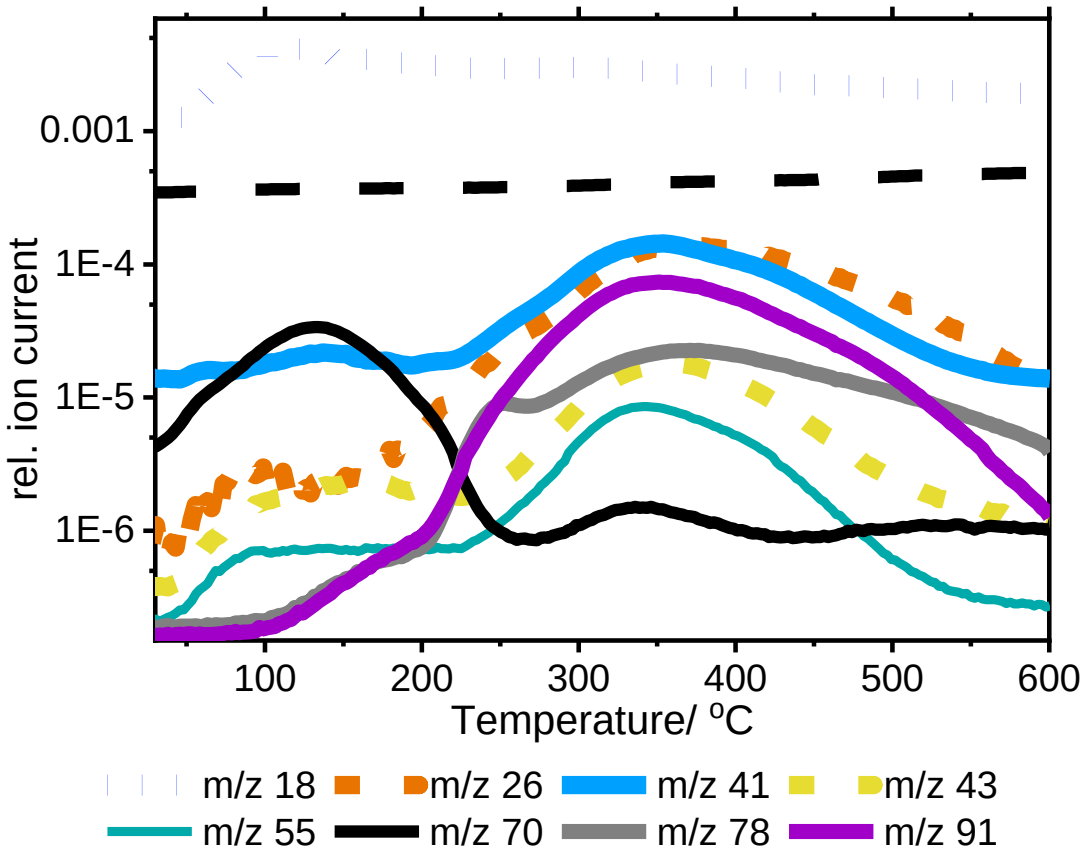

Figure 140 MS data collected during temperature programmed reaction of 2,3-dihydrofuran over H-ZSM-5 from 30 to 600 °C.

The Raman spectra recorded during reaction from (a) 50 to 150 °C and (b) 200 to 300 °C are displayed in Figure 141. The strongest band at 1600 cm^{-1} is, again, ambiguous but likely corresponds to conjugated C=C bonds in di- or trienylic systems.[18] The broad feature at 1200 – 1500 cm^{-1}, and strong band at 1600 cm^{-1} intensify as the temperature is increased from 50 to 150 °C, indicating greater resonance enhancement. Meanwhile, a stronger band grows at 892 cm^{-1}.

The MS data recorded during temperature-programmed reaction of 2,3-dihydrofuran over H-ZSM-5 are shown in Figure 140. Water is produced at 100 °C, and unreacted 2,3-dihydrofuran is desorbed. The formation of products including toluene, benzene, ethene and propene are formed above 200 °C, as followed by *m/z* 91, 78, 26 and 41. At 250 °C the benzene signal drops in relation to toluene (this behaviour is also observed in the following chapter so is unlikely to be an artefact). Higher alkenes including butene and pentene isomers and

some paraffins are formed above 250 °C as followed by *m/z* 55 and 43, respectively. In this experiment it is unlikely that *m/z* 43 is contributed to by acetone as an unlikely product.

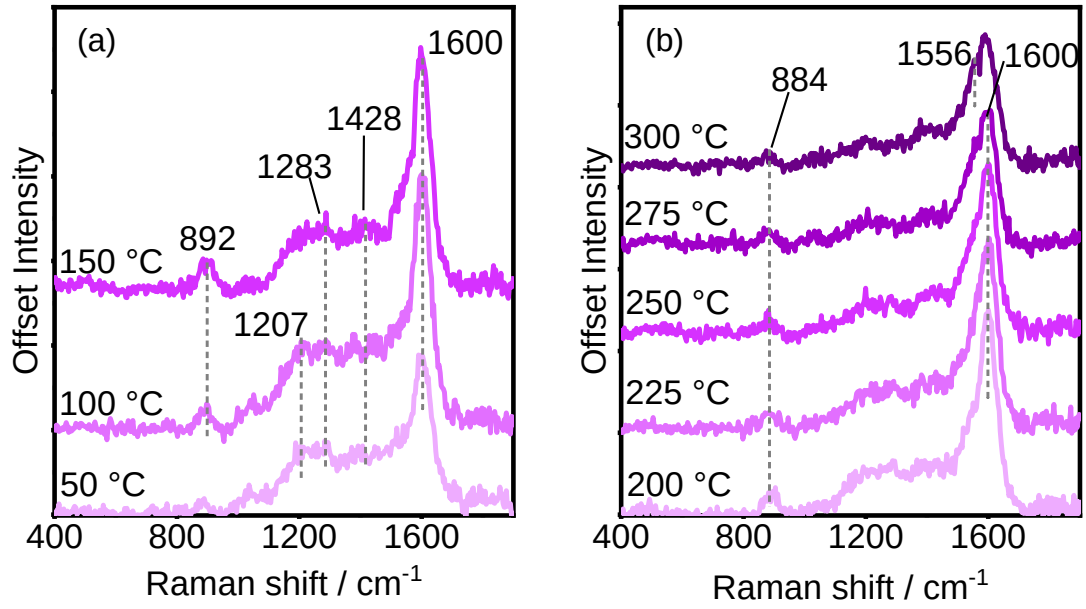

Figure 141 Kerr-gated Raman spectra acquired during temperature programmed reaction of 2,3-dihydrofuran on H-ZSM-5 from (a) 50 - 150 °C and (b) 200 - 300 °C.

The band at 884 cm^{-1} is stable until 275 °C when it starts to drop in intensity, fading into the noise of the spectrum. Figure 141b highlights a new band growing in the C=C stretch region at 1560 cm^{-1} at 275 °C, while the most intense band shifts towards 1593 cm^{-1}. Bands in the region of 1560 cm^{-1} are usually assigned to polyene-type species as was discussed in Chapter 3.[18]

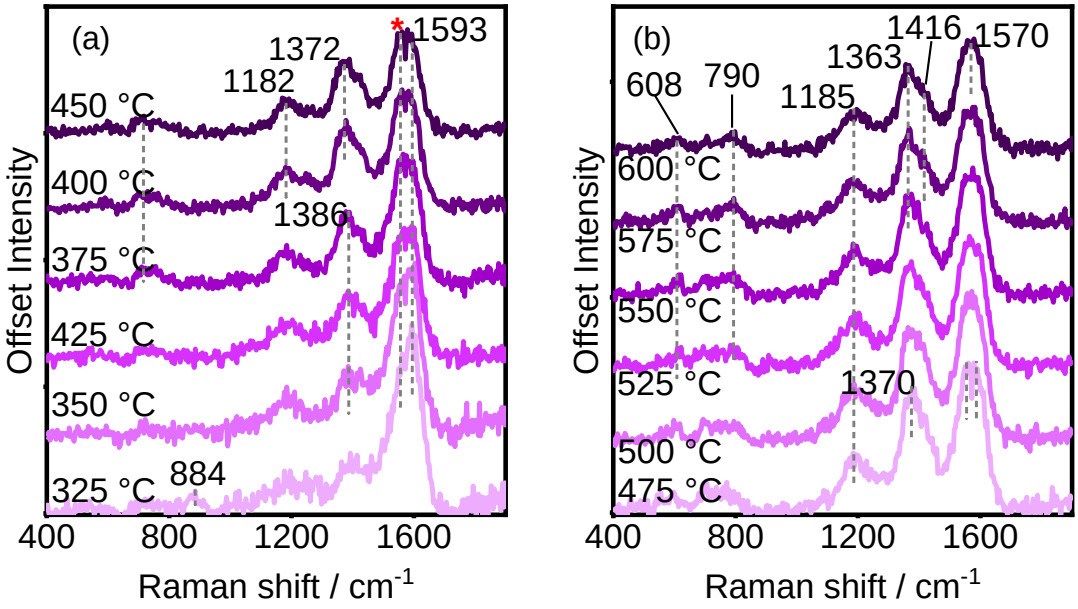

Figure 142 Kerr-gated Raman spectra acquired during temperature programmed reaction of 2,3-dihydrofuran on H-ZSM-5 from (a) 325 - 425 °C and (b) 450 - 600 °C.

In Figure 142, the spectra recorded during heating from 325 to 450 °C and 475 to 600 °C are shown. Significant changes in speciation occur between 325 and 400 °C; the band at 1560 cm^{-1} continues to grow in relative intensity to the band at 1593 cm^{-1}, and the band at 1400 cm^{-1} at 325 °C becomes overshadowed by a new band at 1381 cm^{-1}. As previously discussed, the emerging band at 1381 cm^{-1} indicates that bicyclic aromatic species have formed, although a shoulder at 1420 cm^{-1} remains. These changes occur as aromatic formation reaches its maximum and starts to decline. The band at 1593 cm^{-1} is consistently strong in this temperature range, and most likely belongs to a benzenium ion.[44]

Moving beyond 475 cm^{-1}, the C=C stretch vibrations that are observed at 1560 cm^{-1} and 1590 cm^{-1} are no longer separately distinguished – forming one broad band centred at 1570 cm^{-1}. The ring-breathing modes of bicyclic aromatic species or polyaromatic species shift from 1381 cm^{-1} at 400 °C to 1372 cm^{-1} at 450 °C to 1366 cm^{-1} at 600 °C, which is consistent with a change from more methylated to less methylated naphthalene,[32] which is rationalised because dealkylations take place at higher temperatures. A shoulder at 1408 cm^{-1} indicates that polyaromatics such as fluorene or anthracene formed.[32] In the low frequency region some weak bands are present at 610 and 790 cm^{-1} which have previously been attributed to the presence of polyaromatics.[18]

5.4 Quenched spectra

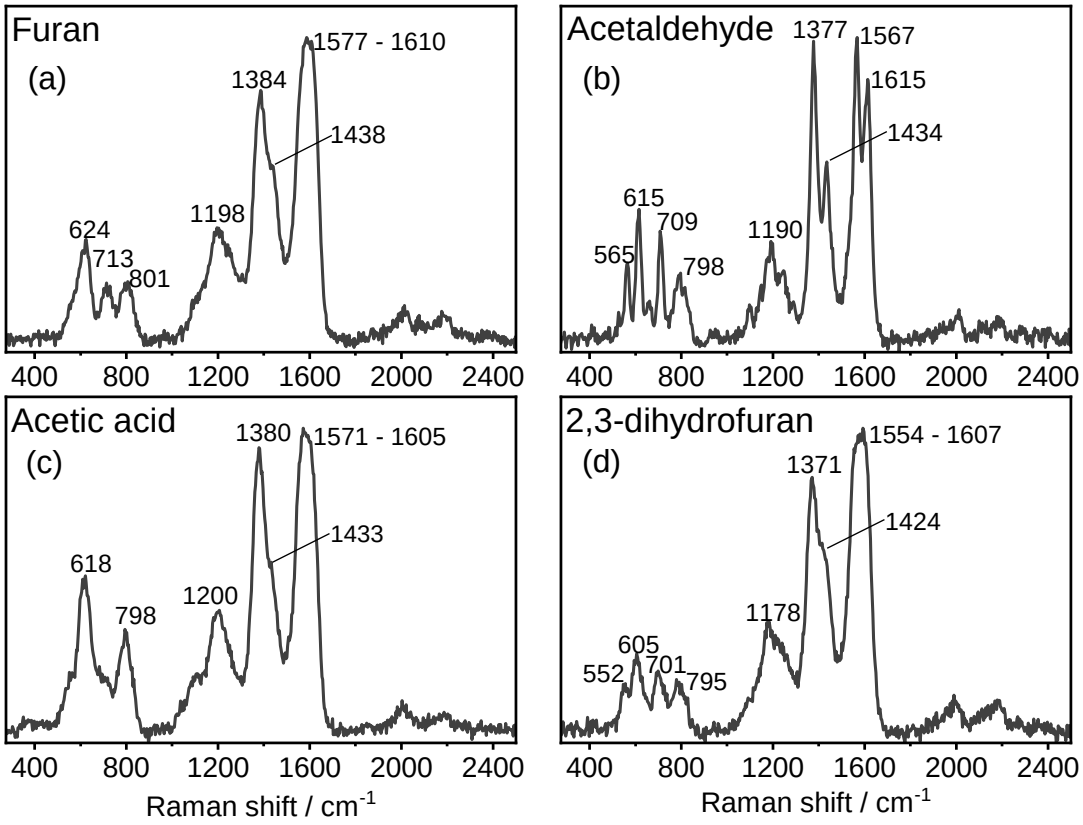

Figure 143 Kerr-gated Raman spectra acquired after the reactor was quenched following reaction with (a) furan, (b) acetaldehyde (c) acetic acid and (d) 2,3-dihydrofuran. Spectra collected in 5 acquisitions of 10 seconds with 2 mW power.

After reaching 600 °C, the reactor was cooled at 20 °C min^{-1} under flowing He, and spectra acquired with longer acquisition times. There are strong similarities in the Raman spectra, including broad C=C stretches from 1570 – 1610 cm^{-1} and strong ring-breathing modes of polyaromatics at 1370 – 1380 cm^{-1} with a shoulder at 1424 – 1438 cm^{-1} and C-C stretching between sp^2-sp^3 carbon atoms at 1200 cm^{-1}.[42,43] There are typically four low frequency bands, which were also observed in the reaction of furan on H-ZSM-5 in Chapter 4 at or near 560, 615, 710 and 800 cm^{-1}, but we note that through changing the feedstocks here all four bands are only present after the reaction of acetaldehyde and in 2,3-dihydrofuran, while after furan reaction the band at 560 cm^{-1} is missing and from the reaction of acetic acid the bands at 560 and 710 cm^{-1} are missing. The band near 560 cm^{-1} is related to the C-C stretches trivalent C atoms co-ordinated with 3 other C atoms, such as those in branched aromatic hydrocarbons or small branched olefins.[18]

5.5 Discussion and comparison

During the conversion of model compounds on the zeolite, typically at low temperatures, MS detects that water is released as the species undergo condensation and form more conjugated species on the surface as observed by Raman. At intermediate and high temperatures, MS data shows that aromatic and olefinic products form in all cases, showing that all four oxygenated hydrocarbons tested can be converted into these higher value products. The order and temperature at which products form differ in each case because their initial mechanisms of formation are distinct. By Raman, significant differences are observed at low and intermediate temperatures that lead to the formation of pools of hydrocarbons that are different. However, at high temperatures above 400 – 450 °C, the Raman datasets become much more similar.

In acetaldehyde conversion, during the most catalytically active temperature range until aromatic formation reaches a maximum, a broad band of at 1415 cm^{-1} accompanies the C=C stretch at 1602 cm^{-1}. The strength of the band at 1415 cm^{-1} as well at the catalytic activity observed during its growth show that the species is important, and an assignment is made to vinylic groups, i.e. $-C=CH_2$ by their in-plane CH_2 deformation vibrations which according to Socrates are of medium-strong intensity.[16] The formation of such species would explain the preference for branched aromatic species which we see by the lower temperature that branched aromatics form (*m/z* 91) at 200 °C than benzene (m/z 78) at 250 °C.

During the conversion of acetic acid, a very strong Raman band at 885 cm^{-1} grows during a catalytically relevant window as illustrated by Figure 135b. Currently its most likely but tentative assignment is to branched aliphatic aldehydes that result from acetone polymerisation.[16,45] This shows the impact of the initial decarboxylation of acetic acid on the overall reaction mechanism since the formation of this intermediate also occurs prior and during the formation of alkenes and aromatic hydrocarbons.

As in Chapter 4, the reaction of furan on H-ZSM-5 results in the formation of benzofuran as an intermediate, and this mainly dominates the reaction chemistry observed by Raman. The relative intensity of Raman bands is different to Chapter

4 and the initial spectrum after absorption of furan on the zeolite indicates a lesser degree of polymerisation which is rationalised by the lower partial pressure of furan in the gas stream. The unusual MS data collected in this reaction requires further investigation to determine whether this is real, as it may be an effect of experimental problems such as liquid condensation in the narrow gas lines.

The hydrocarbons in 2,3-dihydrofuran were more difficult to assign at low to intermediate temperatures with fewer significant features, apart from an ambiguous C=C stretch and broad bands in the 1200 – 1400 cm^{-1} region. The simultaneous detection by MS of olefins and aromatics would suggest the direct formation of aromatics from small olefins such as propene/butene.

As the catalyst in each reaction reaches the temperatures where the MS shows decreasing aromatic and olefin production, there are broad similarities in the spectra across each feed molecule tested. In the C=C stretch region a new band at 1560 – 1570 cm^{-1} becomes dominant. This vibration is assigned, as in previous chapters, to the C=C stretching of extended polyenes.[18] Separately, the growth of a band at ~1370 cm^{-1} indicated the formation of bi- or polyaromatic hydrocarbons such a naphthalene and anthracene.[32,47] These similarities at high temperature might indicate that eventually here, the hydrocarbon pool becomes a function of the H-ZSM-5 catalyst.

A hydrocarbon pool is defined as a mixture of hydrocarbon species that build up during reaction as a result of the primary reaction of the initial reactant(s) that then themselves become catalytically active and undergo successive reactions either with themselves or with the initial reactant(s) to yield final products that leave the catalyst. The concept of Hydrocarbon Pool chemistry is discussed mainly in the field of Methanol-to-Hydrocarbons and sometimes CFP. In these experiments we were able to observe a pool of initial hydrocarbons on the zeolite by Raman that were further converted (e.g., through polymerisation, decarbonylation or cyclization) to yield the final products, showing hydrocarbon pool-type behaviour where the final products were not formed from the initial reactant only.

In the context of CFP, these results show that the hydrocarbon pools formed are not simply a function of H/C_{eff} ratio, initially because molecules might promote reactions such as condensation or decarboxylation at low and intermediate temperatures that change the H/C_{eff} of the pool during the catalytically active period. At longer reaction times/higher temperatures, the ease of formation of polyaromatic hydrocarbons also appears to be unrelated to the H/C_{eff} of the reactant. The similarity of the Raman spectra observed at high temperature (and quenched spectra after reaction as shown in Figure 143) suggests that in the formation of internal coke, the molecules which form are much more strongly related to the zeolite itself. Since in these experiments we only loaded the zeolite once with small model reactants, rather than running a continuous feed, we cannot comment on the formation of external coke at very long reaction times, which has been discussed as the reason for H-ZSM-5 deactivation in MTH chemistry.

5.6 Conclusions

Through changing the model compound to be studied between furan, 2,3-dihydrofuran, acetaldehyde and acetic acid, four different pools of hydrocarbons were formed at intermediate temperatures which all lead to aromatic and olefinic products through different mechanisms. At higher temperatures the hydrocarbon pool appears to become a function of the H-ZSM-5 catalyst.

5.7 References

1. J. D. Adjaye and N. N. Bakhshi, Biomass and Bioenergy, 1995, 8, 131–149.
2. H. Zhang, Y.-T. Cheng, T. P. Vispute, R. Xiao and G. W. Huber, Energy & Environmental Science., 2011, 4, 2297–2307.
3. U. V. Mentzel and M. S. Holm, Applied Catalysis A: General, 2011, 396, 59–67.
4. U. Olsbye, S. Svelle, M. Bjørgen, P. Beato, T. V. W. Janssens, F. Joensen, S. Bordiga and K. P. Lillerud, Angewandte Chemie International Edition, 2012, 51, 5810–5831.
5. M. Bjørgen, S. Svelle, F. Joensen, J. Nerlov, S. Kolboe, F. Bonino, L. Palumbo, S. Bordiga and U. Olsbye, Journal of Catalysis, 2007, 249, 195–207.
6. A. C. Psarras, C. M. Michailof, E. F. Iliopoulou, K. G. Kalogiannis, A. A. Lappas, E. Heracleous and K. S. Triantafyllidis, Molecular Catalysis, 2019, 465, 33–42.
7. A. Gumidyala, T. Sooknoi and S. Crossley, Journal of Catalysis, 2016, 340, 76–84.

8. A. Oasmaa, D. C. Elliott and J. Korhonen, Energy Fuels, 2010, 24, 6548–6554.
9. S. Czernik and A. V. Bridgwater, Energy Fuels, 2004, 18, 590–598.
10. I. Neves, F. Jayat, P. Magnoux, G. Pérot, F. R. Ribeiro, M. Gubelmann and M. Guisnet, Journal of Molecular Catalysis, 1994, 93, 169–179.
11. S. Gutiérrez-Rubio, M. Shamzhy, J. Čejka, D. P. Serrano, I. Moreno and J. M. Coronado, Applied Catalysis B: Environmental, 2021, 285, 119826.
12. A. P. Singh and A. K. Pandey, Journal of Molecular Catalysis A: Chemical, 1997, 123, 141–147.
13. K. K. Ramasamy, M. A. Gerber, M. Flake, H. Zhang and Y. Wang, Green Chemistry, 2014, 16, 748–760.
14. R. Lindenmaier, S. D. Williams, R. L. Sams and T. J. Johnson, Journal of Physical Chemistry A, 2017, 121, 1195–1212.
15. C. Liu, T. J. Evans, L. Cheng, M. R. Nimlos, C. Mukarakate, D. J. Robichaud, R. S. Assary and L. A. Curtiss, Journal of Physical Chemistry C, 2015, 119, 24025–24035.
16. J. Socrates, Infrared and Raman characteristic group frequencies tables and charts, 3rd ed, John Wiley and Sons, Chichester, 2001.
17. V. V. Ordomsky, V. L. Sushkevich and I. I. Ivanova, Journal of Molecular Catalysis A: Chemical, 2010, 333, 85–93.
18. I. Lezcano-Gonzalez, E. Campbell, A. E. J. Hoffman, M. Bocus, I. V. Sazanovich, M. Towrie, M. Agote-Aran, E. K. Gibson, A. Greenaway, K. De Wispelaere, V. Van Speybroeck and A. M. Beale, Nature Materials, 2020, 19, 1081–1087.
19. G. Spoto, F. Geobaldo, S. Bordiga, C. Lamberti, D. Scarano and A. Zecchina, Topics in Catalysis, 1999, 8, 279.
20. E. Borodina, F. Meirer, I. Lezcano-González, M. Mokhtar, A. M. Asiri, S. A. Al-Thabaiti, S. N. Basahel, J. Ruiz-Martinez and B. M. Weckhuysen, ACS Catalysis, 2015, 5, 992–1003.
21. S. Bordiga, G. Ricchiardi, G. Spoto, D. Scarano, L. Carnelli, A. Zecchina and C. Otero Areán, Journal of the Chemical Society, Faraday Transactions, 1993, 89, 1843–1855.
22. Q. Qian, C. Vogt, M. Mokhtar, A. M. Asiri, S. A. Al-Thabaiti, S. N. Basahel, J. Ruiz-Martínez and B. M. Weckhuysen, ChemCatChem, 2014, 6, 3396–3408.
23. P. J. Garratt, UV-vis atlas of organic compounds, Heinz-Helmut Parkampus, Weinheim, 2nd Ed., 1992, vol. 5.
24. S. Yang, J. N. Kondo and K. Domen, Chemical Communications, 2001, 0, 2008–2009.
25. J. E. Bertie and K. H. Michaelian, Journal of Chemical Physics, 1982, 77, 5267–5271.
26. N. Nishi, T. Nakabayashi and K. Kosugi, Journal of Physical Chemistry A, 1999, 103, 10851–10858.
27. L. M. Parker, Studies in Surface Science and Catalysis, Elsevier, 1988, vol. 36, 589–595.
28. O. Kresnawahjuesa, R. J. Gorte and D. White, Journal of Molecular Catalysis A: Chemical, 2004, 208, 175–185.
29. P. K. Dutta and M. Puri, Journal of Physical Chemistry, 1987, 91, 4329–4333.

30. S. Mintova, B. Mihailova, V. Valtchev and L. Konstantinov, Journal of the Chemical Society, Chemical Communications., 1994, 0, 1791–1792.
31. J. J. Orlando and G. S. Tyndall, Journal of Photochemistry and Photobiology A: Chemistry, 2003, 157, 161–166.
32. P. M. Allotta and P. C. Stair, ACS Catalysis, 2012, 2, 2424–2432.
33. C. Pazè, B. Sazak, A. Zecchina and J. Dwyer, Journal of Physical Chemistry B, 1999, 103, 9978–9986.
34. M. Fabbiani, G. Confalonieri, S. Morandi, R. Arletti, S. Quartieri, M. Santoro, F. Di Renzo, J. Haines, R. Fantini, G. Tabacchi, E. Fois, G. Vezzalini, G. Ricchiardi and G. Martra, Microporous and Mesoporous Materials, 2021, 311, 110728.
35. I. Kiricsi and H. Förster, Journal of the Chemical Society, Faraday Transactions 1: Physical Chemistry in Condensed Phases, 1988, 84, 491–499.
36. F. Billes, H. Böhlig, M. Ackermann and M. Kudra, Journal of Molecular Structure: THEOCHEM, 2004, 672, 1–16.
37. G. Bouchoux, F. Djazi, Y. Hoppilliard, R. Houriet and E. Rolli, Organic Mass Spectrometry, 1986, 21, 209–213.
38. F. Mauriello, M. Armandi, B. Bonelli, B. Onida and E. Garrone, Journal of Physical Chemistry C, 2010, 114, 18233–18239.
39. P. J. Linstrom and W. G. Mallard,'Mass Spectra' in NIST Chemistry WebBook, NIST Standard Reference Database Number 69, National Institute of Standards and Technology, Gaithersburg MD.
40. E. Cloutis, P. Szymanski, D. Applin and D. Goltz, Icarus, 2016, 274, 211–230.
41. E. D. Hernandez and F. C. Jentoft, ACS Catalysis, 2020, 10, 5764–5782.
42. A. Sadezky, H. Muckenhuber, H. Grothe, R. Niessner and U. Pöschl, Carbon, 2005, 43, 1731–1742.
43. A. C. Ferrari and J. Robertson, Physical Reviews B, 2000, 61, 14095–14107.
44. M. Bjørgen, F. Bonino, S. Kolboe, K.-P. Lillerud, A. Zecchina and S. Bordiga, Journal of the American Chemical Society, 2003, 125, 15863–15868.
45. A. Panov and J. J. Fripiat, Langmuir, 1998, 14, 3788–3796.
46. V. B. Singh, Spectrochimica Acta Part A: Molecular and Biomolecular Spectroscopy, 2006, 65, 1125–1130.
47. M. Signorile, F. Bonino, A. Damin and S. Bordiga, The Journal of Physical Chemistry C, 2015, 119, 11694–11698.

6 UV Raman Spectroscopy

6.1 Introduction

The probability of Raman scattering is directly proportional to the fourth power of the frequency of light, meaning that scattering is more likely to occur moving from infrared to visible to UV wavelengths of excitation.[1,2] This is represented in Equation (2) where the intensity of a Raman signal, I, is proportional to the fourth power of the incident frequency, ω^4.[1,2]

$$I = k\,L\,\alpha^2\omega^4 \qquad (8)$$

Such a strong dependence of signals on a higher frequency might lead to increased sensitivity across all Raman active vibrations. However, changing the wavelength of laser excitation can cause significant changes in the relative intensities of Raman signals, where different chromophores exist in the molecules which absorb at different energies.[3] When a sample contains an electronic transition near the laser excitation wavelength, scattering is enhanced by up to 10^6 times, and this scattering enhancement is selective to the chromophore of the molecule. This amplification for some vibrations by use of an excitation laser wavelength in resonance with an electronic transition in the sample, is known as Resonance Raman Spectroscopy.[1,4]

In the case of a mixture of chemicals, Resonance Raman may be used to identify individual components in the mixture through selectively enhancing specific absorption bands.[2] It is therefore possible that through probing a complex catalytic system such as in hydrocarbon pool systems, by changing the wavelength of excitation, Raman bands of different species can be identified, giving a fuller picture of the mechanisms at play.

The application of Raman spectroscopy to studying organic catalytic mechanisms has to date focused heavily on the use of UV-Raman,[2,5–10] because the common problem of fluorescence – which commonly hinders Raman signals from being collected – can be mostly suppressed. Sources of fluorescence might include hydrocarbon impurities, metal ion impurities or crystal defects or, during catalysis,

fluorescent molecules might form on the surface.[2] Fluorescence is a problem inherent to visible wavelengths and therefore one way to avoid it would be through use of an excitation wavelength in the infrared of ultraviolet energies. Infrared excitation is usually too low in energy to make use of resonance enhancement and is also at the expense of poor scattering intensity. UV excitation on the other hand might still induce fluorescence, but this appears at longer wavelengths i.e. in the visible region and therefore does not interfere with the detector and Raman signals are detected.[2,11]

Sample photodecomposition is a major drawback of UV-Raman,[12,13] and efforts have been made to design reaction cells that minimise the contact time of the laser with one spot on the sample, through beds with a spinning pellet,[13,14] or a fluidized bed where gas is blown through the sample to agitate the bed and move particles around.[12,13] As in all of our experiments the sample was moved by a stage in random directions so that the laser spot was exposed overall to a square of approximately 2.5 mm^2, and occasionally the position of the bed moved to compare Raman spectra at a new spot on the surface to determine if any sample damage had occurred.

In this chapter, we view the data collected by UV-Raman in systems which were analysed in previous chapters, starting with methanol-to-hydrocarbons (MTH) studies over small-pore zeolites and then on to the conversion of biomass model compounds. The aim is to provide a comparison of the species that can be detected by UV-Raman or with a visible excitation wavelength (at 400 nm).

The same Ti-Sapphire laser system was used, where the beam was frequency doubled twice to achieve the higher energy 267 nm laser, and without the optics required for Kerr-gating and without a second gating pulse. PTFE was used to calibrate the detector. Reactions were carried out in the CCR1000 Linkam Cell with on-line gas analysis by Mass Spectrometer (MS). We found that in most cases, there was still strong emission after excitation with the UV-wavelength laser within the window of measurement, but it was possible to subtract the emission as a background in almost all cases. Measurements at room temperature were particularly affected by emission and quite commonly as the temperature of the reaction increased, the emission dropped. Measurements

shown in Figure 144 illustrate that this effect may be largely related to the quartz window: a measurement of H-SAPO-34 catalyst alone shows some emission with a maximum > 4000 cm^{-1}, but when the quartz window was placed on the reactor the emission became significantly stronger. During catalyst calcination, while the catalyst was held at 550 °C, the emission was removed completely, and upon cooling to the starting reaction temperature 100 °C the emission increased again to approximately half of the intensity. This behaviour led us to believe that the quartz window was partly responsible, where hydroxyl groups can be emissive in the UV region.[15,16]

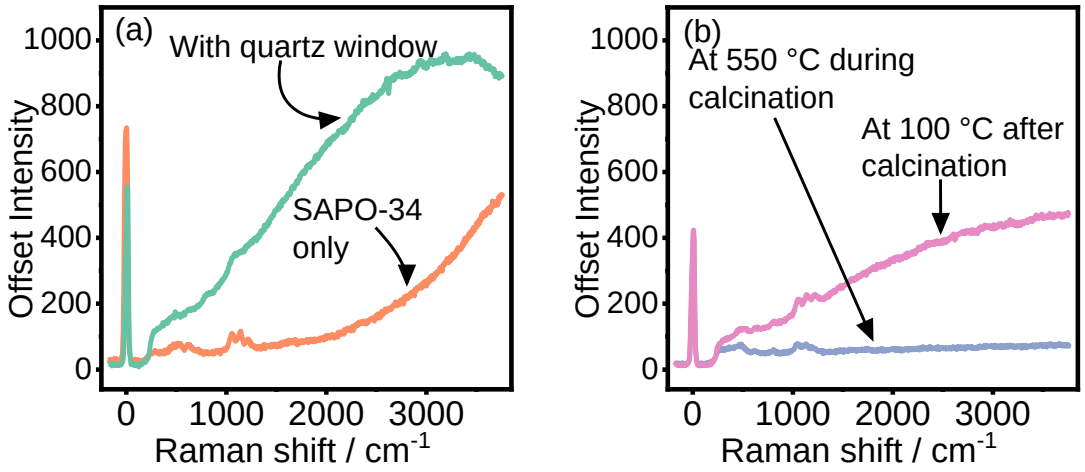

Figure 144 Spectra acquired without background subtraction of H-SAPO-34 collected with a 267 nm probe (a) without window and with the quartz window in place, and (b) during calcination at 550 °C and cooled to 100 °C after calcination.

6.2 Methanol-to-Olefins

6.2.1 H-SAPO-34

We repeated the experiment where methanol was reacted over H-SAPO-34 with UV-Raman, under temperature ramping conditions. 50 mg of H-SAPO-34 was pre-calcined at 550 °C for 1 hour in 20 % O_2 in He, then the reactor cooled to 100 °C under 30 ml min^{-1} flowing He. Methanol was injected to the He stream at 1.7 µL min^{-1} by a syringe pump at 100 °C, and the temperature increased by 10 °C min^{-1}. Gases were analysed by on-line MS and Raman measurements acquired every 10 °C, using the 277 nm probe, at 8 mW for 12 repeats of 4 second acquisitions. Many short acquisitions were collected to account for possible sudden jumps in the intensity of the emission background that might cause the detector to become saturated.

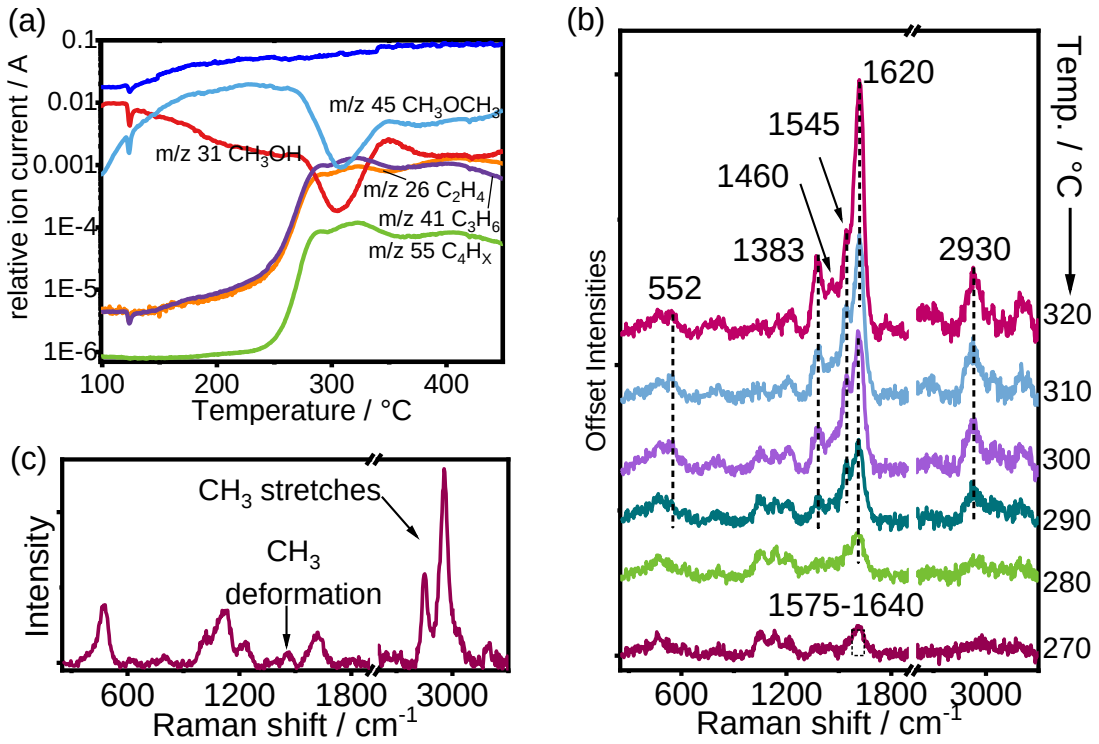

Figure 145 (a) MS data collected during MTH from 100 to 450 °C on H-SAPO-34 with 1 °C min^{-1} temperature ramp, (b) Raman spectra collected during ramp at 10 °C intervals collected using a 277 nm Raman probe and (c) spectrum collected with methanol adsorbed at 100 °C.

MS data recorded is shown in Figure 145a, which shows that until 245 °C the main reaction is the formation of dimethyl ether (DME) from methanol, due to the increasing signal at *m/z* 45 for DME and decreasing *m/z* 31 for methanol. Around 270 °C there is a sudden drop in methanol and DME production indicating high consumption, and the formation of olefinic products increases including ethene, C_3-C_4 alkenes and C_4-C_5 alkenes followed by *m/z* 26, 41 and 55 signals. The maximum methanol consumption is at 304 °C, after which point the *m/z* 31 signal increases again. Note that above 350 °C there is a slight increase in olefin formation, this occurs as the catalyst enters the reanimation period – where higher temperatures promote dealkylation reactions so that bulky intermediates that have been previously hindered reactivity can again become active through dealkylation to give olefinic products.[17]

In Figure 145c, the spectrum of methanol adsorbed on H-SAPO-34 at 100 °C is shown which looks almost identical to that recorded during the initial experiment with the Kerr-gate and 400 nm probe (Chapter 3). Vibrations at 480, 1022, 1118 and 1223 cm^{-1} are related to the framework.[18] Strong methanol bands at 2850 and 2956 cm^{-1} are caused by the CH_3 symmetric and asymmetric stretching modes and a weaker band at 1465 cm^{-1} due to the CH_3 deformation mode.[19,20] Again, as in Chapter 3, the C-O stretch of methanol is obscured by the SAPO-34 framework vibrations. In Figure 145b, Raman spectra at 10 °C intervals between 270 and 320 °C are displayed. At 270 °C prior to the increased methanol conversion, the weak Raman band measured sits at 1575 – 1640 cm^{-1}, like the spectrum acquired at this temperature in Chapter 3 by Kerr-gated Raman at 400 nm, where the band was assigned to short chain olefins including small polyenes,[21] and monoenylic carbocations.[22]

From 290 °C, a strong band grows at 1610 cm^{-1} which is assigned to the C=C stretches in methylated benzenes,[21,23] and there is a clearly visible and growing band at 1545 cm^{-1}, a vibration assigned to the C=C stretching in long-chain polyenes.[21] This vibration is clearly visible at 290 – 320 °C by probing with UV-wavelength laser. For comparison, Figure 146a shows the spectra collected using the 400 nm probe with the Kerr-gated spectrometer from Chapter 3 overlaid with the data collected with the 267 nm probe, at 300, 310 and 320 °C. Using the 400 nm wavelength probe, the vibration at 1545-1550 cm^{-1} was not very distinct, and in Chapter 3, the growing intensity at 1575 cm^{-1} was described as possibly a combination of the vibrational frequencies of long-chain polyenes and methylbenzenium ions,[21,23] or alternatively due to the presence of shorter chain polyenes with vibrational frequency nearer to 1570 cm^{-1} rather than 1545 cm^{-1}.[21,24] The UV Raman data presented in this chapter would suggest that the former option is the case, and now without the resonance enhancement effect of methyl benzenium ions, protonated naphthalenes, and dienylic carbocations,[25,26] this signal of long-chain polyenes is clearly defined.

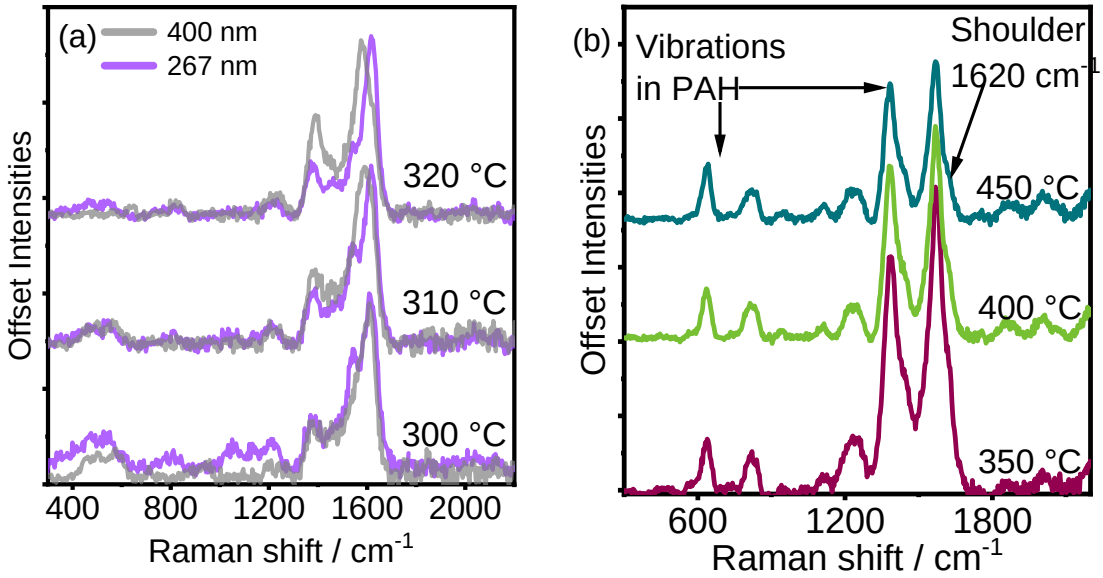

Figure 146 Kerr-gated Raman spectra collected with 400 nm wavelength probe (presented in Chapter 3) overlaid for comparison with UV-Raman (267 nm) data at (a) 300, 310 and 320 °C during the active period of the catalyst, all normalised to zero for ease of comparison and (b) Kerr-gated Raman spectra at 350, 400 and 450 °C.

In the UV-Raman data shown in Figure 145b, at 320 °C the 1545 cm^{-1} band stops growing, and the C=C stretch vibration, now sitting at 1620 cm^{-1} is enhanced by 50 %. This vibrational frequency is in line with naphthalene formation,[5,9,21] or isolated double bonds in olefins.[21] A small band is present at 1460 cm^{-1} is likely to correspond to the C=C stretching of conjugated double bonds in cyclopentadienyl species, or possibly to bent polyaromatics such as fluorene and phenanthrene.[9,27] The assignment to polyaromatics would be in line with the growth at 1620 cm^{-1} since they also exhibit C=C stretching here,[9] however protonated polyaromatic hydrocarbons would be expected to absorb at higher wavelengths.[25,26] During this period, by MS a decreased production of olefins and a pronounced drop in methanol conversion, which would support the presence of polyaromatic hydrocarbons as pore-blocking species.[28]

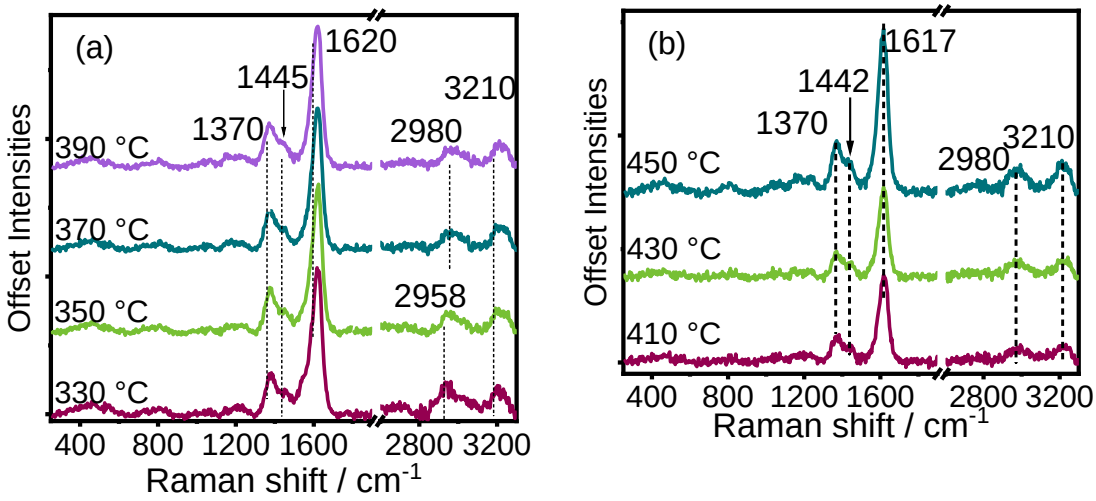

Figure 147 Raman spectra collected using a 277 nm Raman probe during MTH reaction on H-SAPO-34 during temperature ramp at 20 °C intervals form (a) 300 – 390 and (b) 410 – 450 °C.

With increasing temperature from 330 to 450 °C in the data shown in Figure 147, in the mid-frequency region of the spectrum two bands dominate, at 1620 and 1370 cm^{-1}, which are assigned to the C=C stretch in polyaromatic hydrocarbons, and their ring breathing vibrations, respectively.[5,9,21,29] A shoulder at 1445 cm^{-1} is assigned to C=C stretching in bent polyaromatic hydrocarbons.[9] In the high frequency region two bands are observed at 2980 and 3210 cm^{-1}, which are likely to be a combination band and an overtone of the C=C stretch vibration.

In contrast, the data shown in Figure 146b collected during the Kerr-gated Raman experiment with a 400 nm probe demonstrates that polyaromatics form through the strong ring-breathing mode observed at 1392 cm^{-1} and clear low frequency vibrations at 630 and 780 cm^{-1}.[21] By UV-Raman, the breathing modes are suppressed by comparison, which is documented when comparing Raman bands of coke or graphitic carbon, whereby the D band (generally at 1300 – 1400 cm^{-1} and relating to ring-breathing modes in aromatic rings) is suppressed by use of UV-Raman.[30,31] The low frequency bands related to the ring-opening vibrations of polyaromatic species are not observed by UV-Raman.

6.2.2 MTH SSZ-13

The effect of recording Raman spectra using a UV-wavelength probe compared with that at 400 nm was also investigated on H-SSZ-13 during MTH in a temperature ramp experiment, under the conditions previously described: after a catalyst pre-treatment in 20 % O_2/He at 550 °C, the catalyst was flushed and cooled in 30 ml min^{-1} He to 100 °C, when methanol was injected into the He stream at 1.7 µL min^{-1}. The temperature was increased linearly from 100 to 450 °C at 1 °C min^{-1}.

Figure 148a shows MS data recorded in the period from 150 to 450 °C, where initially DME is formed from methanol. At 260 °C a sudden increase in the signals at *m/z* 26, 41 and 55 indicates formation of olefins to a maximum point at 280 °C, as the methanol signal *m/z* 31 drops. The production of olefins decreases at 290 °C. At higher temperatures above 330 °C the reanimation period is again observed by again increasing olefin signals.[17]

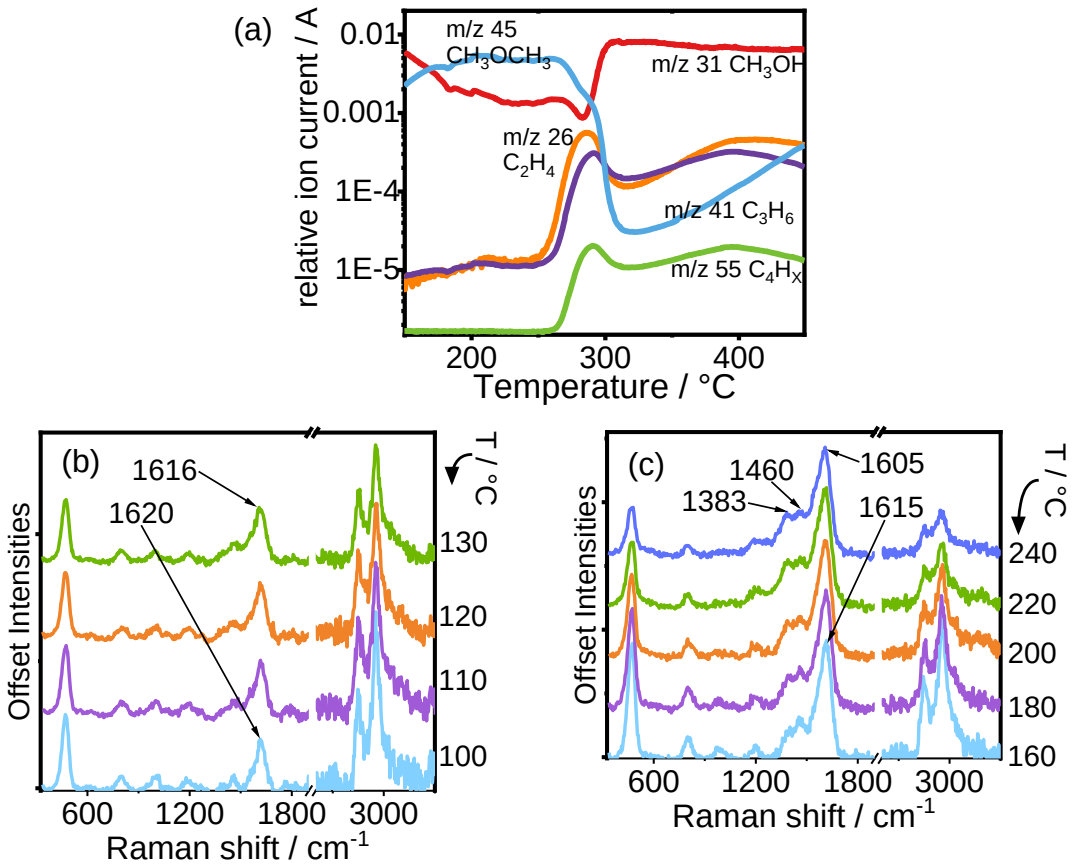

Figure 148 (a) MS data recorded during methanol conversion on H-SSZ-13 from 150 to 450 °C, and Kerr-gated Raman spectra acquired at (b) very low reaction temperatures 100 - 130 °C and (b) 160 - 250 °C.

At the very early stages of reaction, as shown in Figure 148b, the symmetric and asymmetric CH stretches in methanol are observed at 2855 and 2955 cm^{-1},[20,21] while the zeolite framework vibration is observed at 470 cm^{-1}.[10,32] A strong band at 1620 cm^{-1} is due to C=C stretching vibrations as the HCP builds up,[21] in particular small olefins and other species containing isolated C=C bonds, which would be resonance enhanced in the UV region.[33] By 160 °C two bands are developed, one at 1383 cm^{-1} in the region of CH_3 and CH_2 deformations most likely of olefins,[21,27] and another at 1460 cm^{-1} where the ring stretching in cyclopentadienyl species are exhibited which would be resonance enhanced at this wavelength.[10,34,35] As the temperature increases to 240 °C the zeolite vibrations are attenuated, related to the build-up of hydrocarbon species in the zeolite pores. The data in Figure 148 shows that by UV-Raman, we are able to detect early HCP species prior to the autocatalytic period, including short chain olefins and cyclopentadienyl species, that went undetected at such low temperatures in the data presented in Chapter 3 and published in ref 21. Under

these conditions using a UV-wavelength probe, we are able to detect the precursors of the aromatic cycle.

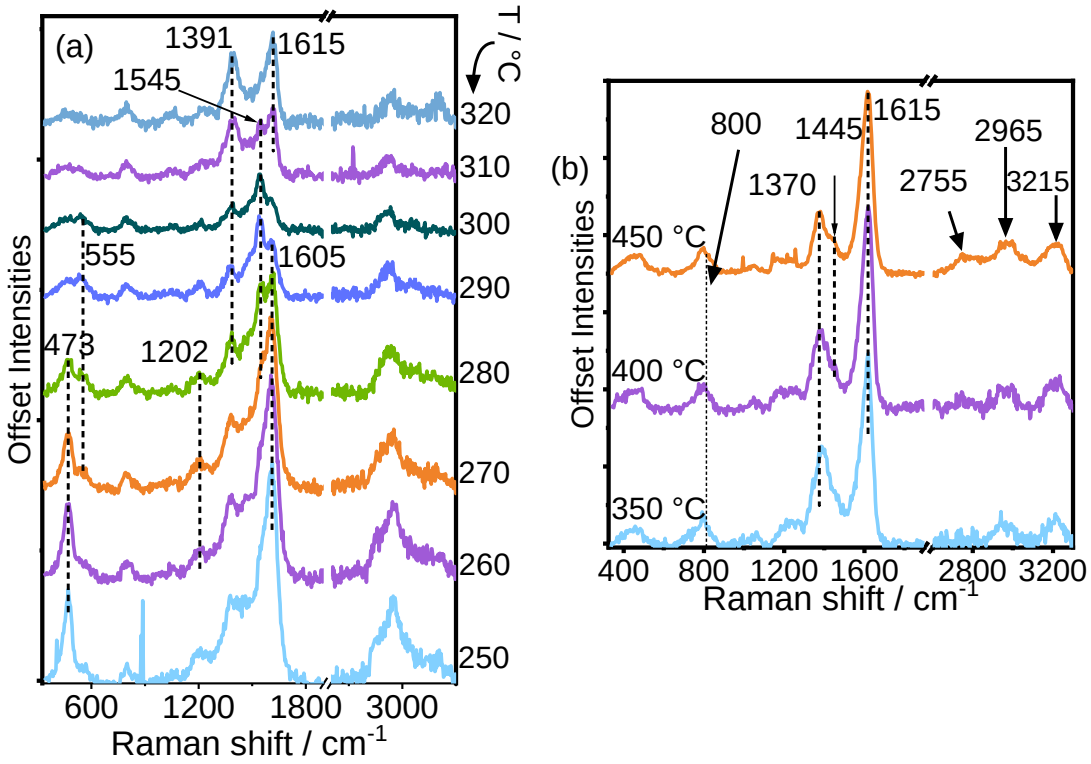

Figure 149 Raman spectra collected using a 277 nm Raman probe during MTH reaction on H-SSZ-13 during temperature ramp 100 to 450 °C. Raman spectra are displayed from (a) 250 to 330 and (b) 350 to 450 °C. The spectrum at 450 °C was collected with 10 times the acquisitions for improved S/N.

Raman spectra recorded from 250 to 320 °C – when the catalyst enters its most active period – are shown in Figure 149a, and Figure 149b from 350 to 450 °C. At 250 °C, an intense C=C stretch at 1605 cm^{-1} dominates the spectrum, with the broad shoulder at 1380 cm^{-1} still indicating the deformations of CH_2 and CH_3 groups.[27] As the temperature is increased to 260 and 270 °C, the vibrations of the zeolite framework further weaken, with the C=C stretch becoming relatively much stronger. In the low frequency region of Figure 149a, note the weak band at 555 cm^{-1} which theoretical calculations predicted to be caused by the C-C-C bending modes of alkyl groups on aromatics or alkylated dienes.[21] During this temperature period, olefin production sharply increases as shown in Figure 148a, and at 280 °C as the maximum in methanol consumption is passed, a new C=C stretch at 1545 cm^{-1} emerges, signalling the formation of long-chain polyenes.[21] These polyenes were observed by Chua and Stair by UV-Raman who first

proposed the assignment to polyenes,[8] before Lezcano-Gonzalez *et al.* by combining *operando* studies and advanced molecular simulations were finally able to confirm the assignment and linked the species with initial catalyst deactivation and eventually, to the formation of polyaromatics.[21] This is shown again beyond 300 °C, as the relative intensity of the 1545 cm^{-1} band drops, and a strong band at 1391 cm^{-1} grows significantly and a more intense band at 1615 cm^{-1} which together indicate the formation of polycyclic aromatic hydrocarbons.[5,9,29]

From 350 to 450 °C, few spectral changes are observed. The strong C=C stretch recorded at 1615 cm^{-1} remains constant in frequency but becomes relatively stronger, and a shift in the signal assigned to breathing modes is observed from 1391 to 1370 cm^{-1}. A shoulder present at higher temperatures at 1445 cm^{-1} is again in agreement with the formation polyaromatics and can be assigned to fluorene or phenanthrene.[9] At high frequency, three bands develop at 2755, 2965 and 3215 cm^{-1} which are second-order Raman bands of the carbon deposits. The band at 2755 cm^{-1} is an overtone of the ring breathing mode at 1370 cm^{-1}, at 2965 cm^{-1} is a combination band of the ring-breathing mode and symmetric C=C stretch at 1615 cm^{-1}, while that at 3215 cm^{-1} is an overtone of the symmetric C=C stretch.[31] These second order transitions are commonly observed in graphitic type carbonaceous species.[31]

6.2.3 Discussion on the application of UV-Raman to MTO

When comparing the Raman results collected using the 267 nm or 400 nm wavelengths as a probe into MTO in H-SSZ-13, the species detected are majorly the same, including methylated benzenium ions, polyenes, and polycyclic aromatic hydrocarbons. Stronger vibrations were observed at lower temperatures of reaction during the induction period by 267 nm excitation which were not observed at 400 nm, namely short-chain olefins and cyclopentadienyl cations. In order to identify these species more clearly, it might be useful in future to use an alternative spectral grating that gives us the opportunity to collect at a higher resolution (though at the expense of spectral range).

In studying H-SAPO-34 using 400 nm, the signal corresponding to polyenes causing the onset of catalyst deactivation is slightly perturbed by strong resonance enhancement of other strongly absorbing species, but this is not the case when studying by 267 nm where a band at 1545 cm^{-1} is clearly identified. Using the UV laser source, the lower frequency vibrations of polyaromatic hydrocarbons were hindered, while with the 400 nm probe these helped to clearly assign polyaromatic hydrocarbons.

6.3 Conversion of furan, acetaldehyde, acetic acid and 2,3-dihydrofuran

During the experiments in this section, the methodology applied in Chapter 5 was repeated to study the conversion of the different model compounds of biomass vapours – furan, acetaldehyde, acetic acid and 2,3-dihydrofuran – over ZSM-5, with a UV-Raman probe. NH_4-ZSM-5 purchased from Zeolyst International with Si/Al 15 was calcined in a muffle furnace at 550 °C to give the proton form of the zeolite, and 30 mg placed in the CCR1000 Linkam Cell. Temperature programmed reactions were performed; an initial catalyst calcination was conducted in 20 % O_2/He at 600 °C for 60 minutes, then the catalyst cooled to 30 °C in 30 ml min^{-1} He before either furan, acetic acid, acetaldehyde or 2,3-dihydrofuran (DHF) was adsorbed on the zeolite by injection of a syringe pump at 1 µl min^{-1} for 1 h into the He stream. The catalyst was flushed with He for 1 h to remove much of the weakly adsorbed species, before the temperature was linearly increased by 5 °C/min from 30 to 600 °C, recording Raman spectra every 5 min and analysing outlet gases by MS. Raman spectra in this section were collected with 6 acquisitions of 4 s at 3 mW power.

6.3.1 Furan

After furan adsorption at 30 °C, a strong and broad C=C stretch is measured at 1615 – 1640 cm^{-1}. In studying the structure of polyfuran with different laser excitation wavelengths, it was found that as wavelength decreased, the C=C stretch vibration increased,[36] this is a result of enhancement of the different chromophores of polyfuran. Upon increasing temperature, some slight changes occur in the Raman spectra, including increased intensity at 1410 cm^{-1}.

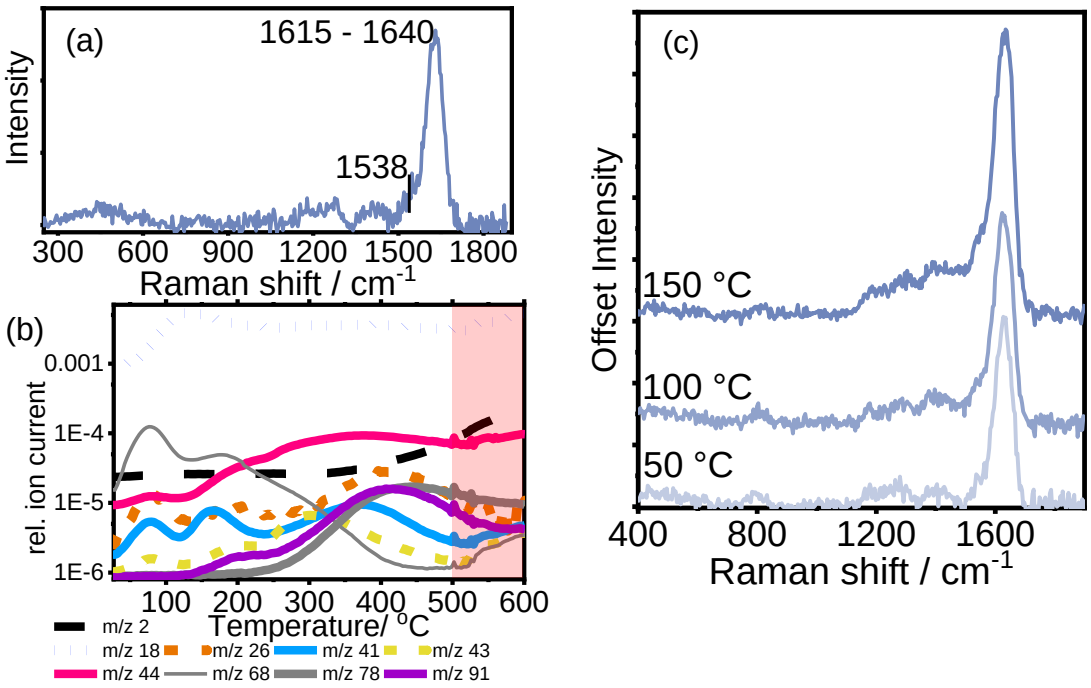

Figure 150 Data collected during furan conversion on H-ZSM-5 (Zeolyst) (a) Spectrum recorded at 30 °C after 1 h of furan adsorption and 1 h of flushing, (b) MS data recorded during the temperature ramp from 100 to 600 °C (from 500 – 600 °C in the area highlighted in red, the MS was in error) and (c) Raman spectra recorded during ramp at 50, 100 and 150 °C.

With an increase in temperature from 150 to 175 °C, a sudden jump in the emission was recorded, this is displayed in Figure 151 which shows the recorded spectra at 25 °C intervals from 150 to 250 °C, without any emission background subtraction, no normalization has been carried out. From 175 to 225 °C, the emission is so strong that no Raman spectrum can be recorded. The emission is observed to have two maxima within the measurement window, at 284 and 293 nm, and containing a regular a pattern of peaks that looks to be attributable to a vibronic effect. This highlights how the use of UV wavelengths for Raman excitation does not always allow emission to be avoided or minimised, as it still here dominates the spectrum and obscures the much weaker Raman signal. During this temperature period it is reasonable to predict that benzofuran might have formed, a molecule with derivatives that are heavily applied as fluorescent probes and even employed as light emitting compounds.[37,38] This strong fluorescent behaviour could be then attributed to the formation of benzofuran but without either the vibrational frequency of the molecule nor the full emission signal this is not possible nor fair to assign.

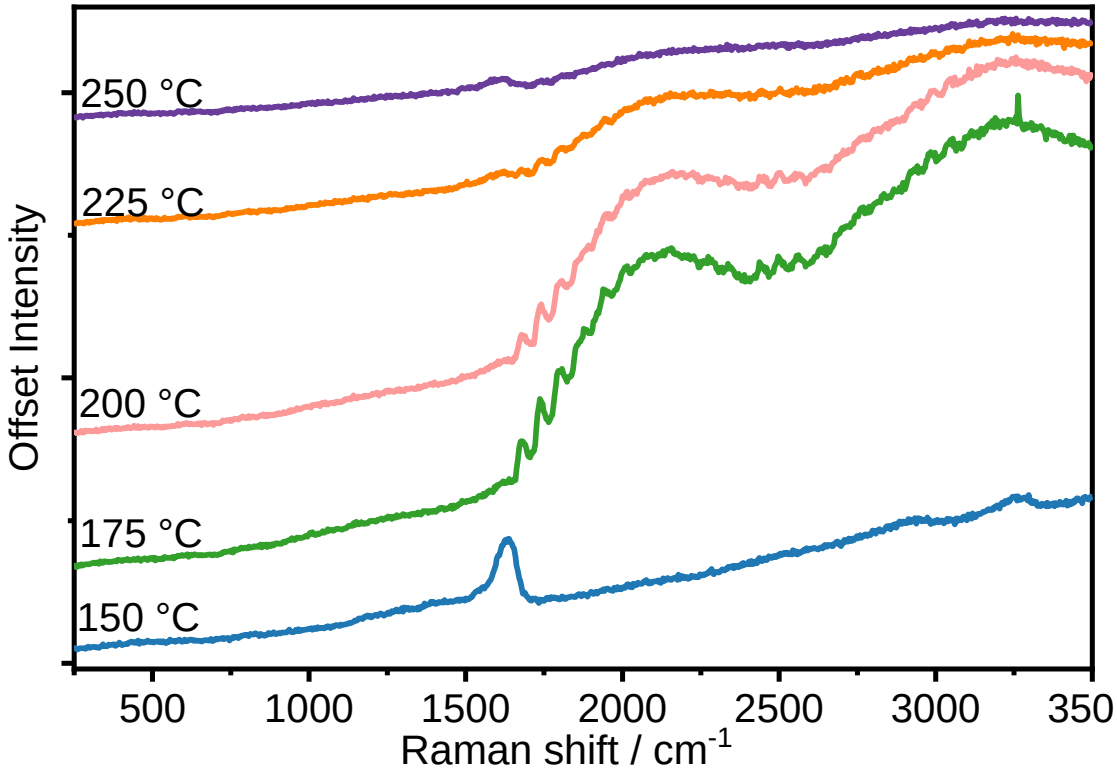

Figure 151 Spectra acquired during furan conversion on H-ZSM-5 zeolite using 267 nm excitation wavelength, from 150 to 250 °C. No backgrounds are subtracted, and the data is not normalized, plotted offset for ease of comparison.

The Raman signal returns from 250 °C where the emission has dropped significantly, the subtracted spectrum is shown in Figure 152a, although a completely clean subtraction was not possible as some of the vibronic signal at 1685 cm^{-1} is still present. Nevertheless, a C=C stretch at 1607 cm^{-1} is recorded and a weaker band at 1512 cm^{-1} in a region where carbocations exhibit their C-C=C^{+} stretch.[22,25]

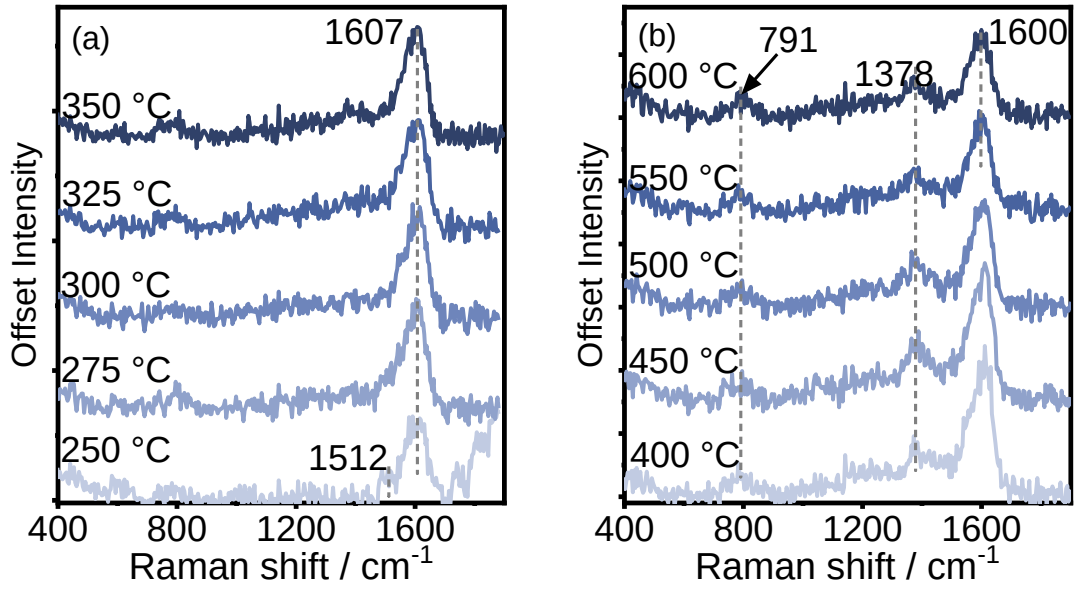

Figure 152 UV-Raman spectra collected during furan conversion at (a) 250 to 350 °C and (b) 400 to 600 °C.

With increasing temperature beyond 250 °C, where aromatic and olefin formation are observed by the MS data presented in Figure 150, little change is observed by Raman. With increasing temperature to 325 °C, the broad C=C stretch becomes sharper and then at 350 °C a new band develops at 1378 cm^{-1} that due to the ring-breathing modes in bi- or polycyclic aromatic hydrocarbons. At lower frequencies, a band at 791 cm^{-1} also grows which was observed in previous chapters at low temperatures and tentatively assigned to an ether-type species,[27] however at high temperatures a vibration here was attributed to the ring-opening vibrations of polyaromatics as shown through theoretical calculations.[21]

In recording spectra with UV-Raman, we missed a key intermediate that was observed in furan conversion on H-ZSM-5 in Chapters 4 and 5 – benzofuran. It may have been possible to assign the fluorescence to benzofuran had we measured across a broader window to get the full emission spectrum.

6.3.2 Acetaldehyde

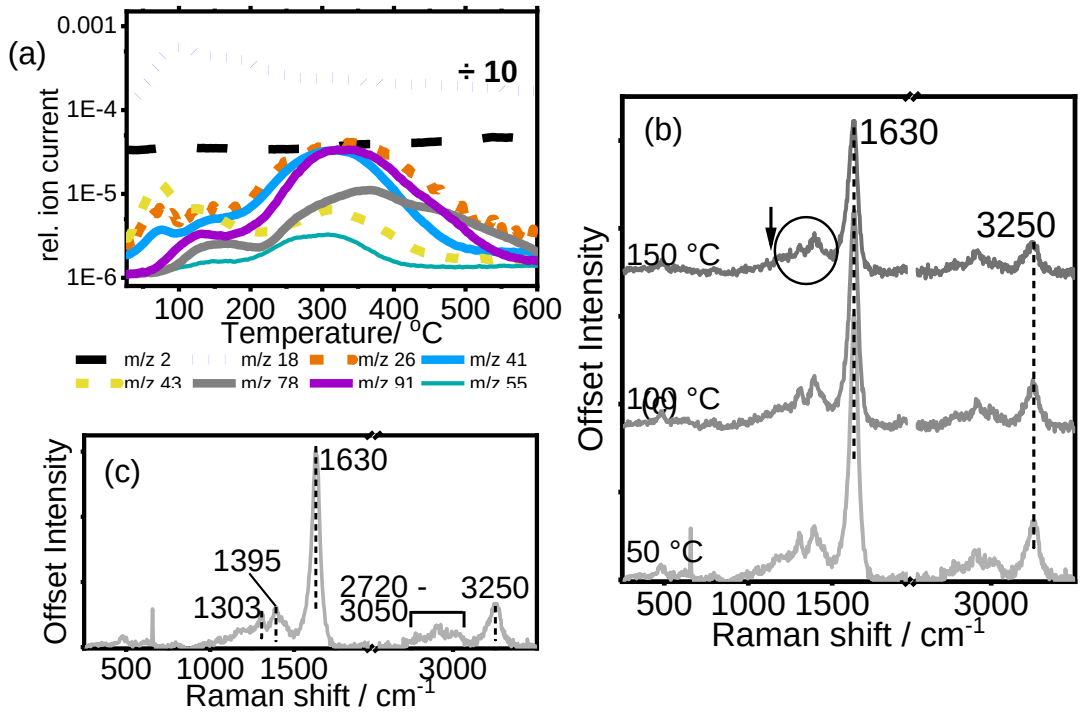

Figure 153 MS data collected during temperature programmed reaction of acetaldehyde from 30 to 600 °C, and (b) Raman spectrum acquired at 30 °C after 1 h of adsorption followed by 1 h of flushing under inert gas and (c) Raman spectra acquired at 50, 100 and 150 °C during ramp.

While overall many signals of the reaction products are convoluted, as in Chapter 5, olefinic and aromatic products are mainly formed above 200 °C. Olefins are the first to form and are observed by the rise in *m/z* 26 and 41, then toluene forms as *m/z* 91 increases, with benzene, *m/z* 78, forming slightly later at 230 °C. Toluene reaches its maximum at 315 °C and then starts to decline, very shortly after olefins decline, possibly due to olefin cyclization to branched aromatics.

At room temperature, a relatively high frequency C=C stretch at 1630 cm^{-1} is assigned to isolated double bonds, which are more likely to be enhanced by the UV-wavelength excitation. The vibration at 1395 cm^{-1} is near the asymmetric CH_3 deformation of acetaldehyde or the H-C=O bend of the aldehyde group,[39,40] and at 1303 cm^{-1} to the in-plane C=C-H bend nearest to the methyl group.[39] Crotonaldehyde contains a C=C stretch which has a frequency observed between 1642 and 1649 cm^{-1}, higher than observed in our spectrum, and a bend

of the C-C=C-C bonds at 465 cm^{-1}.[39,40] The region from 1000 to 1300 cm^{-1} contains some weak convoluted peaks that could be attributed to the C-C stretch of the aliphatic aldehyde, the C=C-H bend near the aldehyde group and asymmetric methyl group deformations.[27,39,41] At 2720 – 3050 cm^{-1} C-H stretches of C-H and CH_3 groups are observed.[39,40] The strong vibration at 3250 cm^{-1} is likely an overtone of the strong C=C stretch. These vibrations are different to those recorded in Chapter 5 – the shorter conjugated species are those enhanced in this case.

With increasing temperature from 150 °C, the C=C stretch shifts to lower frequencies in agreement with increasing conjugation of the surface species, as the vibrations at 1303 and 1395 cm^{-1} are attenuated.

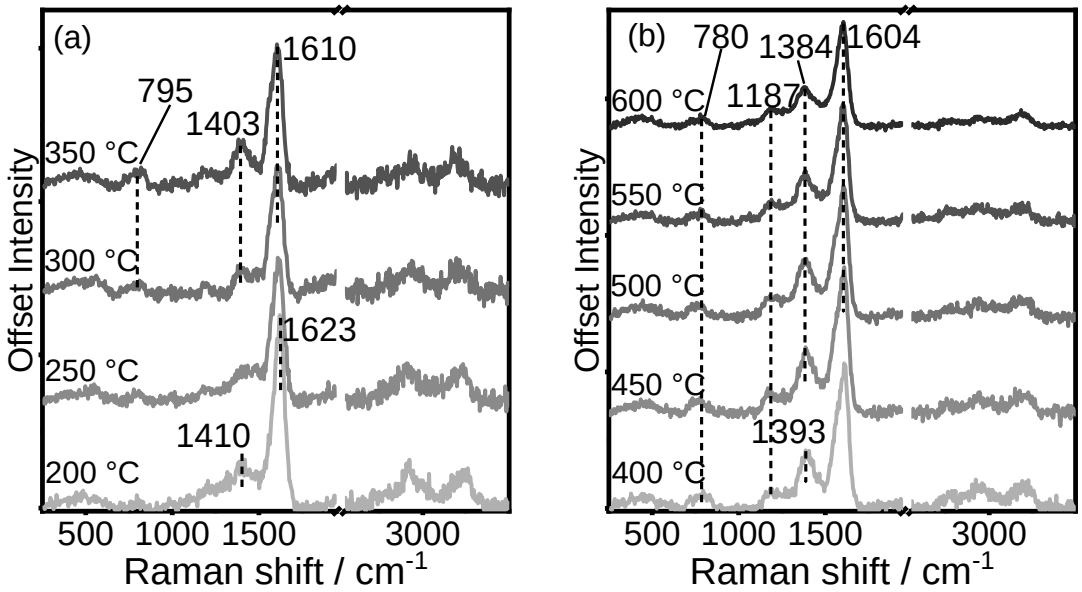

Figure 154 UV-Raman spectra collected during temperature programmed reaction of acetaldehyde on H-ZSM-5 at (a) 200 to 350 and (b) 400 to 600 °C.

The assignment of high frequency bands to overtones is confirmed when the increase in temperature at 200 and 250 °C in Figure 154, which results in a blue shift of the fundamental C=C stretch to 1623 cm^{-1} along with a shift from 3250 to 3230 cm^{-1}. A weak and broad band develops at 1403 cm^{-1} at 200 °C, likely due to methyl group deformations.[27] As this band becomes sharper up to 350 °C it might indicate a stronger vibration, such as ring-breathing modes of polyaromatics,[9] as MS data shows that olefins and toluene formation slows down.

With further temperature increase to 600 °C, as shown in Figure 154b, the C=C stretch shifts to 1604 cm^{-1} and the ring-breathing vibration to 1384 cm^{-1}. [9]

6.3.3 Acetic acid

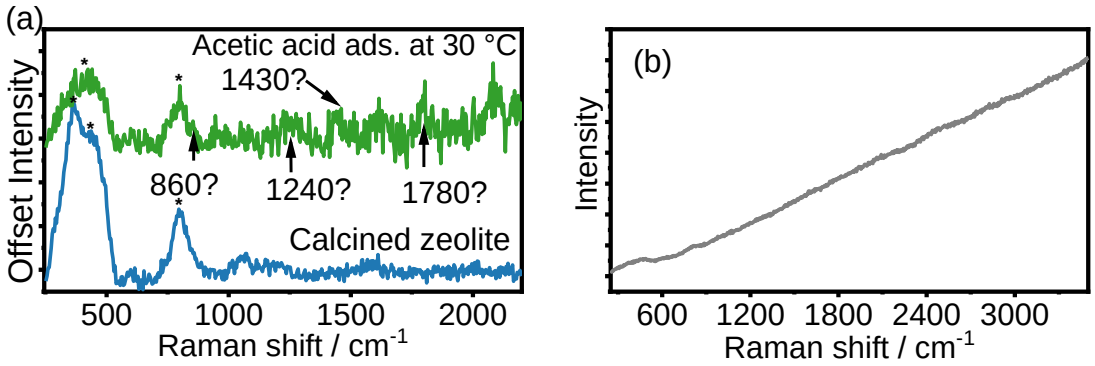

Figure 155 (a) Spectrum collected after adsorption of acetic acid on H-ZSM-5 at 30 °C (green) and of calcined catalyst holding temperature at 600 °C under flowing He (blue), zeolite vibrations are marked with an asterisk. (b) Raw spectrum acquired by UV-Raman probe of acetic acid on H-ZSM-5 (zeolyst) at 30 °C showing the strong emission background compared with low signal intensity.

During the study of acetic acid with H-ZSM-5 by UV-Raman, strong fluorescence was detected. Figure 155a shows the spectrum collected at 30 °C after acetic acid adsorption on H-ZSM-5 in green, with a spectrum of calcined H-ZSM-5 underneath in blue to show clearly where the zeolite vibrations lie. The spectrum shown of the pure, calcined zeolite was collected at 600 °C because in general during these experiments, spectra collected at high temperature resulted in lower levels of emission during experiments and so the spectrum at 600 °C is shown. The higher emission observed at low temperatures seems likely to be due to surface hydroxyl groups and adsorbed water at surfaces,[15,16] which are removed upon heating and return when the reactor is cooled, as shown in Section 6.1.

The spectrum of acetic acid on the zeolite shown in Figure 155b may show some weak signals at 860, 1240 and 1430 cm^{-1}. Similar vibrations were observed in Chapter 5 owing to the C-C stretch, C-O stretch and CH_3 deformation vibrations of acetic acid adsorbed on the zeolite surface.[42,43] There may also be a signal at 1780 cm^{-1} which would correspond to the C=O stretch vibration.[42,43] These

signals are tentatively pointed out since the high level of noise in the spectrum make it difficult to distinguish true Raman signals.

The MS data presented in Figure 156 confirms catalytic activity through the formation of acetone, olefins, CO_2, toluene, and benzene, (by *m/z* 43, 41, 44, 91 and 78, respectively). The behaviour observed is very similar to that in the previous chapter, where acetone and CO_2 form first, followed by C_{3-4} and C_{4-5} olefins, and very closely by aromatic.

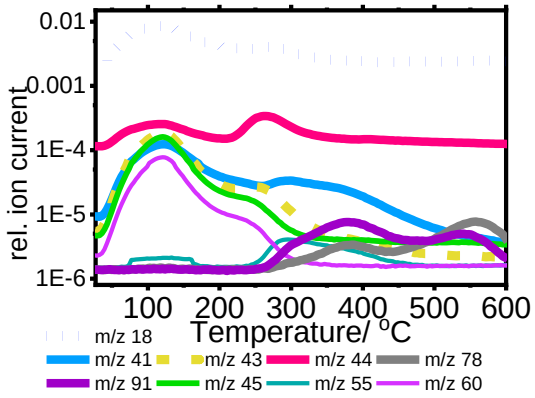

Figure 156 MS data following the reaction products of temperature programmed reaction of acetic acid on H-ZSM-5 from 30 to 600 °C.

Figure 157 shows the UV-Raman spectra collected during the temperature programmed reaction of acetic acid on H-ZSM-5 from 50 to 600 °C at 50 °C intervals. Even though UV excitation should induce greater scattering intensity due to the dependency of scattering intensity on the fourth power of the laser frequency, and additionally, UV excitation is more likely to cause a resonance enhancement effect, a very low signal-to-noise ratio is observed.

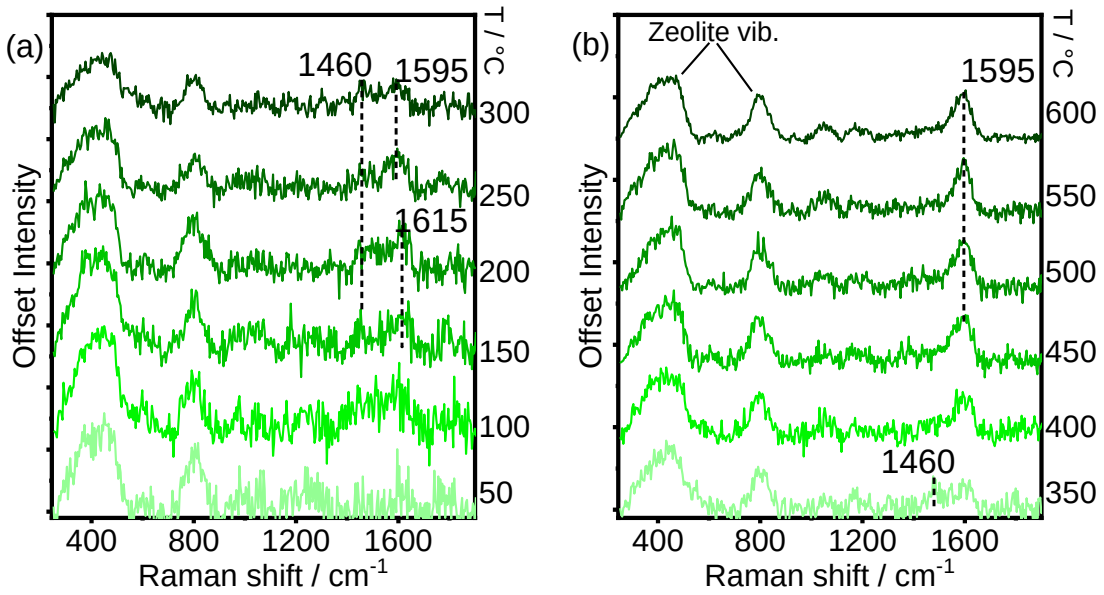

Figure 157 UV-Raman spectra acquired during temperature programmed reaction of acetic acid on H-ZSM-5 (Zeolyst). At 600 °C the spectrum was acquired with 10 acquisitions.

With increasing temperature to 100 °C, two weak and broad signals are recorded at 1460 and 1615 cm^{-1}, which may be assigned to the C=C stretches in cyclopentadienyl species,[10,34] and linear dienes,[21] respectively. As the temperature increases, a red shift is observed for the higher frequency signal from 1615 to 1595 cm^{-1} between 200 and 250 °C, as CO_2 and acetone are detected by MS. A similar change was observed in Chapter 5 while the strong vibration at 885 cm^{-1} signalled the transformation of the acetyl intermediate formed by acetic acid reaction on the zeolite acid site to a more conjugated olefinic species or even to monocyclic aromatics with C=C stretches at 1590 cm^{-1}.[23]

Further heating to 350 °C does not give improved signal intensity, despite seeing a formation of products by MS that would be in resonance with the 267 nm laser. This is possibly due to the high emission background that was collected behind the Raman spectrum and the strong zeolite vibrations may hide some vibrations of the organic species. At 375 °C the band at 1460 cm^{-1} is lost. This band might link an MTH-style aromatic cycle where cyclopentadienyl species as 5-memebered ring species expand to 6-membered rings.[44,45] Interestingly by MS here, the disappearance of this band at 375-400 °C corresponds with a drop in *m/z* 78 and 91 by MS meaning that aromatics are no longer being produced. Any

alternative intermediates were missed which may have been due to the high emission to Raman ratio, or the low Raman cross-section of intermediate species which required excitation by 400 nm to resonance enhance functional groups outside of the C=C stretch of aromatic hydrocarbons at 1595 cm^{-1} and cyclopentadienes at 1460 cm^{-1}.[10,23,35] The band at 1595 cm^{-1} becomes stronger from up to 600 °C, and at 600 °C was collected with 10 collections of 24 seconds to give an enhanced signal-to-noise ratio but still, the only bands detected were zeolite vibrations and a strong band at 1595 cm^{-1} which might be due to a cationic aromatic species.[21,23]

Overall, from this experiment few species were revealed, despite MS data showing that the catalytic activity of acetic acid on H-ZSM-5 in this reaction followed the same pattern that we saw previously. One significant finding from this experiment was the identification of cyclopentadienyl species during the reaction. The acetyl intermediate, which was identified in Chapter 5, Section 5.3.2, was not proven here which further proves that the species absorbs at 400 nm and not at UV wavelengths.

6.3.4 2,3-dihydrofuran

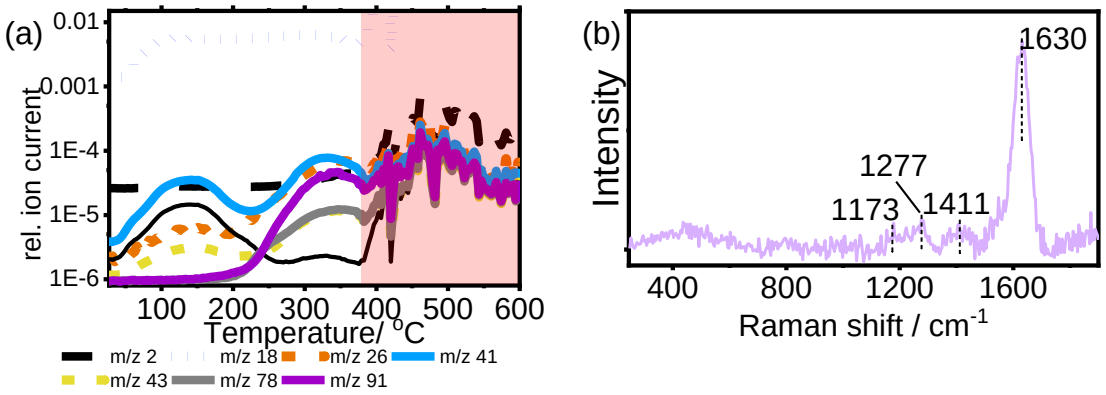

Figure 158 (a) MS data collected during the conversion of 2,3-dihydrofuran on H-ZSM-5 (Zeolyst) during temperature programmed reaction from 30 to 600 °C. The noisy data above 400 °C highlighted in red is due to a technical problem with the equipment and means it is not possible to follow the reaction at this temperature. (b) Spectrum collected after adsorption of 2,3-dihydrofuran on H-ZSM-5 at 30 °C.

Figure 158a shows MS data collected during the reaction of 2,3-dihydrofuran on H-ZSM-5. Initially, 2,3-dihydrofuran is desorbed, and products are formed above

200 °C including olefins followed by the increasing signals at *m/z* 26 and 41, and aromatics by *m/z* 78 and 91. For an unknown reason the MS data above 380 °C became unstable and is therefore unusable, but we can still observe the maxima in $C_{3\text{-}4}$ olefin and toluene production at 330 and 345 °C.

In Figure 158b the spectrum of 2,3-dihydrofuran adsorbed on H-ZSM-5 is shown, which includes a strong C=C stretch at 1632 cm^{-1} that most likely is caused by isolated and neutral C=C bonds,[21] as these would be resonance enhanced in the UV region at 267 nm.[33] Some weaker Raman bands are observed at 1173 – 1277 and 1411 cm^{-1}.

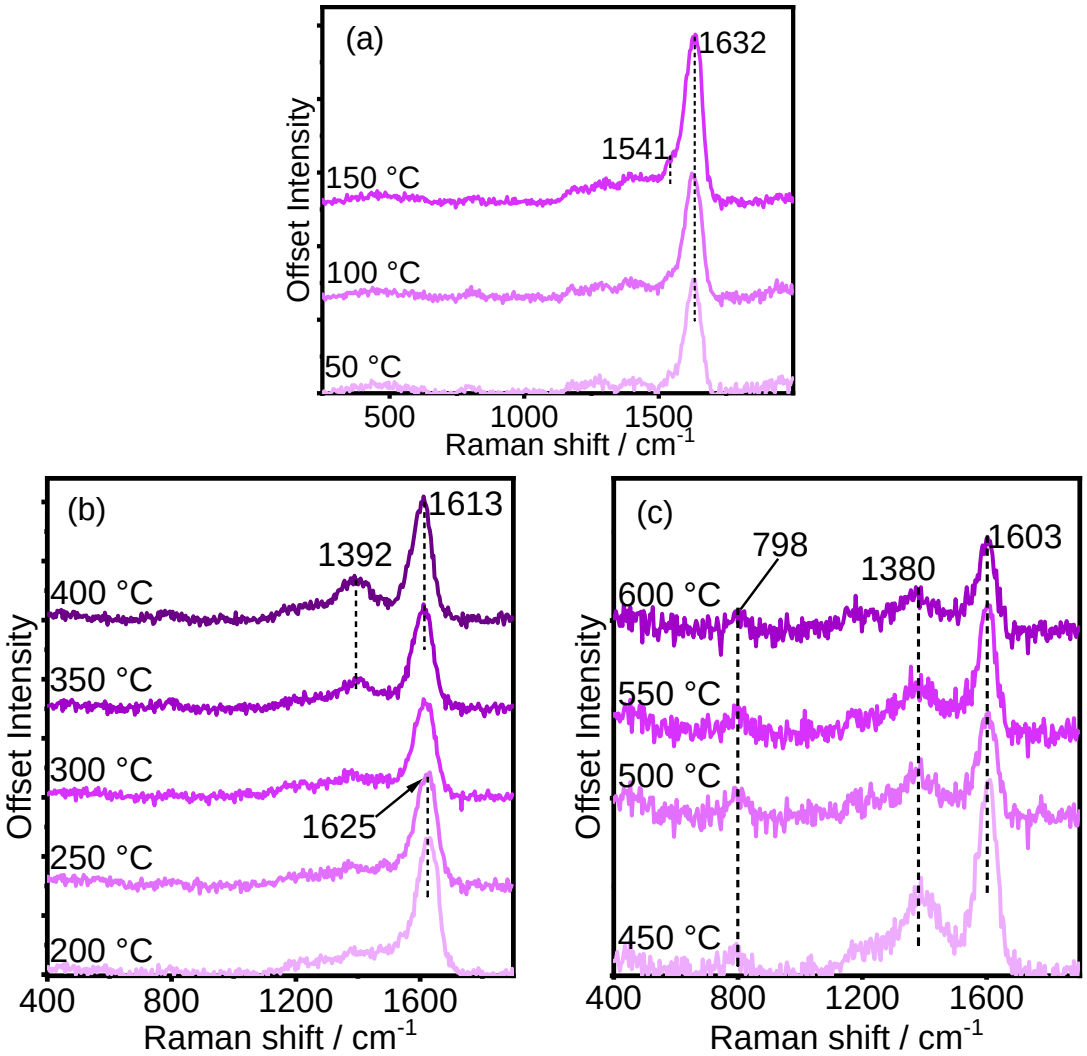

Figure 159 UV-Raman spectra collected during temperature programmed reaction of 2,3-dihydrofuran on H-ZSM-5 at 50 °C from (a) 50 to 150 °C (b) 200 to 400 °C and (c) 450 to 600 °C.

Figure 159 shows the Raman spectra acquired during temperature ramping. In Figure 159a, from 50 to 150 °C, an overall increased intensity is observed. As the temperature is increased to 200 and 250 °C the C=C stretch drops in frequency to 1625 cm^{-1} – this is still a relatively high vibrational frequency that would typically indicate isolated C=C bonds. Another shift is observed from 250 to 350 °C to 1613 cm^{-1} as the carbonaceous species undergo further conjugation to form the aromatic products. At 350 °C the development of a signal at 1392 cm^{-1} could signify CH_3 deformation, but assignment to the breathing modes of bicyclic aromatic hydrocarbons seems the most likely.[9]

In Figure 159c, the spectra at high temperature demonstrate an overall dropping signal intensity. The relative intensity of the breathing mode increases with increasing temperature, as further evidence that these vibrations are caused by the evolving bi- or polycyclic aromatic hydrocarbons and not CH_3 deformations. This vibration drops in frequency to 1384 and then to 1366 cm^{-1}. The C=C stretching vibration also decreases, first to 1610 cm^{-1} and eventually 1603 cm^{-1}. According to the data, the slowing formation of aromatics at 345 °C occurs simultaneously with bicyclic aromatic formation by the growing band at 1392 cm^{-1}.

6.4 Conclusions

Use of UV-wavelength in some cases allowed us to view intermediates that were not detected by KG Raman with using the 400 nm probe. This applies to the clear observation of long-chain polyenes by 267 nm probe in H-SAPO-34; i.e., when using the 400 nm probe combined with Kerr-gating the polyene vibration at 1545 – 1550 cm^{-1} was partially obscured by the stronger vibration of methylbenzenium ions. Also, in the case of conversion of acetic acid – different intermediates were observed in Chapter 5 that were not observed here by UV-Raman. However, by UV-Raman one of two Raman bands that we clearly observe is at 1460 cm^{-1} corresponding to the in-phase C=C stretches in cyclopentadienyl species, species that also absorb with a λ_{max} at 276 nm and would therefore be in resonance with the 267 nm laser.[34] In the conversion of 2,3-dihydrofuran, only a C=C stretch of isolated olefins and then aromatics, and ring breathing modes of bi- or polycyclicaromatics are observed, compared with the KG Raman experiment where an important intermediate with C=C stretch at 1566 cm^{-1} was

observed. By combining UV and visible wavelength excitation a more complete picture can be viewed of these reaction mechanisms.

During the study of furan, acetaldehyde, acetic acid and 2,3-dihydrofuran conversion by UV-Raman, the breathing modes of bicyclic aromatic hydrocarbons were suppressed. Ferrari *et al.* showed that the D-band of amorphous and graphitic carbon are suppressed by use of UV excitation, so that this effect is applicable across systems.[30] The low frequency vibrations associated with the ring-opening of polyaromatic hydrocarbons which were clearly visible during the deactivation of H-SAPO-34 and H-SSZ-13 in MTH when a 400 nm probe was used,[21] are also not observed by UV-Raman.

Use of UV-wavelength does not entirely remove the problem of emission, but in almost all cases the emission could be subtracted to leave a Raman spectrum that could be interpreted. The only case where this was not possible was in the conversion of furan in the temperature period where benzofuran is likely to have formed, here no Raman signal was detected and only very strong emission.

6.5 References

1. E. Smith and G. Dent, Modern Raman Spectroscopy: a practical approach, John Wiley & Sons Ltd., Chichester, England, 2004.
2. P. C. Stair, Advances in Catalysis, 2007, 51, 75–98.
3. S. P. A. Fodor, R. P. Rava, T. R. Hays and T. G. Spiro, Journal of the American Chemical Society, 1985, 107, 1520–1529.
4. H. Kim, K. M. Kosuda, R. P. V. Duyne and P. C. Stair, Chemical Society Reviews, 2010, 39, 4820–4844.
5. M. Signorile, F. Bonino, A. Damin and S. Bordiga, The Journal of Physical Chemistry C, 2015, 119, 11694–11698.
6. M. Signorile, D. Rojo-Gama, F. Bonino, P. Beato, S. Svelle and S. Bordiga, Physical Chemistry Chemical Physics, 2018, 20, 26580–26590.
7. H. An, F. Zhang, Z. Guan, X. Liu, F. Fan and C. Li, ACS Catalysis, 2018, 8, 9207–9215.
8. Y. T. Chua and P. C. Stair, Journal of Catalysis, 2003, 213, 39–46.
9. P. M. Allotta and P. C. Stair, ACS Catalysis, 2012, 2, 2424–2432.
10. Y. T. Chua, P. C. Stair, J. B. Nicholas, W. Song and J. F. Haw, Journal of the American Chemical Society, 2003, 125, 866–867.
11. S. A. Asher and C. R. Johnson, Science, 1984, 225, 311–313.

12. P. Beato, E. Schachtl, K. Barbera, F. Bonino and S. Bordiga, Catalysis Today, 2013, 205, 128–133.
13. Y. T. Chua and P. C. Stair, Journal of Catalysis, 2000, 196, 66–72.
14. Y. T. Chua, P. C. Stair and I. E. Wachs, Journal of Physical Chemistry B, 2001, 105, 8600–8606.
15. G. Careri, V. Mazzacurati, M. Sampoli and G. Signorelli, Journal of Catalysis, 1972, 26, 494–496.
16. H. Jeziorowski and H. Knözinger, Chemical Physics Letters, 1977, 51, 519–522.
17. H. Schulz, Z. Siwei and H. Kusterer, in Studies in Surface Science and Catalysis, eds. T. lnui, S. Namba and T. Tatsumi, Elsevier, 1991, vol. 60, pp. 281–290.
18. J. Tan, Z. Liu, X. Bao, X. Liu, X. Han, C. He and R. Zhai, Microporous and Mesoporous Materials, 2002, 53, 97–108.
19. J. Li, G. Xiong, Z. Feng, Z. Liu, Q. Xin and C. Li, Microporous and Mesoporous Materials, 2000, 39, 275–280.
20. Y. Yu, Y. Wang, K. Lin, N. Hu, X. Zhou and S. Liu, Journal of Physical Chemistry A, 2013, 117, 4377–4384.
21. I. Lezcano-Gonzalez, E. Campbell, A. E. J. Hoffman, M. Bocus, I. V. Sazanovich, M. Towrie, M. Agote-Aran, E. K. Gibson, A. Greenaway, K. De Wispelaere, V. Van Speybroeck and A. M. Beale, Nature Materials, 2020, 19, 1081–1087.
22. C. Pazè, B. Sazak, A. Zecchina and J. Dwyer, Journal of Physical Chemistry B, 1999, 103, 9978–9986.
23. M. Bjørgen, F. Bonino, S. Kolboe, K.-P. Lillerud, A. Zecchina and S. Bordiga, Journal of the American Chemical Society, 2003, 125, 15863–15868.
24. A. Baruya, D. L. Gerrard and W. F. Maddams, Macromolecules, 1983, 16, 578–580.
25. G. Spoto, F. Geobaldo, S. Bordiga, C. Lamberti, D. Scarano and A. Zecchina, Topics in Catalysis, 1999, 8, 279.
26. S. Bordiga, G. Ricchiardi, G. Spoto, D. Scarano, L. Carnelli, A. Zecchina and C. Otero Areán, Journal of the Chemical Society, Faraday Transactions, 1993, 89, 1843–1855.
27. J. Socrates, Infrared and Raman characteristic group frequencies tables and charts, John Wiley and Sons, Chichester, 3rd ed., 2001.
28. E. Borodina, H. Sharbini Harun Kamaluddin, F. Meirer, M. Mokhtar, A. M. Asiri, S. A. Al-Thabaiti, S. N. Basahel, J. Ruiz-Martinez and B. M. Weckhuysen, ACS Catalysis, 2017, 7, 5268–5281.
29. E. Cloutis, P. Szymanski, D. Applin and D. Goltz, Icarus, 2016, 274, 211–230.
30. A. C. Ferrari and J. Robertson, Physical Reviews B, 2000, 61, 14095–14107.
31. A. Sadezky, H. Muckenhuber, H. Grothe, R. Niessner and U. Pöschl, Carbon, 2005, 43, 1731–1742.
32. C. L. Angell, Journal of Physical Chemistry, 1973, 77, 222–227.
33. P. J. Garratt, UV-vis atlas of organic compounds, Heinz-Helmut Parkampus, Weinheim, 2nd Ed., 1992.
34. E. D. Hernandez and F. C. Jentoft, ACS Catalysis, 2020, 10, 5764–5782.

35. E. Gallinella, B. Fortunato and P. Mirone, Journal of Molecular Spectroscopy, 1967, 24, 345–362.
36. V. Hernandez, F. J. Ramirez and J. T. Lopez Navarrete, Chemical Physics Letters, 1992, 191, 419–422.
37. J. R. Hwu, K. S. Chuang, S. H. Chuang and S. C. Tsay, Organic Letters, 2005, 7, 1545–1548.
38. P. Krawczyk, Journal of Molecular Modelling, 2020, 26, 272.
39. R. Lindenmaier, S. D. Williams, R. L. Sams and T. J. Johnson, Journal of Physical Chemistry A, 2017, 121, 1195–1212.
40. H. J. Oelichmann, D. Bougeard, B. Schrader, Journal of Molecular Structure, 1981, 77, 179–194.
41. V. V. Ordomsky, V. L. Sushkevich and I. I. Ivanova, Journal of Molecular Catalysis A: Chemical, 2010, 333, 85–93.
42. J. E. Bertie and K. H. Michaelian, Journal of Chemical Physics, 1982, 77, 5267–5271.
43. N. Nishi, T. Nakabayashi and K. Kosugi, Journal of Physical Chemistry A, 1999, 103, 10851–10858.
44. M. Bjørgen, S. Svelle, F. Joensen, J. Nerlov, S. Kolboe, F. Bonino, L. Palumbo, S. Bordiga and U. Olsbye, Journal of Catalysis, 2007, 249, 195–207.
45. J. Goetze, F. Meirer, I. Yarulina, J. Gascon, F. Kapteijn, J. Ruiz-Martínez and B. M. Weckhuysen, ACS Catalysis, 2017, 7, 4033–4046.

7 Conclusions and future work

7.1 Conclusions

The initial study in Chapter 3 presenting the reaction of methanol over H-SSZ-13 catalyst highlights polyenes as an important intermediate in the deactivation pathway. Under both temperature ramping conditions and isothermal conditions, methanol consumption as recorded semi-quantitatively by mass spectrometry (MS) slows down as polyenes are detected by Raman. After polyenes form, polyaromatic hydrocarbons soon follow, rendering the catalyst completely deactivated. H-ZSM-5 and H-SSZ-13 were impregnated with Ca with the aim of preventing the “aromatic cycle” in the methanol-to-hydrocarbons (MTH) mechanism. In Ca-ZSM-5 this was mostly successful, though some aromatics were observed as products by MS at very high reaction temperatures, and Raman and UV-Vis results also suggested the formation of minor amounts of aromatic hydrocarbons on the surface, but UV-Vis results proved that these aromatics were neutral and not carbocationic as would typically be expected during MTH. The hydrocarbon fingerprints of aromatics are clear during MTH in Ca-SSZ-13, indicating that not enough Brønsted acidity was removed to prevent hydride transfer reactions, probably due to the majority of Ca species being located in the outer surface of the zeolite crystals.

The MTH reaction (which is presently used commercially) will almost certainly continue to play a role in small olefin production as an alternative source than steam cracking of naphtha, and towards building up hydrocarbons from C1 sources, potentially as a source of bio-olefins through bio-derived methanol. For this project, beginning the thesis by studying the MTH reaction was particularly helpful as a reaction that has been studied extensively in literature. It gave us an idea and understanding of the typical species that could be detected in the Raman data and certainly gave us a foundation to begin studying the more exploratory Catalytic Fast Pyrolysis reaction.

In comparing 4 zeolites in the conversion of furan, Chapter 4 highlights the significance of benzofuran as an intermediate in H-ZSM-5, leading to monocyclic

aromatics probably through decarbonylation reactions, which later condense to polyaromatic hydrocarbons as coke. These findings were observed by Kerr-gated Raman and UV-Vis spectroscopy. In H-ferrierite, intra-molecular reactions were seriously hindered, with intermediate temperatures required to decarboxylate furan to propene and CO_2. In contrast, larger pore zeolites H-Y and H-beta allowed the formation of large extended polymers of furan at low temperatures. Of the zeolites tested, the 3-dimensional medium pores of ZSM-5 offer a compromise between the inhibited diffusion limitations in ferrierite and the poor compartmentalization of Y and Beta that allow the formation of bulky “intermediates” that lead to coke. The combination of UV-Vis spectroscopy with Raman is very helpful in identifying groups of hydrocarbons that might be present and for supporting assignments.

The comparisons in converting furan, 2,3-dihydrofuran, acetaldehyde and acetic acid showed that the hydrocarbon pools formed in each case at low-intermediate temperatures were composed of different intermediates. In all cases, at high temperatures aromatic and olefinic products were detected. In all cases at high temperatures the speciation of the pools become broadly similar, as the maximum aromatic formation is followed by the growth of a band at 1566 cm^{-1}. The identification and behaviour of this new species requires further investigation but its prevalence in all tested feed molecules in H-ZSM-5 suggests that at higher temperatures, the hydrocarbon pool becomes more of a function of the zeolite.

A limitation to working with isolated model compounds is that we may not see the full picture of all possible reaction pathways, but they are useful for understanding step-wise mechanisms. Nonetheless, from these studies the next logical step could be to compare with mixtures of model compounds or more realistic vapours of biomass pyrolysis to study more real-life systems.

UV Raman has highlighted some intermediate species that were otherwise not observed by 400 nm excitation. These experiments prove that resonance enhancement plays a major role in the intermediates that might be detected – in most cases giving us different insights by use of the 267 or 400 nm wavelength laser. The repeated experiments by UV-Raman highlighted that cyclopentadienyl species are present during aromatic formation by reaction of acetic acid on

H-ZSM-5. In an ideal world, such *operando* Raman experiments would be conducted with probes of UV, visible and NIR wavelengths to allow us to understand the electronic properties of molecules through the selective enhancement of chromophores within the molecules as well as their vibrational identification.

Overall, the application of Kerr-gated Raman spectroscopy has offered a useful method for the analysis of hydrocarbon species on zeolite catalysts, the analysis of which can often be hindered by strong fluorescence from benchtop Raman spectrometers, or by sample darkening by IR. Thus, offering opportunities to probe structure-activity relationships through studying under *operando* methods. Currently, the use of the optical Kerr-gate for this application is heavily dependent on access to a unique facility at the Central Laser Facility, and time allocated is very limited and a strong case for running experiments is required each time. Alternative time-gating technologies do exist that can be used in lab settings, although not with such a fast rejection as 1 – 3 ps. The first commercialised Time-gated Raman Spectrometer available known as PicoRaman boasts 100 ps rejection. In our experiments we always noted strong emission at very short time delays within a few ps of the maximum Raman signal and is lost by 10 or 50 ps, which would not be cut from reaching the detector by the PicoRaman system.

During data collection, we had to compromise signal-to-noise ratio in many cases by decreasing the laser power to prevent sample burning. This was particularly a problem in the conversion of furan, because the red/orange samples were highly absorbing and initial measurements with > 8 mW power led to a visibly burnt sample. To avoid damage, for example, we ran the experiments of Chapter 4 using 1 mW power, do the detriment of Raman signal intensity. The limited facility access meant that we were not always able to perfectly optimise the conditions for each measurement/reaction as we might under normal lab conditions.

7.2 Future work

If time were allowing, it would be helpful to completely analyse the effluent gases by GC (off-line). The semi-quantitative data acquired herein is helpful for understanding trends in the catalytic activity but between reactions it is not

possible to compare reactivity in terms of selectivity and conversion that might add value in some cases. Additionally, by MS it can be complicated to know how many species contribute to each mass-to-charge ratio. Regarding assignments in converting biomass model compounds, some theoretical calculations would aid us in assignments and in understanding most of the Raman observations, as they did in MTH. Chapter 5 could be expanded with further experiments with UV-Vis to support Raman assignments and understand the character of many intermediates. Particularly in conversion of acetic acid and acetaldehyde, IR data at low temperatures (prior to sample darkening) would help to follow C-O bond changes. In all cases, PXRD studies might be helpful to determine where in the catalyst structure carbon laydown occurs first, inside the pore channels, intersections, or externally.

Appendix

Isothermal reaction of H-SSZ-13 catalyst at 450 °C

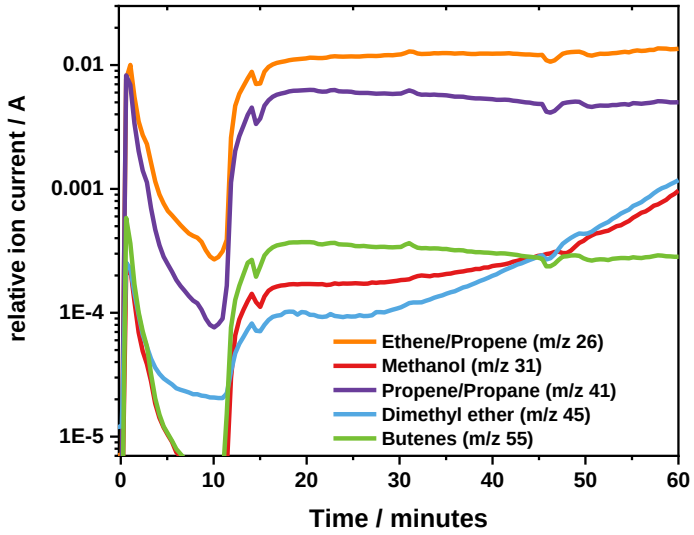

Figure 160 MS data acquired during reaction of methanol on H-SSZ-13 catalyst at 450 °C where the methanol was not delivered uniformly and a drop in signal is observed after the initial dosing until 10 minutes later when the methanol delivery recovers.

Unfortunately, due to an issue with the methanol delivery system, a burst of methanol was delivered to the sample and then a stable methanol flow lost for 10 minutes. The MS data is shown in Figure 160 where signals for products, the olefins, as well as methanol and DME initially rise, and then drop significantly over the next 10 minutes before recovering. The data collected at 450 °C cannot be deemed reliable with respect to activity of the catalyst, and unfortunately due to the restricted but a comment can still be made on the speciation observed. The experiment was repeated in our lab in combination with UV-Vis data, to confirm the catalyst behaviour and further understand the effect of increasing temperature in an isothermal reaction, this data is shown in Figure 162.

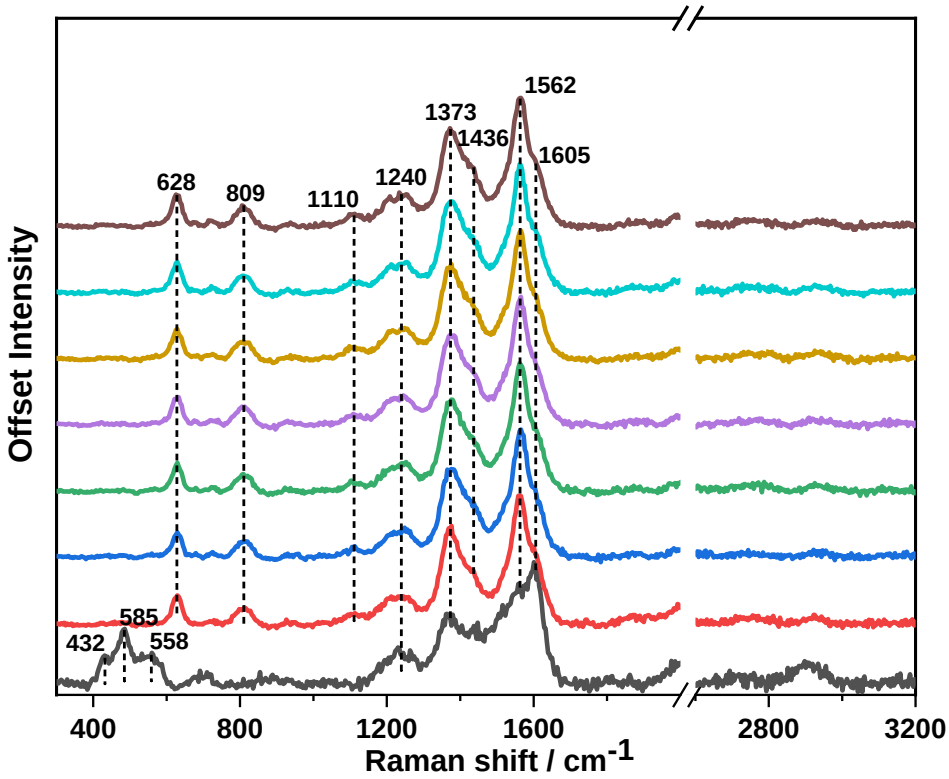

Figure 161 Kerr-gated Raman spectra collected during methanol reaction on H-SSZ-13 at 450 °C with a fault in the methanol delivery system.

Upon the introduction of methanol, the hydrocarbon pool rapidly develops, with mainly typical bands at 1605 cm^{-1}, 1370 cm^{-1}, 1240 cm^{-1} and the low frequency at 432 cm^{-1} and 558 cm^{-1}. The zeolite band at 475 cm^{-1} has already become very low in intensity. By the second measurement at 5 minutes, intense bands have formed at 628 cm^{-1} and 809 cm^{-1} relating to polyaromatic hydrocarbon species. The band at 1373 cm^{-1} again signals the formation of bicyclic or polyaromatic ring breathing modes. A shoulder at 1436 cm^{-1} suggests the formation of polycyclic aromatic species such as fluorene containing a 5-membered ring.

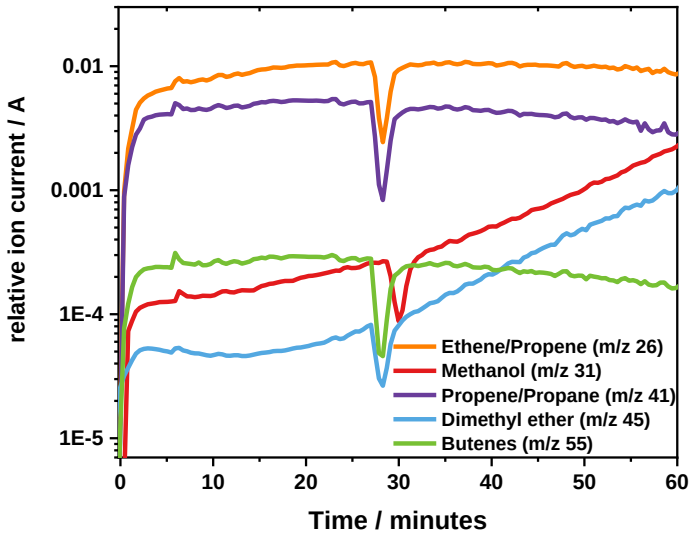

Figure 162 MS data acquired during methanol reaction over H-SSZ-13 at 450 °C repeated in a lab setting without the Raman probe.